

© Copyright by Richa Raj 2014
All Rights Reserved

**Kinetics and Mechanistic Studies of Hydrocarbon Oxidation
and Selective Catalytic Reduction of NO_x in Monolith Reactors**

A Dissertation

Presented to

the Faculty of the Department of Chemical and Biomolecular Engineering

University of Houston

In Partial Fulfillment

of the Requirements for the Degree

Doctor of Philosophy

in Chemical Engineering

by

Richa Raj

December 2014

**Kinetics and Mechanistic Studies of Hydrocarbon Oxidation
and Selective Catalytic Reduction of NO_x in Monolith Reactors**

Richa Raj

Approved:

Co-Chairman of the Committee
Vemuri Balakotaiah, Professor,
Chemical and Biomolecular Engineering

Co-Chairman of the Committee
Michael P. Harold, Professor,
Chemical and Biomolecular Engineering

Committee Members:

William S. Epling, Associate Professor,
Chemical and Biomolecular Engineering

Matthew A. Franchek, Professor,
Mechanical Engineering

Karolos Grigoriadis, Professor,
Mechanical Engineering

Suresh Khator, Associate Dean,
Cullen College of Engineering

Michael P. Harold, Professor and Chair
Chemical and Biomolecular Engineering

Acknowledgements

I would like to express my sincere gratitude to my advisors Prof. Michael P. Harold and Prof. Vemuri Balakotaiah for their guidance, continuous support and motivation throughout my PhD. I thank them for sharing their knowledge and giving me sufficient time in my research. I am thankful to the other members of my dissertation committee, Prof. William S. Epling, Prof. Matthew A. Franchek, and Prof. Karolos Grigoriadis, for making their time available to me, despite their busy schedules. Additionally, I would like to acknowledge the faculty and staff of the Department of Chemical and Biomolecular Engineering at the University of Houston.

I would like to thank all my coworkers, Priyank Maheswari, Pankaj Kumar, Aseem, Arun Kota, Santosh Gundlapally, Imran Alam, Sachi Shrestha, Yang Zhang, and Ram Ratnakar for their support through the course of this work and for making our lab such a pleasant place to work. I would like to thank Pranit Metkar and Di Wang for helping me with my experiments. I would like to express my gratitude to Bijesh Shakya for his help with FORTRAN and for educative discussions during my PhD. I would like to thank all my friends, Rahul Pandey, Ashutosh Srivastava, Meenakshi Sharma, Ushashi Ghosh, Garima Srivastava, and Swati Vishwas for making my stay in Houston so memorable. I would like to thank my very good friends Sarika Goel and Hera Naaz for their constant encouragement, support and cheerful phone conversations. I really consider myself fortunate to have become friends with these great and amazing personalities. I wish all of them great success. I would also like to acknowledge Saurabh Joshi and Ashok kumar for their help during my PhD.

Finally, I would like to express my love and gratitude to my parents for their unconditional love, encouragement, motivation, strong support, and many sacrifices. I am grateful to have such amazing parents. I would also like to thank my sisters and brothers, Surabhi Raj, Shikha Raj, Saurabh Raj, Manish Chaudhary, and Navneet Kumar for all of their fruitful advice, help and support throughout my life.

**Kinetics and Mechanistic Studies of Hydrocarbon Oxidation
and Selective Catalytic Reduction of NO_x in Monolith Reactors**

An Abstract

of a

Dissertation

Presented to

the Faculty of the Department of Chemical and Biomolecular Engineering

University of Houston

In Partial Fulfillment

of the Requirements for the Degree

Doctor of Philosophy

in Chemical Engineering

by

Richa Raj

December 2014

vii

Abstract

The integrated LNT/SCR system is a promising technology for the reduction of NO_x emission from the exhaust of lean-burn or diesel engine vehicles. The LNT/SCR operating concept involves the storage of NO_x during the lean phase while unreacted hydrocarbons (C_3H_6 , C_2H_4 etc.) and generated NH_3 exit the LNT during the rich phase. In addition to NH_3 , olefinic hydrocarbons and/or partially oxidized species that break through the LNT may also adsorb on the SCR catalyst leading to additional NO_x reduction by those species.

In first part of the work, we performed bench-flow reactor and *in-situ* DRIFTS experiments to elucidate the propylene + NO + O_2 reaction system on Cu-SSZ13 (chabazite) monolithic catalyst. Experiments were conducted under both steady state and transient conditions for application relevant feed conditions. Based on the bench-flow reactor studies and *in-situ* DRIFTS experiments a phenomenological reaction mechanism is proposed that involves reaction between oxygenates (partially oxidized hydrocarbon species) and NO to form isocyanates species ($-\text{NCO}$), detected by DRIFTS which are further reduced to N_2 .

The experimental work is followed by developing a mechanistic-based kinetic model is developed for selective catalytic reduction of NO with C_3H_6 on Cu chabazite (Cu-SSZ13) monolithic catalyst based on bench scale flow reactor studies and *in-situ* DRIFTS measurements. The kinetic model was developed in steps, starting with steady-state CO oxidation, followed by C_3H_6 oxidation, and then the C_3H_6 + NO + O_2 reaction system. The models for $\text{CO}+\text{O}_2$, $\text{C}_3\text{H}_6+\text{O}_2$ and $\text{C}_3\text{H}_6+\text{NO}+\text{O}_2$ were also validated using a new set of steady state experiments. The model provides insight about non- NH_3 pathways

(hydrocarbons, oxygenates, isocyanates etc.) for NO_x reduction across the SCR. Finally, we developed a global kinetic model for co oxidation of CO and C_3H_6 over $\text{Pt}/\text{Al}_2\text{O}_3$ monolithic catalyst. The kinetic model developed is used to elucidate the dynamic and steady state hysteresis behavior observed during oxidation of $\text{CO}+\text{C}_3\text{H}_6$ mixture on $\text{Pt}/\text{Al}_2\text{O}_3$.

Table of Contents

Acknowledgement	v
Abstract	viii
Table of Contents	x
List of Figures	xiv
List of Tables	xxiii
Nomenclature	xxiv
CHAPTER 1 Introduction.....	1
1.1 Background	1
1.2 Diesel oxidation catalyst.....	6
1.3 Diesel particulate filter.....	8
1.4 Lean NO _x reduction technologies	9
1.4.1 NO _x storage and reduction (NSR).....	10
1.4.2 Selective catalytic reduction (SCR).....	13
1.4.3 Combined LNT+SCR	18
1.5 Research objectives and outlines	19
CHAPTER 2 Experimental.....	23
2.1 Introduction.....	23
2.2 Catalysts	23
2.3 Bench scale reactor setup.....	24
2.2.1 Gas supply system.....	25
2.2.2 Reactor system.....	26
2.2.3 Analysis system	27

2.2.4	Data acquisition	28
2.3	<i>In-situ</i> DRIFTS	28
CHAPTER 3 Mathematical Modeling of Catalytic Monoliths.....		29
3.1	Introduction.....	30
3.2	Modeling of monolith reactors.....	31
3.2.1	One-dimensional model.....	32
3.2.2	(1+1)-dimensional model.....	35
3.2.3	Detailed 3D model.....	37
3.3	Numerical solution methods	40
CHAPTER 4 Selective Catalytic Reduction of NO _x with C ₃ H ₆ over Cu-SSZ13		
Monolithic Catalyst: Steady-State and Transient Bench-flow Reactor Studies		41
4.1	Introduction.....	41
4.2	Experimental.....	44
4.2.1	Catalyst	44
4.2.2	Bench-scale reactor setup	44
4.2.3	Steady state experiments.....	45
4.2.4	Transient experiments.....	46
4.2.5	Varied catalyst length experiments.....	47
4.3	Results and discussion	47
4.3.1	NO/NO+C ₃ H ₆ adsorption – desorption.....	47
4.3.2	NO oxidation/NO ₂ decomposition	49
4.3.3	Effect of catalyst pretreatment on NO ₂ adsorption	50
4.3.4	C ₃ H ₆ oxidation	53

4.3.5 NO ₂ reduction with C ₃ H ₆ under lean conditions.....	58
4.3.6 NO reduction with C ₃ H ₆ under lean conditions.....	65
4.4 Conclusions.....	75
CHAPTER 5 In-situ DRIFTS Studies of Selective Catalytic Reduction of NO with C ₃ H ₆ over Cu-SSZ13 Catalyst	77
5.1 Introduction.....	77
5.2 Experimental.....	78
5.3 Results and discussion	78
5.5 Conclusions.....	84
CHAPTER 6 Kinetic Modeling of NO Selective Reduction with C ₃ H ₆ over Cu-SSZ13 Monolithic Catalyst.....	85
6.1 Introduction.....	85
6.2 Model development	87
6.2.1 Reactor model	87
6.2.2 Reaction mechanism and parameter estimation.....	90
6.2.3 Kinetic model for CO oxidation (CO + O ₂)	92
6.2.4 Kinetic model for C ₃ H ₆ oxidation C ₃ H ₆ + O ₂	97
6.2.5 Kinetic model for C ₃ H ₆ + NO + O ₂	102
6.3 Results and discussion	106
6.4 Conclusions.....	123
CHAPTER 7 Steady-state and Dynamic Hysteresis Effects During Co-oxidation of CO and C ₃ H ₆ over Pt/Al ₂ O ₃ Diesel Oxidation Monolithic Catalyst	126
7.1 Introduction.....	126

7.2 Model development	127
7.2.1 Reactor model	127
7.2.2 Kinetic model and parameter estimation	132
7.2.2.1 Global kinetic model for CO oxidation	133
7.2.2.2 Global kinetic model for C ₃ H ₆ oxidation.....	134
7.2.2.3 Global kinetic model for CO + C ₃ H ₆ oxidation	136
7.3 Results and discussion	141
7.3.1 Dynamic hysteresis.....	141
7.3.2 Steady state hysteresis.....	148
7.4 Conclusions and discussion	156
CHAPTER 8 Conclusions and Recommendations for Future Work.....	158
8.1 Conclusions.....	158
8.2 Recommendations for future work	162
References.....	163
Appendix.....	185

List of Figures

Figure 1-1 Fuel consumption and conversion of key pollutants (CO, NO _x and HC) as a function of air-fuel (A/F) ratio.....	2
Figure 1-2 Emission standards for the heavy-duty trucks in the U.S., g/bhp-hr.....	4
Figure 1-3 Schematic of diesel aftertreatment system.....	5
Figure 2-1 Schematic diagram of the experimental set-up used in this study	24
Figure 3-1 Typical catalytic converter used in automobile	30
Figure 3-2 Schematic of catalytic channel with arbitrary shape showing different notations and domains.....	37
Figure 4-1 NO adsorption and desorption over fresh catalyst (NO = 500 ppm, Balance gas: Ar).....	48
Figure 4-2 NO adsorption and desorption over catalyst pre adsorbed with 500 ppm C ₃ H ₆ (NO = 500 ppm, Balance gas: Ar)	49
Figure 4-3 Steady state conversion as a function of temperature for NO/NO ₂ feed (NO = 500 ppm, O ₂ = 5%, Balance gas: Ar) (NO ₂ = 500 ppm, O ₂ = 5%, Balance gas: Ar)	50
Figure 4-4 NO ₂ and NO outlet concentration with time on exposure of NO ₂ over O ₂ pretreated and H ₂ pretreated catalysts (NO ₂ = 500 ppm, Balance gas: Ar)	52
Figure 4-5 (a) Light- off curves of C ₃ H ₆ for different oxygen concentrations in the feed (C ₃ H ₆ =500 ppm, O ₂ =0.5 or 1 or 5%, Bal gas: Ar), (b) Light-off curves of C ₃ H ₆ for different C ₃ H ₆ concentrations (C ₃ H ₆ = 200 or 500 ppm, O ₂ = 1 %, Bal gas: Ar).....	68
Figure 4-6 CO selectivity curve in C ₃ H ₆ oxidation (C ₃ H ₆ = 500 ppm, O ₂ = 1 or 5%, Balance gas: Ar).....	54

Figure 4-7 (a) Dependence of C₃H₆ oxidation rates on C₃H₆ (1% O₂, 200–800 ppm C₃H₆)
(b) Dependence of C₃H₆ oxidation rates on O₂ (0.5-3% O₂, 500 ppm C₃H₆), (Rate is in moles.m⁻³.s⁻¹, concentration is in moles.m⁻³)56

Figure 4-8 CO, H₂O and CO₂ peaks obtained during temperature ramp from 200 °C to 600 °C in presence of O₂ (O₂ = 5%, Balance gas: Ar).....57

Figure 4-9 C₃H₆ conversion in presence of 2.5% H₂O (C₃H₆ = 500 ppm, O₂ = 1%, H₂O = 2.5%, Balance gas: Ar)58

Figure 4-10 (a) C₃H₆ light off curves with and without NO₂ in feed (C₃H₆ = 500 ppm, NO₂ = 0 or 500 ppm, O₂ = 1%), (b) C₃H₆ light off curves with and without NO₂ in feed (C₃H₆ = 500 ppm, NO₂ = 0 or 500 ppm, O₂ = 5%) (Balance gas: Ar).....60

Figure 4-11 (a) NO₂ and C₃H₆ conversion (C₃H₆ = 500 ppm, NO₂ = 500 ppm, O₂ = 1%, Balance gas: Ar), (b) NO and N₂ outlet concentration (C₃H₆ = 500 ppm, NO₂ = 500 ppm, O₂ = 1%, Balance gas: Ar).....61

Figure 4-12 Spatially resolved steady state NO concentration at different temperatures (C₃H₆ = 500 ppm, NO₂ = 500 ppm, O₂ = 1%, Balance gas: Ar)63

Figure 4-13 a) Spatially resolved steady state NO₂ conversion at different temperatures
(b) Spatially resolved steady state C₃H₆ conversion at different temperatures (C₃H₆ = 500 ppm, NO₂ = 500 ppm, O₂ = 1%, Bal. gas: Ar).....64

Figure 4-14 C₃H₆, NO₂ and NO outlet concentration with time (C₃H₆ = 500 ppm, NO₂ = 0 or 500 ppm, O₂ = 1%, Balance gas: Ar)65

Figure 4-15 (a) C₃H₆ light off curves with and without NO in feed (C₃H₆ = 500 ppm, NO = 0 or 500 ppm, O₂ = 1%), (b) C₃H₆ light off curves with and without NO in feed (C₃H₆ = 500 ppm, NO = 0 or 500 ppm, O₂ = 5%) (Balance gas: Ar).....66

Figure 4-16 C ₃ H ₆ light off curves with and without NO in feed in presence of H ₂ O (C ₃ H ₆ = 500 ppm, NO = 0 or 500 ppm, O ₂ = 5%, H ₂ O = 2.5%, Balance gas: Ar)	67
Figure 4-17 C ₃ H ₆ and NO conversion at different temperatures (C ₃ H ₆ = 500 ppm, NO = 500 ppm, O ₂ = 1%, Balance gas: Ar), C ₃ H ₆ and NO conversion at different temperatures (C ₃ H ₆ = 500 ppm, NO = 500 ppm, O ₂ = 5%, Balance gas: Ar)	70
Figure 4-18 (a) C ₃ H ₆ conversion at different temperatures (b) NO conversion at different temperatures (C ₃ H ₆ = 500 ppm, NO = 500 ppm, O ₂ = 1%, H ₂ O = 0 or 2.5%, Balance gas: Ar).....	70
Figure 4-19 (a) C ₃ H ₆ and NO outlet concentration with time at 300 °C, (b) 350°C, (C ₃ H ₆ = 500 ppm, NO = 0 or 500 ppm, O ₂ = 1%, Balance gas: Ar)	71
Figure 4-20 C ₃ H ₆ and NO outlet concentration with time at 380°C (C ₃ H ₆ = 500 ppm, NO = 0 or 500 ppm, O ₂ = 1%, Balance gas: Ar)	72
Figure 4-21 Dependence of C ₃ H ₆ oxidation rate on NO. C ₃ H ₆ = 500 ppm, NO = 200- 800 ppm, O ₂ = 1%, Catalyst: Cu-chabazite. Balance gas: Ar. Total flow rate = 1000 sccm. (Rate is in moles.m ⁻³ .s ⁻¹ , concentration is in moles.m ⁻³)	73
Figure 4-22 (a) C ₃ H ₆ and NO outlet concentration with time at 300 °C, (b) 325°C, (C ₃ H ₆ = 500 ppm, NO = 0 or 500 ppm, O ₂ = 5%, Balance gas: Ar)	73
Figure 4-23 C ₃ H ₆ and NO outlet concentration with time at 350°C (C ₃ H ₆ = 500 ppm, NO = 0 or 500 ppm, O ₂ = 5%, Balance gas: Ar)	74
Figure 4-24 C ₃ H ₆ and NO outlet concentration with time at 350 °C in presence of H ₂ O (C ₃ H ₆ = 500 ppm, NO = 0 or 500 ppm, O ₂ = 1%, H ₂ O = 2.5%, Balance gas: Ar)	75

Figure 5-1 DRIFTS spectra obtained at different times upon Cu-SSZ13 exposure to 500 ppm NO after 45 minutes of exposure to 500 ppm C ₃ H ₆ at 300 °C (500 ppm C ₃ H ₆ , 1% O ₂ , balanced by He).....	79
Figure 5-2 DRIFTS spectra obtained at different times upon Cu-SSZ13 exposure to 500 ppm C ₃ H ₆ at 380 °C (500 ppm C ₃ H ₆ , 1% O ₂ , balanced by He).....	80
Figure 5-3 Emergence of new peak upon exposure to 500 ppm NO after 45 minutes of exposure to 500 ppm C ₃ H ₆ at 380 °C (500 ppm C ₃ H ₆ , 500 ppm NO, 1% O ₂ , balanced by He)	81
Figure 5-4 Emergence of new peak upon exposure to 500 ppm NO after 45 minutes of exposure to 500 ppm C ₃ H ₆ at 325 °C (500 ppm C ₃ H ₆ , 500 ppm NO, 5% O ₂ , balanced by He)	82
Figure 5-5 Reaction steps involved in selective catalytic reduction of NO with C ₃ H ₆	83
Figure 6-1 DRIFTS spectra for CO adsorption on Cu-SSZ13 pretreated with O ₂ at 200°C (CO=500 ppm, Balance gas: He).....	93
Figure 6-2 Fitted light- off curves of CO (a) CO = 200 ppm, O ₂ = 1 %, Balance gas: Ar, (b) CO = 300 ppm, O ₂ = 1 and 5 %, Balance gas: Ar.....	95
Figure 6-3 Comparison between measured and predicted CO conversion versus temperature (a) CO = 200 ppm, O ₂ = 5 %, Balance gas: Ar, (b) CO = 500 ppm, O ₂ = 1 and 5 %, Balance gas: Ar.....	96
Figure 6-4 Fitted light- off curves of C ₃ H ₆ (a) C ₃ H ₆ = 200 ppm, O ₂ = 5 %, Balance gas: Ar, (b) C ₃ H ₆ = 500 ppm, O ₂ = 1 and 5 %, (c) C ₃ H ₆ = 300 ppm, O ₂ = 5 %, Balance gas: Ar.....	100

Figure 6-5 Comparison between measured and predicted C ₃ H ₆ conversion versus temperature (a) C ₃ H ₆ = 200 and 500 ppm, O ₂ = 1 and 0.5%, Balance gas: Ar, (b) C ₃ H ₆ = 750 ppm, O ₂ = 5 %, Balance gas: Ar.....	101
Figure 6-6 Fitted C ₃ H ₆ and NO conversion versus temperature (C ₃ H ₆ = 500 ppm, NO = 500 ppm, O ₂ = 5%, Balance gas: Ar.....	105
Figure 6-7 Comparison between measured and predicted C ₃ H ₆ and NO conversion versus temperature (a) C ₃ H ₆ = 500 ppm, NO = 250 ppm, O ₂ = 5%, Balance gas: Ar, (b) C ₃ H ₆ = 750 ppm, NO = 250 ppm, O ₂ = 5%, Balance gas: Ar	106
Figure 6-8 (a) Predicted dependence of CO oxidation rates on CO (5% O ₂ , 400–800 ppm CO), (b) Predicted dependence of CO oxidation rates on O ₂ . Feed for CO order: 0.5-5% O ₂ , 500 ppm CO, Balance gas: Ar) GHSV = 57,000 h ⁻¹	107
Figure 6-9 Predicted light- off curves of C ₃ H ₆ (C ₃ H ₆ = 100-800 ppm, O ₂ = 1 %, Balance gas: Ar).....	109
Figure 6-10 Predicted light- off curves of C ₃ H ₆ (a) C ₃ H ₆ = 100-750 ppm, O ₂ = 5 %, Balance gas: Ar, (b) C ₃ H ₆ = 500 ppm, O ₂ = 0.5-5 %, Balance gas: Ar.....	109
Figure 6-11 (a) Predicted dependence of C ₃ H ₆ oxidation rates on C ₃ H ₆ (5% O ₂ , 200–800 ppm C ₃ H ₆) (b) Predicted dependence of C ₃ H ₆ oxidation rates on O ₂ . Feed for C ₃ H ₆ order: 0.5-5% O ₂ , 500 ppm C ₃ H ₆ , Balance gas: Ar).....	110
Figure 6-12 Predicted coverage of C ₃ H ₄ O(Cu(I)) within the washcoat (C ₃ H ₆ = 500 ppm, O ₂ = 1 %, Balance gas: Ar).....	112
Figure 6-13 Predicted coverage of Cu(I) within the washcoat (C ₃ H ₆ = 500 ppm, O ₂ = 1 %, Balance gas: Ar)	113

Figure 6-14 a) NO conversion versus temperature ($C_3H_6 = 500, 750, 1000$ ppm, NO = 250 ppm, $O_2 = 5\%$), (b) NO conversion versus temperature for different inlet O_2 concentration ($C_3H_6 = 500$ ppm, NO = 500 ppm, $O_2 = 5\%$ & 10%)115

Figure 6-15 Predicted NO conversion for different ion exchange ratios (NO = 500 ppm, $C_3H_6 = 500$ ppm, $O_2 = 5\%$, Balance gas: Ar)116

Figure 6-16 (a) Ratio of cup-mixing C_3H_6 mole fraction in fluid phase to intrawashcoat C_3H_6 mole fraction with axial position, (b) Ratio of cup-mixing NO mole fraction in fluid phase to intrawashcoat NO mole fraction with length117

Figure 6-17 (a) C_3H_6 light off curves with and without NO in feed ($C_3H_6 = 500$ ppm, NO = 0 or 500 ppm, $O_2 = 5\%$), (b) C_3H_6 light off curves with and without NO in feed ($C_3H_6 = 750$ ppm, NO = 0 or 250 ppm, $O_2 = 5\%$)118

Figure 6-18 (a) C_3H_6 and NO outlet concentration with time at (b) $300^\circ C$, (b) $325^\circ C$, (c) $350^\circ C$ (Experiment) (d) $300^\circ C$, (e) $325^\circ C$, (f) $350^\circ C$ ($C_3H_6 = 500$ ppm, NO = 0 or 500 ppm, $O_2 = 5\%$, Balance gas: Ar, Model predictions).....120

Figure 6-19 Predicted averaged oxygenate and isocyanate species coverage on Cu sites with time ($C_3H_6 = 500$ ppm, NO = 0 or 500 ppm $O_2 = 5\%$, Balance gas: Ar). ..121

Figure 6-20 Predicted coverage of $-NCO$ species within the wash-coat ($C_3H_6 = 500$ ppm, NO = 500 ppm $O_2 = 5\%$, Balance gas: Ar).....123

Figure 7-1 Fitted light-off curve of CO (Abedi et al. [155], CO = 1000 ppm, $10\% O_2$, $10\% H_2O$, $10\% CO_2$; Space velocity of $25,000 h^{-1}$ at STP; Temperature ramp = $3^\circ C/min$).....135

Figure 7-2 Fitted light-off curve of C ₃ H ₆ (Abedi et al. [155], C ₃ H ₆ = 800 ppm, 10% O ₂ , 10% H ₂ O, 10% CO ₂ ; Space velocity of 25,000 h ⁻¹ at STP; Temperature ramp = 3°C/min).....	135
Figure 7-3 (a) Fitted light-off curve of CO (b) Fitted light-off curve of C ₃ H ₆ (CO = 1000 ppm, C ₃ H ₆ = 800 ppm, 10% O ₂ , 10% H ₂ O, 10% CO ₂ ; Space velocity of 25,000 h ⁻¹ at STP; Temperature ramp = 3°C/min).....	137
Figure 7-4 (a) Comparison between measured and predicted CO conversion (b) Comparison between measured and predicted C ₃ H ₆ conversion (CO = 1000 ppm, C ₃ H ₆ = 500 ppm, 10% O ₂ ; Temperature ramp = 3°C/min [155]).....	139
Figure 7-5 (a) Comparison between predicted CO oxidation rates in absence and in presence of C ₃ H ₆ in the feed, (b) Comparison between predicted C ₃ H ₆ oxidation rates in absence and in presence of CO in the feed.....	140
Figure 7-6 (a) Predicted steady state CO conversion versus inlet fluid temperature (b) Predicted steady state C ₃ H ₆ conversion versus inlet fluid temperature (CO = 500 ppm, C ₃ H ₆ = 300 ppm, 10% O ₂ ; Space velocity of 25,000 h ⁻¹ at STP).....	143
Figure 7-7 (a) Predicted CO conversion versus inlet fluid temperature (b) Predicted C ₃ H ₆ conversion versus inlet fluid temperature (CO = 500 ppm, C ₃ H ₆ = 300 ppm, 10% O ₂ ; GHSV of 25,000 h ⁻¹ at STP; Temperature ramp = 3°C/min).....	144
Figure 7-8 (a) Predicted CO conversion versus inlet fluid temperature (b) Predicted C ₃ H ₆ conversion versus inlet fluid temperature (CO = 500 ppm, C ₃ H ₆ = 300 ppm, 10% O ₂ ; GHSV of 25,000 h ⁻¹ at STP; Temperature ramp = 10°C/min).....	145

Figure 7-9 (a) Predicted spatial profile of solid temperature (a) during ramp up from 80°C to 190°C (b) during ramp down from 190°C to 80°C (CO = 500 ppm, C₃H₆ = 300 ppm, 10% O₂; Temperature ramp = 10°C/min)146

Figure 7-10. (a) Predicted CO conversion versus inlet fluid temperature (b) Predicted C₃H₆ conversion versus inlet fluid temperature (CO = 500 ppm, C₃H₆ = 300 ppm, 10% O₂; Temp. ramp = 10°C/min; Heat of reaction = 0 kJ/mol)147

Figure 7-11. Predicted steady state spatial profile of solid temperature when inlet fluid temperature is decreased in steps of 5°C from 200°C to 70°C (CO = 2000 ppm, C₃H₆ = 2000 ppm, 10% O₂; GHSV of 25,000 h⁻¹ at STP, Pe_h = 5)149

Figure 7-12. (a) Predicted steady state CO conversion vs inlet fluid temperature (b) Predicted steady state C₃H₆ conversion vs inlet fluid temperature (CO = 2000ppm, C₃H₆ = 1200ppm, 10%O₂; GHSV of 25,000 h⁻¹ at STP, Pe_h = 5).....150

Figure 7-13. (a) Predicted steady state CO conversion versus inlet fluid temperature (b) Predicted steady state C₃H₆ conversion versus inlet fluid temperature (CO = 2000ppm, C₃H₆=2000ppm, 10%O₂; GHSV of 25,000 h⁻¹ at STP, Pe_h = 5).....151

Figure 7-14 (a) Predicted CO conversion vs inlet fluid temperature (b) Predicted C₃H₆ conversion vs inlet fluid temperature (CO = 2000 ppm, C₃H₆ = 1200 ppm, 10% O₂; GHSV of 25,000 h⁻¹ at STP; Pe_h = 5; Temp ramp = 3°C/min).....152

Figure 7-15. (a) Predicted steady state CO conversion versus inlet fluid temperature (b) Predicted steady state C₃H₆ conversion versus inlet fluid temperature (CO =2000ppm, C₃H₆=1200ppm, 10%O₂; GHSV of 25,000h⁻¹ at STP; Pe_h = 51).....154

Figure 7-16 (a) Predicted CO conversion vs inlet fluid temperature (b) Predicted C₃H₆ conversion vs inlet fluid temperature (CO = 2000 ppm, C₃H₆ = 1200 ppm, 10% O₂; GHSV of 25,000 h⁻¹ at STP; Pe_h = 51; Temp ramp = 3°C/min).....155

List of Tables

Table 1-1 Proposed Tier 3 Standards (FTP-75; 150,000 miles), mg/mil.....	3
Table 2-1 Specifications of the gases used in this study.....	25
Table 2-2 Gas standards used for FTIR	27
Table 5-1 Wavenumber corresponding to adsorbed species.....	83
Table 6-1 Constant parameters used in the simulation	89
Table 6-2 Temperature dependent parameters used in the simulation	90
Table 6-3 Catalyst properties	91
Table 6-4 Kinetic steps involved in CO oxidation.....	92
Table 6-5 Experiments with CO + O ₂	94
Table 6-6 Reaction steps involved in C ₃ H ₆ oxidation	98
Table 6-7 Experiments with C ₃ H ₆ + O ₂	99
Table 6-8. Reaction steps involving NO	103
Table 6-9 Experiments with C ₃ H ₆ +NO+O ₂	103
Table 6-10 Kinetic parameters used in the simulation.....	104
Table 7-1 Constant parameters used in the simulation	130
Table 7-2 Temperature dependent parameters used in the simulation	131
Table 7-3 Catalyst properties	132
Table 7-4 Kinetic parameters used in the simulation.....	138

Nomenclature

a	width/hydraulic diameter of the channel (m)
$C_{fm,j}$	cup-mixing concentration of species j in fluid phase
$\langle C_{wc} \rangle_j$	volume averaged concentration of species j in the washcoat
C_{S1}	concentration of Cu sites (mol/m ³ _{wc})
C_{S2}	concentration of Bronsted sites (mol/m ³ _{wc})
$c_{p,f}$	specific heat capacity of fluid (J/kg-K)
$c_{p,w}$	specific heat capacity of solid (wall) (J/kg-K)
$D_{f,j}$	diffusivity of species j in the fluid phase (m ² /s)
$D_{e,j}$	effective diffusivity species j in the washcoat (m ² /s)
$k_{me,j}$	external mass transfer coefficient of species j (m/s)
$k_{mi,j}$	internal mass transfer coefficient of species j (m/s)
L	length of the monolith (m)
k_w	thermal conductivity of solid (wall) (W/m-K)
k_f	thermal conductivity of fluid (W/m-K)
R_{Ω_1}	effective transverse diffusion length for flow area (m)
R_{Ω_2}	effective transverse diffusion length for washcoat area (m)
S_i	cycle-averaged selectivity of species i
Sh_e	external Sherwood number
Sh_i	internal Sherwood number
t	time (s)
T_f	fluid phase temperature (K)

$T_{f,in}$	inlet fluid phase temperature (K)
T_{f0}	initial fluid phase temperature (K)
T_s	monolith temperature (K)
T_{s0}	initial monolith temperature (K)
$\langle u \rangle$	average fluid velocity in the fluid phase(m/s)
$x_{fm,j}$	cup-mixing mole fraction of species j in fluid phase
$x_{fm,j}^0$	initial cup-mixing mole fraction of species j in fluid phase
$x_{wc,j}$	cup-mixing mole fraction of species j in washcoat
z	axial coordinate (m)

Greek letters

δ_c	washcoat thickness
Γ	site concentration (mol/m _{wc} ³)
ϑ_{jr}	stoichiometric coefficient species j for reaction r
θ_k	fractional surface coverage of species k
Ω_1	cross-sectional domains of the fluid phase
Ω_2	cross-sectional domains of the washcoat phase
ε_{wc}	porosity of washcoat
ρ_f	density of fluid (kg/m ³)
ρ_w	density of solid (wall) (kg/m ³)
ΔH_j	heat of reaction j (kJ/mol)

Abbreviations

EGR	Exhaust Gas Recirculation
EPA	Environmental Protection Agency
FTP	Federal Test Procedure
LNT	Lean NO _x Trap
NSR	NO _x Storage and Reduction
PGM	Precious group metal
SCR	Selective Catalytic Reduction
TWC	Three-Way Catalyst

CHAPTER 1 Introduction

1.1 Background

The use of fossil fuels for internal combustion engines inherently cause emissions that have environmental and health implications. Higher fuel efficiency and stringent regulations on emissions are the major driving force for the development of the advanced engine design and exhaust aftertreatment systems [1-3]. A gasoline engine is a spark-ignition engine which uses a spark plug to ignite an air fuel mixture. In contrast to the gasoline engine, a diesel engine, also known as a compression-ignition engine, uses the heat of compression to initiate ignition to burn the fuel. Diesel or lean-burn engine vehicles are more fuel efficient compared to traditional gasoline engine. Other benefits of diesel engine include lower CO₂ emissions, higher power production and durability.

Emissions are formed in following ways: (i) incomplete combustion creates CO and unburned hydrocarbons, as well as soot (ii) other hydrocarbon reactions can form polynuclear aromatic components and other volatile organic compounds (VOCs) (iii) NO_x forms from the nitrogen in air during combustion. NO_x emissions are primary pollutants as they undergo photochemical reaction that lead to ground level ozone formation, and cause various respiratory related health hazards [3]. Thus the US EPA (Environmental Protection Agency) has set stringent emission standards to minimize the emissions of harmful pollutants into the atmosphere. These standards have become more and more stringent over the last few decades.

The conventional three-way catalyst (TWC) used in the normal gasoline engine vehicle is capable of removing the three key pollutants *viz.* carbon monoxide (CO), nitrogen oxides (NO_x) and hydrocarbon (HC) or unburned fuel, simultaneously from the

exhaust. Figure 1-1 shows a typical plot of fuel consumption and three-way performance, defined as the removal of CO, NO_x and HC, of a gasoline engine vehicle as a function of air-fuel (A/F) ratio [4]. The stoichiometric A/F ratio is defined as the amount of air required to completely oxidize the fuel. For gasoline, the (A/F)_{stoichiometric} is approximately 14.6 (wt/wt). A typical lean-burn engine operates at the air-fuel (A/F) ratio of 25:1 and above, which gives better fuel economy. While efficient oxidation of CO and HC can be attained by the traditional approach, higher NO_x conversion cannot be achieved over the TWC converter under these conditions [4]. Therefore, both auto and catalyst industries are working to develop new technologies for higher fuel efficiency and to meet stringent emissions regulations.

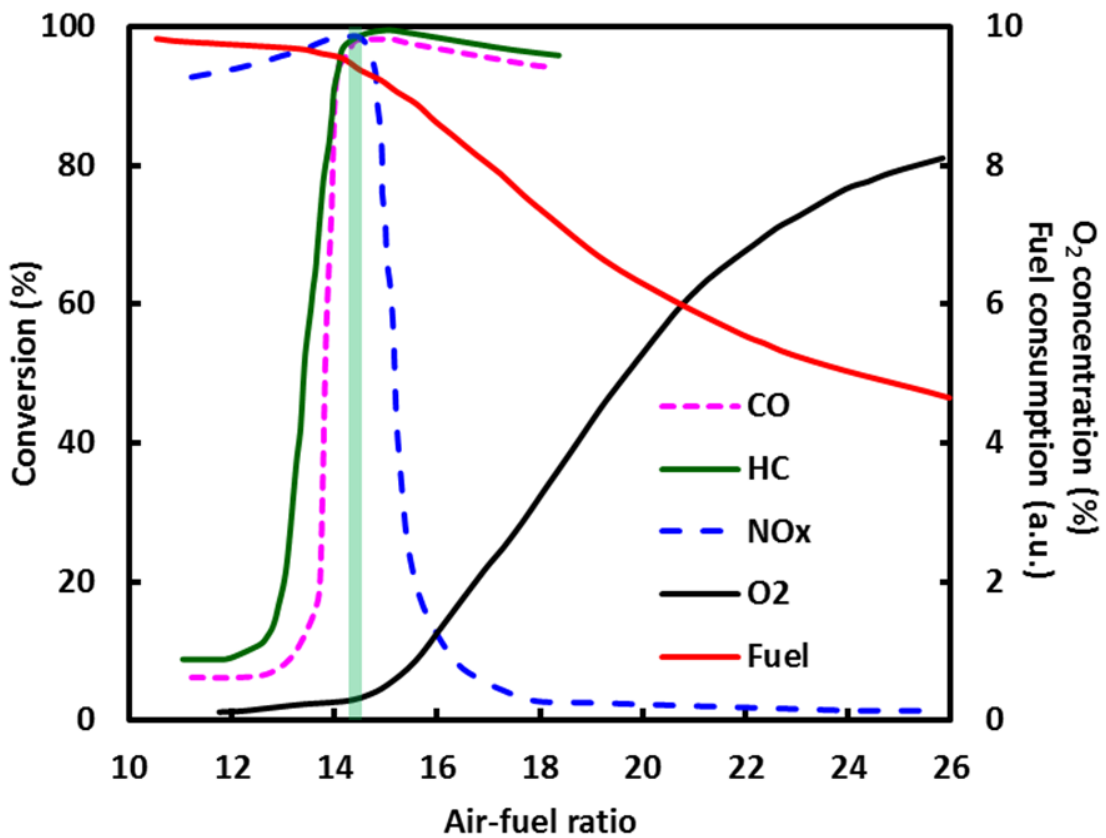


Figure 1-1. Fuel consumption and conversion of key pollutants (CO, NO_x and HC) as a function of air-fuel (A/F) ratio [4]

The United States Environmental Protection Agency (EPA) has been imposing stricter regulations on fuel economy and vehicular emission standards. The amendments to the U.S. Federal Clean Air in 1990 introduced two standards (Tier 1 and 2) for the light-duty vehicles [3]. Tier 1 and 2 standards were implemented between 1994 – 1997 and 2004 – 2009, respectively [3]. Tier 3 emission standard for light-duty vehicles were proposed in March 2013 and signed into law on March 3, 2014. The Tier 3 standards are closely aligned with California LEV III standards and are phased in over the period from 2017 through 2025 [5]. The structure of Tier 3 standards is similar to the Tier 2 standard and manufacturers must certify vehicles to one of seven available “certification bins”. Table 1-1 shows the Tier 3 standards for all seven bins. The Tier 3 rule also includes emission standards for heavy-duty vehicles (HDV).

Table 1-1. Proposed Tier 3 Standards (FTP-75; 150,000 miles) [5].

Bin	NMOG+NO _x (mg/mil)	PM (mg/mil)	CO (g/mil)	HCHO (mg/mil)
Bin 160	160	3	4.2	4
Bin 125	125	3	2.1	4
Bin 70	70	3	1.7	4
Bin 50	50	3	1.7	4
Bin 30	30	3	1.0	4
Bin 20	20	3	1.0	4
Bin 0	0	0	0	0

The emission standards for diesel engine were introduced in mid-1980s when both EPA and CARB began to regulate both NO_x and PM (Particulate Matters). The first

diesel emission standards were introduced during the amendment of the Clean Air Act in 1990, and required that by 1994 the particulate emissions be reduced from 0.25 g/bhp-hr to 0.1 g/bhp-hr. Recently, a new more stringent emission standards (EPA 2010) were implemented that required the use of the catalytic device to meet the regulations [6]. The summary of development of the emission regulations for the U.S. heavy-duty trucks is provided in the Figure 1-2.

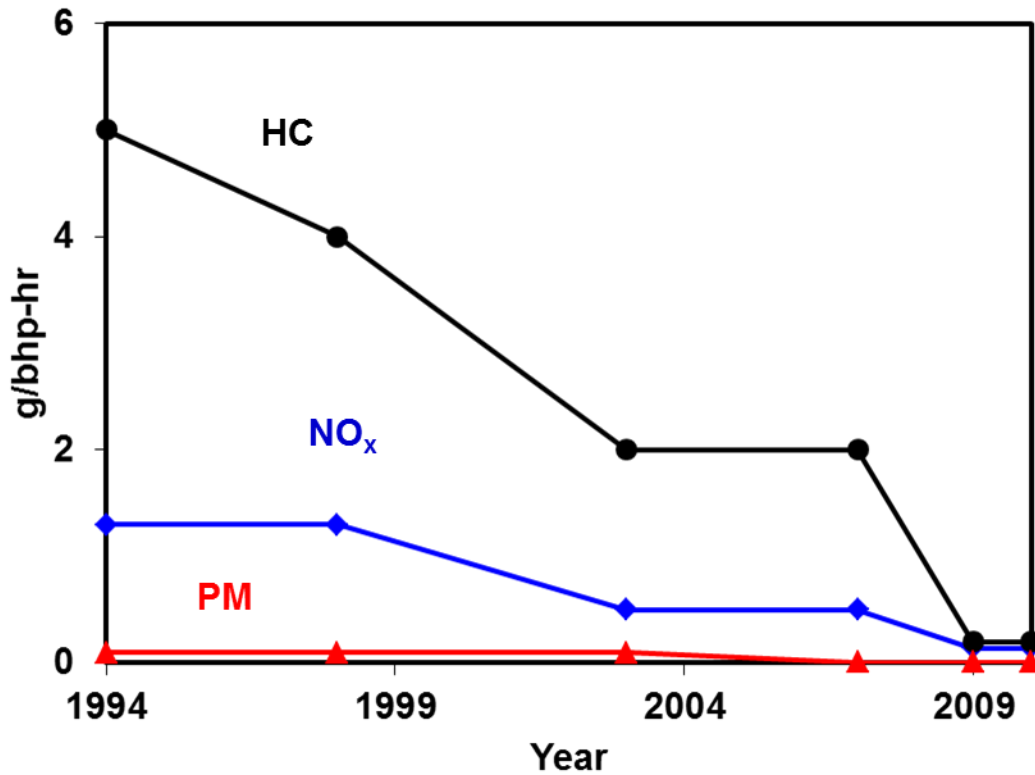


Figure 1-2. Emission standards for the heavy-duty trucks in the U.S., g/bhp-hr [6]

Diesel engines are lean burn engines and during lean burn operation ($\lambda > 1$) there is almost complete combustion of fuel resulting in lower CO and HCs emissions. The overall operating temperature is lower for diesel engines and hence there is lower NO_x emission. However, the particulate emission in the diesel engines is higher. Due to strict emission standards even though there is great progress in designing the engines to

achieve higher efficiency and lower emissions there is still requirement for the aftertreatment system in diesel engines. Hence, in order to meet these stringent emissions regulations, different parts of diesel aftertreatment system are being developed, commercialized and constantly improved. Figure 1-3 shows schematic of diesel aftertreatment system. Conventional technologies, such as oxidation and three way catalyst based on Pt group metals, are unable to provide the activity and selectivity required to significantly convert NO_x to N_2 in oxygen rich environments to meet the legislated limits. Therefore automotive and catalyst manufacturers have been looking at different solutions to address the challenge. Solutions that are relatively well known today consist of after treatment systems that may include one or more of the following: Diesel Oxidation Catalyst (DOC), non-coated and coated Diesel Particulate Filter (DPF), Selective Catalytic Reduction (SCR), Lean NO_x Trap (LNT), and Ammonia Slip Catalyst (ASC). Advanced solutions may include a wide range of multifunctional catalysts derived from classic technologies coupled with advanced combustion control strategies. Novel technologies are also being investigated to target both emissions and fuel consumption whilst also addressing exhaust system costs.

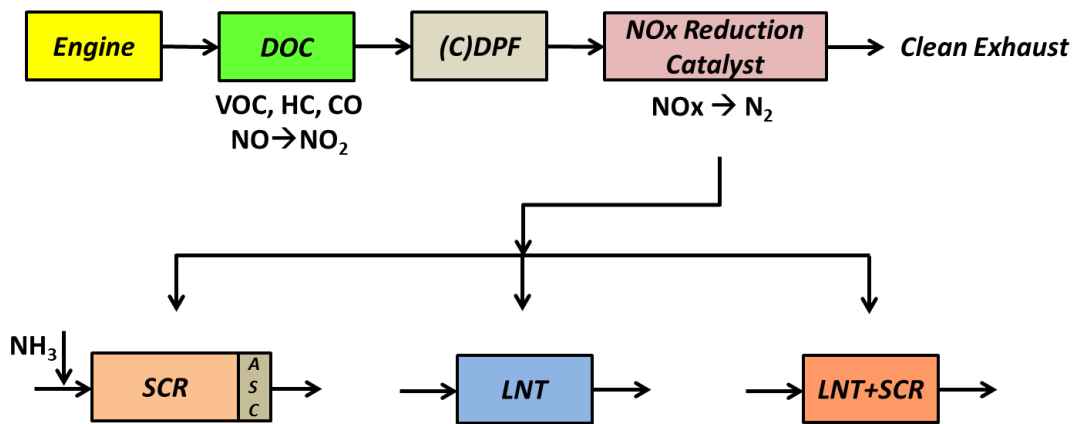
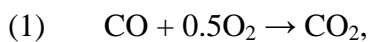
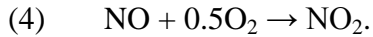


Figure 1-3. Schematic of diesel aftertreatment system.

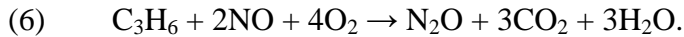
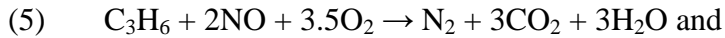
1.2 Diesel oxidation catalyst

The diesel oxidation catalyst (DOC) has been part of diesel exhaust system since emission regulations were introduced for diesel or lean burn engines. The principal functions of DOC are oxidation of CO, unburned hydrocarbons, and NO. Hydrocarbon oxidation on the diesel oxidation catalyst also generates exotherms required for downstream diesel aftertreatment units. In many cases the DOC plays an important role by pretreating the exhaust gas for further processing by subsequent units in modern aftertreatment systems [7-16]. DOC also converts some of the NO present in the exhaust gas to NO₂. NO₂ plays an important role in the effectiveness of both LNT (Lean NO_x Trap) and SCR (Selective catalytic reduction) units [12-16]. It has been shown in literature that NO₂ increases the efficiencies of those systems in the reduction of NO_x to N₂ and it is also beneficial for low temperature continuous DPF regeneration [11-12]. In addition to NO oxidation reaction, the reduction of NO by the hydrocarbon species also occur on monometallic Pt group catalysts in presence of excess O₂, with Pt being the most active for NO reduction [9-10]. Products of reduction include N₂O and N₂, and the product selectivity is a function of the hydrocarbon species present in the exhaust gas and the temperature of operation [9-10]. N₂O is a highly undesirable oxide of nitrogen as it contributes significantly to global warming and consequently the EPA has recently introduced N₂O monitoring requirements for both fixed and some mobile sources. C₃H₆ is taken as a model hydrocarbon to represent all hydrocarbons (HCs) present in the exhaust. The reactions occurring on the DOC are listed as





Over PGM catalyst, selective catalytic reduction of NO with hydrocarbon (HCs) can be represented by the following global reactions:



DOCs are based on cordierite (ceramic) “honeycomb” or metal monoliths. The materials used for washcoat are Al_2O_3 , SiO_2 , zeolites or combination of these. The precious metals used for DOC catalysts are Pt and Pd. Pt was the preferred choice for DOC catalysts due to the metal resistance to sulfur poisoning. Pt activity decreases due to thermal degradation because of sintering at higher temperatures attained in DOC during DPF regeneration. On the other hand Pd has shown more resistance to sintering at higher temperatures than Pt [17-18]. The introduction of fuel with low sulfur content and decline in the price of Pd as compared to Pt results in development of bimetallic DOC catalysts. Both Pt and Pt/Pd DOC technologies are today available for diesel applications. The DOC technology is now well established and used commercially in all the light-duty and heavy-duty vehicles. However, Recent advances in low temperature combustion (LTC) diesel engines lead to higher net efficiencies and lower NO_x and particulate matter (PM) emissions as compared to current diesel engine technologies. However, the LTC engine has lower exhaust temperature that results in higher levels of CO and hydrocarbons (HCs) than that of today’s engine. The design of the diesel oxidation catalyst (DOC) for treatment of exhaust gases from LTC engines is more challenging.

1.3 Diesel particulate filter

Diesel particulate filters (DPF), also known as traps in the mid to late 1970s, were being developed for heavy duty diesel vehicles. However, advancement in engine design enabled diesel vehicles to meet extremely low emission limits, including particulate matter (PM) without the need for DPF's or other auxiliary emission control devices. Late in 2000, the US EPA finalized its heavy-duty diesel emission standards and established the lowest limits ever. Particulate matter (PM), or soot, is noxious emission for diesel engines. Engine modification and combustion improvements have reduced that amount of PM produced, although complete elimination from engine-out exhaust has not been achieved. An upstream DOC can oxidize hydrocarbons of the soluble organic fraction (SOF) of PM at low temperature and thus reduces the soot load on the DPF. The current standard DPF has catalyst coated on a wall-flow filter, where exhaust enters channels that are blocked at the filter outlet, forcing the gas through the filter wall where the alternate ends are blocked [19]. The Continuously Regenerating Trap [12] is another type of filter that continuously oxidize the soot from filter by using NO_2 at much lower temperatures (greater than $300\text{ }^\circ\text{C}$) and with oxygen at higher temperatures ($500\text{--}600\text{ }^\circ\text{C}$) [19-21]. The Continuously Regenerating Trap (CRT[®]) is used in heavy-duty diesel vehicles (buses, trucks etc.) due to higher temperatures required for NO oxidation to form NO_2 . As, the performance of DPF is improved in presence of NO_2 , DOCs can be placed upstream of a DPF. For passenger vehicles and other applications where exhaust temperatures are lower (low speed), periodic regeneration of the DPF is required. The exhaust temperature is increased to soot oxidation temperatures with fuel injection. Recently, DPFs incorporate DOC oxidation functionality on the PM filter, which provides a more thermally efficient

system as heat generated during oxidation can directly be used for DPF regeneration [20-21]. The addition of a Pt catalyst in the DPF also lowers the CO and HC emissions from the DPF during regeneration.

1.4 NO_x reduction technologies

NO_x is a generic term representing NO and NO₂. NO_x is formed by the reaction between N₂ and O₂ during the combustion process when the temperature inside the engine cylinder exceeds 1100°C. Approximately, 90% of the nitrogen oxides (emitted from diesel engine vehicles) are in the form of NO. NO_x has harmful effects on both environment and human health. Hence, the EPA standards for NO_x emissions have become stringent in past few years. To comply with NO_x emission regulations, vehicle manufacturers and catalyst companies have developed and commercialized various lean NO_x reduction technologies [3, 6].

Different techniques have been developed and commercialized in the past two decades to reduce the NO_x in the fuel lean environment. The catalytic decomposition of NO_x to N₂ and O₂ over the copper zeolite catalysts such as Cu-ZSM5 was extensively studied during the early 1990s. However, the catalyst activity degrades dramatically in presence of H₂O and also due to SO₂ poisoning [22]. Hence, this technique is not commercialized for NO_x reduction in diesel engines. The focus then shifted towards using fuel or hydrocarbon as a reductant to reduce the NO_x under lean conditions. The lean NO_x reduction with hydrocarbon was studied extensively on different types of catalyst (Pt/Al₂O₃, Cu-ZSM5, Fe-ZSM5, Pt-ZSM5, Ag/Al₂O₃ etc.) [23-25]. However, this approach of NO_x reduction was not able to meet the stringent limits for 2010 [6]. Recently, NO_x storage and reduction (NSR) and selective catalytic reduction (SCR) by

ammonia (urea) technologies have been successfully commercialized to meet the EPA 2010 emission standards. The combined NSR+SCR technology has also been studied extensively in the past decade and has been shown to be a viable solution to NO_x abatement for the light- to medium-duty vehicle applications [26]. The NSR, SCR and combined NSR+SCR are currently the prominent technologies for the NO_x reduction under lean conditions. The details of these techniques are discussed next.

1.4.1 NO_x storage and reduction (NSR)

NO_x storage and reduction (NSR) or Lean NO_x trap (LNT) is one of the commercialized technologies for reducing NO_x from lean burn vehicles. The NSR concept, was first introduced by Toyota researchers in the mid-1990s [27], is implemented in a multifunctional monolithic catalytic reactor. The LNT catalyst contains a precious metal with oxidation and reduction activity to oxidize NO to NO₂ and also to reduce stored NO_x to N₂. LNT catalyst also contains an alkali or alkaline earth-metal oxide as a storage component for NO_x. NSR operates with periodic fuel-lean and fuel-rich cycles and operating concept involves storage of NO_x during the lean phase and during the rich phase stored NO_x is reduced. Commonly-used precious metals include Pt and Rh while oxides of Ba, Mg, Sr and Ca are used as storage compounds [3]. The most commonly studied catalyst formulation is Pt/BaO/Al₂O₃. Rh is added for additional NO_x reduction activity while ceria (CeO₂) is added for precious metal dispersion control and improved low temperature performance [28].

Numerous studies have been done to study the mechanism of NO_x storage and reduction mechanisms [28-43]. An extensive compilation of such mechanisms can be found in reviews by Roy and Baiker [3] and Epling et al., [29]. The first step of NO_x

storage on Pt/BaO/Al₂O₃ is the oxidation of NO to NO₂ on Pt as NO₂ adsorbs effectively as compared to NO [29]. Forzatti et al., [31] proposed two parallel routes for NO_x storage on Pt/BaO/Al₂O₃ catalyst in the presence of excess O₂, namely the “nitrate route” and the “nitrite route”. In the “nitrate route”, NO is first oxidized to NO₂ on Pt which is then converted to Ba(NO₃)₂ via the disproportionation reaction ($3\text{NO}_2 + \text{BaO} \rightarrow \text{Ba}(\text{NO}_3)_2 + \text{NO}$). Whereas, in the “nitrite route” NO is oxidized on Pt and directly stored on the neighboring BaO sites to form nitrites that are subsequently oxidized to nitrates. The disproportionation storage mechanism is dominant during the longer storage times, when the 3:1 stoichiometry between NO₂ stored and NO produced is satisfied whereas, during initial period of storage the 3:1 disproportionation ratio is not satisfied [29]. Hence, this points to two different mechanisms for NO_x storage. Epling et al., [30] proposed two different storage sites for NO_x storage on the basis of their proximity to Pt. Proximal storage sites or so-called “alpha” sites are sites close to Pt and NO₂ is stored with the aid of adsorbed O atom on Pt whereas, non-proximal sites store NO₂ via the disproportionation mechanism. For the NO_x storage on the proximal sites 3:1 disproportionation ratio is not satisfied. Similarly, Kabin et al., [32] proposed a “hybrid” mechanism in which the storage is initiated by the spillover of O adatoms from Pt to BaO followed by the addition of NO₂. Kwak et al., [34] proposed a different NO_x storage mechanism. During the initial period, complete NO_x uptake results from the spillover of NO₂ formed by NO oxidation on the Pt crystallites, to the neighboring BaO. After this the NO_x uptake slows down as the BaO sites in the vicinity of the Pt particles are converted to Ba(NO₃)₂. The storage process is limited by the diffusion rate of nitrate ions to BaO sites farther from the Pt. Hence, NO₂ that desorbs from the Pt to breakthrough, causing

NO_x slip. Kumar et al., [33] carried out isotopic exchange studies (¹⁵NO) using TAP (Temporal Analysis of Products) reactor on Pt/BaO/Al₂O₃ powder catalyst in order to elucidate the role of the Pt/BaO interface during NSR. The data reported clearly shows the existence of a stored NO_x concentration gradient and transport in the storage phase. They proposed that NO_x storage proceeds radially away from the Pt/BaO interface and there is mobility of the stored NO_x species on the storage (BaO) phase. The mobility of nitrate/nitrite species was also confirmed in an *ab initio* molecular dynamic simulation studies by Broqvist et al., [45]. They predicted diffusion events for both nitrate and nitrite on the BaO(100) surface. The interaction and coupling between Pt and BaO has been previously reported by a host of researchers [38, 40, 44, 46-49].

A number of regeneration mechanisms have been reported [29, 35, 39-40, 46, 49-55]. Nova et al. [40] proposed that the reduction of stored NO_x occurs via Pt catalyzed reaction and that it is only possible when both Pt and BaO are dispersed on the same support. Zhou et al., [44] showed that Ba(NO₃)₂ did not react with H₂ in the absence of Pt while a relatively small amount of Pt was sufficient to completely reduce Ba(NO₃)₂ to N₂ at temperatures below 400 K. Once again it was established that the coupling between Pt and BaO phase is essential during the reduction. Clayton et al., [48] studied the effects of Pt dispersion during the storage and reduction on Pt/BaO/Al₂O₃ catalyst. They observed increased storage and reduction with an increase in Pt dispersion and it could be attributed to the larger Pt/BaO interfacial perimeter, which promotes the spillover of NO_x from Pt to BaO during the storage and reverse spillover of stored NO_x, and/or the spillover of activated hydrogen from Pt to BaO, during the regeneration. More recently, Luo and Epling [37] proposed that the regeneration of NO_x proceeds via spillover and

diffusion of activated hydrogen on the exposed alumina support as an alternative mechanism.

As fuel is used as reductant so LNT does not require any additional infrastructure for supply of reductant. As it operates in fuel lean and rich cycles hence, it definitely requires sophisticated, adaptive control strategies for the lean-rich diesel engine operations. One major disadvantage is very high cost associated with the use of precious Pt/Rh/Pd metals used in NSR catalysts. The other disadvantages include NSR catalysts being prone to sulfur poisoning [31-34] and precious metal sintering at higher temperatures. Even for ultra-low sulfur fuel, a regular desulfation of the catalyst is required to achieve desired NO_x removal performance. The desulfation is carried out at higher temperatures (550-650°C) and at such elevated temperatures, Pt and Pd sintering takes place resulting in decreased deNO_x efficiency. Hence, due to these drawbacks the applicability of NSR technology is limited.

1.4.2 Selective catalytic reduction

Selective catalytic reduction is other commercialized technology for lean NO_x reduction. In this technology NO_x is selectively reduced to N_2 in the presence of excess oxygen by using reductant such as NH_3 and hydrocarbons (HCs). Selective catalytic reduction of NO_x by ammonia is the most promising NO_x abatement technology that is widely used in the heavy-duty diesel engine vehicles. The potential of SCR for NO_x removal in vehicular applications was realized in the 1990s and it has gained considerable attention in the last few years. The first commercial NH_3 SCR application for a diesel truck was launched in 2004 by Nissan Diesel in Japan and by DaimlerChrysler in Europe. In the NH_3 -SCR system, ammonia is generated on board

using the external source and is utilized to reduce the NO_x from the lean exhaust to desired products such as nitrogen and water [5]. The external source of ammonia is usually consists of a urea tank and a decomposition reactor. The urea is injected to the hot exhaust stream which is then hydrolyzed to ammonia in the decomposition reactor [5]. The SCR technology is very robust and is able to provide high NO_x conversion over wide temperature range. However, the drawback is need of external NH₃ supply system that leads to extra cost and space requirement. This limits the use of SCR technology in light- to medium-duty vehicles.

The viable SCR catalytic materials can be divided into two groups. They are vanadium-based SCR catalyst and Cu- or Fe- exchanged zeolites. The vanadium-based SCR catalysts, e.g. V₂O₅/WO₃/TiO₂, have been used to remove NO_x under net oxidizing conditions for decades in the both stationary and mobile applications [56]. However, the US EPA 2010 regulations require the DPF regeneration at higher temperatures and this makes Vanadium-based catalysts impractical as they cannot withstand high temperatures (ca. 550 – 600 °C) [56]. On the other hand, zeolite-based SCR catalysts give excellent deNO_x efficiency over wide temperature range and possess exceptional hydrothermal stability [56, 57].

The overall SCR chemistry is well established in the literature and has been found to be similar in both vanadium-based and zeolite-based SCR catalysts [58, 59]. The main SCR reaction is the so-called “standard SCR” reaction and can be expressed as



It is well known in the literature that the presence of NO₂ in the feed significantly improves the NO_x reduction activity [58, 59]. When both NO and NO₂ in the feed react

simultaneously to produce N₂ and H₂O; it is called as “fast SCR” reaction (1-5) because it is much faster than the standard SCR reaction (1-4). The reaction between NH₃ and equimolar mixture of NO and NO₂, gives the highest NO_x reduction activity.



Similarly, the reaction between NO₂ and NH₃, which is comparatively slower than the “fast SCR” reaction, is referred to as “NO₂-SCR” or “slow SCR” reaction [58, 59] and is given by



In addition to the above key reactions, other side reactions such as NH₃ oxidation and NO oxidation also take place. Cu-zeolites are more active for NH₃ oxidation as compared to Fe-zeolites. The higher NH₃ oxidation rate at higher temperatures, reduces the NO_x reduction activity of Cu-zeolite SCR catalysts at higher temperatures [40]. Finally, the formation of surface nitrites and nitrates also become important in the presence of NO₂ in the feed [59, 60]. The surface nitrates thus formed reacts with NH₃ to form ammonium nitrate which decomposes at higher temperatures to give N₂O [57-60].

There is a vast number of experimental and modeling studies available in the literature that focus on understanding of the kinetics and mechanistic aspects of SCR reactions on vanadium and zeolite based SCR catalysts ([57-67] and references within). Likewise, there are several kinetic models with varying complexities that describes transient and steady-state behavior of various catalyst formulations [57-67]. Olsson et al., [64, 65] developed a detailed kinetic model of NH₃ SCR over Cu-ZSM-5 using the experimental data obtained from the flow reactor experiments. In another study [66], they developed a global transient kinetic model for a commercial Fe-zeolite catalyst.

Likewise, Colombo et al., [62] developed a dynamic micro-kinetic model with particular focus on the NO_2 -related SCR catalytic chemistry over a Cu-zeolite catalyst. Their tuned model is able to predict the most of the transient behavior observed during temperature-ramp experiments. Recently, Metkar et al., [57] developed global kinetic model for the commercial Cu-Chabazite and Fe-ZSM-5 monolithic catalyst that gave good steady-state predictions over wide feed conditions and temperatures. The developed model was also used to predict the performance of the dual-layer and dual-brick Fe/Cu combined catalyst [57].

A large number of studies have been reported in the literature on selective catalytic reduction of NO_x with hydrocarbons (HC-SCR) over different catalytic materials. During the last few years, several works have been focused on the development of a reaction mechanism for HC-SCR of NO. The review by Burch et al., [23] concluded that for non-zeolitic oxides, species that are strongly adsorbed on the surface, such as nitrates/nitrites and acetates, are likely key intermediates in the formation of various reduced and oxidized species of nitrogen which, on further reaction, leads to the desired formation of N_2 . In contrast, for transition metal catalysts the mechanism of NO_x reduction involves the dissociative adsorption of NO over the reduced metal surface with subsequent recombination of N adatoms to form N_2 . The role of hydrocarbons in this type of mechanism is to remove the adsorbed atomic O species, generated during the NO dissociation, thereby restoring the initial catalytic surface [70].

Other studies have been carried out on mechanistic aspects of NO_x reduction with C_3H_6 over Cu-based zeolitic catalysts. One proposed pathway involves direct decomposition of NO over Cu with hydrocarbon playing the role of oxygen scavenger

[71, 72]. The second proposed pathway involves $R-N_tO_x$ compounds (R=hydrocarbon group) as intermediates, resulting from the reaction of adsorbed NO_x and HC species. These intermediates may either directly result in formation of molecular N_2 or decompose to other intermediates such as isocyanates, ammonia, nitriles, oximes, azo or azoxy compounds [73-81]. The third proposed pathway involves the formation of oxygenates which then serve as reductants of NO_x [82]. Finally, the fourth pathway involves the oxidation of NO to NO_2 , which then react with hydrocarbons to form $R-N_tO_x$ species that decompose to form N_2 in subsequent reaction steps [83-85]. Luo et al., [86] showed that C_3H_6 has an inhibiting effect on selective catalytic reduction of NO_x with NH_3 on larger pore Cu/Beta zeolite above $200^\circ C$ due to the formation of surface intermediates formed during C_3H_6 oxidation; these include acrolein-like species and coke-like species. More recently, Ye et al., [87] studied the propene poisoning resistance of Cu- exchanged small pore zeolite catalysts such as Cu-SSZ13. They found that hydrocarbon deposition is less on Cu-SSZ13 because of the smaller pores and cage diameters compared to the medium pore Cu-ZSM5. Hence, the storage of hydrocarbons and their role as reductant of NO_x leads to a complex reaction system that requires further investigations especially for the emerging class of small pore zeolites.

Only few studies had been carried out on the kinetic modeling of selective catalytic reduction of NO with hydrocarbons. Ansell et al., [88] developed a kinetic model for $C_3H_6 + NO + O_2$ on Pt/ Al_2O_3 monolithic catalyst using a 1-dimensional monolith model comprising global Langmuir-Hinshelwood rate expressions. Wilber et al., [89] developed a global kinetic model for $C_2H_4 + NO + O_2$ on Cu-ZSM5 monolithic catalyst. Captain et al., [90] studied selective catalytic reduction of NO by propylene over

supported Pt catalysts. Based on the data, a mechanistic based kinetic model was developed that included the sequential hydrocarbon partial oxidation and subsequent formation of surface cyanide and isocyanate intermediates.

Cu-chabazite (SSZ-13) has emerged as an important synthetic zeolite for lean NO_x reduction on diesel vehicles due to its superior hydrothermal durability and hydrocarbon resistance. The few studies that have appeared in the literature focused primarily on the effect of hydrocarbons on the activity of SCR catalyst for NO_x reduction with NH_3 [86, 87] while other studies have only showed that non- NH_3 pathways play important role for NO_x reduction for combined LNT/SCR systems [68, 69]. To our knowledge there have been no published studies on elucidating the mechanistic steps involved in lean NO_x reduction via non- NH_3 pathways (hydrocarbons, oxygenates, isocyanates, amines etc.).

1.4.3 Combined LNT+SCR

Both NSR and SCR have drawbacks. Particularly, NSR catalysts are expensive and prone to catalyst deactivation (PM sintering and sulfur poisoning) while there is a need of additional infrastructure for the supply of NH_3 to the SCR system. Due to these issues, interest has shifted to using the integrated NSR/SCR technologies in order to lower the infrastructure cost associated with the SCR and the material cost associated with the precious metal-based NSR catalysts. The main advantages afforded by NSR/SCR are (i) *in-situ* generation of NH_3 in the upstream NSR process (or lean NO_x trap, LNT) and (ii) reduction of a potentially significant fraction of the NO_x by the much less expensive SCR catalyst. The NSR/SCR operating concept involves the storage of NO_x during the lean phase while unreacted hydrocarbons (C_3H_6 , C_2H_4 etc.) and generated

NH₃ exit the LNT during the rich phase. The ammonia produced during the regeneration adsorbs on the downstream SCR catalyst where it reacts with NO_x not converted in the LNT. In addition, olefinic hydrocarbons and/or partially oxidized species that break through the LNT may also adsorb on the SCR catalyst leading to additional NO_x reduction by those species [68, 69, 91-99].

Wang et al., [68] also studied the combined LNT-SCR system using low PGM loaded Pt/Rh LNT catalyst and commercial Cu-SCR catalyst. They used a mixture of CO+H₂+C₃H₆ as the reductant and found that in addition to NH₃-SCR reactions, hydrocarbon (HC)-SCR reactions contributed significantly to NO_x reduction. This indicated that during the actual driving conditions, non-NH₃ pathway to NO_x reduction becomes important. Similarly, Xu et al., [69] have showed on the basis of both laboratory and vehicle tests that the LNT plus in situ SCR catalyst approach for diesel emissions aftertreatment result in higher NO_x conversion and wider operating temperature window due to the non-ammonia NO_x reduction mechanism over the SCR catalyst in addition to the standard mechanism based on ammonia storage and also the improved hydrocarbon oxidation efficiency owing to the SCR catalyst. However, the detailed study of HC SCR chemistry on Cu-SSZ13 has not been studied.

. 1.5 Research Objectives and Outline

The first objective of this work is to perform systematic steady state and transient bench flow reactor studies to elucidate the mechanistic steps involved in NO_x reduction with C₃H₆ on Cu-chabazite (Cu-SSZ13) catalyst. Here we conduct steady state and transient bench flow reactor experiments for feeds containing C₃H₆, O₂, and NO and/or NO₂ in order to elucidate the key mechanistic steps involved in NO_x selective catalytic

reduction with C_3H_6 . In particular, we identify the key mechanistic step in NO_x reduction with C_3H_6 by identifying the conditions for which inhibition by NO and/or NO_2 on propylene oxidation are present. Differential kinetics measurements augment the integral reactor data by quantifying apparent reaction orders. DRIFTS measurements are carried to help identify the inhibiting surface species formed during lean NO_x reduction with C_3H_6 . A phenomenological reaction mechanism is proposed that is consistent with these data.

The second objective is to develop a predictive kinetic model for lean NO selective catalytic reduction with C_3H_6 over Cu-SSZ13 monolithic catalyst based on our bench flow reactor studies and in-situ DRIFTS measurements. The SCR mechanism involves reaction between oxygenates (partially oxidized hydrocarbon species) and NO to form isocyanates species ($-NCO$), detected by DRIFTS which are further reduced to N_2 . The developed kinetic model is incorporated into a (1+1)-dimensional monolith reactor model. Kinetic parameters are estimated using steady state data obtained from bench scale flow reactor studies on NO selective reduction with C_3H_6 . The model is also validated with separate set of experimental data. The model captures the key features observed experimentally and predictions for conversion and selectivity fit well with experimental data. The monolith model predicts the observed negative order with respect to C_3H_6 and positive order with respect to O_2 for C_3H_6 oxidation reaction. For the $C_3H_6+NO+O_2$ reaction system, the predicted NO and C_3H_6 conversions agree well with both steady state and transient experimental data. The model captures the significant shift of C_3H_6 light-off to higher temperature in the presence of NO due to formation of

inhibiting -NCO surface species as well as slow transients associated with surface intermediates and their effect on the extent of reactions.

The third objective is to develop the global kinetic model for co-oxidation of CO and C_3H_6 on Diesel oxidation Pt/ Al_2O_3 monolithic catalyst based on the bench-flow reactor experiments. The global kinetic model is developed in steps, starting with CO oxidation, followed by C_3H_6 oxidation and then the CO+ C_3H_6 reaction system. The global kinetic model developed is used to study the hysteresis that occurs during temperature ramp-up and ramp-down experiments at a constant rate with a CO and C_3H_6 mixture. This work also focused on steady state hysteresis and in particular the effect of inlet feed composition and heat Peclet number on the region of multiplicity. The specific objectives of this study are summarized below:

1. Conduct a comprehensive steady-state and transient bench-flow reactor studies of selective catalytic reduction of NO_x with C_3H_6 over Cu-SSZ13 commercial SCR catalyst.
2. Carry-out *in-situ* DRIFTS studies using powder Cu-SSZ13 catalyst in order to investigate the key surface intermediates formed during lean NO_x reduction with C_3H_6 .
3. Elucidate the mechanistic steps involved in selective catalytic reduction of NO_x with C_3H_6 over Cu-SSZ13 catalyst based on bench-flow reactor and *in-situ* DRIFTS studies.
4. Develop a mechanistically based kinetic model of C_3H_6 -SCR that provides useful insight in the role of hydrocarbon species for NO_x reduction over wide temperature range and for different feed compositions.

5. Develop a global kinetic model of co oxidation of CO and C₃H₆ on Pt/Al₂O₃ diesel oxidation catalyst in order to study the steady state and transient hysteresis behavior for CO + C₃H₆ mixture.

The dissertation is organized as follows. Chapter 2 describes generic mathematical models of the catalytic monolith including 1D two phase model, low dimensional model, (1+1)-D model and detailed 3D model. Chapter 3 describes the experimental setup and catalysts used in this study. Chapter 4 presents the transient and steady-state bench flow reactor studies of lean NO_x reduction with C₃H₆ over Cu-SSZ13 monolithic catalyst. Chapter 5 focuses on the in-situ DRIFTS experiments carried out in order to investigate the key surface intermediates formed and their evolution with time during selective catalytic reduction of NO with C₃H₆ on Cu-SSZ13 powder catalyst. Chapter 6 describes the development of mechanistic-based kinetic model for selective catalytic reduction of NO with C₃H₆ on Cu chabazite (Cu-SSZ13) monolithic catalyst based on bench scale flow reactor studies and *in-situ* DRIFTS measurements. Chapter 7 presents development of global kinetic model for CO and C₃H₆ oxidation over Pt/Al₂O₃ diesel oxidation catalyst and discusses the transient as well as steady-state hysteresis behavior for CO and C₃H₆ mixture. Finally, the main contributions and findings of the current study are summarized in Chapter 8. A few recommendations for the future direction of the research are also provided.

CHAPTER 2 Experimental

2.1 Introduction

This chapter consists of a detailed description of the experimental set-up and procedures used in this study. Most of the experiments were carried out on bench-scale flow reactor set-up. Bench flow reactor experiments were performed using the monoliths of length 0.5 to 2 cm. In addition to this *in-situ* DRIFTS experiments were also performed using powder catalyst.

2.2 Catalysts

Cu-chabazite (SSZ-13) has emerged as an important synthetic zeolite for lean NO_x reduction on diesel vehicles due to its superior hydrothermal durability and hydrocarbon resistance. The commercial Cu-zeolite catalyst was supplied by BASF (Iselin, NJ). It is a small-pore Cu-chabazite type catalyst, established in patents and communicated in recent papers to possess excellent hydrothermal stability [100-102]. The pore size of the chabazite structure is about 0.36 nm and is small compared to that of ZSM-5 with a pore size of 0.55 nm. More detail about the synthesis and structure of this Cu-chabazite catalyst can be found in [102]. This catalyst was provided in a cylindrical shaped honeycomb structure where Cu-chabazite powder was deposited on the solid support. The cell density of this catalyst was 400 cells per square inch (cpsi). A commercially used catalyst piece with 15 cm diameter and 7.5 cm length was provided by BASF. The Cu loading was about 2.5% (by weight). The bench scale reactor (described in the following section) used in this study required a small catalyst piece. In order to obtain a catalyst piece of required dimensions, a dry diamond saw was used.

2.3 Bench-scale reactor set-up

The experimental setup used in this study is a typical bench-scale reactor system [103-105]. It consists of a gas supply system, a reactor system, an analytical system, and a data acquisition system. The simplified schematic of the experimental setup showing the major components is shown in Figure 2-1.

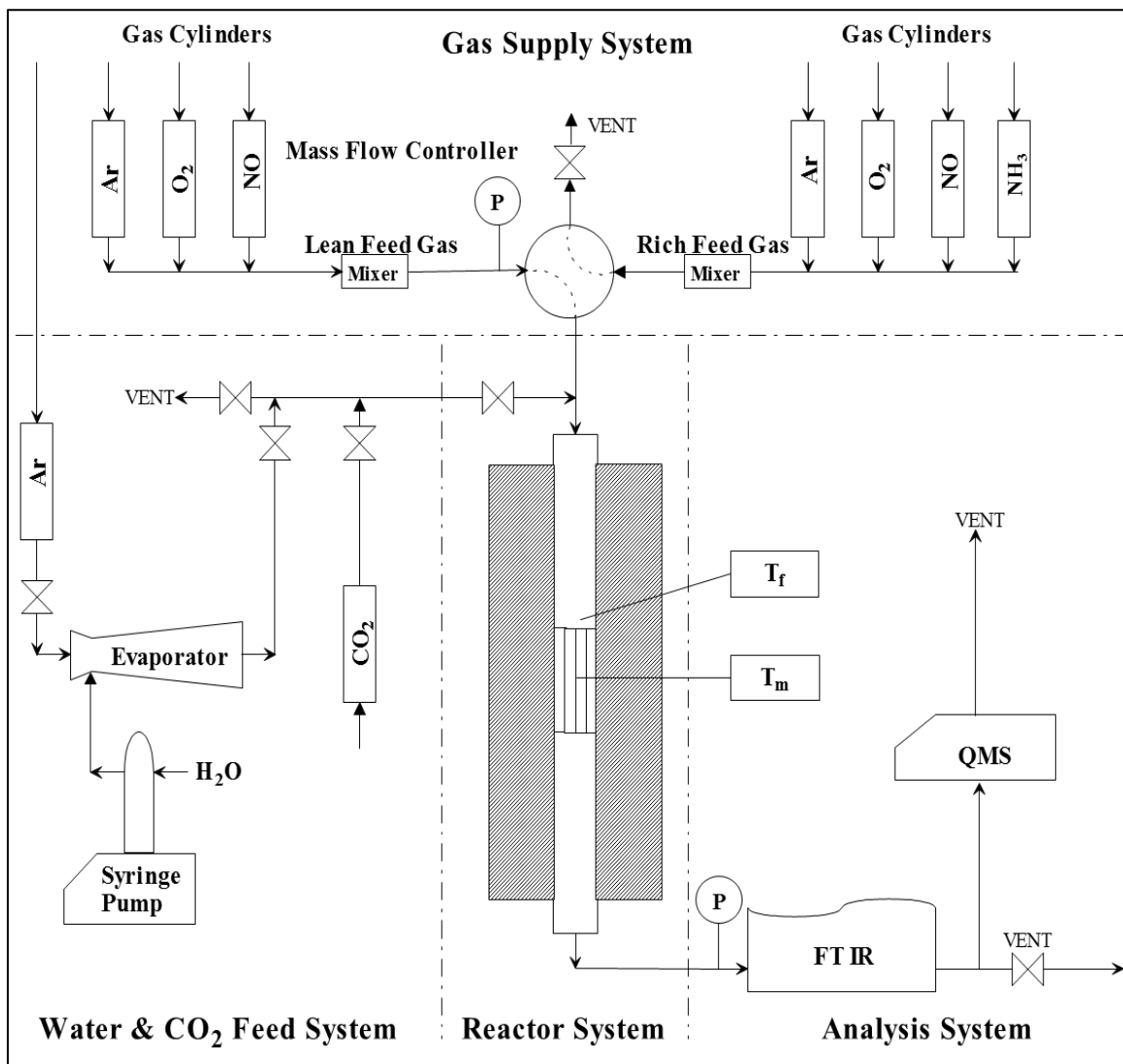


Figure 2-1. Schematic diagram of the experimental set-up used in this study [104].

2.2.1 Gas supply system

The gas supply system consists of series of compressed gas cylinders (Matheson Tri-Gas), regulators and mass flow controllers (MFC, MKS Inc.). The specifications of the various gases used in the study are provided in Table 2-1. The mass flow controllers were calibrated by using a digital flow meter (Humonics Hewlett Packard Optiflow 520). All gases are premixed in an in-line static mixer prior to entering the reactor. The total flow rate in all experiments was maintained at 1000 sccm which corresponds to ca. 60,000 hr⁻¹ to 240,000 hr⁻¹ GHSV (gas hourly space velocity) on the basis of the total monolith volume.

Table 2-1. Specifications of the gases used in this study.

Gas	Uses	Specifications
Ar	Diluent for reactive feed, purge gas for reactor, QMS calibration	Ultra high purity: > 99.999% purity, < 1 ppm CO ₂ , < 1 ppm CO, < 15 ppm N ₂ , < 3 ppm O ₂ , 5 ppm H ₂ O
He	Pressurizing of switching valve	Ultra high purity: > 99.999% purity
O ₂	Reactant	Ultra high purity: > 99.98% purity, < 1 ppm CO ₂ , < 1 ppm CO, < 15 ppm N ₂ , 5 ppm H ₂ O
1% C ₃ H ₆	FTIR calibration, Reactant	Certified mixture grade; balance Ar
1% NH ₃	FTIR calibration	Certified mixture grade; balance Ar
1% NO	FTIR calibration, Reactant	Certified mixture grade; balance Ar

Table 2-1 (Continued)

1% NO ₂	FTIR calibration, Reactant	Certified mixture grade; balance Ar
5% N ₂ O	FTIR calibration	Certified mixture grade; balance Ar
1% CO	FTIR calibration, Reactant	Certified mixture grade; balance Ar
1% CO ₂	FTIR calibration, Reactant	Certified mixture grade; balance Ar
1% N ₂	QMS calibration	Certified mixture grade; balance Ar

2.2.2 Reactor system

The reactor system consisted of a quartz tube flow reactor placed inside a 500 W Mellen single zone furnace (model SC11). The quartz reactor was approximately 15” long with dimensions of 0.32” I.D. and 0.50” O.D. The furnace temperature was controlled by a Mellen Temperature Control System (model PS305). The maximum operating temperature of the furnace is 1100 °C. A four-port, dual-actuated switching valve was placed immediately upstream of the reactor and was operated by Labtech software. The monolith samples were wrapped with Fiberfrax[®] ceramic paper in order to prevent any bypassing around the catalyst during the experiments. The reactor temperatures were measured by two type-K stainless steel sheathed thermocouples; one placed inside the monolith sample to measure the catalyst temperature and the second placed ca. 1 cm before the inlet of the monolith to measure the inlet fluid temperatures.

2.2.3 Analysis system

The analysis system included a FT-IR spectrometer (Thermo-Nicolet, Nexus 470) and a quadrupole mass spectrometer (QMS; MKS Spectra Products; Cirrus LM99). Both the analytical instruments were placed downstream of the reactor system. All the gas lines between reactor system and analysis system were heated to avoid condensation of gases in the pipelines. The gas cell of the FT-IR was an ultra-low volume (25 cm³) gas cell (Axiom, Mini Linear Flow Cell) with BaF₂ windows and with flow rate of 1000 sccm, the residence time in the gas cell is ca. 1.5 s under standard conditions. The FT-IR was used to measure NO, NO₂, N₂O, C₃H₆, CO, CO₂ and H₂O while QMS was used to measure N₂ concentration. Table 2-2 shows the gas standards used for FT-IR calibration.

Table 2-2 Gas standards used for FT-IR [104].

Component	Pressure (mm Hg)	Region (cm ⁻¹)
NO	880	1871.4-1940.0
NO ₂	880	1578.8-1613.8
N ₂ O	880	1248.8-1325.3
CO	880	2144-2177
C ₃ H ₆	880	2917.0-2986.0
NH ₃	880	920.0-970.0
H ₂ O	880	3750.0-3950.0

2.2.4 Data acquisition

The data acquisition system consisted of an ADAM 5000 TCP module and two PCs containing software for FTIR and QMS. ADAM 5000 TCP module (Advanced Ind.)

was used to convert the analog signals from the thermocouples, pressure gauge and mass flow controllers into digital signals which were then recorded in the PC installed with the Labtech[®] software. The same PC was also installed with Process Eye software to collect the data from QMS. OMNIC[®] software (Thermo Nicolet; version 6.2), installed in the second PC, was used to record the FT-IR composition data. At the start of each experiment, it was attempted to start both the software simultaneously. Any difference in the start time were recorded and accounted for when the data from different instruments were analyzed. In addition to this, there is also a difference in time delays in these instruments because of their locations from the reactor. In order to align the signals from both analytical instruments, tracer experiments were conducted to accurately measure the time delays. This time delay and the difference in the start time of the data collections in both PCs must be taken into account to accurately analyze the transient data. The detailed operating and shut down procedure of the bench scale reactor set-up along with safety considerations are described elsewhere [104].

2.3 *In-situ* DRIFTS

In-situ DRIFTS was performed using a Nicolet Nexus 470 spectrometer, equipped with a small collector with a dual sample environmental chamber (Thermo Fisher Scientific). The powder sample of catalyst was prepared by scraping the washcoat off the monolith channels. The feed gas, at a total flow rate of 50 cm³/min at STP, was mixed using Bronkhorst mass flow controllers; and its composition, with all gases present, was 500 ppm C₃H₆, 500 ppm NO, 1% or 5% O₂, balanced by He. Before each experiment, the catalyst sample of 60 mg was treated with 5% O₂ in He for 1 hour at 600°C.

CHAPTER 3 Mathematical Modeling of Catalytic Monoliths

3.1 Introduction

The catalytic monolith reactors are most widely used in the exhaust aftertreatment systems of the diesel and gasoline engine vehicles. They are also commonly used in the abatement of emissions from stationary sources like power plants. They offer high heat and mass transfer rates, lower pressure drop, higher geometric surface area, smaller thermal gradients in the washcoat, relatively lower internal diffusion limitations, ease of scale-up and superior hydrodynamics when compared to conventional packed bed reactors [106-109]. Because of the advantages of the monolithic reactors, they are gaining more interests in other applications such as hydrogen generation for the fuel cell applications, steam reforming of hydrocarbons to generate syngas ($\text{CO}+\text{H}_2$), water-gas shift (WGS) catalysis, etc. [109].

A typical design of a catalytic converter used in automobiles that utilizes ceramic monolith catalyst is shown in Figure 3-1. The monolith reactors consist of large number of narrow parallel channels that are coated with thin layer of catalytic washcoat (typical washcoat thickness of ca. 20 – 50 μm). They come in different cell geometries including square, triangular, hexagonal, and sinusoidal. The most common support or substrate material for the monolith reactor is ceramic (typically cordierite, $2\text{MgO}\cdot 2\text{Al}_2\text{O}_3\cdot 5\text{SiO}_2$). Depending on the application, metallic substrates that have low thermal capacity are also used to reduce the catalyst warm up period and hence lowering the cold start emission.

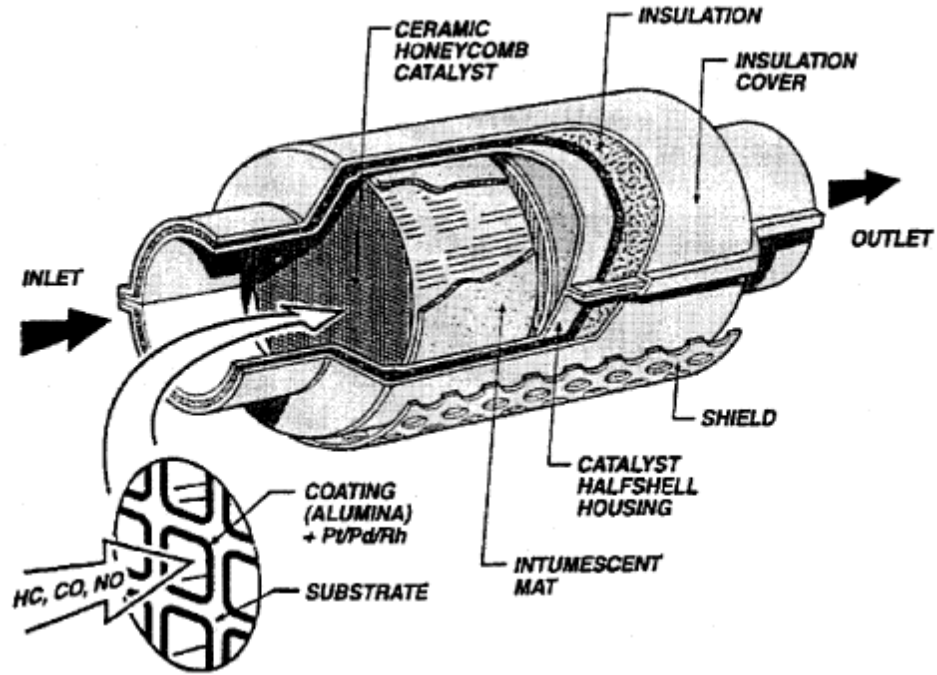


Figure 3-1. Typical catalytic converter used in automobile [108]

The catalytic reactors are characterized multiple length/time scales. The reacting fluid enters the channel diffuses transverse to the flow direction and into the washcoat where it reacts to form product which then diffuses back to the fluid phase and leaves the channel. A significant heat may be generated in the washcoat due to exothermic reactions when high concentration of reactants is present. This may ultimately lead to non-uniform temperature distribution along the reactor length that leads to complex nonlinear behavior. Therefore, in order to accurately represent the reacting system, a mathematical model of catalytic monolith needs to account for the interactions between chemistry and transport processes occurring at different length scales. Various mathematical models varying levels of details and complexities are available in the literature. A current status of exhaust aftertreatment modeling and summary of different models have been reviewed

by Guthenke et al., [110]. The relevant survey of different monolithic reactor models is provided in the following section.

3.2 Modeling of monolith reactors

The exhaust aftertreatment system is becoming more and more complex. The performance of one component in the system affects the performance of the downstream component. For example, the NO oxidation activity of a diesel oxidation catalyst (DOC) affects the NO_x reduction efficiency of downstream selective catalyst reduction (SCR) catalyst. As a result, a purely experimental approach to system development becomes very time consuming and expensive. A use of mathematical modeling and simulation in such scenario can provide huge contribution in helping complex aftertreatment systems. A large number of mathematical models have been developed in the literature each with their advantages and disadvantages [110]. In this section, we review some of the models widely used in the modeling and simulation of catalytic monolith reactor.

There are mainly three different levels of model that are mostly used in modeling catalytic monolith [110]. They differ in the description of heat and mass transfer processes occurring in the channel. The first model is the tradition one dimensional model in which gradient in the washcoat is either neglected or accounted in the estimated kinetic parameters. In some variation of the model, the concept of overall mass transfer coefficient is used to account for the diffusion in the washcoat [111-113]. In these models, the transverse gradient in the fluid phase is represented by the use of external mass transfer concept. The second level of model is the so-called (1+1)-dimensional model in which 1D radial diffusion and reaction equations are solved at each axial position of the monolith along with 1D model in the fluid phase of the channel. Finally,

the detailed level of model is the full 3D convection/diffusion/reaction model that accounts for the gradient in the fluid as well as in the washcoat phase. While the 3D is an accurate representation of the catalytic reactor, it requires larger computation power. The general assumptions made in developing the model (applicable for most models) are as follows: (i) flow distribution is uniform resulting in identical channels, therefore, only single channel is considered, (ii) flow is laminar because of the small channel diameter, (iii) cross-section of the channel is invariant with the axial position i.e., washcoat thickness is uniform along the catalyst length, (iv) variation of physical properties with composition is negligible, and (v) pressure drop across the monolith channel is minimal. The details of the three mathematical model of catalytic channel are discussed below.

3.2.1 One-dimensional model

The one dimensional two-phase model is the most commonly used monolithic reactor model. In 1D model, the transverse or radial variation in the fluid phase is accounted for by the effective heat and mass transfer between the fluid phase and solid phase [110, 114, 115]. The model neglects the transverse temperature and concentration gradient in the washcoat i.e., the washcoat is assumed as a catalytic wall where the chemical reaction takes place. This assumption may lead to over prediction of computed conversion, especially when the diffusion in the washcoat becomes significant. In some studies [114, 116], the effect the washcoat diffusion is lumped into the estimated kinetic parameters. Despite the drawback, 1D model is still the choice of model in auto industry, largely because of fast computation and reasonable representation of the system [110].

To overcome the drawback of traditional 1D 2-phase model, Balakotaiah [117] developed a novel low-dimensional model of the catalytic channel which is the

generalization of the classical two-phase model. The model is developed by averaging the convection-diffusion-reaction (CDR) equations in the transverse direction and applying the concept of external and internal mass transfer coefficients [114, 117]. In a series of papers by Joshi et al., the benefits of using low dimensional model are explored in greater details. They showed that the low dimensional model gives all the qualitative trends of the detailed model which are not captured by the conventional 1D model without washcoat diffusion. The details of the low dimensional model are provided in the aforementioned references [111, 112, 114]. For completeness, the main governing equations of the generic low dimensional model are given below.

The species balances in the gas phase consist of accumulation, convection and external mass transfer from bulk fluid to washcoat is

$$\frac{\partial C_{fm,j}}{\partial t} + \langle u \rangle \frac{\partial C_{fm,j}}{\partial z} = -\frac{1}{R_{\Omega_1}} k_{mo,j} \left(C_{fm,j} - \langle C_{wc} \rangle_j \right), \quad (3-1)$$

where, $C_{fm,j}$ and $\langle C_{wc} \rangle_j$ represent the cup-mixing mole concentration of species j in the fluid phase and volume averaged concentration of species j in the washcoat, respectively. $\langle u \rangle$ is the average fluid velocity, R_{Ω_1} is the hydraulic radius defined as the ratio of channel area (open to flow) to channel perimeter, and $k_{mo,j}(z)$ is the overall mass transfer coefficient of species j at the axial position z given by

$$\frac{1}{k_{mo,j}} = \frac{1}{k_{mi,j}} + \frac{1}{k_{me,j}}, \quad (3-2)$$

where, $k_{mi,j}$ and $k_{me,j}$ are the internal and external mass transfer coefficients, respectively.

The mass transfer coefficients are computed using the following relations:

$$k_{me,j}(z) = \frac{Sh_e(z)D_{f,j}}{4R_{\Omega_1}} \text{ and} \quad (3-3)$$

$$k_{mi,j} = \frac{Sh_{i,\infty}D_{e,j}}{R_{\Omega_2}}, \quad (3-4)$$

where, $D_{f,j}$ and $D_{e,j}$ are the fluid phase diffusivity and effective washcoat diffusivity of species j , respectively. R_{Ω_2} is the effective transverse diffusion length in the washcoat defined as the ratio of washcoat cross-sectional area to the interfacial perimeter. $Sh_e(z)$ is the position-dependent external Sherwood number [115] and, Sh_i is the internal Sherwood number [111, 112, 114].

The species balances for component j in the washcoat are given as

$$\varepsilon_{wc} R_{\Omega_2} \frac{\partial \langle C_{wc} \rangle_j}{\partial t} = k_{mo,j} (C_{fm,j} - \langle C_{wc} \rangle_j) + R_{\Omega_2} \sum_{i=1}^N \mathcal{G}_i R_i (\langle C_{wc} \rangle_1, \langle C_{wc} \rangle_2, \dots, \langle C_{wc} \rangle_s, T_s), \quad (3-5)$$

where, ε_{wc} , \mathcal{G}_i , R_i and T_s represent the washcoat porosity, stoichiometric coefficients of species j in reaction i , reaction rate per unit washcoat volume of reaction i , and solid temperature, respectively.

The energy balances in fluid and solid phase are given below:

$$\rho_f c_{pf} \frac{\partial T_f}{\partial t} + \langle u \rangle \rho_f c_{pf} \frac{\partial T_f}{\partial z} = -\frac{1}{R_{\Omega_1}} h(z) (T_f - T_s) \text{ and} \quad (3-6)$$

$$R_{\Omega_w} \rho_w c_{pw} \frac{\partial T_s}{\partial t} = R_{\Omega_w} k_w \frac{\partial^2 T_s}{\partial z^2} + h(z) (T_f - T_s) + R_{\Omega_2} \sum_{j=1}^N R_j (\langle C_{wc} \rangle_1, \langle C_{wc} \rangle_2, \dots, \langle C_{wc} \rangle_s, T_s) (-\Delta H_j), \quad (3-7)$$

where, $\rho_f, c_{p,f}, h_f, T_f$ and T_s are the density of gas, specific heat capacity of gas, heat transfer coefficient, gas phase temperature and solid (washcoat + support) temperature respectively. The effective solid phase (wall) heat capacity and thermal conductivity are computed as $R_{\Omega_w} \rho_w c_{p,w} = R_{\Omega_2} \rho_c c_{p,c} + R_{\Omega_s} \rho_s c_{p,s}$ and $R_{\Omega_w} k_w = R_{\Omega_2} k_c + R_{\Omega_s} k_s$ respectively. The subscripts c and s refer to catalyst (washcoat) and support respectively

The initial, inlet and boundary conditions are given below:

$$\begin{aligned} C_{fm,j}(z, t=0) &= C_{fm,j0}(z) \\ \langle C_{wc} \rangle_j(z, t=0) &= \langle C_{wc} \rangle_{j0}(z) \text{ and} \\ C_{fm,j}(z=0, t) &= C_{j,in}(t) \end{aligned} \quad (3-8)$$

$$\begin{aligned} T_f(z=0, t) &= T_{fin}(t) \\ T_f(z, t=0) &= T_{f0}(z) \\ T_s(z, t=0) &= T_{s0}(z), \\ \frac{\partial T_s}{\partial z}(z=L, t) &= 0 \end{aligned} \quad (3-9)$$

where, $C_{fm,j0}(z)$, $\langle C_{wc} \rangle_{j0}(z)$, $T_{f0}(z)$, and $T_{s0}(z)$ are initial fluid phase concentration of species j , initial washcoat concentration of species j , and initial fluid and solid temperatures, respectively. $C_{j,in}(t)$ and $T_{fin}(t)$ are inlet concentration of species j and inlet fluid temperature, respectively.

3.2.2 (1+1)-dimensional model

The (1+1)-dimensional model explicitly accounts for the diffusion of species in the washcoat. The model consists of one dimensional species and energy balance in the fluid phase. The transverse gradient in the fluid phase is modeled by applying external mass transfer term in the fluid phase balance equation. A one-dimensional diffusion and reaction equation in the washcoat is included in the model to account for the diffusion in

the washcoat. The (1+1)-D model is often used when a detailed concentration profile in the washcoat is desired.

The model consists of species balance in the fluid phase,

$$\frac{\partial C_{fm,j}}{\partial t} = -\langle u \rangle \frac{\partial C_{fm,j}}{\partial z} - \frac{k_{me,j}(z)}{R_{\Omega_4}} (C_{fm,j} - C_{s,j}). \quad (3-10)$$

Similarly, species balance in washcoat phase is given as

$$\varepsilon_{wc} \frac{\partial C_{wc,j}}{\partial t} = \frac{\partial}{\partial y} \left(D_{e,j} \frac{\partial C_{wc,j}}{\partial y} \right) + \sum_{r=1}^{rxn} g_{jr} R_r (C_{wc1}, \dots, C_{wc,s}, T_s). \quad (3-11)$$

Finally, the energy balances in fluid phase and in solid phase are as follows:

$$R_{\Omega_w} \rho_w c_{pw} \frac{\partial T_s}{\partial t} = R_{\Omega_w} k_w \frac{\partial^2 T_s}{\partial z^2} + h(z) (T_f - T_s) \quad \text{and} \quad (3-12)$$

$$+ \int_0^{R_{\Omega_2}} \sum_{j=1}^N R_j (\langle C_{wc} \rangle_1, \langle C_{wc} \rangle_2, \dots, \langle C_{wc} \rangle_s, T_s) (-\Delta H_j) dy$$

$$\rho_f c_{pf} \frac{\partial T_f}{\partial t} + \langle u \rangle \rho_f c_{pf} \frac{\partial T_f}{\partial z} = -\frac{1}{R_{\Omega_4}} h(z) (T_f - T_s). \quad (3-13)$$

The above governing equations are solved along with following initial and boundary conditions:

$$t = 0 : \begin{aligned} x_{fm,j} &= x_{fm,j}^o \\ x_{wc,j} &= x_{wc,j}^o \end{aligned}, \quad (3-14)$$

$$z = 0 : x_{fm,j}(t) = x_{fm,j}^{in}(t), \quad (3-15)$$

$$y = 0 : k_{me,j} (x_{fm,j} - x_{s,j}) = -D_{e,j} \frac{\partial x_{wc,j}}{\partial y} \Big|_{x_{wc,j}=x_{s,j}}, \text{ and} \quad (3-16)$$

$$y = R_{\Omega_2} : \frac{\partial x_{wc,j}}{\partial y} = 0$$

$$\begin{aligned}
T_f(z=0, t) &= T_{fin}(t) \\
T_f(z, t=0) &= T_{f0}(z) \\
T_s(z, t=0) &= T_{s0}(z) \\
\frac{\partial T_s}{\partial z}(z=0, L, t) &= 0
\end{aligned} \tag{3-17}$$

3.2.3 Detailed 3D model

In the detailed 3D model we solve for species and heat balance equations in all the three dimensions. Figure 3-2 shows the schematic diagram of a single catalytic monolithic channel with arbitrary geometry showing different domains and boundaries. Ω_1 and Ω_2 denote the cross-sectional regions of the fluid phase and washcoat, respectively. We have not used 3D model in our current work as solving 3D model equations is numerically expensive.

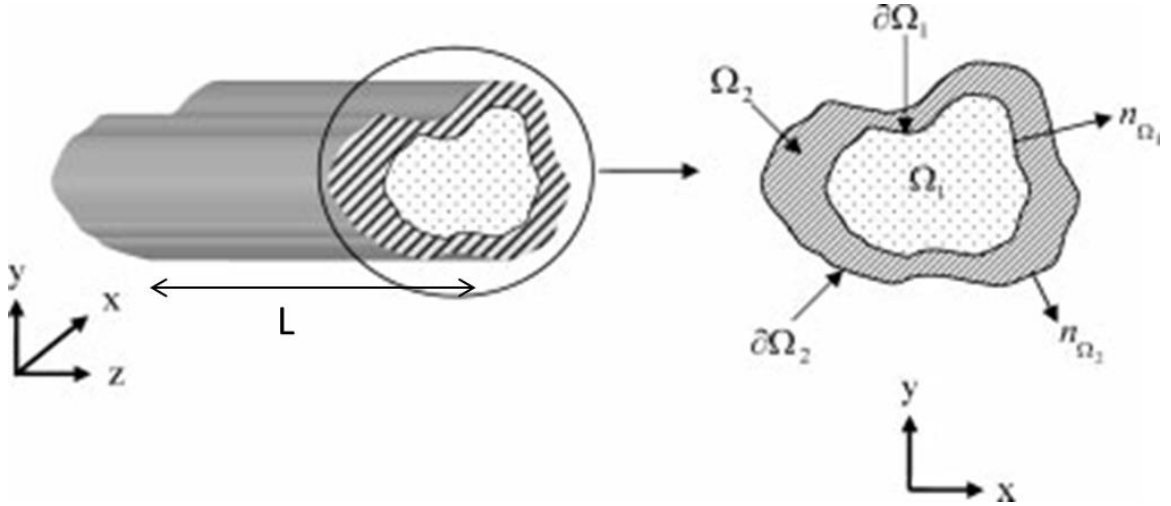


Figure 3-2. Schematic of catalytic channel with arbitrary shape showing different notations and domains [114].

The governing equations of the detailed model are discussed next. The species balance in the fluid phase is given by

$$\frac{\partial C_1}{\partial t} + \langle u \rangle f(x, y) \frac{\partial C_1}{\partial z} = D_f \left(\nabla_T^2 C_1 + \frac{\partial C_1}{\partial z^2} \right) \quad 0 < z < L \text{ in } \Omega_1, \tag{3-18}$$

where, C_1 is the reactant concentration in the fluid phase. ∇_T^2 is the transverse Laplacian operator in Ω_1 and Ω_2 . $f(x,y)$ is the normalized local velocity profile within the channel.

The following are the initial and boundary conditions:

$$\langle u \rangle f(x,y) C_{in} = \langle u \rangle f(x,y) C_1 - D_f \frac{\partial C_1}{\partial z} \quad \text{at } z = 0, \quad (3-19)$$

$$\frac{\partial C_1}{\partial z} = 0 \quad \text{at } z = L, \quad (3-20)$$

$$\left. \begin{array}{l} C_1 = C_2 \\ n_{\Omega_1} \cdot (D_f \nabla_T C_1 - D_e \nabla_T C_2) = 0 \end{array} \right\} \text{on } \partial\Omega_1 \text{ and} \quad (3-21)$$

$$C_1 = C_{10} \quad \text{at } t = 0. \quad (3-22)$$

Similarly, the species balance in the washcoat is expressed as

$$\varepsilon_{wc} \frac{\partial C_2}{\partial t} = D_e \left(\nabla_T^2 C_2 + \frac{\partial C_2}{\partial z^2} \right) - R(C_2, T_s) \quad 0 < z < L \text{ in } \Omega_2, \quad (3-23)$$

where, C_2 is the species concentration in the washcoat (Ω_2). The initial and boundary conditions are as follows:

$$n_{\Omega_1} \cdot \nabla_T C_2 = 0 \quad \text{on } \partial\Omega_2, \quad (3-24)$$

$$\frac{\partial C_2}{\partial z} = 0 \quad \text{at } z = 0, L \text{ in } \Omega_2, \text{ and} \quad (3-25)$$

$$C_2 = C_{20} \quad \text{at } t = 0. \quad (3-26)$$

Finally, the enthalpy balance in the fluid phase and solid phase along with initial and boundary conditions are as follows:

$$\rho_f c_{pf} \frac{\partial T_1}{\partial t} + \rho_f c_{pf} \langle u \rangle f(x,y) \frac{\partial T_1}{\partial z} = k_f \left(\nabla_T^2 T_1 + \frac{\partial T_1}{\partial z^2} \right) \quad 0 < z < L \text{ in } \Omega_1, \quad (3-27)$$

$$\rho_f c_{pf} \langle u \rangle f(x, y) T_{in} = \rho_f c_{pf} \langle u \rangle f(x, y) T_1 - T_f \frac{\partial T_1}{\partial z} \quad \text{at } z = 0, \quad (3-28)$$

$$\frac{\partial T_1}{\partial z} = 0 \quad \text{at } z = L, \quad (3-29)$$

$$\left. \begin{array}{l} T_1 = T_2 \\ n_{\Omega_3} \cdot (k_f \nabla_T T_1 - k_w \nabla_T T_2) = 0 \end{array} \right\} \text{on } \partial\Omega_1, \quad (3-30)$$

$$R_{\Omega_w} \rho_w c_{pw} \frac{\partial T_2}{\partial t} = R_{\Omega_w} k_w \left(\nabla_T^2 T_2 + \frac{\partial T_2}{\partial z^2} \right) + R_{\Omega_2} R(C_2, T_s) (-\Delta H_R) \quad 0 < z < L \text{ in } \Omega_2, \quad (3-31)$$

$$n_{\Omega_3} \cdot \nabla_T T_2 = 0 \quad \text{on } \partial\Omega_2, \quad (3-32)$$

$$\frac{\partial T_2}{\partial z} = 0 \quad \text{at } z = 0, L \text{ in } \Omega_2, \text{ and} \quad (3-33)$$

$$T_1(z, t = 0) = T_{10}(z) \quad (3-34)$$

$$T_2(z, t = 0) = T_{20}(z),$$

where, T_1 and T_2 are the temperature of the fluid phase and washcoat, respectively.

3.3 Numerical solution methods

In this section, we discuss about the numerical methods used in solving the transient and steady-state equations. The transient monolith reactor model is a set of coupled partial differential equations (PDEs). The PDEs were discretized using finite volume discretization scheme which results in a set of ODEs. The ODEs thus obtained are integrated by using backward differentiation formula method (LSODE subroutine in ODEPACK [113]). The optimization code (ODRPACK [118]) based on the trust-region Levenberg-Marquardt algorithm was also used in this study to estimate the kinetic parameters in Chapter 6 and 7.

CHAPTER 4 Selective Catalytic Reduction of NO_x with C₃H₆ over Cu-SSZ13 Monolithic Catalyst: Steady-State and Transient Bench-flow Reactor Studies

4.1 Introduction

Lean burn gasoline and diesel engines are more fuel efficient than the traditional stoichiometric engines. However, the major drawback of such engines is the elimination of NO_x (NO + NO₂) from lean exhaust. NO_x is hazardous to both environment and human health, and as a result stringent regulations have been imposed worldwide.

NO_x storage and reduction (NSR) and selective catalytic reduction (SCR) are the two commercialized aftertreatment technologies for the reduction of NO_x emissions from lean-burn engines. Both NSR and SCR have drawbacks which their combination attempts to mitigate. In particular, NSR catalysts are expensive and prone to catalyst poisoning (sulfur exposure) and deactivation (precious metal sintering) while SCR requires infrastructure for supplying the NH₃ reductant. For this reason interest has increased in the integrated NSR/SCR technology in order to lower the infrastructure cost associated with the SCR and materials cost associated with the expensive precious metal based NSR catalysts. The main advantages afforded by NSR/SCR are (i) in situ generation of NH₃ by the upstream NSR (or lean NO_x trap, LNT) catalyst and (ii) reduction of a potentially significant fraction of the NO_x by the much less expensive SCR catalyst. The NSR/SCR operating concept involves the storage of NO_x during the lean phase while unreacted hydrocarbons (C₃H₆, C₂H₄ etc.) and generated NH₃ are released from the LNT during the rich phase. The ammonia produced during the regeneration is

stored in the downstream SCR where it reacts with NO_x that leaves the upstream LNT unreacted. Added complexity is the storage of olefinic hydrocarbons in the SCR catalyst and their role as co-reductants of the NO_x coming out from LNT during lean phase [68, 69].

A large number of studies have been reported in the literature on selective catalytic reduction of NO_x with hydrocarbons (HC-SCR) over different catalytic materials. During the last few years, several works have been focused on the development of a reaction mechanism for HC-SCR of NO. The review by Burch et al., [23] concluded that for non-zeolitic oxides, species that are strongly adsorbed on the surface, such as nitrates/nitrites and acetates, are likely key intermediates in the formation of various reduced and oxidized species of nitrogen which, on further reaction, leads to the desired formation of N_2 . In contrast, for transition metal catalysts the mechanism of NO_x reduction involves the dissociative adsorption of NO over the reduced metal surface with subsequent recombination of N adatoms to form N_2 . The role of hydrocarbons in this type of mechanism is to remove the adsorbed atomic O species, generated during the NO dissociation, thereby restoring the initial catalytic surface [70].

Other studies have been carried out on mechanistic aspects of NO_x reduction with C_3H_6 over Cu-based zeolitic catalysts. One proposed pathway involves direct decomposition of NO over Cu with hydrocarbon playing the role of oxygen scavenger [71, 72]. The second proposed pathway involves R- N_tO_x compounds (R=hydrocarbon group) as intermediates, resulting from the reaction of adsorbed NO_x and HC species. These intermediates may either directly result in formation of molecular N_2 or decompose to other intermediates such as isocyanates, ammonia, nitriles, oximes, azo or azoxy

compounds [73-81]. The third proposed pathway involves the formation of oxygenates which then serve as reductants of NO_x [82]. Finally, the fourth pathway involves the oxidation of NO to NO_2 , which then react with hydrocarbons to form $\text{R-N}_t\text{O}_x$ species that decompose to form N_2 in subsequent reaction steps [83-85]. Luo et al., [86] showed that C_3H_6 has an inhibiting effect on selective catalytic reduction of NO_x with NH_3 on larger pore Cu/Beta zeolite above 200°C due to the formation of surface intermediates formed during C_3H_6 oxidation; these include acrolein-like species and coke-like species. More recently, Ye et al., [87] studied the propene poisoning resistance of Cu- exchanged small pore zeolite catalysts such as Cu-SSZ13. They found that hydrocarbon deposition is less on Cu-SSZ13 because of the smaller pores and cage diameters compared to the medium pore Cu-ZSM5. Hence the storage of hydrocarbons and their role as reductant of NO_x leads to a complex reaction system that requires further investigations especially for the emerging class of small pore zeolites.

The objective of this study is to elucidate the mechanistic steps involved in NO_x reduction with C_3H_6 on Cu-chabazite (small pore zeolites) monolithic catalyst. Cu-chabazite (SSZ-13) has emerged as an important synthetic zeolite for lean NO_x reduction on diesel vehicles due to its superior hydrothermal durability and hydrocarbon resistance. The few studies that have appeared in the literature focused primarily on the effect of hydrocarbons on the activity of SCR catalyst for NO_x reduction with NH_3 [86, 87] while other studies have only showed that non NH_3 pathways play important role for NO_x reduction for combined LNT/SCR systems [68, 69]. To our knowledge there have been no published studies on elucidating the mechanistic steps involved in lean NO_x reduction via non- NH_3 pathways (hydrocarbons, oxygenates, isocyanates, amines etc.). Here we

conduct steady state experiments of propylene oxidation and NO_x reduction in a bench scale monolith reactor to quantify the conversion and selectivity for feeds containing C₃H₆, O₂, and NO and/or NO₂. Differential kinetics measurements augment the integral reactor data by quantifying apparent reaction orders. Transient experiments are carried out to elucidate key mechanistic steps involved in lean NO_x reduction with C₃H₆ over small pore Cu-chabazite catalyst. In-situ DRIFTS experiments are also carried out to identify the surface intermediates formed during selective reduction of NO_x with C₃H₆. In-situ DRIFTS results are discussed in chapter 5. A phenomenological reaction mechanism is proposed that is consistent with these data.

4.2 Experimental

4.2.1 Catalyst

The catalyst used for these experiments were monolith-supported samples provided by BASF Catalysts LLC (Iselin, New Jersey). The sample had a cell density of 400 cells per square inch (cpsi). Large cylindrical cores were cut using a dry diamond saw to smaller, nearly cylindrical shapes (28 channels, diameter ~0.8 cm, L = 0.5-2 cm). The monoliths were then wrapped in heat treated Fiberfrax ceramic paper and inserted into a quartz reactor tube.

4.2.2 Bench-scale reactor setup

The experimental setup was the same as described in our earlier studies [119]. It includes a gas supply, a reactor, analytical system and data acquisition. The furnace temperature was set with a temperature controller. A FT-IR spectrometer (Thermo-Nicolet, Nexus 470) was positioned downstream of the reactor to analyze various effluent gases including C₃H₆, NO, NO₂, CO, CO₂ and H₂O. A quadrupole mass spectrometer

(QMS; MKS Spectra Products; Cirrus LM99) was used to measure N_2 . Argon was used as a balance gas and the total flow rate was kept constant at 1000 sccm in all the experiments. This corresponds to a gas hourly space velocity (GHSV) of about 57,000 h^{-1} and a linear velocity of 0.62 m/s (150 °C). Before the start of each experiment, each catalyst was pretreated at 600 °C in the presence of 5% O_2 and balance Ar for 60 min.

4.2.3 Steady state experiments

The NO oxidation steady state experiments included fixed concentration of NO (500 ppm) and O_2 (5%) over a range of temperatures (150–500°C). As in all the steady state experiments reported here, sufficient time was given to achieve the steady state effluent concentrations. The NO_2 decomposition reaction was studied using 500 ppm feed NO_2 over temperature range of 150-550°C.

The C_3H_6 oxidation steady state experiments included a fixed concentration of C_3H_6 (500 ppm) and varying O_2 concentration (0.5%, 1% and 5%) over a wide temperature range (200°C – 550 °C). Similar experiments were repeated with varying C_3H_6 concentration (200 ppm and 500 ppm) and fixed O_2 concentration (1%). The C_3H_6 oxidation experiment with fixed concentrations of C_3H_6 (500 ppm), O_2 (1%) and H_2O (3%) was also carried out to study the effect of H_2O on C_3H_6 oxidation.

NO and NO_2 effects were studied by feeding a mixture containing C_3H_6 (500 ppm) and NO or NO_2 (500 ppm) over the catalyst for the temperature range of 200-550°C. The reduction of NO_2 with C_3H_6 was carried out in the presence of excess oxygen, experiments carried out included the fixed concentrations of NO_2 (500 ppm), C_3H_6 (500 ppm) and varying concentrations of oxygen (1 or 5%). The reduction of NO with C_3H_6 was carried out in the presence of excess oxygen; experiments performed included the

fixed concentration of NO (500 ppm) and varying concentrations of oxygen (1 or 5%). Finally, the effect of H₂O on the NO reduction with C₃H₆ was studied in the presence of 2.5% H₂O.

4.2.4 Transient experiments

NO uptake and temperature programmed desorption (TPD) experiments were carried out on both fresh and C₃H₆ pre-adsorbed catalyst through the following steps. The catalyst was exposed to a gas mixture containing 500 ppm NO in balance Ar for 45 minutes at 150°C. The NO feed was then switched off and catalyst was flushed only with Ar for 10 min to remove loosely-bound NO. Finally, a temperature ramp of 10°C/min was applied to increase the catalyst temperature to 600°C. A similar approach was used for NO₂ TPD experiment.

Temperature programmed oxidation experiments were carried out on the monolith catalyst at the end of the steady state C₃H₆ oxidation experiment at 200°C, 250°C and 300°C. These experiments checked for the deposition of coke like species formed by the oligomerization of C₃H₆ derived hydrocarbon species. The catalyst was flushed with Ar to remove the loosely-bound C₃H₆ followed with C₃H₆ TPD in which temperature ramp of 10°C/min was applied to increase the catalyst temperature to 600°C. Then the catalyst sample was cooled to initial temperature and finally temperature was increased to 600°C linearly at the rate of 10°C/min in presence of 5% O₂ and balance to burn the coke deposited on catalyst.

In order to study the effect of NO₂ on C₃H₆ oxidation, transient experiments were carried out over a temperature range of 300°C–400°C. The catalyst sample was first exposed to a fixed C₃H₆ concentration (500 ppm) and O₂ concentration (1% or 5%) for

45 minutes, then 500 ppm NO₂ was included in the feed for 20 min and then switched off. A similar experiment was carried out to study the effect of NO on C₃H₆ oxidation for the same operating conditions.

The effect of catalyst pretreatment (reduction) was examined by exposure of the catalyst to H₂ prior to NO₂ adsorption. The catalyst was first pretreated with 5% O₂ in balance Ar for 60 min to oxidize the catalyst and then the catalyst sample was treated with 5% H₂ for 60 min to reduce the catalyst at 600 °C. The reduced catalyst sample was cooled to 200 °C and catalyst sample was exposed to 500 ppm NO₂ in balance Ar.

4.2.5 Varied catalyst length experiments

Spatially-resolved data were obtained using monoliths of different lengths. The standard catalyst length used in the experiments was 2 cm. Shorter length pieces were obtained by cutting the 2 cm long sample with a diamond saw, or sanding the larger sample if the change in length was very small ($\Delta L < 0.1$ cm). The monolith lengths employed were 0.5, 1 and 2 cm. Steady state experiments performed were NO₂ decomposition in presence of C₃H₆, NO₂ reduction with C₃H₆ under lean conditions and NO reduction with C₃H₆ under lean conditions.

4.3 Results and Discussion

4.3.1 NO/NO + C₃H₆ adsorption – desorption

In order to study the effect of C₃H₆ on NO adsorption two NO TPD experiments were performed. Figure 4-1 shows NO-TPD run over fresh catalyst. NO breakthrough occurred after 15 seconds and the NO concentration rapidly approached the NO feed value. A small NO desorption peak was obtained at 225°C on applying the temperature ramp. These data shows that NO uptake on the Cu-chabazite is negligible, in agreement

with previous studies [120-122]. NO adsorbs only on Cu sites and not on Bronsted acid sites [75]. Similarly, in a second NO TPD run, the catalyst was first exposed to C₃H₆ in balance Ar for 30 minutes, exposed to NO in balance Ar for 45 minutes, flushed with Ar for 10 minutes, and finally exposed to a temperature ramp of 10°C/min up to 600°C. Figure 4-2 shows NO outlet signal as soon as NO was introduced in the feed and no peak of NO was observed during the temperature ramp. NO does not react with C₃H₆ at 150°C in absence of O₂ as shown by Wang et al., [68]. These data show that C₃H₆ adsorb on Cu-sites and thus block the sites for NO adsorption. Hence, C₃H₆ adsorb on the Bronsted sites as well as on Cu-sites [68].Figure

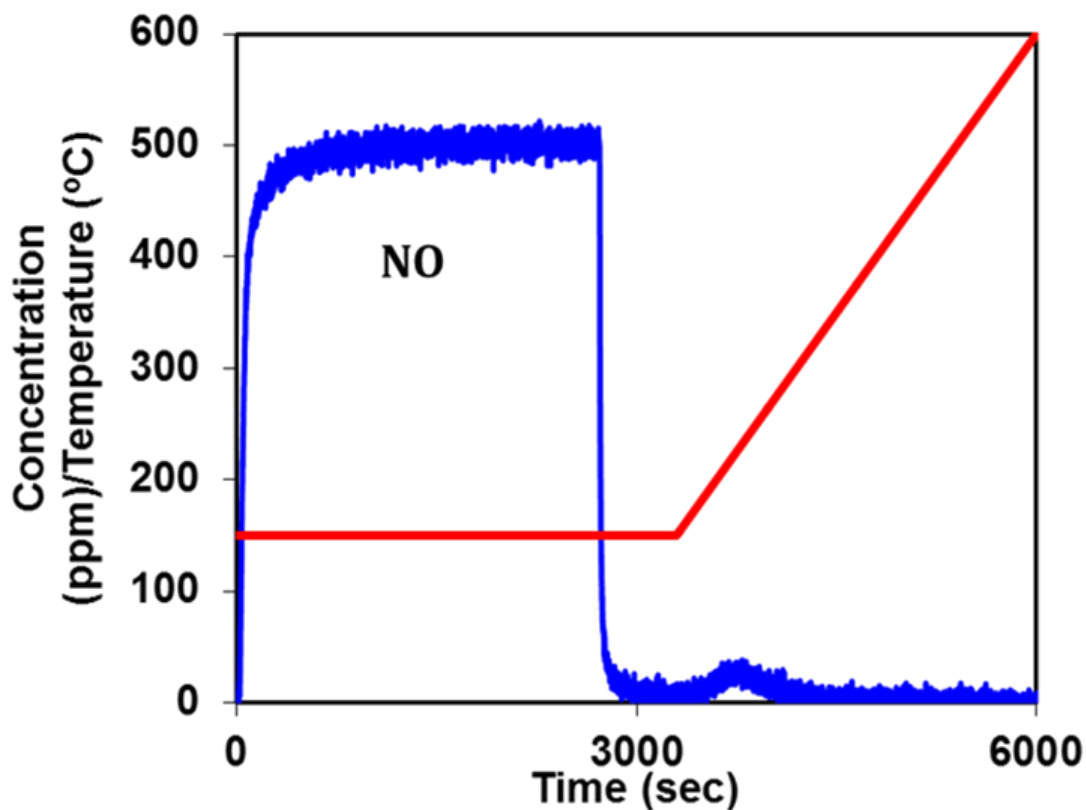


Figure 4-1. NO adsorption and desorption over fresh catalyst (NO = 500 ppm, Balance gas: Ar)

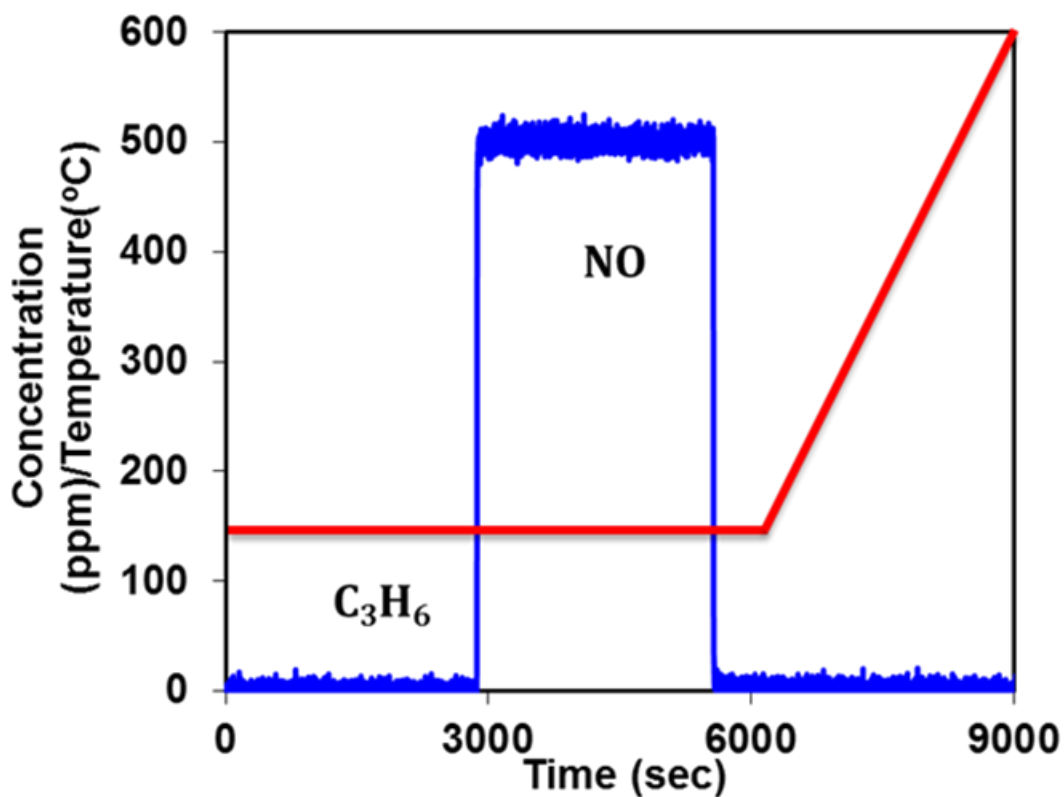
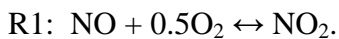


Figure 4-2. NO adsorption and desorption over catalyst pre adsorbed with 500 ppm C_3H_6 (NO = 500 ppm, Balance gas: Ar)

4.3.2 NO oxidation/ NO_2 decomposition

Figure 4-3 shows the dependence of NO conversion on temperature for a feed containing 500 ppm NO and 5% O_2 . In this steady state experiment temperature was increased in steps of $50^\circ C$ from $100^\circ C$ to $550^\circ C$. As expected, the NO conversion increases with temperature for the temperatures below $400^\circ C$ (kinetically controlled regime) and attains a maximum conversion of ca. 37%. Above $400^\circ C$, the conversion decreases with temperature because of the thermodynamic limitations as [121]



A similar experiment was conducted with a feed containing 500 ppm NO₂ and 5% O₂. Figure 4-3 shows that NO₂ conversion increased with temperature. The NO₂ decomposition to N₂ and O₂ commenced at 300°C and attained 80% conversion at 550°C.

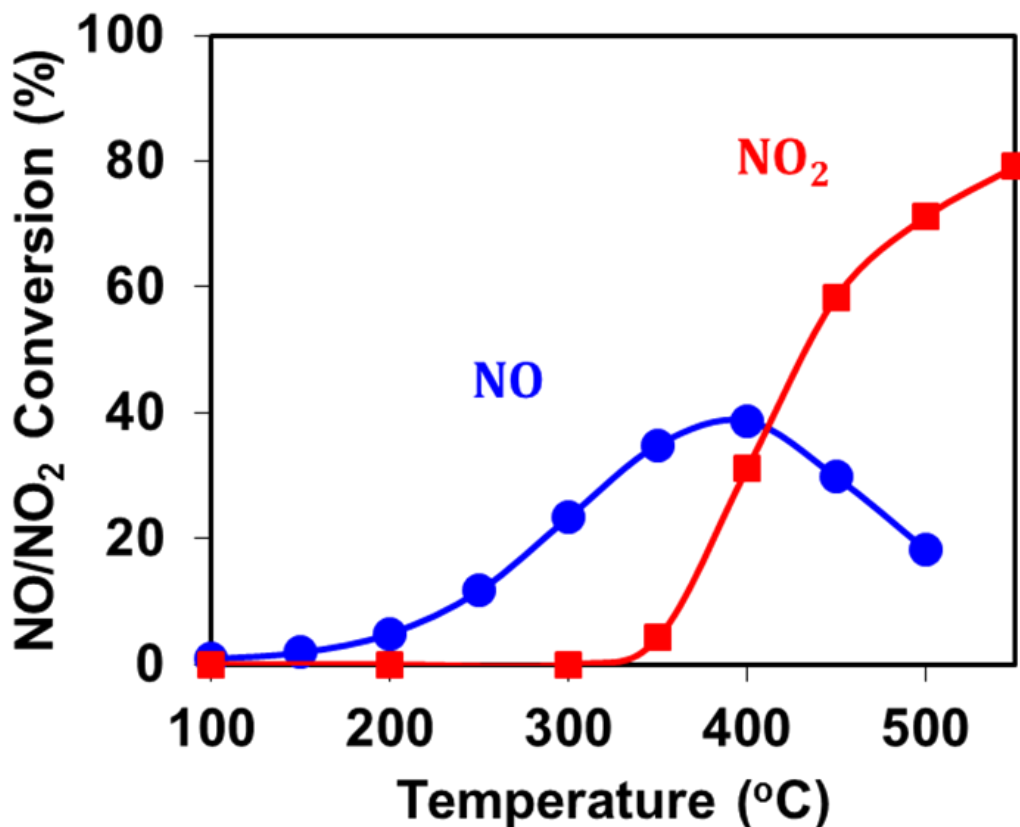
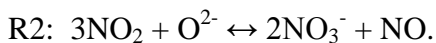


Figure 4-3. Steady state conversion as a function of temperature for NO/NO₂ feed (NO = 500 ppm, O₂ = 5%, Balance gas: Ar) (NO₂ = 500 ppm, O₂ = 5%, Balance gas: Ar)

4.3.3 Effect of catalyst pretreatment on NO₂ adsorption

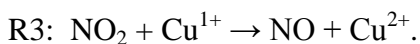
In order to better understand the effect of the oxidation state of Cu on the NO₂ adsorption, two different pretreatments of catalyst were compared for NO₂ uptake. The catalyst was pretreated in the presence of 5% O₂ in balance Ar for 60 minutes to oxidize the Cu sites, cooled to 200°C, and then exposed to 500 ppm NO₂ at 200°C. A NO peak

was observed during the initial period of NO₂ adsorption as shown in Figure 4-4. This is attributed to the disproportionation reaction from NO₂ to produce NO and nitrates [120-122]:



The ratio of NO formed/inlet NO₂ that exhibits maxima of about 0.3 (Figure 4-4b), which is in accordance with the stoichiometry of the disproportionation reaction.

A similar experiment was carried out in which the catalyst was pretreated with 5% H₂ in balance Ar for 60 minutes to reduce the Cu sites [123]. The extent of pre-reduction of the catalyst was studied at 200°C by admitting 500 ppm NO₂ over catalyst pretreated with H₂. The data in Figure 4-4a show a large NO peak appeared immediately attaining a maximum of 350 ppm. The ratio of NO formed/inlet NO₂ as shown in Figure 4-4b attained a maximum of about 0.7 and then decreased to the baseline level. The measured stoichiometry in these data indicate that NO₂ disproportionation reaction was not the major pathway; rather, NO₂ served to oxidize Cu¹⁺ sites to Cu²⁺, liberating NO:



These data show that the oxidation state of the Cu plays a potentially important role in the reaction chemistry and pathways.

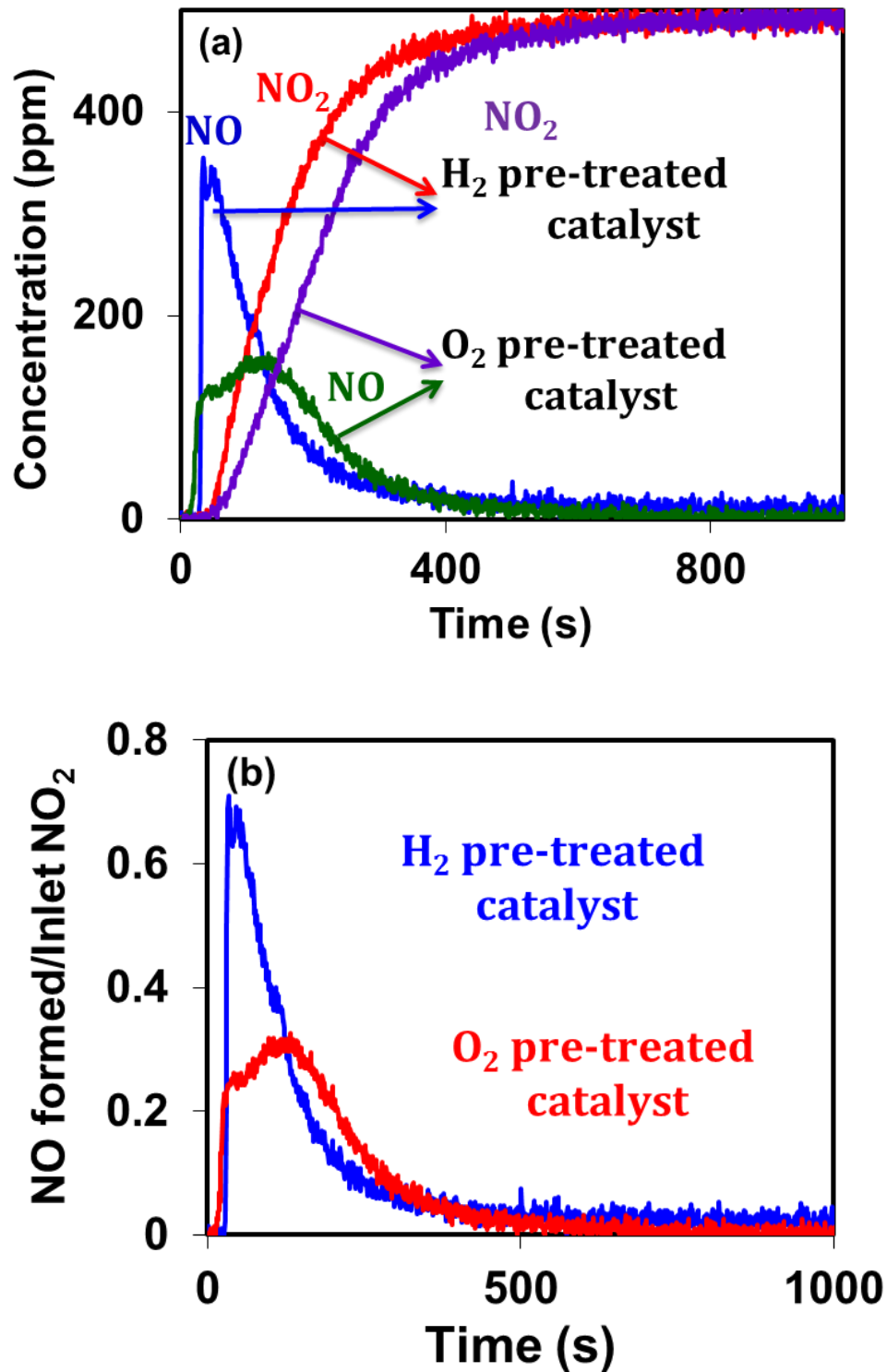


Figure 4-4. NO₂ and NO outlet concentration with time on exposure of NO₂ over O₂ pretreated and H₂ pretreated catalysts (NO₂ = 500 ppm, Balance gas: Ar)

4.3.4 C₃H₆ oxidation

The oxidation of propylene leads to formation of CO₂ and CO, as follows:



Figure 4-5a shows the dependence of the conversion of C₃H₆ on temperature for different feed oxygen concentrations. As the oxygen concentration increases from 0.5 to 5% the light-off temperature of C₃H₆ oxidation decreases. This suggests a positive reaction order with respect to oxygen [124, 125]. There is a decrease of 50°C in the light off temperature on increasing the O₂ concentration in feed from 1 to 5%, showing that adsorbed O₂ plays role in maintaining the active oxidation state of the Cu [126]. The adsorbed O₂ oxidizes the reduced Cu sites. Similar experiments were performed with varying C₃H₆ feed concentration. Figure 4-5b shows that there is increase in light-off temperature with an increase in C₃H₆ concentration. Figure 4-6 shows the corresponding CO selectivity curve which exhibits a maximum at 450°C and 350°C for a feed containing 1 and 5% O₂, respectively. These data suggest that at higher temperatures CO₂ is the major product via complete C₃H₆ oxidation and CO oxidation.

Differential kinetic studies were also performed in temperature range of 250°C-300°C to determine (conversion < 15%) the reaction orders with respect to C₃H₆ and O₂. The reaction order with respect to C₃H₆ is -0.75 and with respect to O₂ is 0.25. This shows that C₃H₆ has an inhibiting effect on C₃H₆ oxidation. These data are shown in the Figs. 4-7a and 4-7b. The results confirm the kinetic features inferred by the light-off data.

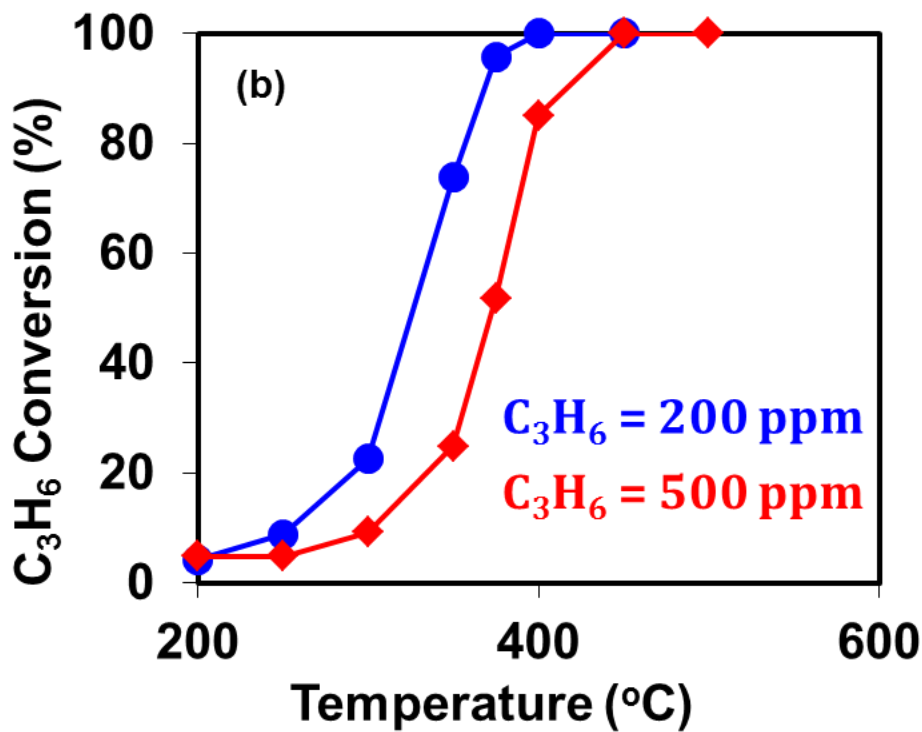
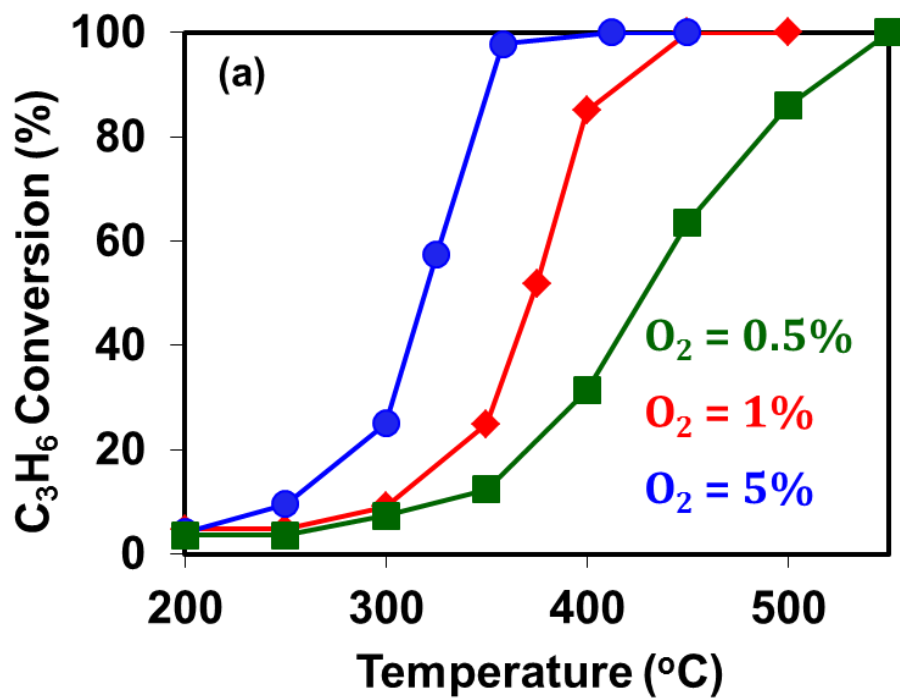


Figure 4-5. (a) Light- off curves of C_3H_6 for different oxygen concentrations in the feed ($C_3H_6 = 500$ ppm, $O_2 = 0.5$ or 1 or 5%, Balance gas: Ar), (b) Light- off curves of C_3H_6 for different C_3H_6 concentrations ($C_3H_6 = 200$ or 500 ppm, $O_2 = 1\%$, Balance gas: Ar)

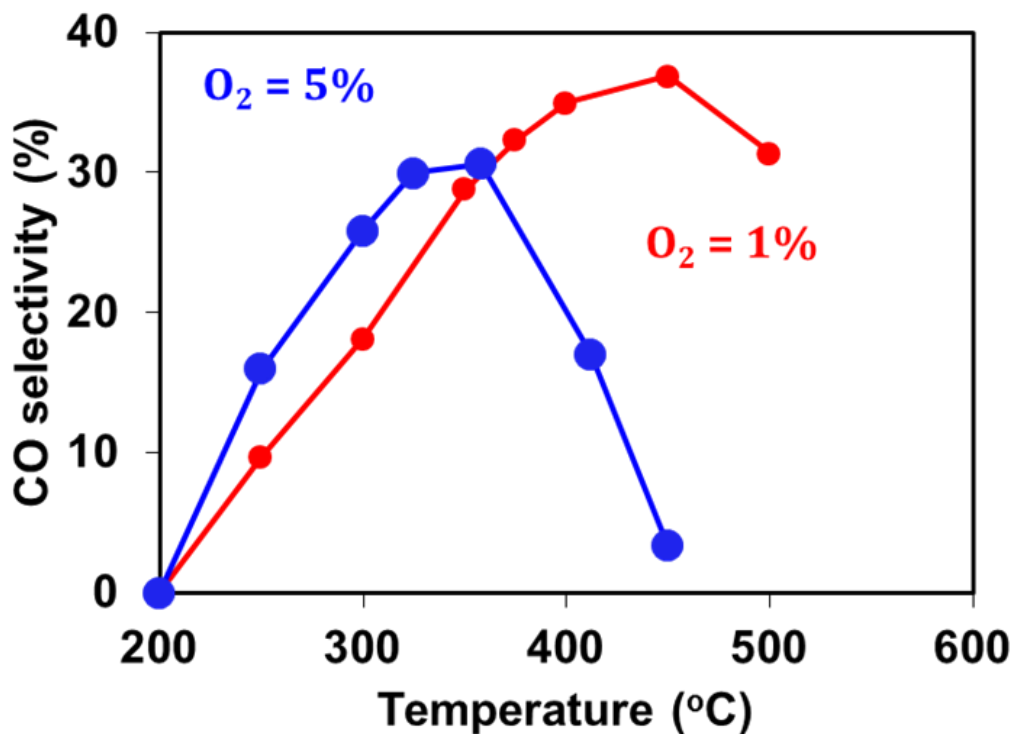


Figure 4-6. CO selectivity curve in C₃H₆ oxidation (C₃H₆ = 500 ppm, O₂ = 1 or 5%, Balance gas: Ar)

Coke deposition and oxidation occur at all temperatures [75, 127]. At temperatures above 400 °C the rate of coke oxidation exceeds its formation rate and there is no accumulation. At lower temperatures there is accumulation of coke. To confirm the formation of coke temperature programmed oxidation (TPO) was carried out at the end of steady-state C₃H₆ oxidation in which the catalyst was maintained at 200°C, 250°C and 300°C. In order to isolate the oxidation of coke-like species from adsorbed/loosely-bound C₃H₆, the catalyst was first flushed with Ar under a temperature ramp of 10°C/min up to 600°C. Once all the adsorbed C₃H₆ was removed, the catalyst sample was cooled back to its initial temperature (200°C) and temperature ramp of 10°C/min was applied in presence of 5% O₂ and balance Ar to increase the temperature to 600°C. Figure 4-8 shows CO,

CO₂ and H₂O peaks during TPO, confirming the accumulation of condensed hydrocarbon species.

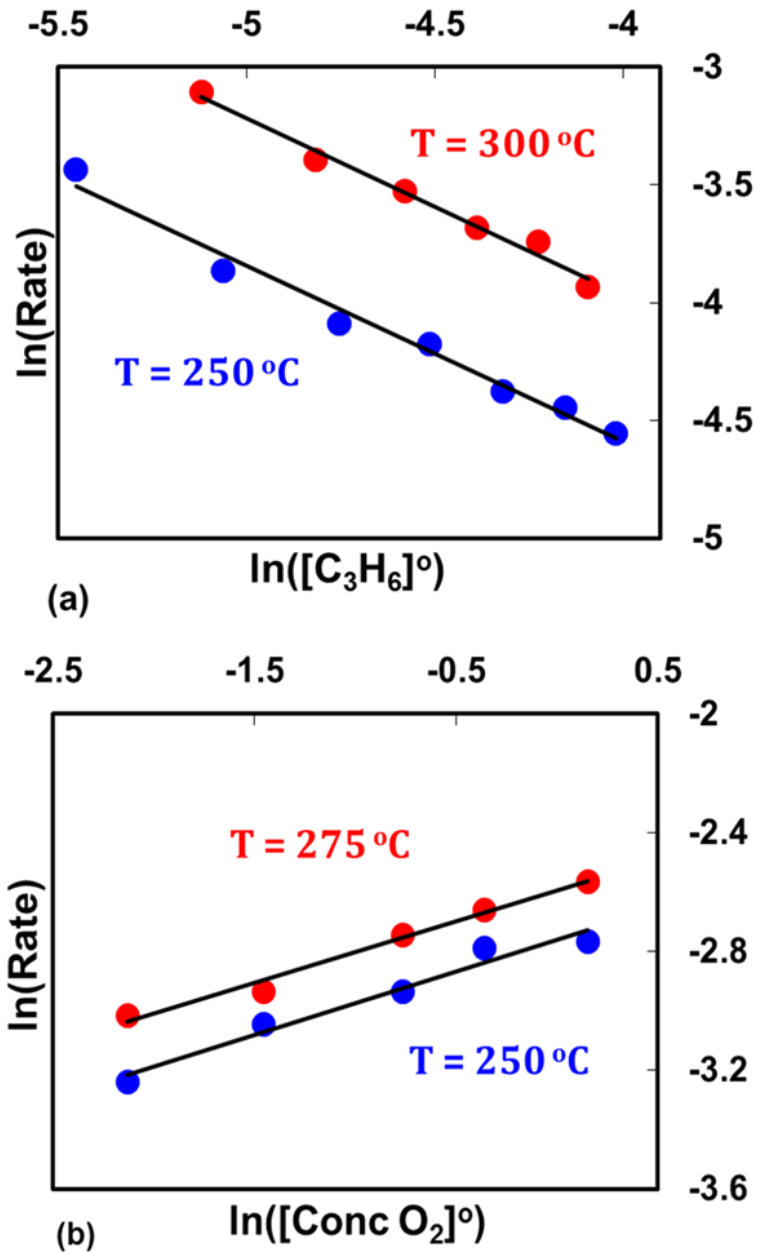


Figure 4-7. (a) Dependence of C_3H_6 oxidation rates on C_3H_6 (1% O_2 , 200–800 ppm C_3H_6) (b) Dependence of C_3H_6 oxidation rates on O_2 (0.5–3% O_2 , 500 ppm C_3H_6), (Rate is in $\text{moles}\cdot\text{m}^{-3}\cdot\text{s}^{-1}$, concentration is in $\text{moles}\cdot\text{m}^{-3}$)

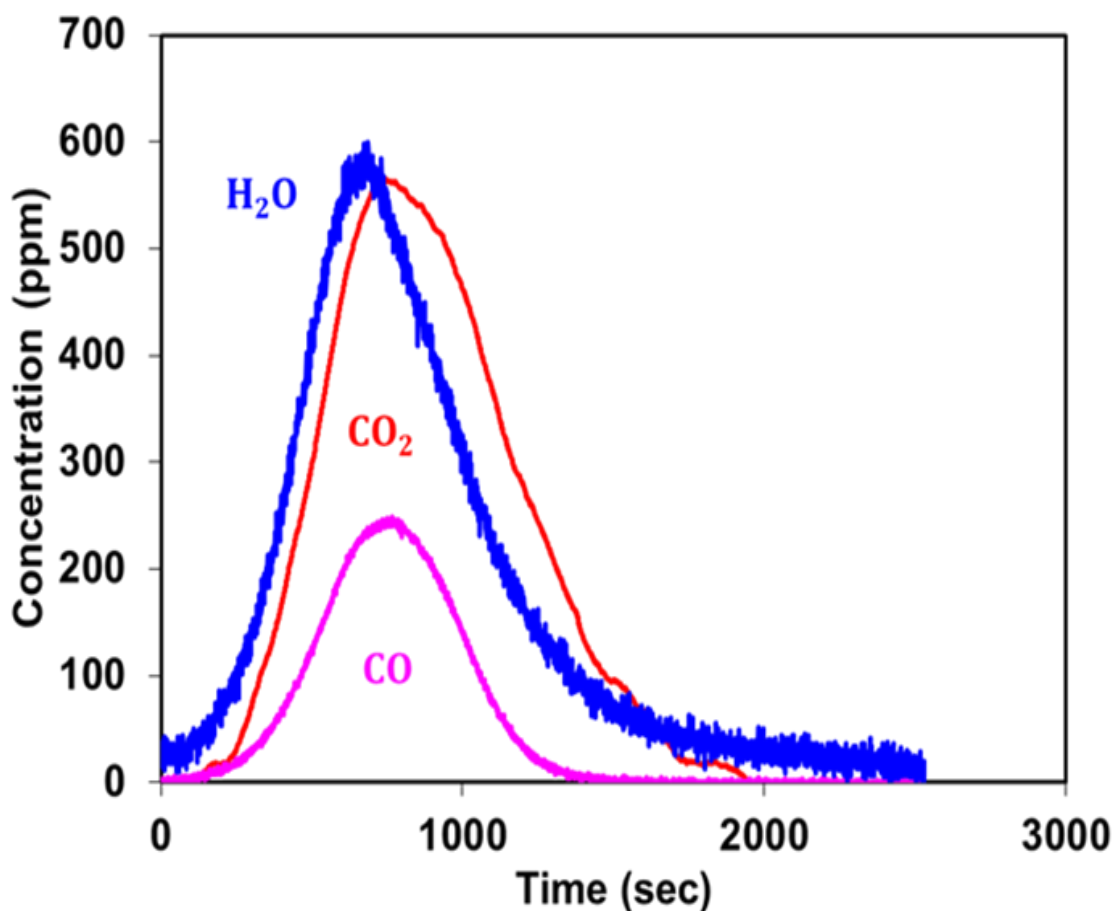


Figure 4-8. CO, H₂O and CO₂ peaks obtained during temperature ramp from 200 °C to 600 °C in presence of O₂ (O₂ = 5%, Balance gas: Ar)

Finally, the effect of H₂O on the C₃H₆ oxidation was checked by exposing the catalyst to the same 500 ppm C₃H₆, 1% O₂ and 2.5% H₂O. Fig 4-9 shows that C₃H₆ light-off temperature decreased by 50°C in presence of water. Water presumably plays a role of maintaining the Cu²⁺ for C₃H₆ oxidation.

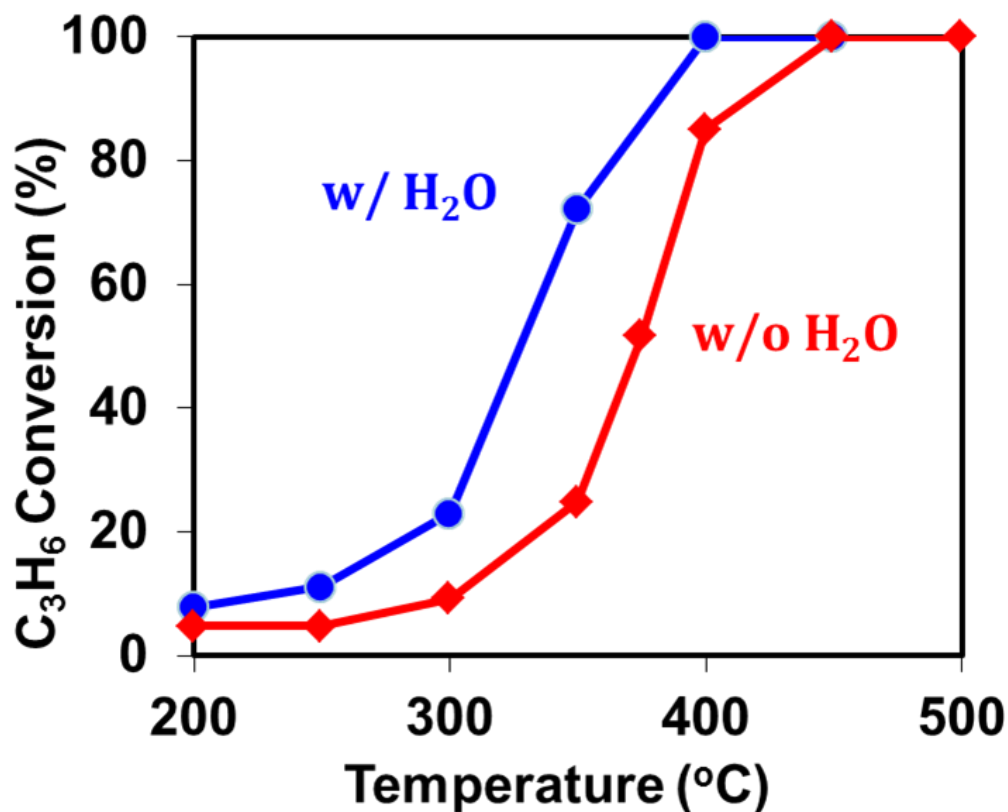
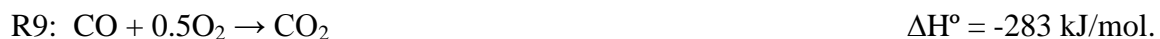


Figure 4-9. C₃H₆ conversion in presence of 2.5% H₂O (C₃H₆ = 500 ppm, O₂ = 1%, H₂O = 2.5%, Balance gas: Ar)

4.3.5. NO₂ reduction with C₃H₆ under lean conditions

The effect of NO₂ on the C₃H₆ oxidation and of its reduction to NO and N₂ was systematically studied through a combination of steady state and transient experiments. The catalyst sample was exposed to 500 ppm NO₂, 500 ppm C₃H₆ and 1% or 5% O₂ over a temperature range of 200–550 °C. Figure 4-10a and Figure 4-10b shows the dependence of C₃H₆ conversion on temperature for 1% and 5% O₂ in the feed, with and without NO₂ in the feed in both cases. The C₃H₆ light-off curve for C₃H₆ oxidation without NO₂ has a rather sharp sigmoidal shape while the C₃H₆ light-off curve for feed with NO₂ is much more gradual. For temperatures below 350 °C the C₃H₆ conversion with NO₂ in the feed

is higher than the corresponding conversion without NO₂ in the feed. This qualitative feature is observed at the low (Figure 4-10a) and high (Figure 4-10b) O₂ concentration although the differences are more significant at the lower O₂ concentration. Another feature on increasing the O₂ feed concentration from 1% to 5% is a lowering of the transition temperature from 350°C to 325°C. The unusual shape of the C₃H₆ light-off curve with NO₂ suggests some inhibitive mechanism that delays the light-off of propylene. The unidentified inhibiting component may require a reaction pathway that involves NO₂ and surface species in the propylene oxidation reaction system. A set of independent global reactions involving these reacting species is as follows:



A comparison of the propylene and the NO₂ conversions is shown in Figure 4-11a. The data show a much sharper increase in the NO₂ conversion compared to the propylene conversion. NO₂ is in fact depleted by 300 °C whereas C₃H₆ is not depleted till 550°C. Figure 4-11b shows the dependence of the effluent concentrations of the N-containing products NO and N₂ with temperature. At lower temperature NO₂ is partially reduced to NO, while at higher temperature SCR of NO₂ to N₂ occurs to a larger extent. It was shown earlier that NO₂ decomposition starts above 350°C for a feed containing 500 ppm NO₂ and 5% O₂. The enhancement in the conversion of NO₂ to NO in presence of C₃H₆ may be attributed to the reduction of active catalytic sites by C₃H₆. The NO outlet concentration increases with temperature and achieves a maximum at about 350°C. This

is a manifestation of the coupling between reactions R7 (NO formed) and R8 (NO consumed).

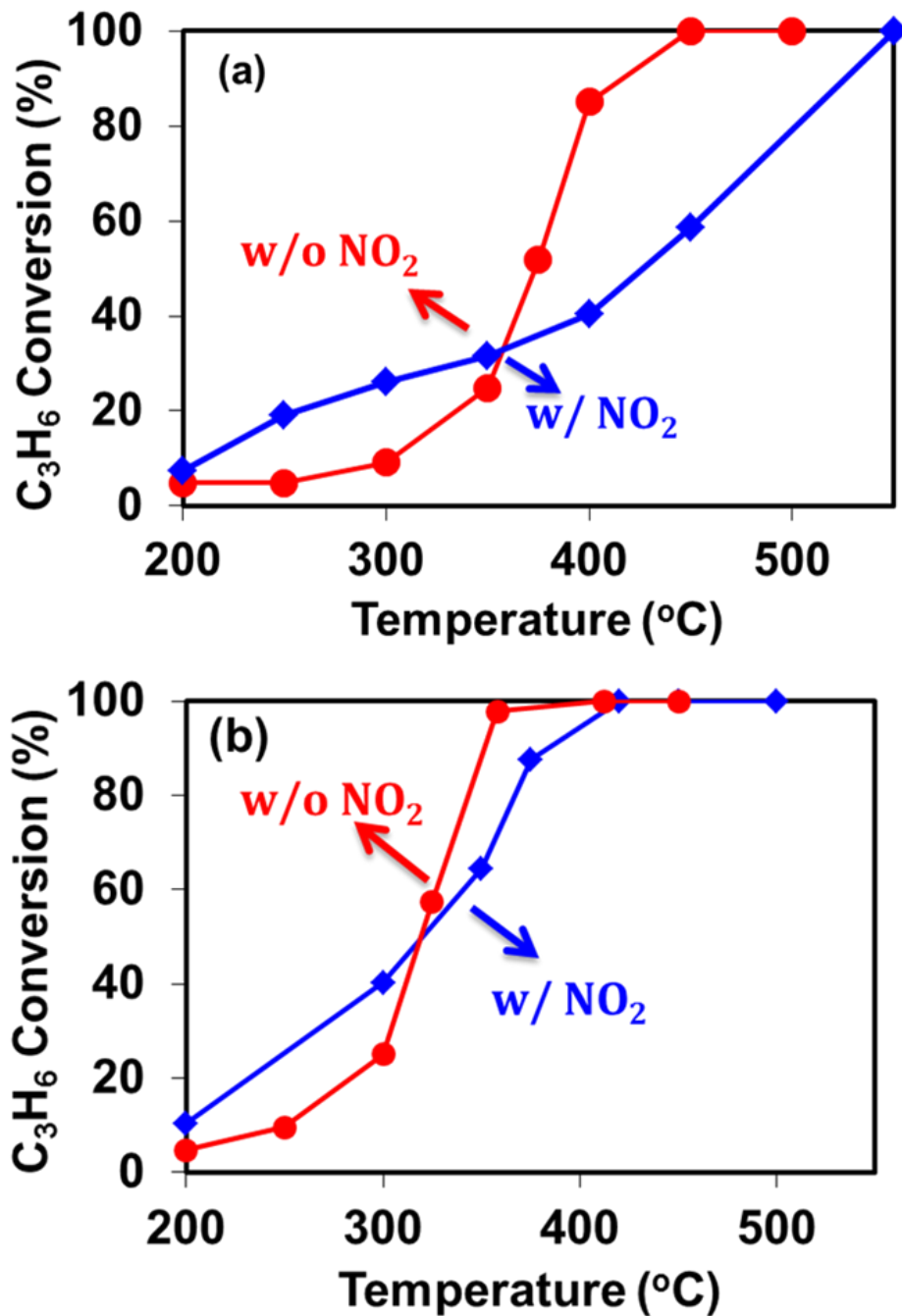


Figure 4-10 (a) C₃H₆ light off curves with and without NO₂ in feed (C₃H₆ = 500 ppm, NO₂ = 0 or 500 ppm, O₂ = 1%), (b) C₃H₆ light off curves with and without NO₂ in feed (C₃H₆ = 500 ppm, NO₂ = 0 or 500 ppm, O₂ = 5%) (Bal gas: Ar)

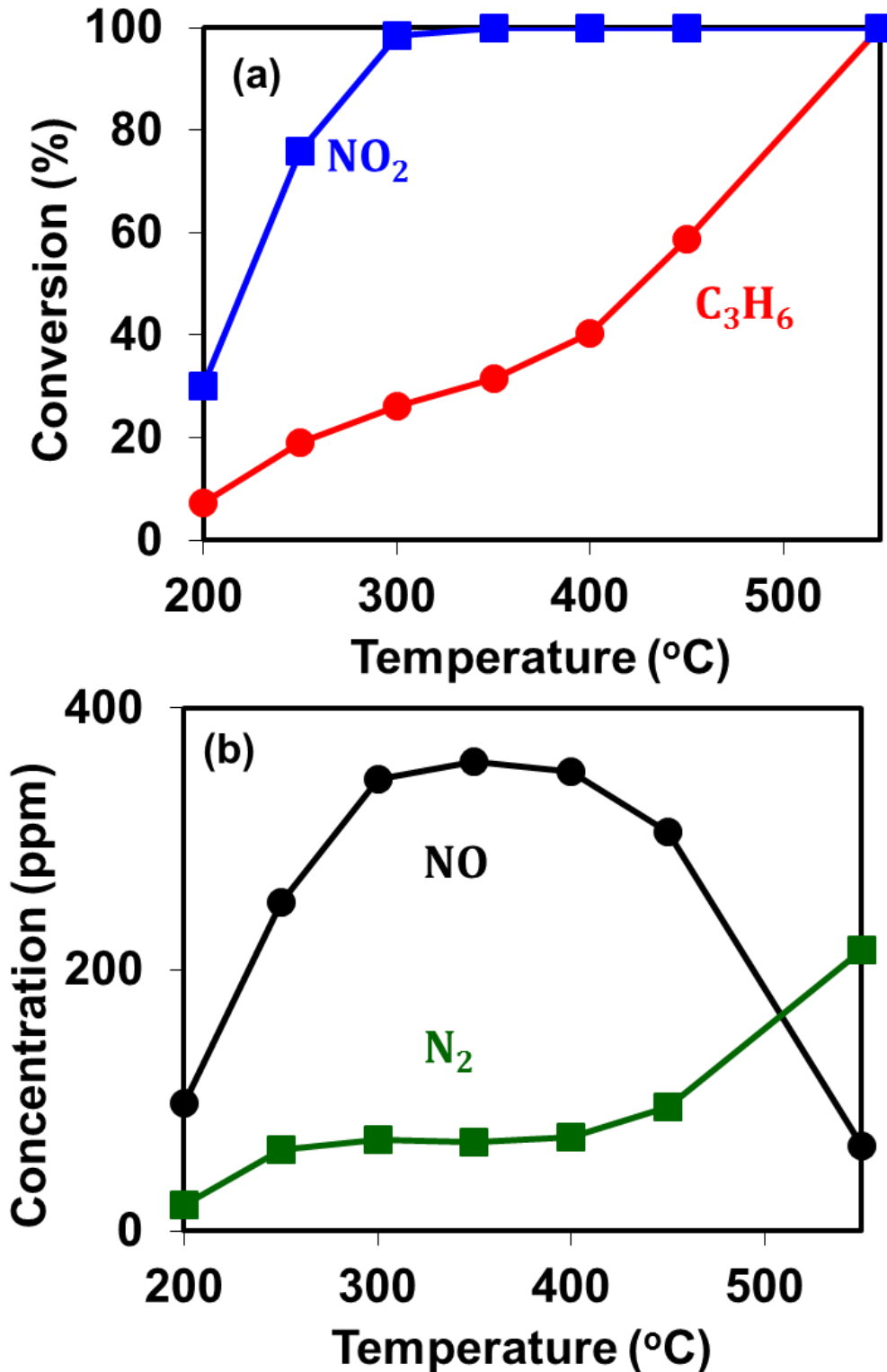


Figure 4-11. (a) NO_2 and C_3H_6 conversion ($\text{C}_3\text{H}_6 = 500$ ppm, $\text{NO}_2 = 500$ ppm, $\text{O}_2 = 1\%$, Balance gas: Ar), (b) NO and N_2 outlet concentration ($\text{C}_3\text{H}_6 = 500$ ppm, $\text{NO}_2 = 500$ ppm, $\text{O}_2 = 1\%$, Balance gas: Ar)

A set of steady state and transient experiments were carried out to elucidate the underlying mechanism. The first set of experiments involved the measurement of the spatial distribution of reactants and products along the monolith axis for a feed containing 500 ppm NO_2 , 500 ppm C_3H_6 and 1% O_2 over the temperature range of 200°C – 550°C . In these experiments three monoliths with length 0.5, 1 and 2 cm were exposed to 500 ppm NO_2 , 500 ppm C_3H_6 and 1% O_2 . Figure 4-12a shows spatial profile of NO_2 conversion between 200°C and 550°C . The data reveal that below 350°C NO_2 is present along the entire catalyst length whereas above 350°C NO_2 is completely reduced to NO and N_2 near the inlet region of the monolith. The reactant NO_2 is only present in the inlet region while the remainder of the catalyst is exposed to the NO formed from NO_2 reduction. NO_2 being a stronger oxidizing agent than O_2 will oxidize C_3H_6 more efficiently. This results in an increase in C_3H_6 conversion for the NO_2 containing feed below 350°C . Figure 4-12b shows that C_3H_6 conversion expectedly increases with temperature. Figure 4-13 shows the more complex spatial distribution of NO concentration over the same temperature range. The NO concentration increases along the length of monolith between 200°C to 350°C and achieves a maximum in the range of 400°C – 550°C . This suggests that above 350°C the NO formed by the NO_2 reduction also take part in the reaction. Above 350°C NO_2 is completely reduced to NO and N_2 within 0.5 cm of monolith length while the rest of the catalyst is exposed only to NO . These data further suggest that NO is the key NO_x species that participates in the surface chemistry at the transition point given its predominance in this regime.

In order to further illustrate the point that NO_2 is not directly involved in the inhibition of the propylene light-off, transient NO_2 exposure of the catalyst was

performed. In this case the catalyst was exposed to 500 ppm C_3H_6 and 1% O_2 for 45 minutes at $300^\circ C$ and then NO_2 was introduced in the feed for 10 minutes. Figure 4-14 shows that upon introduction of NO_2 in the feed there is an instantaneous decrease in outlet concentration of C_3H_6 from 450 ppm to 350 ppm. This may be explained by the strong oxidizing ability of NO_2 ; i.e. C_3H_6 is rapidly oxidized and NO_2 is reduced to NO and N_2 . After switching off the NO_2 from the feed the C_3H_6 outlet concentration approaches its initial concentration of 450 ppm. These transient data clearly show that introduction of NO_2 in the feed does not alter the catalyst activity for C_3H_6 oxidation. Thus, NO_2 does not directly take part in formation of stable intermediates that poison the catalytic surface and delay the C_3H_6 light off. Rather, NO_2 is reduced to NO which appears to play a direct role in the formation of intermediates that results in blocking the active sites for the C_3H_6 oxidation.

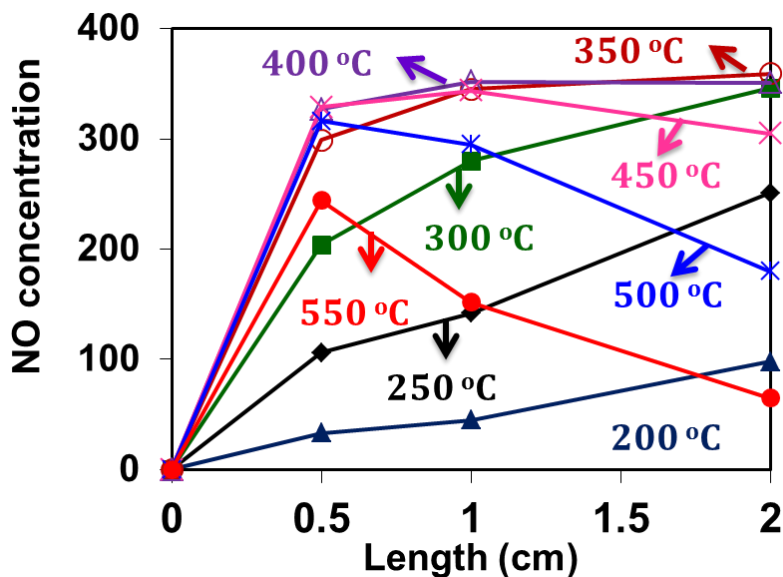


Figure 4-12. Spatially resolved steady state NO concentration at different temperatures ($C_3H_6 = 500$ ppm, $NO_2 = 500$ ppm, $O_2 = 1\%$, Balance gas: Ar)

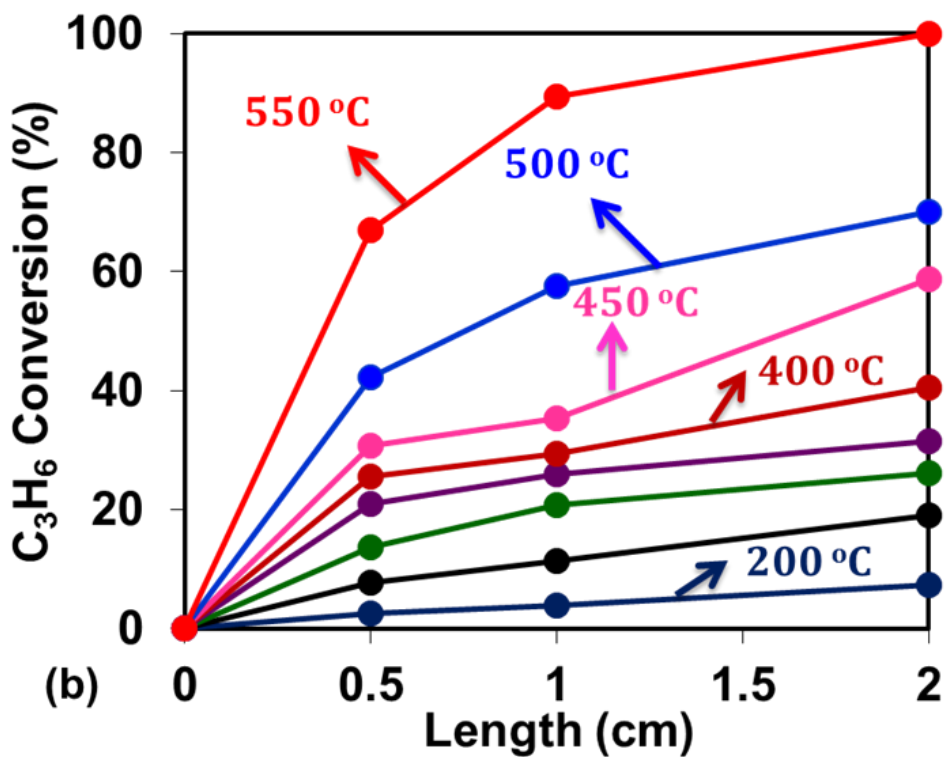
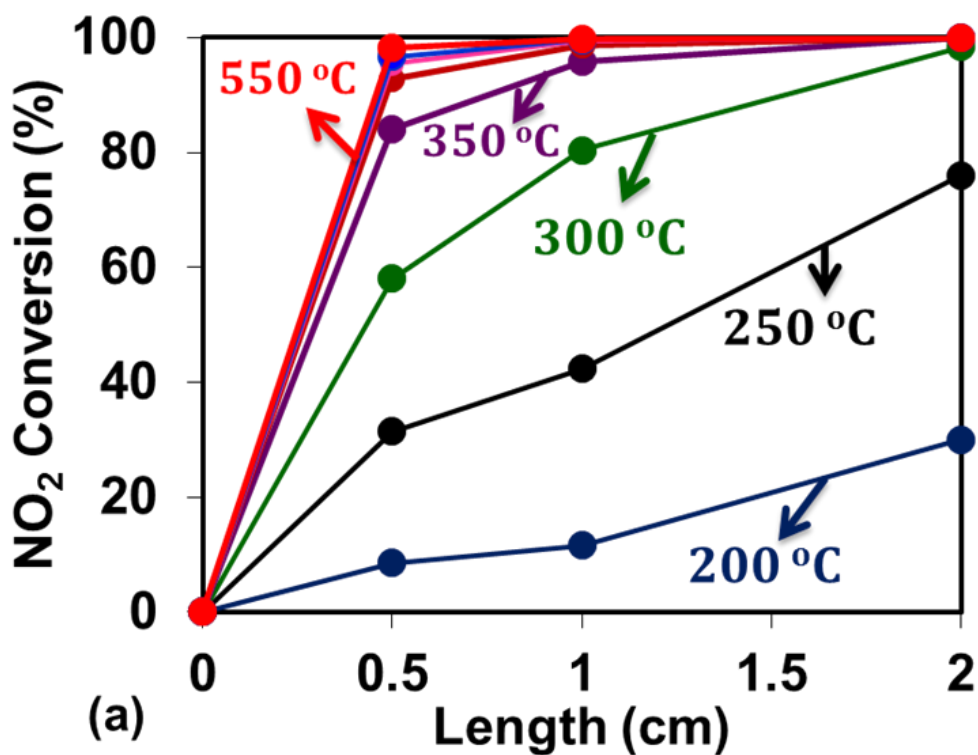


Figure 4-13. (a) Spatially resolved steady state NO₂ conversion at different temperatures (b) Spatially resolved steady state C₃H₆ conversion at different temperatures (C₃H₆ = 500 ppm, NO₂ = 500 ppm, O₂ = 1%, Bal. gas: Ar)

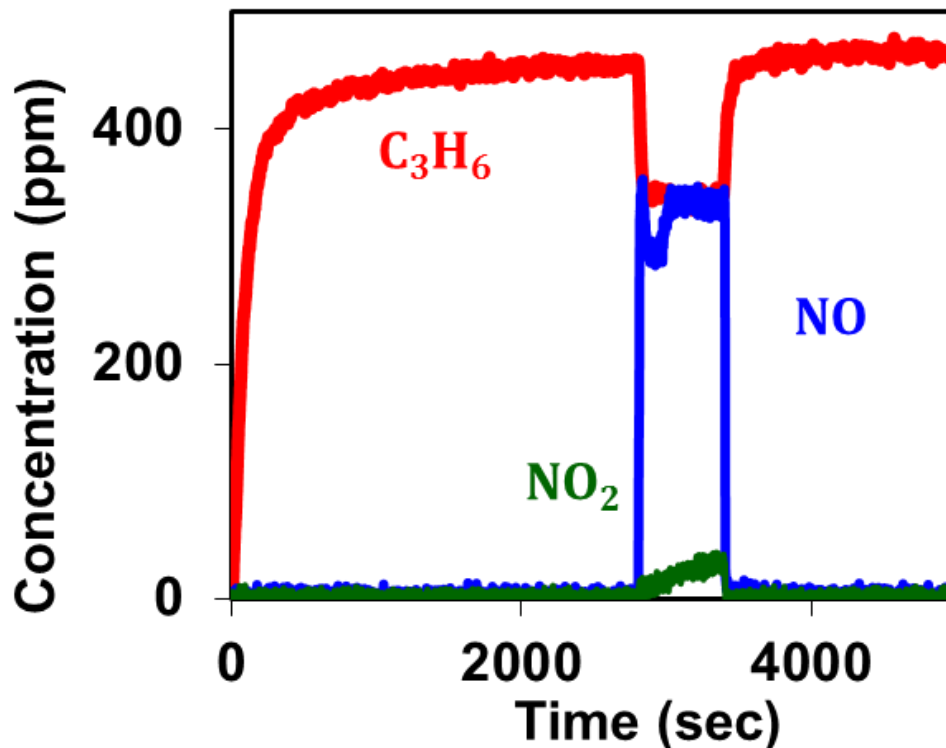


Figure 4-14. C_3H_6 , NO_2 and NO outlet concentration with time ($C_3H_6 = 500$ ppm, $NO_2 = 0$ or 500 ppm, $O_2 = 1\%$, Balance gas: Ar)

4.3.6. NO reduction with C_3H_6 under lean conditions

In order to explore the role of NO during propylene oxidation, the propylene oxidation conversion was compared in the absence and presence of NO . Figure 4-15a shows the C_3H_6 light-off curves for a feed containing 500 ppm C_3H_6 and 1% O_2 with and without 500 ppm NO . These data clearly show the NO inhibition on C_3H_6 oxidation reaction similar to the trend shown earlier for NO_2 . The inhibition is observed over the temperature range of $350^\circ C$ to $500^\circ C$. Below $350^\circ C$ there is little effect of NO on C_3H_6 conversion. The results in Figure 4-15b also show NO inhibition for feed for a higher O_2 concentration (5%). Figure 4-16 show that NO inhibition also occurs in presence of 2.5% H_2O . These data suggest that mechanistic steps involved in NO_x reduction with C_3H_6 are

similar with and without H₂O in the feed. The important take-away from these results is the fact that NO must be involved in the formation of an intermediate surface species, which blocks sites.

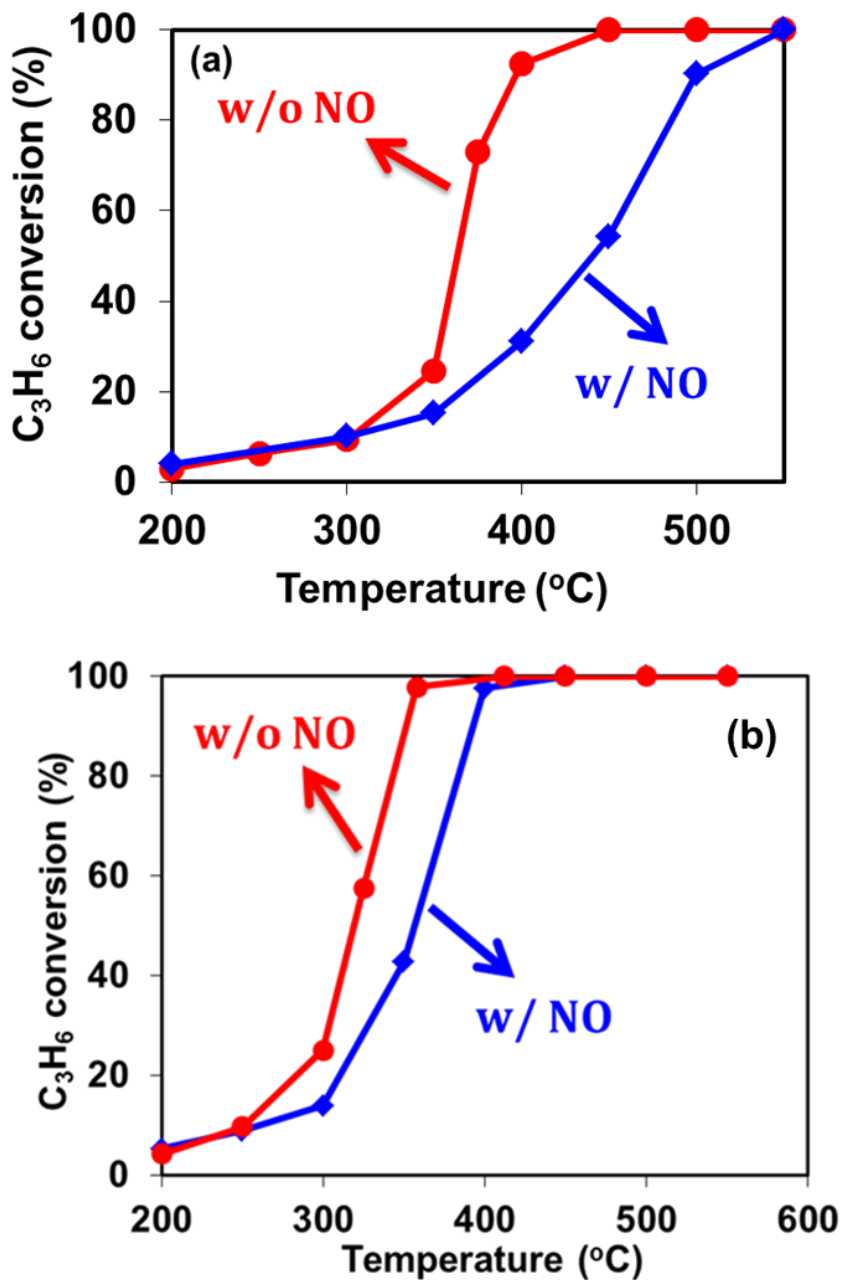


Figure 4-15 (a) C₃H₆ light off curves with and without NO in feed (C₃H₆ = 500 ppm, NO = 0 or 500 ppm, O₂ = 1%), (b) C₃H₆ light off curves with and without NO in feed (C₃H₆ = 500 ppm, NO = 0 or 500 ppm, O₂ = 5%) (Balance gas: Ar)

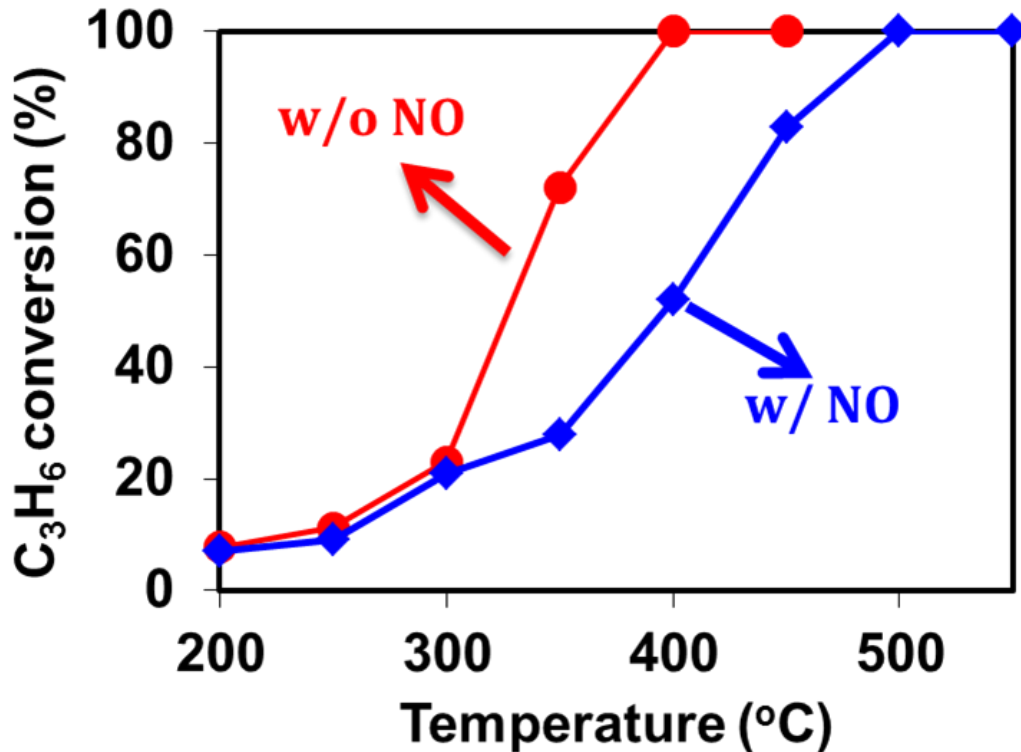


Figure 4-16. C₃H₆ light off curves with and without NO in feed in presence of H₂O (C₃H₆ = 500 ppm, NO = 0 or 500 ppm, O₂ = 5%, H₂O = 2.5%, Balance gas: Ar)

Steady-state experiments were conducted to examine the selective catalytic reduction of NO in excess O₂. In these experiments the catalyst was exposed to 500 ppm NO, 500 ppm C₃H₆ and 1% or 5% O₂ over the temperature range of 200°C to 550°C. Figure 4-17 shows that NO reduction occurs in range of 350°C to 550°C with maximum NO conversion obtained of 80% in the presence of 1% O₂. At higher O₂ concentration (5%), Figure 4-17 reveals the maximum NO conversion is only 60%, most likely due to a higher rate of C₃H₆ oxidation. Figure 4-18 shows C₃H₆ and NO conversion with and without water in the feed. It shows that there is enhancement in NO conversion in temperature range of 300°C to 450°C. It could be due to the formation of amines in

presence of H₂O which lead to higher NO conversion. Above 450°C due to higher rate of C₃H₆ oxidation in presence of H₂O there is decrease in NO conversion.

Additional transient experiments were carried out to gain further insight about the mechanistic steps involved during the lean NO reduction with C₃H₆. The first set of experiments was performed for a feed containing 500 ppm C₃H₆, 0 or 500 ppm NO, and 1% O₂. The catalyst was first exposed to 500 ppm C₃H₆ and 1% O₂. After reaching the steady state (ca. 45 minutes) 500 ppm NO was introduced for 10 minutes and then switched off. The experiment was performed at 300°C, 350°C and 380°C. Figure 4-19a shows that at 300°C there is no effect of NO on the measured outlet C₃H₆ concentration. Earlier it was shown in a NO exposure and TPD experiment that NO adsorbs only weakly with negligible NO adsorption on a catalytic surface pre-adsorbed with C₃H₆. At the somewhat higher temperature of 350°C, Figure 4-19b shows a slight increase in the C₃H₆ outlet concentration upon introduction of NO. A slight increase in the C₃H₆ concentration is observed at 350°C whereas at 380°C (Figure 4-20) which is the light-off temperature of C₃H₆ oxidation there is an instantaneous increase in the C₃H₆ outlet concentration upon the introduction of NO. Differential kinetics studies were performed to determine the order of C₃H₆ oxidation reaction with respect to NO at 380°C. The reaction order with respect to NO is -0.5 and is shown in Figure 4-21. Finally, Figure 4-20 also reveals that upon switching off the NO the C₃H₆ concentration did not return to its previous value immediately and rather attained new value which was higher than the previous concentration. This shows the poisoning of the active catalytic sites for oxidation by the formation of stable intermediates during the introduction of NO pulse.

These data point to a mechanism for lean NO_x reduction with propylene in which NO selectively reacts with partially oxidized hydrocarbon species to form N-containing hydrocarbons. Another set of transient experiment was carried out at higher O_2 concentrations as we know that on increasing O_2 concentration in the feed the C_3H_6 light-off temperature decreases. In these experiments, the catalyst sample was first exposed to 500 ppm C_3H_6 and 5% O_2 for 45 minutes and then 500 ppm NO pulse was introduced; after 10 minutes NO was switched off from feed. The experiments were carried out at 300°C, 325°C and 350°C. Figure 4-22a shows no effect of NO on the C_3H_6 concentration at 300°C. But at 325°C and 350°C there is increase in the C_3H_6 outlet concentration upon introduction of NO in feed, as shown in the Figs. 4-22a and 4-23. This further supports the proposed mechanism as NO inhibition on C_3H_6 oxidation reaction was observed even at lower temperatures by decreasing the light off temperature for C_3H_6 oxidation reaction. Finally, Figure 4-24 shows the NO inhibition on C_3H_6 oxidation in presence of water, which shows that even in presence of water C_3H_6 -derived, oxygenates react selectively with NO to form stable intermediates that block the active sites.

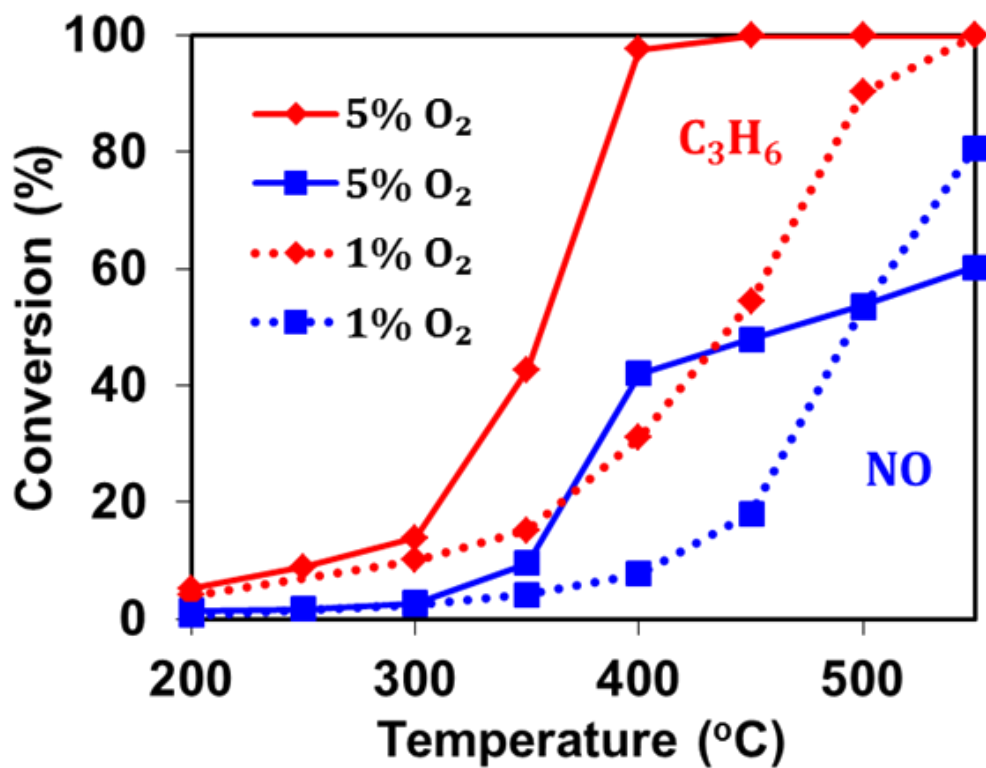
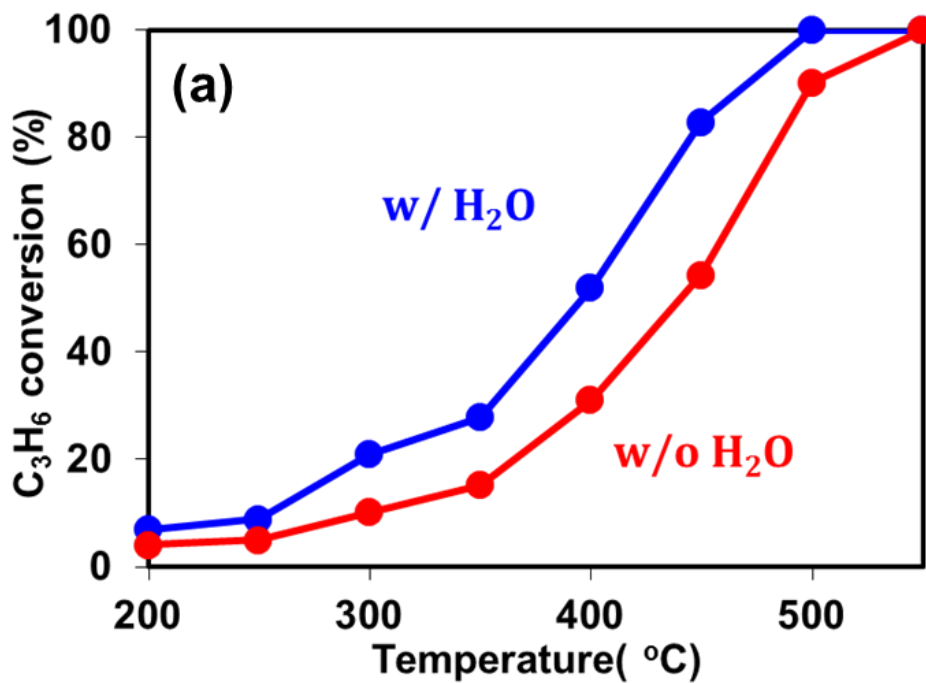


Figure 4-17. C₃H₆ and NO conversion at different temperatures (C₃H₆ = 500 ppm, NO = 500 ppm, O₂ = 1%, Balance gas: Ar), C₃H₆ and NO conversion at different temperatures (C₃H₆ = 500 ppm, NO = 500 ppm, O₂ = 5%, Balance gas: Ar)



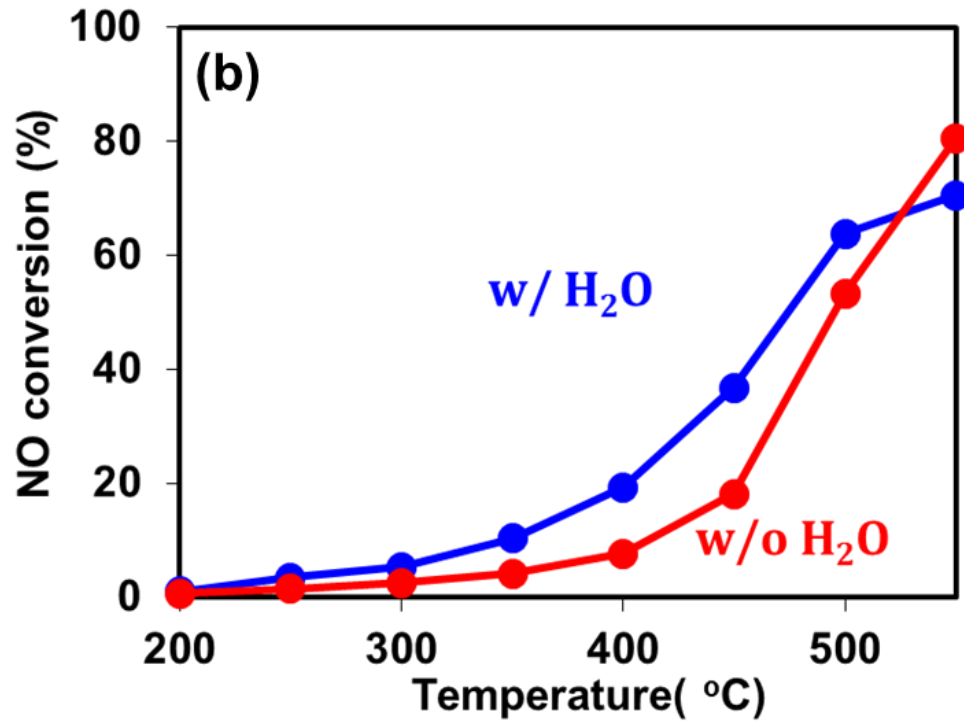
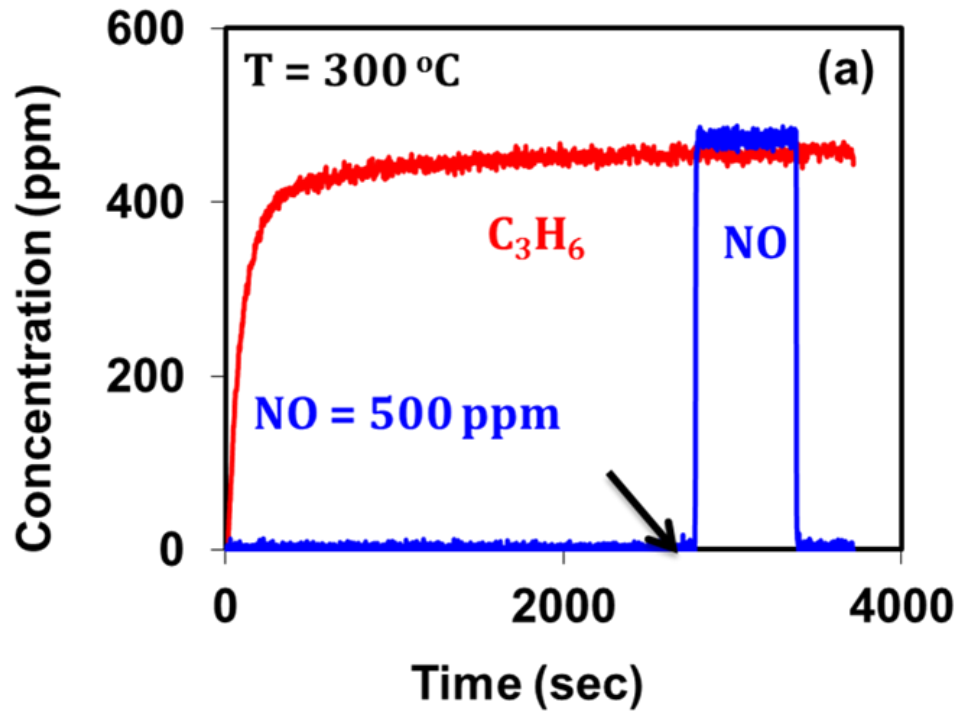


Figure 4-18. (a) C_3H_6 conversion at different temperatures (b) NO conversion at different temperatures ($C_3H_6 = 500$ ppm, $NO = 500$ ppm, $O_2 = 1\%$, $H_2O = 0$ or 2.5% , Balance gas: Ar)



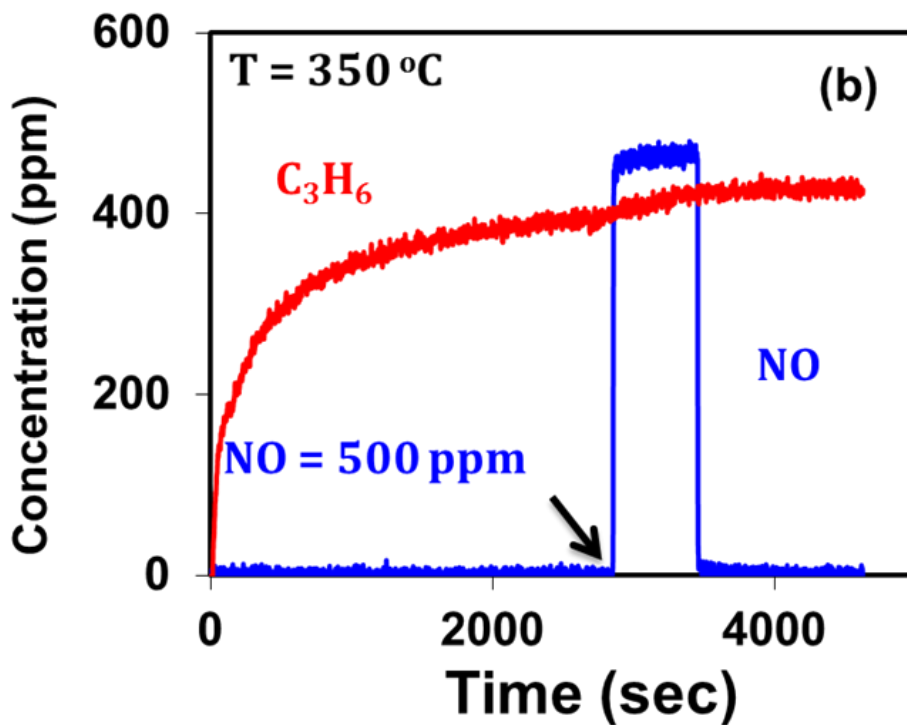


Figure 4-19. (a) C_3H_6 and NO outlet concentration with time at 300 °C, (b) 350°C, (C_3H_6 = 500 ppm, NO = 0 or 500 ppm, O_2 = 1%, Balance gas: Ar)

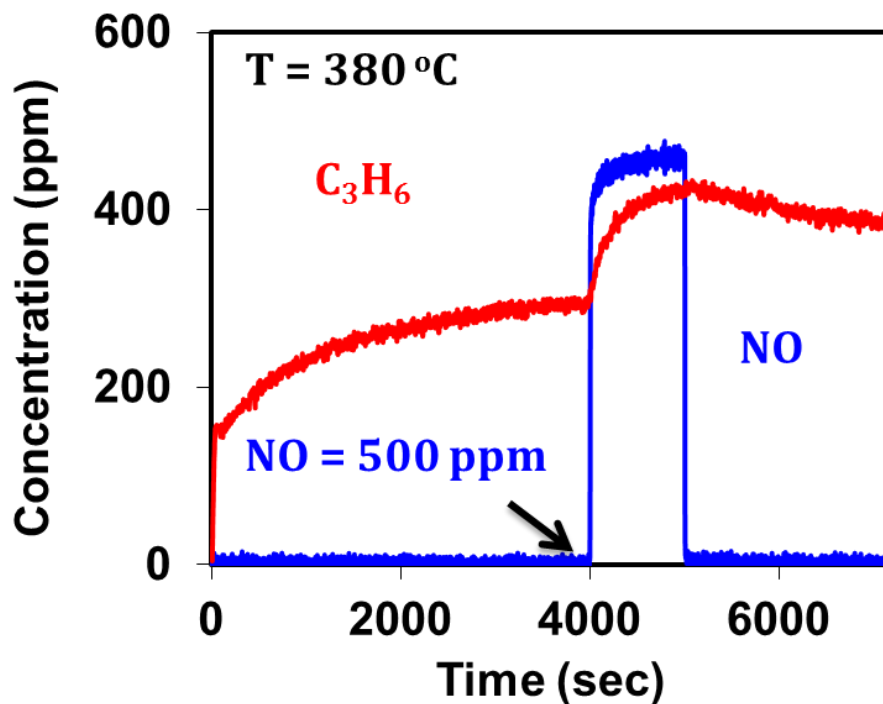


Figure 4-20. C_3H_6 and NO outlet concentration with time at 380°C (C_3H_6 = 500 ppm, NO = 0 or 500 ppm, O_2 = 1%, Balance gas: Ar)

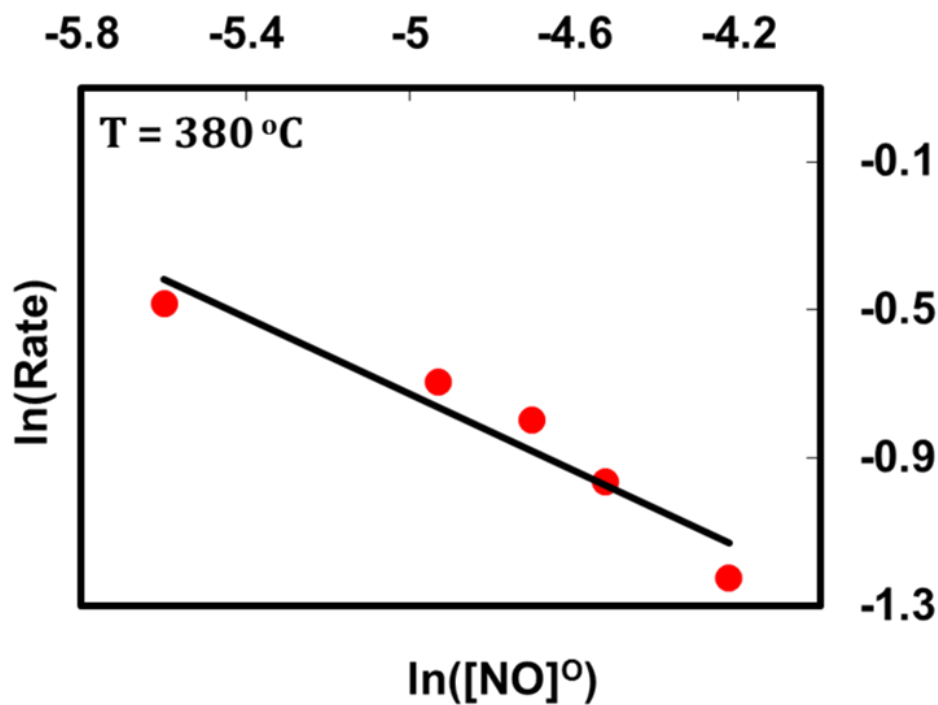
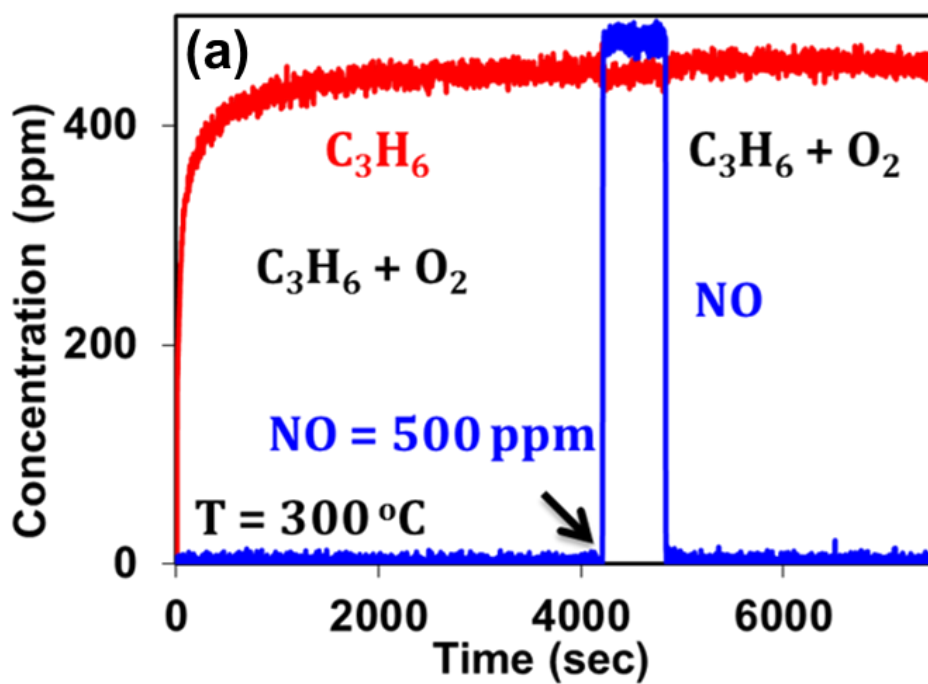


Figure 4-21. Dependence of C_3H_6 oxidation rate on NO. $C_3H_6 = 500$ ppm, NO = 200-800 ppm, $O_2 = 1\%$, Catalyst: Cu-chabazite. Balance gas: Ar. Total flow rate = 1000 sccm. (Rate is in $\text{moles}\cdot\text{m}^{-3}\cdot\text{s}^{-1}$, concentration is in $\text{moles}\cdot\text{m}^{-3}$)



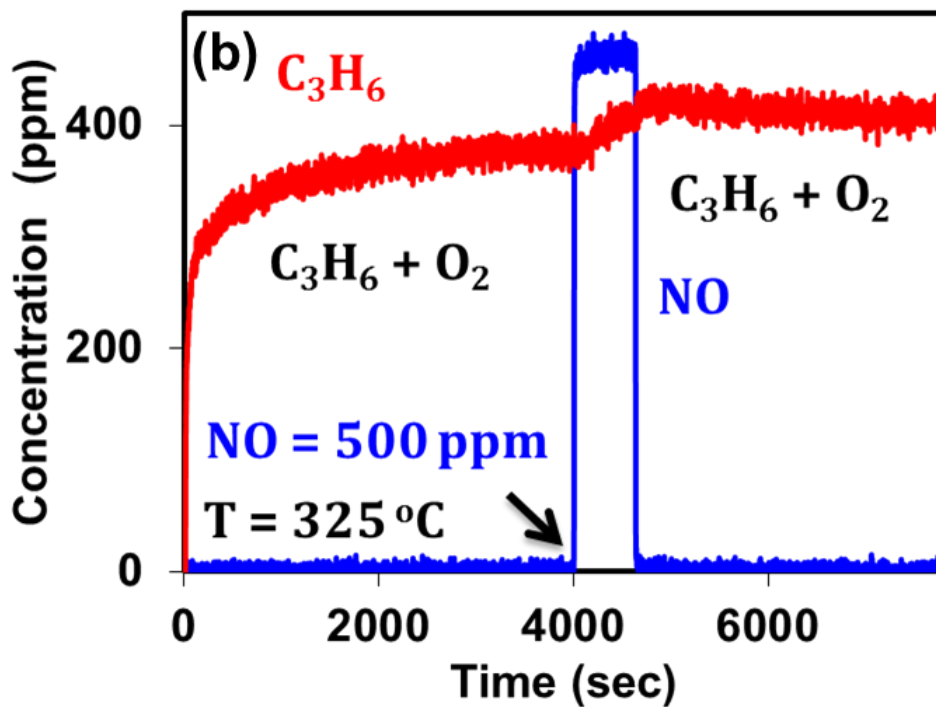


Figure 4-22. (a) C_3H_6 and NO outlet concentration with time at 300 °C, (b) 325°C, (C_3H_6 = 500 ppm, NO = 0 or 500 ppm, O_2 = 5%, Balance gas: Ar)

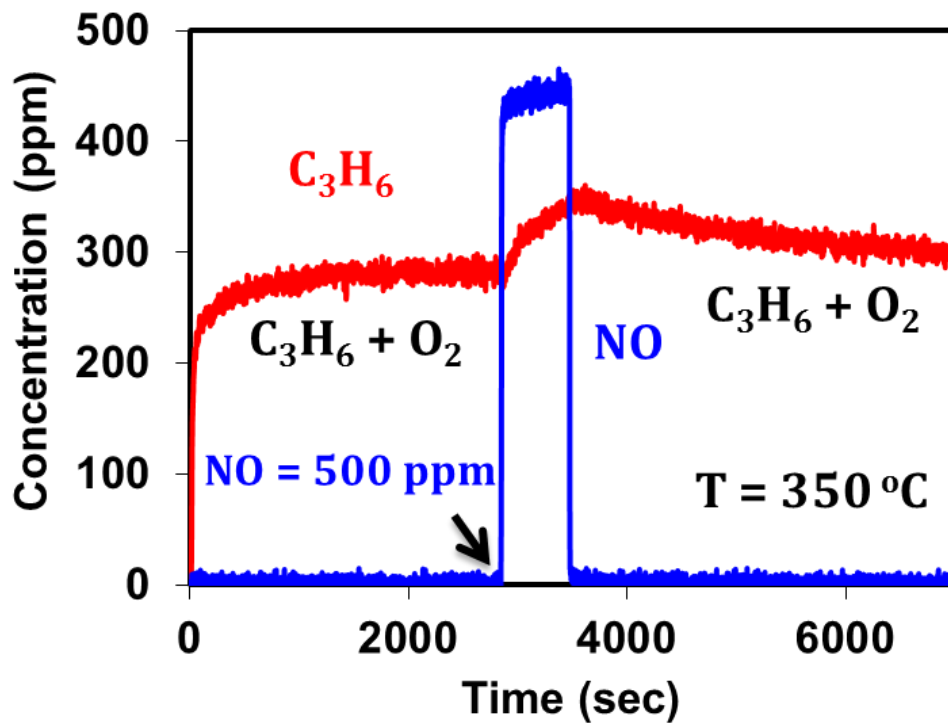


Figure 4-23. C_3H_6 and NO outlet concentration with time at 350°C (C_3H_6 = 500 ppm, NO = 0 or 500 ppm, O_2 = 5%, Balance gas: Ar)

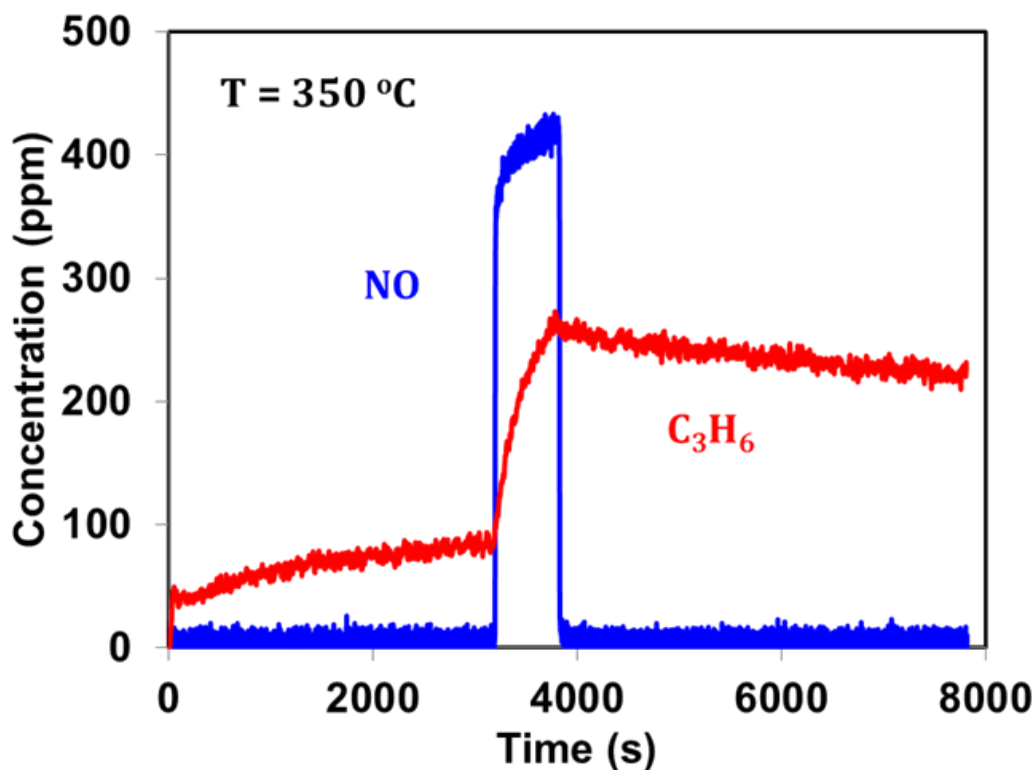


Figure 4-24. C_3H_6 and NO outlet concentration with time at 350 °C in presence of H_2O ($C_3H_6 = 500$ ppm, NO = 0 or 500 ppm, $O_2 = 1\%$, $H_2O = 2.5\%$, Balance gas: Ar)

4.4 Conclusions

We have carried out a comprehensive experimental study on NO_x reduction with C_3H_6 on Cu-SSZ13 using bench flow reactor. To our knowledge, this is the first study on the detailed understanding of underlying mechanism of NO_x reduction with C_3H_6 on small pore Cu zeolite. This experimental study focused on determining the key mechanistic step in NO_x reduction with C_3H_6 .

The steady state data showed the rate of decomposition of NO_2 to NO is higher in the presence of C_3H_6 and may be attributed to the reduction of active catalytic sites by C_3H_6 . Spatially-resolved concentration profiles using a series of monolith pieces of different lengths provide insight into the reaction pathways. The spatial profiles show that

NO_2 is completely reduced in the front part of monolith at temperatures above 350°C . On the other hand, NO that is formed from the NO_2 reduction increases along the length in temperature range of 200°C - 350°C and exhibits a maximum value above 350°C . The steady state and transient data clearly show that NO inhibits the C_3H_6 oxidation reaction. Transient experiments with $\text{C}_3\text{H}_6 + \text{O}_2 + \text{NO}$ reveal that NO inhibition is observed only around the light-off temperature of C_3H_6 oxidation. This suggests that inhibition is not due to the competition between the NO and C_3H_6 for the active sites but is due to NO selectively reacting with oxygenates which are the intermediates of C_3H_6 oxidation to form N-containing hydrocarbon species ($\text{C}_x\text{H}_y\text{O}_z\text{N}_t$) that poison the active sites.

In-situ DRIFTS studies were also performed to study the nature of the surface intermediates and their evolution with time. *In-situ* DRIFTS studies confirmed the formation of N-containing intermediates. Hence, through both bench flow reactor studies and *in-situ* DRIFTS studies it is concluded that the key mechanistic step in NO_x reduction with C_3H_6 is NO selectively reacting with oxygenates to form $\text{C}_x\text{H}_y\text{O}_z\text{N}_t$ compound that is further reduced to N_2 .

CHAPTER 5 *In-situ* DRIFTS Studies of Selective Catalytic Reduction of NO with C₃H₆ over Cu-SSZ13 Catalyst

5.1 Introduction

The intrinsic mechanism of the selective catalytic reduction (SCR) reaction over a Cu-SSZ13 catalyst was studied by *in-situ* diffuse reflectance infrared Fourier transform spectroscopy (DRIFTS). Based on the mechanisms of HC-SCR proposed by different investigators over various catalysts, the “reduction mechanism” is the widely accepted [128-130]. In this mechanism, the key step is the formation of the organic nitro compounds which are produced by the reaction between nitrates and oxygenates as a result of oxidation of NO and C₃H₆ in the presence of O₂. These organic nitro compounds are then further converted into N₂, CO₂, and H₂O upon interaction with NO and O₂. Among the various mechanisms proposed, –NCO species are widely accepted as an important organic nitro intermediate to yield N₂ by the hydrolysis reaction or reaction with NO and/or O₂ in the HC-SCR reaction [131, 132].

The objective of this study is to investigate the evolution of key surface intermediates formed during the selective catalytic reduction of NO with C₃H₆ over Cu-SSZ13 catalyst. We identify the key surface intermediates formed during lean NO reduction with C₃H₆ are oxygenates formed by C₃H₆ partial oxidation and –NCO species formed when NO reacts with surface oxygenates, which are then reduced to N₂ by reaction with O₂. Finally, we proposed phenomenological reaction mechanism based on our bench-flow reactor studies [133] and *in-situ* DRIFTS studies.

5.2 Experimental

In-situ DRIFTS was performed using a Nicolet Nexus 470 spectrometer, equipped with a small collector with a dual sample environmental chamber (Thermo Fisher Scientific). The powder sample of catalyst was prepared by scraping the washcoat off the monolith channels. The feed gas, at a total flow rate of 50 cm³/min at STP, was mixed using Bronkhorst mass flow controllers; and its composition, with all gases present, was 500 ppm C₃H₆, 500 ppm NO, 1% or 5% O₂, balanced by He. Before each experiment, the catalyst sample of 60 mg was treated with 5% O₂ in He for 1 hour at 600°C.

5.3 Results and Discussion

The inhibition mechanism described in chapter 4 is only speculative without direct measurement of surface species during reaction for similar conditions to the reactor experiments. To this end, *in-situ* DRIFTS experiments were carried. The Cu/chabazite catalyst powder was exposed to 500 ppm C₃H₆ and 1% O₂ for 45 minutes and after that 500 ppm NO was introduced for 20 minutes. The experiment was performed at 300°C and 380°C. The spectra obtained at 300°C at 45 minutes exposure to C₃H₆ and O₂ shows peaks corresponding to adsorbed hydrocarbon species. Hence at 300°C the Catalytic surface is covered only with hydrocarbon species. The DRIFTS results obtained at the lower temperature (300 °C) did not provide any evidence of formation of N- containing surface species during NO exposure. Spectra were compared for the C₃H₆ + O₂ system and the C₃H₆ + O₂ + NO system. The formation of new bands during the NO was not apparent. Results from these experiments are shown in the Figure5-1. This result is in accordance with the transient bench flow reactor studies with feed containing 500 ppm

C_3H_6 , 0 or 500 ppm NO and 1% O_2 that at 300°C there is no change in the outlet C_3H_6 concentration on introduction of NO in the feed.

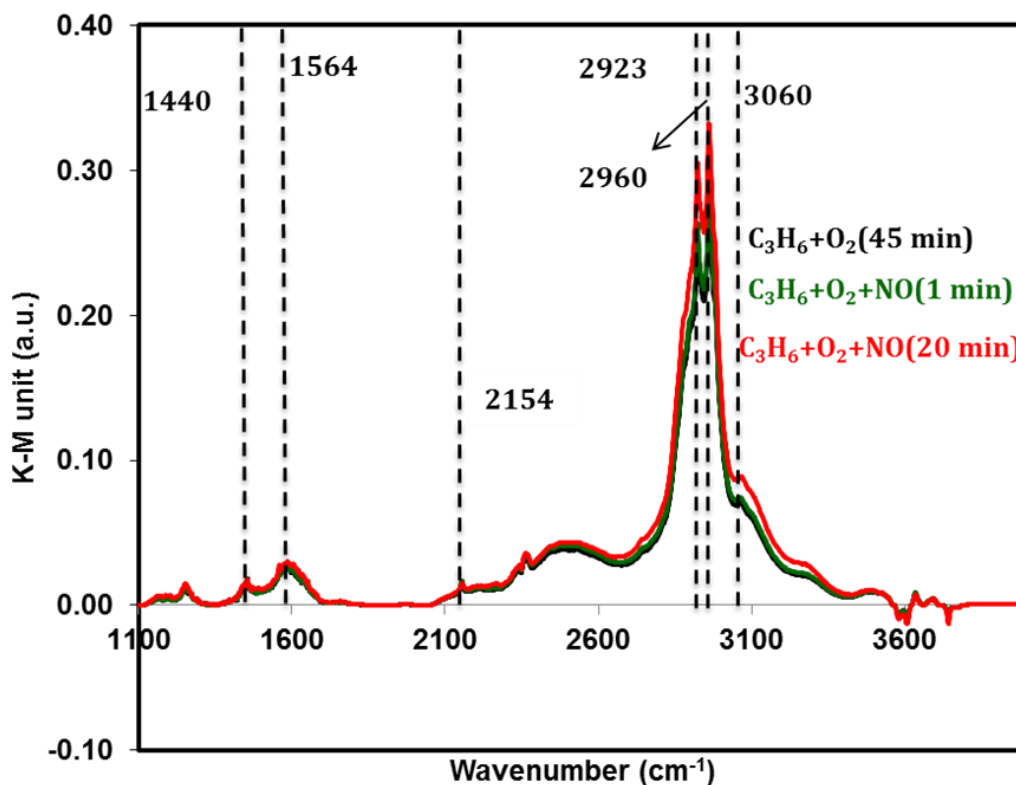


Figure 5-1. DRIFTS spectra obtained at different times upon Cu-SSZ13 exposure to 500 ppm NO after 45 minutes of exposure to 500 ppm C_3H_6 at 300 °C (500 ppm C_3H_6 , 1% O_2 , balanced by He)

Figure 5-2 shows DRIFTS spectra obtained at different times (1, 5, 10, 20, 30 and 45 min) when the catalyst sample was exposed to C_3H_6 under oxidizing conditions at 380°C. The growth of the bands near 1550 cm^{-1} and 2900 cm^{-1} correspond to C-C and C-H stretching respectively, of adsorbed hydrocarbon species. Krishna and Makkee [127] made this assignment in their study of C_3H_6 exposure on HZSM-5 on which oligomerization occurred followed by coke deposition. The broad band around 3060 cm^{-1} corresponding to the - C-H stretching of condensed aromatic rings also increased with

time [127, 134]. Hence, this surface study further confirms the formation of coke-like species on the catalytic surface. The small peaks at 2332 cm^{-1} and 2364 cm^{-1} correspond to gas phase CO_2 . The peak at 2152 cm^{-1} corresponds to CO adsorbed on Cu sites [86, 135]. The appearance of a band around 1660 cm^{-1} can be attributed to a C=O bond vibration of acrolein ($\text{CH}_2=\text{CH}-\text{CHO}$) [86, 134, 136]. The peak around 1440 cm^{-1} and 1540 cm^{-1} correspond to surface carboxylate species [134]. The peak corresponding to 1352 cm^{-1} corresponds to surface formates. Hence, at 380°C along with adsorbed hydrocarbon species oxygenates are also present on the catalytic surface. Therefore, it can be concluded that partially oxidized hydrocarbon species are the intermediates in C_3H_6 oxidation reaction.

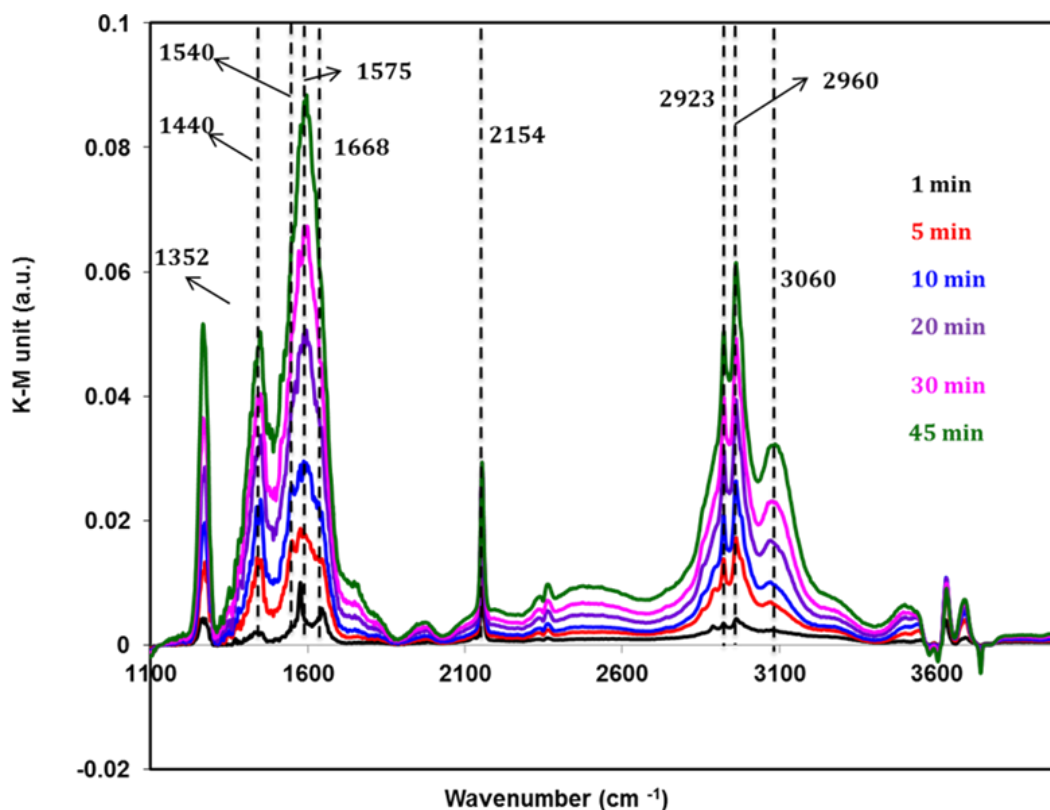


Figure 5-2 DRIFTS spectra obtained at different times upon Cu-SSZ13 exposure to 500 ppm C_3H_6 at 380°C (500 ppm C_3H_6 , 1% O_2 , balanced by He)

Figure 5-3 shows the spectra obtained for different times on introduction of NO in feed after exposure to $C_3H_6 + O_2$. On exposure to NO a new peak at 2250 cm^{-1} is observed which is attributed to $-NCO$ species [78, 86, 135]. Figure 5-3 also shows increase in the intensity of peak corresponding to $-NCO$ species with the time of exposure to NO, which suggests accumulation of $-NCO$ species on the catalyst surface. This clearly indicates that on introduction of NO in feed hydrocarbon species react with NO to form N-containing intermediates. There is decrease in band intensity corresponding to 2152 cm^{-1} (CO adsorbed on Cu sites) with the time of exposure to NO and this also suggests the poisoning of Cu sites by the N-containing intermediates formed during NO exposure. Table 5-1 shows the bands corresponding to surface intermediates formed during the selective catalytic reduction of NO with C_3H_6 .

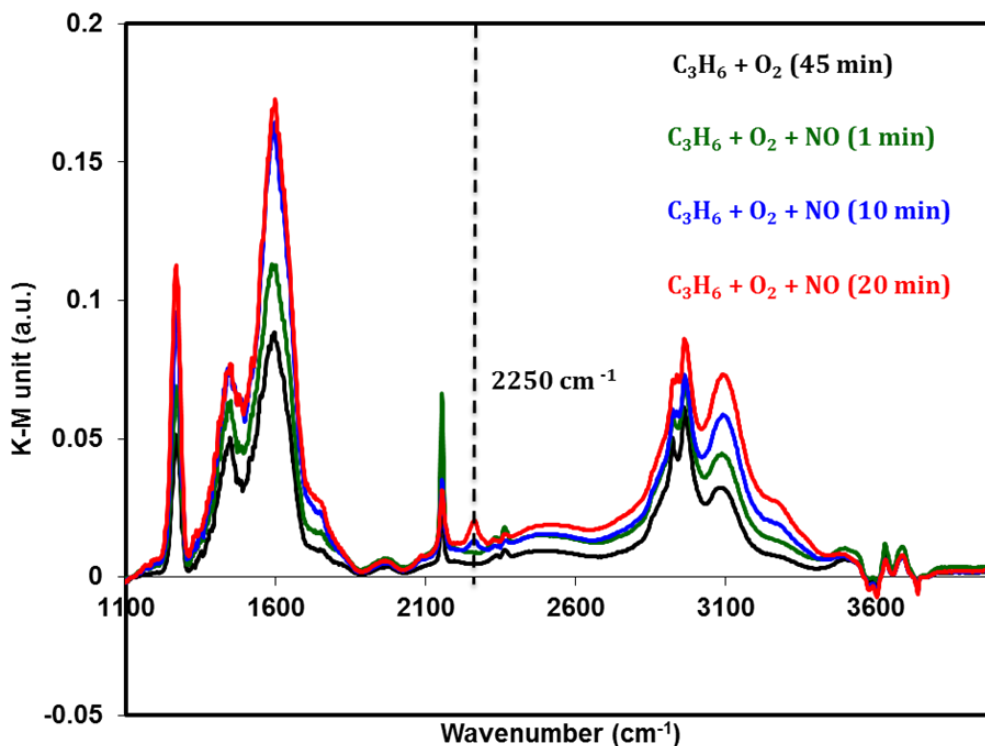


Figure 5-3. Emergence of new peak upon exposure to 500 ppm NO after 45 minutes of exposure to 500 ppm C_3H_6 at $380\text{ }^\circ\text{C}$ (500 ppm C_3H_6 , 500 ppm NO, 1% O_2 , balanced by He)

To further confirm the role of oxygenates as key intermediate in lean NO reduction with C_3H_6 the Cu/chabazite catalyst powder was exposed to 500 ppm C_3H_6 and 5% O_2 for 45 minutes and after that 500 ppm NO was introduced for 20 minutes at 325°C. Based on our bench flow reactor studies [133] the light-off temperature for C_3H_6 oxidation decreases on increasing the O_2 concentration. Hence, oxygenates formed at lower temperature could react with NO selectively to form $-NCO$ species. Figure 5-4 shows the spectra obtained for different times on introduction of NO in feed after exposure to $C_3H_6 + O_2$. On exposure to NO a new peak corresponding to $-NCO$ species is observed.

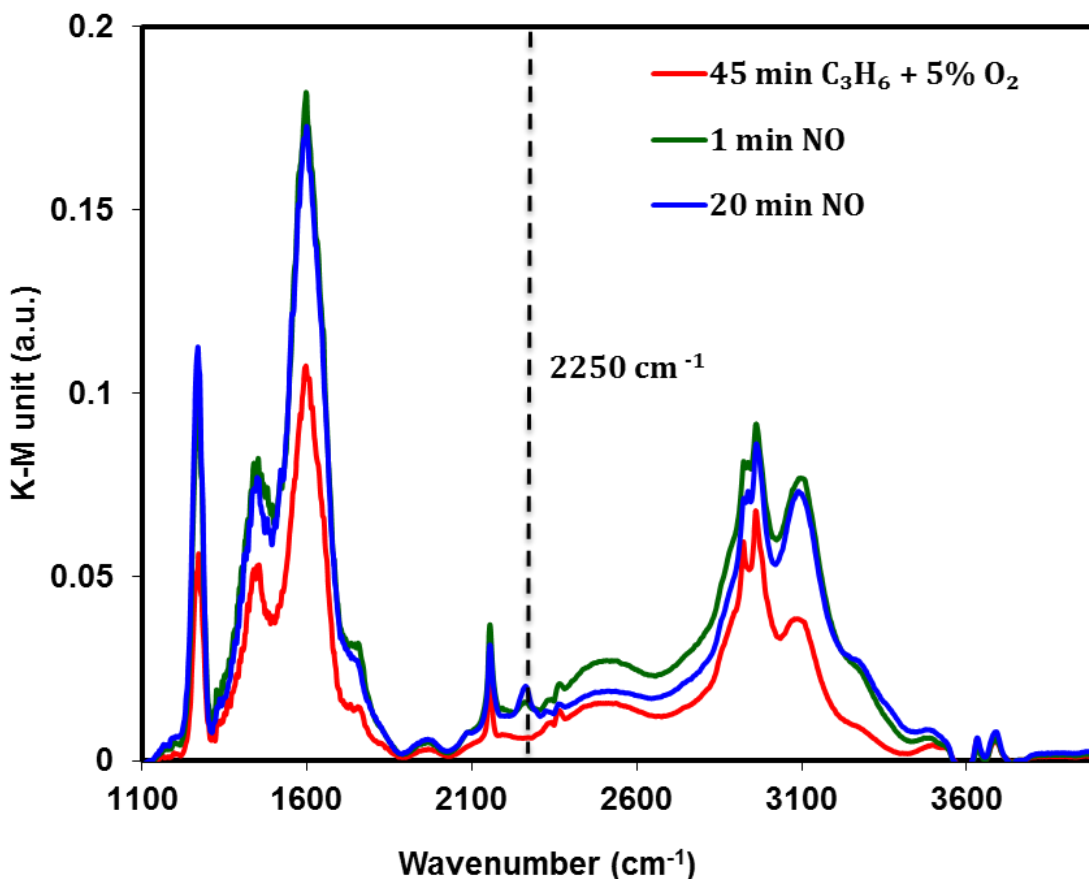


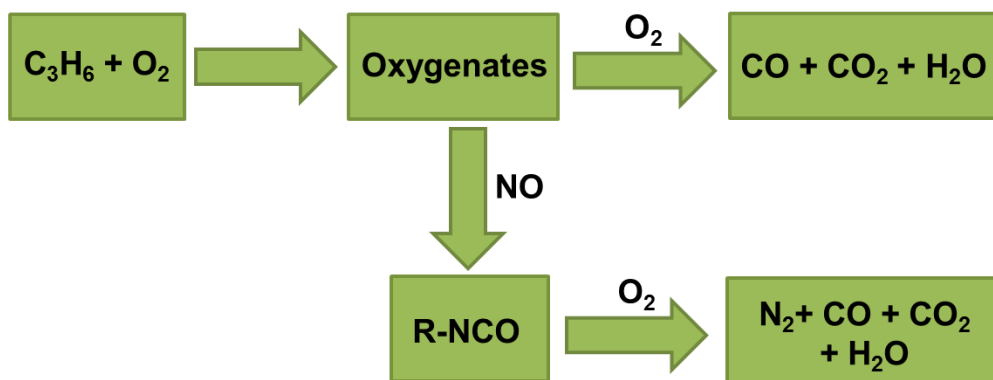
Figure 5-4. Emergence of new peak upon exposure to 500 ppm NO after 45 minutes of exposure to 500 ppm C_3H_6 at 325 °C (500 ppm C_3H_6 , 500 ppm NO, 5% O_2 , balanced by He)

Table 5-1. Wavenumber corresponding to adsorbed species

Band (cm ⁻¹)	Assignment	Reference
1550	C-C of adsorbed hydrocarbon	127
2900	C-H of adsorbed hydrocarbon	127
3060	C-H of condensed aromatic rings	127, 134
2152	CO adsorbed on Cu sites	86, 135
2332, 2364	gas phase CO ₂	86, 134
2250	adsorbed NCO species	78, 86, 135
1660	C=O, acrolein like species	86, 134, 136
1352	formates	134
1440, 1540	surface carboxylate species	134

Based on the bench flow reactor and in-situ DRIFTS studies a phenomenological reaction mechanism is proposed for lean NO reduction with C₃H₆ on Cu-SSZ13 catalyst.

Figure 5-5 shows the schematic of the proposed mechanism.



Mechanistic steps involved in NO + C₃H₆ + O₂ reaction system

Figure 5-5. Reaction steps involved in selective catalytic reduction of NO with C₃H₆

5.4 Conclusions

In-situ DRIFTS studies were also performed to study the nature of the surface intermediates and their evolution with time. It is shown that below the C₃H₆ oxidation light-off temperature, no peak corresponding to nitrogen containing compound is observed upon exposure to NO+C₃H₆+O₂ to the catalyst while above the light-off temperature, peak corresponding to -NCO species is observed. *In-situ* DRIFTS studies confirmed the formation of N-containing intermediates. Hence, through both bench flow reactor studies and *in-situ* DRIFTS studies it is concluded that the SCR mechanism involves reaction between oxygenates (partially oxidized hydrocarbon species) and NO to form isocyanates species (-NCO), which are further reduced to N₂.

CHAPTER 6 Kinetic Modeling of NO Selective Reduction with C₃H₆ over Cu-SSZ13 Monolithic Catalyst

6.1 Introduction

Lean-burn engines are more fuel efficient than the traditional stoichiometric engines. A major challenge of lean-burn engines is removal of NO_x from the exhaust which contains excess oxygen. Due to the harmful effects of NO_x, EPA rules have become stringent regarding the NO_x emissions from lean burn engines.

NO_x storage and reduction (NSR) and selective catalytic reduction (SCR) are the two commercialized after-treatment technologies for the reduction of NO_x emissions from lean-burn engines. Both NSR and SCR have drawbacks. Particularly, NSR catalysts are expensive and prone to catalyst deactivation (PM sintering and sulfur poisoning) while there is a need of additional infrastructure for the supply of NH₃ to the SCR system. Due to these issues, interest has shifted to using the integrated NSR/SCR technologies in order to lower the infrastructure cost associated with the SCR and the material cost associated with the precious metal-based NSR catalysts. The main advantages afforded by NSR/SCR are (i) *in-situ* generation of NH₃ in the upstream NSR process (or lean NO_x trap, LNT) and (ii) reduction of a potentially significant fraction of the NO_x by the much less expensive SCR catalyst. The NSR/SCR operating concept involves the storage of NO_x during the lean phase while unreacted hydrocarbons (C₃H₆, C₂H₄ etc.) and generated NH₃ exit the LNT during the rich phase. The ammonia produced during the regeneration adsorbs on the downstream SCR catalyst where it reacts with NO_x not converted in the LNT. In addition, olefinic hydrocarbons and/or partially

oxidized species that break through the LNT may also adsorb on the SCR catalyst leading to additional NO_x reduction by those species [68, 69, 86].

Only a few studies had been carried out on the kinetic modeling of selective catalytic reduction of NO with hydrocarbons. Ansell et al., [88] developed a kinetic model for C₃H₆ + NO + O₂ on Pt/Al₂O₃ monolithic catalyst using a 1-dimensional monolith model comprising global Langmuir-Hinshelwood rate expressions. Wilber et al., [89] developed a global kinetic model for C₂H₄ + NO + O₂ on Cu-ZSM5 monolithic catalyst. Captain et al., [90] studied selective catalytic reduction of NO by propylene over supported Pt catalysts. Based on the data, a mechanistic based kinetic model was developed that included the sequential hydrocarbon partial oxidation and subsequent formation of surface cyanide and isocyanate intermediates.

Cu-chabazite (SSZ-13) has emerged as an important synthetic zeolite for lean NO_x reduction on diesel vehicles due to its superior hydrothermal durability and hydrocarbon resistance [87]. To our knowledge there have been no published studies of kinetic modeling of NO reduction with C₃H₆ on Cu-SSZ13 monolithic catalyst. In this study, we focus on the development of a predictive kinetic model for lean NO selective catalytic reduction with C₃H₆. This follows from a recent bench scale flow reactor study of this reaction system [133]. In that study a mechanism for Cu-SSZ13 catalyzed NO selective reduction using C₃H₆ was proposed, supported by *in-situ* DRIFTS measurements with which surface intermediates were identified. Here we incorporate the kinetic model into a (1+1) D monolith reactor model. Kinetic parameters are estimated using steady state data obtained from bench scale flow reactor studies on NO selective reduction with C₃H₆. The model is validated with separate set of experimental data. We

show that the model captures the key features observed experimentally and predictions for conversion and selectivity fit well with experimental data.

6.2 Model Development

6.2.1. Reactor model

A (1+1)-dimensional (1D in fluid phase + 1D in washcoat phase) model of a catalytic monolith channel with washcoat diffusion is used in this study. In this model we solve for gaseous species balances in both fluid phase and washcoat, and species balances on the catalytic surface within the washcoat. The key assumptions in the model are: (i) laminar flow in the monolith channel, (channel Reynolds number $(4\langle u \rangle R_{\Omega 1} / \nu) \sim 64$), (ii) axial diffusion in the fluid phase is neglected as compared to convection (high axial Peclet number, $(\langle u \rangle L / D_m) = 340$), (iii) isothermal condition due to low reactant concentration, and (iv) physical properties are constant with respect to composition. The model equations are described below.

The one-dimensional fluid phase species balance consists of accumulation, convection and external mass transfer terms. The transverse diffusion in the fluid phase is incorporated in the model by the use of external mass transfer coefficient as

$$\frac{\partial x_{f m, j}}{\partial t} = -\langle u \rangle \frac{\partial x_{f m, j}}{\partial z} - \frac{k_{m e, j}}{R_{\Omega 1}} (x_{f m, j} - x_{s, j}). \quad (6-1)$$

Here, $x_{f m, j}$ and $x_{s, j}$ are the mole fraction of species j in the fluid phase and at the fluid-washcoat interface, respectively; $\langle u \rangle$, $R_{\Omega 1}$ and $k_{m e, j}$ represent the average fluid velocity, hydraulic radius (the ratio of open channel area to channel perimeter) and external mass transfer coefficient, respectively. The species balance in the washcoat consists of accumulation, diffusion and reaction terms,

$$\varepsilon_{wc} \frac{\partial x_{wc,j}}{\partial t} = D_{e,j} \frac{\partial}{\partial y} \left(\frac{\partial x_{wc,j}}{\partial y} \right) + \frac{1}{C_{tm}} \sum_{r=1}^{rxn} \vartheta_{jr} R_r \left(\underline{x}_{wc}, \underline{\theta}, T \right). \quad (6-2)$$

The terms ε_{wc} , $x_{wc,j}$, $D_{e,j}$ and C_{tm} represent washcoat porosity, mole fraction of species j in the gaseous phase within the washcoat, effective diffusivity of species j in the washcoat phase and total gaseous concentration in the interstitial space of the washcoat, respectively. Similarly, ϑ_{jr} and R_r represents stoichiometric coefficient of species j in reaction r and rate of reaction r (mole/m³_{wc}/s). The effective diffusivity in the washcoat is estimated by assuming a diffusivity ratio, λ ($= \frac{D_f}{D_e}$), of 80 based on λ -value of 80-100 reported by Metkar et al., [137] for a zeolite-based SCR washcoat. Similarly, the site balance equation can be written as

$$C_{S1} \frac{\partial \theta_{k-S1}}{\partial t} = \sum_{r=1}^{rxn} \vartheta_{kr} R_r \left(\underline{x}_{wc}, \underline{\theta}_{S1}, \underline{\theta}_{S2}, T \right) \text{ and} \quad (6-3)$$

$$C_{S2} \frac{\partial \theta_{k-S2}}{\partial t} = \sum_{r=1}^{rxn} \vartheta_{kr} R_r \left(\underline{x}_{wc}, \underline{\theta}_{S1}, \underline{\theta}_{S2}, T \right). \quad (6-4)$$

Here, θ_{k-S1} represents fractional coverage of surface species k on S1 sites and θ_{k-S2} represents fractional coverage of surface species k on S2 sites, C_{S1} and C_{S2} represent concentration of Cu-sites and Bronsted acid sites (mol/m³_{wc}).

The above equations are solved along with following initial and boundary conditions:

$$t = 0; \quad x_{fm,j} = x_{fm,j}^0, \quad x_{wc,j} = x_{wc,j}^0,$$

$$\theta_{k-S1} = \theta_{k-S1}^0, \quad \theta_{k-S2} = \theta_{k-S2}^0 \quad (6-5)$$

$$z = 0; \quad x_{fm,j}(t) = x_{fm,j}^{in}(t) \text{ and} \quad (6-6)$$

$$y = 0; \quad k_{me,j}(x_{fm,j} - x_{s,j}) = -D_{e,j} \frac{\partial x_{wc,j}}{\partial y};$$

$$x_{wc,j} = x_{s,j} \quad (6-7)$$

$$y = R_{\Omega 2}; \frac{\partial x_{wc,j}}{\partial y} = 0. \quad (6-8)$$

Here, $R_{\Omega 2}$ and $x_{s,j}$ correspond to characteristic length scale in washcoat (or effective washcoat thickness) and concentration of species j at the interface of washcoat and fluid phase, respectively. The values of parameters used in the simulation are provided in Tables 6-1 and 6-2.

Table 6-1. Constant parameters used in the simulation

Parameter	Value
a	1.1mm
$R_{\Omega 2}$	50 μm
L	2 cm
Sh_e	3.608
ϵ_{wc}	0.4
λ	80
C_{S1}	524 mol/m ³ _{wc}
C_{S2}	450 mol/m ³ _{wc}

Table 6-2. Temperature dependent parameters used in the simulation

Parameter	Value / Expression
$\langle u \rangle$	$0.49 \times (T/273.15) \text{ m/s}$
C_{tm}	$\frac{1000}{0.082 \times T} \text{ mol/m}^3$
$D_{fm,NO}$	$1.13 \times 10^{-9} \times T^{1.7148} \text{ m}^2/\text{s}$
D_{fm,CO_2}	$0.825 \times 10^{-9} \times T^{1.7148} \text{ m}^2/\text{s}$
D_{fm,O_2}	$1.13 \times 10^{-9} \times T^{1.7019} \text{ m}^2/\text{s}$
D_{fm,C_3H_6}	$4.237 \times 10^{-10} \times T^{1.7844} \text{ m}^2/\text{s}$
D_{fm,N_2}	$1.21 \times 10^{-9} \times T^{1.7019} \text{ m}^2/\text{s}$
D_{fm,H_2O}	$1.62 \times 10^{-9} \times T^{1.7033} \text{ m}^2/\text{s}$
$D_{fm,CO}$	$1.13 \times 10^{-9} \times T^{1.7148} \text{ m}^2/\text{s}$

6.2.2 Reaction mechanism and parameter estimation

The kinetic model for lean NO reduction with C₃H₆ described in more detail below is based on the phenomenological mechanism proposed in our previous study [133]. The mechanism involves inhibiting intermediates formed through the reaction of NO with oxygenates; these intermediates react further to form N₂. The catalyst properties used in the model are summarized in Table 6-3. We consider that the Cu/CHA has two types of sites, Cu-sites and Bronsted acid sites. The loadings of the Cu (524 mol/m³) and Bronsted sites (450 mol/m³) are estimated based on Cu loading (2.5 wt. %) and Cu/Al (0.35) atomic ratio. Recent studies have investigated the Cu oxidation state and coordination environment in Cu-SSZ13 under operando conditions representative of NO_x

selective catalytic reduction (SCR) with NH_3 [138, 139]. It was shown through a combination of X-ray absorption spectroscopy (XAS), density functional theory (DFT), and first-principles based thermodynamic reasoning that mixed Cu(I) and Cu(II) oxidation states exist under reaction conditions [138]. To this end, the current model accounts for Cu(II) reduction to Cu(I) and re-oxidation of Cu(I) to Cu(II) by O_2 . The model also accounts for the formation of surface oxygenates during C_3H_6 oxidation ($\text{C}_3\text{H}_6 + \text{O}_2$) and the reduction of NO by C_3H_6 via intermediate surface $-\text{NCO}$ species. The formation of surface oxygenates such as acrolein-like species, acetate and formate has been shown by *in-situ* DRIFTS studies during propylene oxidation [87, 133, 134, 140-141]. The key mechanistic step in the NO reduction with C_3H_6 is the reaction of NO with oxygenates to form a surface complex ($\text{C}_{x-1}\text{H}_y-\text{NCO}$) that can be further reduced to N_2 . Oxygenates formed can react further with O_2 to form CO and CO_2 or selectively react with NO to form the $-\text{NCO}$ species. In this way, C_3H_6 oxidation to CO/ CO_2 is the undesirable pathway occurring along with NO selective reduction with C_3H_6 . In the model the assumed oxygenate is $\text{C}_3\text{H}_4\text{O}$. Along with the NO selective reduction with C_3H_6 and C_3H_6 oxidation, CO oxidation occurs since CO is formed as a product through both C_3H_6 oxidation and NO selective reduction with C_3H_6 .

Table 6-3. Catalyst properties

Catalyst	Components	Composition (% wt. of washcoat)
SCR	Cu-SSZ13	2.5%

The model kinetic parameters are estimated from steady state bench-flow reactor studies carried out in our previous study [133]. In order to estimate the kinetic parameters

for the complete $C_3H_6 + NO + O_2$ reaction system, we follow a step-wise approach. Kinetic parameters estimated from independent reaction systems (CO and C_3H_6 oxidations) are incorporated into the model for the $C_3H_6 + NO + O_2$ system. Specifically, first a kinetic model for CO oxidation ($CO + O_2$) is developed by fitting the model with steady state bench flow reactor CO effluent concentration data. Then we expand the model to include steady state C_3H_6 oxidation reaction ($C_3H_6 + O_2$) by fitting C_3H_6 and CO effluent concentration data obtained from a second set of experiments. Finally we expand the model further to include NO reduction with C_3H_6 ($NO + C_3H_6 + O_2$) by fitting the steady state C_3H_6 and NO effluent concentration data, enabling the remaining parameters to be estimated. In most cases, the Levenberg-Marquardt method was used to converge on the parameter estimates.

6.2.3 Kinetic model for CO oxidation ($CO + O_2$)

The kinetic model for CO oxidation is described by reactions R1 through R4 in Table 6-4. R1 is reversible CO adsorption on a Cu(II) site. It has been shown through *in-situ* DRIFTS studies that upon exposure to CO, Cu(II) is reduced to Cu(I).

Table 6-4 Kinetic steps involved in CO oxidation

	Reaction	Rate expression
R1	$CO + Cu(II) \leftrightarrow CO(Cu(I))$	$k_{1,f} \cdot X_{wc,CO} \cdot \theta_{Cu(II)} \cdot C_{S1} - k_{1,b} \cdot \theta_{CO} \cdot C_{S1}$
R2	$O_2 + Cu(II) \leftrightarrow O_2(Cu(II))$	$k_{2,f} \cdot X_{wc,O_2} \cdot \theta_{Cu(II)} \cdot C_{S1} - k_{2,b} \cdot \theta_{O_2} \cdot C_{S1}$
R3	$2CO(Cu(I)) + O_2(Cu(II)) \rightarrow 2CO_2 + 2Cu(I) + Cu(II)$	$k_{3,f} \cdot \theta_{CO} \cdot \theta_{O_2} \cdot C_{S1}^2$
R4	$Cu(I) + O_2 \rightarrow O_2(Cu(II))$	$k_{4,f} \cdot \theta_{Cu(I)} \cdot X_{wc,O_2} \cdot C_{S1}$

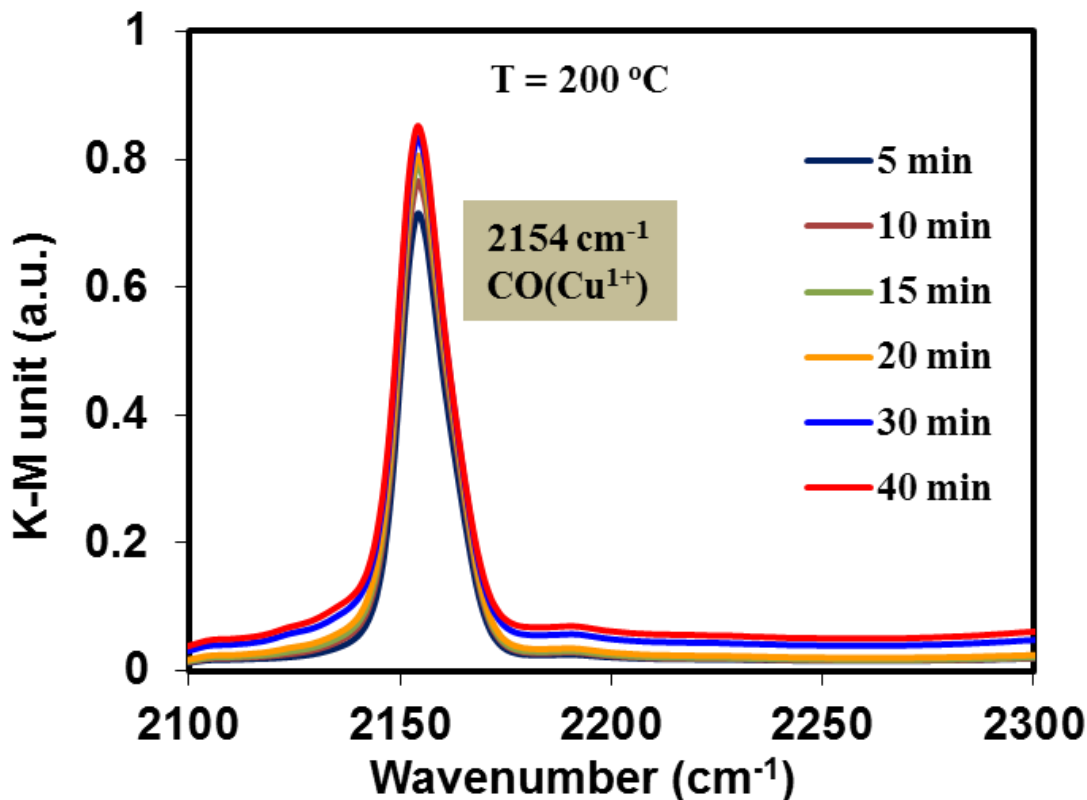


Figure 6-1. DRIFTS spectra for CO adsorption on Cu-SSZ13 pretreated with O₂ at 200°C (CO=500 ppm, Balance gas: He)

Figure 6-1 shows the DRIFTS spectra obtained when CO was exposed to an initially oxidized catalyst at 200°C. The peak at 2154 cm⁻¹ corresponds to the peak for CO(Cu(I)) suggesting that CO reduces the Cu(II) to the Cu(I) [135, 142]. Regarding oxygen adsorption (R2), it has been shown using DFT that dissociative adsorption of O₂ on Cu-SSZ13 is thermodynamically unfavorable because of a positive heat of adsorption whereas the molecular adsorption of O₂ on Cu is favorable. The DFT calculations show that O₂ adsorption on Cu has approximate 4-fold planar coordination with two O coming from the lattice and two from the adsorbate [138, 139]. Thus, we consider molecular adsorption of O₂ on a Cu site. Step R3 represents irreversible surface reaction between adsorbed CO and O₂ to form CO₂. This is obviously not an elementary step but represents

the sequential oxidation of two CO adspecies. Finally, step R4 is the re-oxidation of Cu(I) to Cu(II) with O₂ [138, 143].

The kinetic parameters for R1 to R4 were estimated by fitting the steady state CO effluent concentration data obtained from 3 sets of CO oxidation experiments. The list of experiments used for the parameter estimation and validation of kinetic model are tabulated in Table 6-5. Figures 6-2a and 6-2b show the fitted results. In order to validate the kinetic model, we compared the CO conversion obtained from three additional data sets and model predictions without any further adjustment in the parameters. Figures 6-3a and 6-3b show that the model predicts well the CO conversion for a wide range of CO and O₂ concentrations and temperature.

Table 6-5. Experiments with CO + O₂

	CO concentration (ppm)	O ₂ concentration (%)	Temperature (°C)	Figures
1	200	1	150 – 550	Figure 6-2a
2	300	1	150 – 550	Figure 6-2b
3	300	5	150 – 550	Figure 6-2b
4	200	5	150 – 550	Figure 6-3a
5	500	1	150 – 550	Figure 6-3b
6	500	5	150 – 550	Figure 6-3b

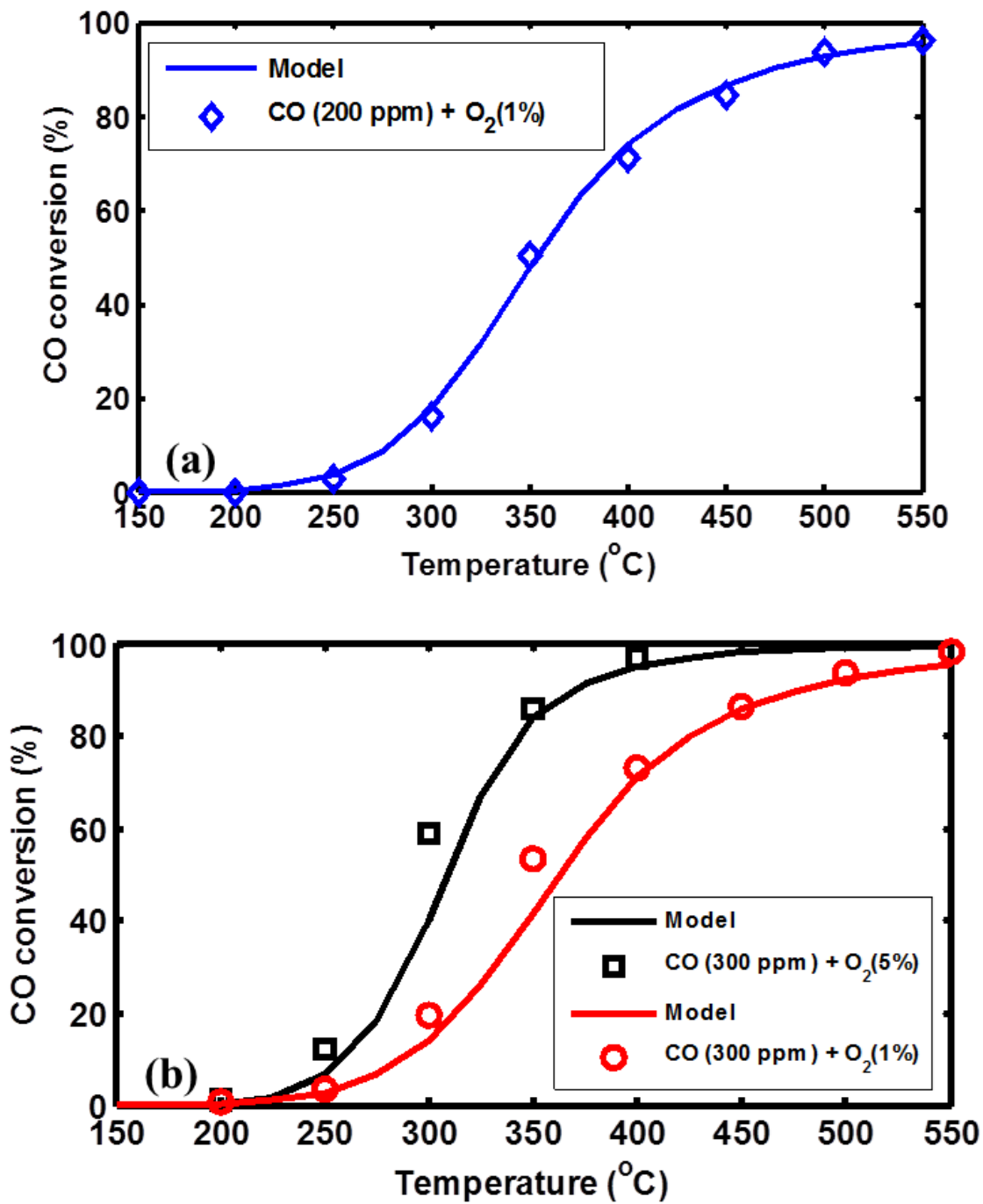


Figure 6-2. Fitted light-off curves of CO (a) CO = 200 ppm, O₂ = 1 %, Balance gas: Ar, (b) CO = 300 ppm, O₂ = 1 and 5 %, Balance gas: Ar.

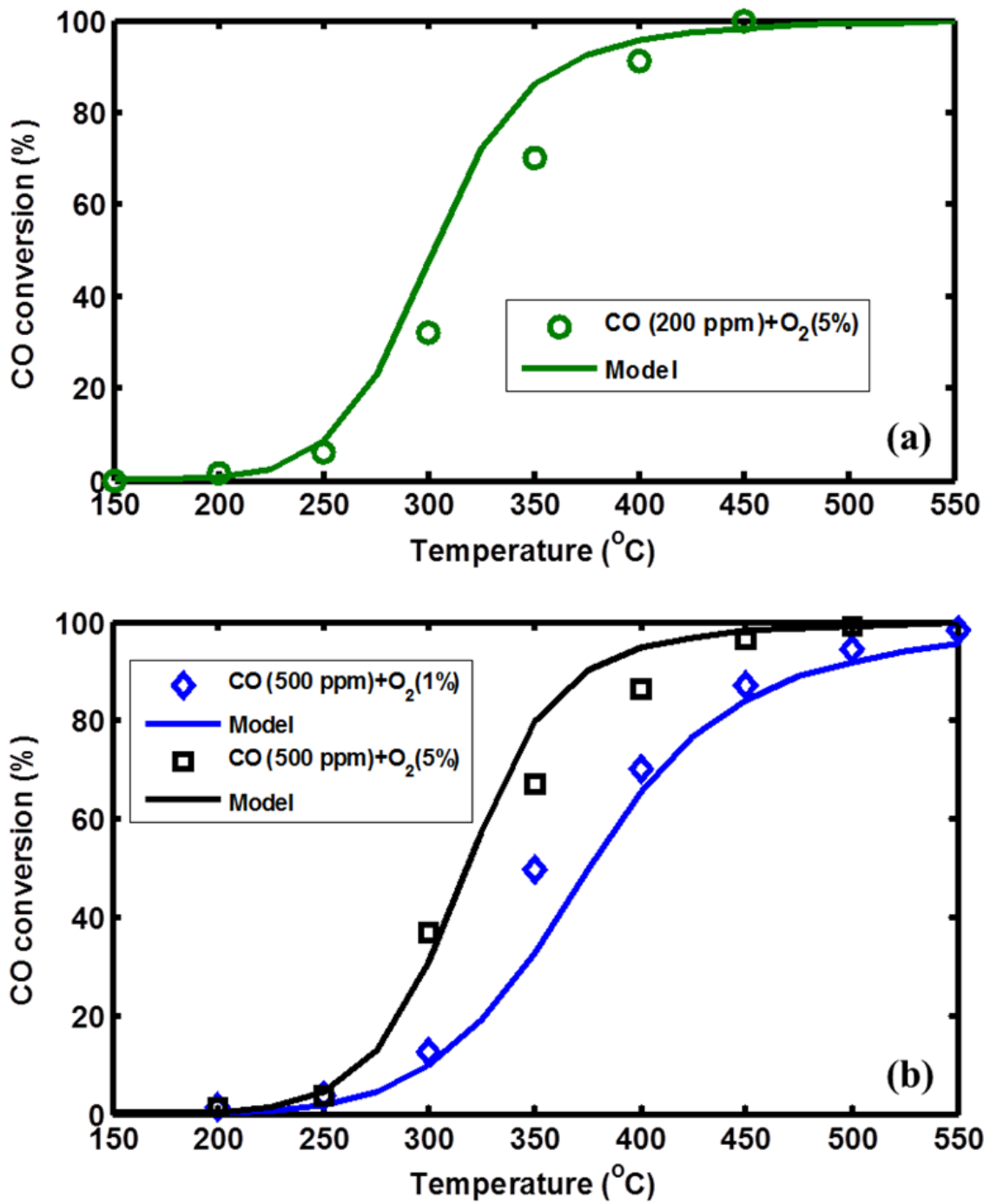


Figure 6-3. Comparison between measured and predicted CO conversion versus temperature (a) CO = 200 ppm, O₂ = 5 %, Balance gas: Ar, (b) CO = 500 ppm, O₂ = 1 and 5 %, Balance gas: Ar.

6.2.4 Kinetic model for C₃H₆ oxidation C₃H₆ + O₂

The next step was to develop a kinetic model for C₃H₆ oxidation. The oxidation of propylene leads to formation of CO₂ and CO via the global reactions:



We consider that C₃H₆ oxidation involves 13 reaction steps (R1-R13) as shown in Table 6-6. The model includes reversible adsorption of C₃H₆ on a Bronsted acid site (R5) which may be completely oxidized to CO₂ (R11). We consider a model oxygenate as an intermediate in C₃H₆ oxidation reaction based on our *in-situ* DRIFTS studies [133]. R7 corresponds to the formation of a surface allyl species resulting from abstraction of H from adsorbed C₃H₆ [144]. R8 represents the formation of a surface oxygenates from oxidation of the allylic species. The C₃H₄O(Cu(I)) formed may be partially oxidized to form CO (R9) or completely oxidized to form CO₂ (R10). R10 was included in the reaction scheme to predict the CO effluent concentration. Overall, there are two routes for CO₂ formation, one route is via CO oxidation and other route is via complete oxidation of the oxygenate. CO formed as partial oxidation product can also be independently oxidized to CO₂ (R3). Reaction steps R7-R11 are taken to be irreversible. Formation of coke-like (C_xH_y) species on Bronsted acid sites is not included in the model [133, 127, 87].

Table 6-6. Reaction steps involved in C₃H₆ oxidation

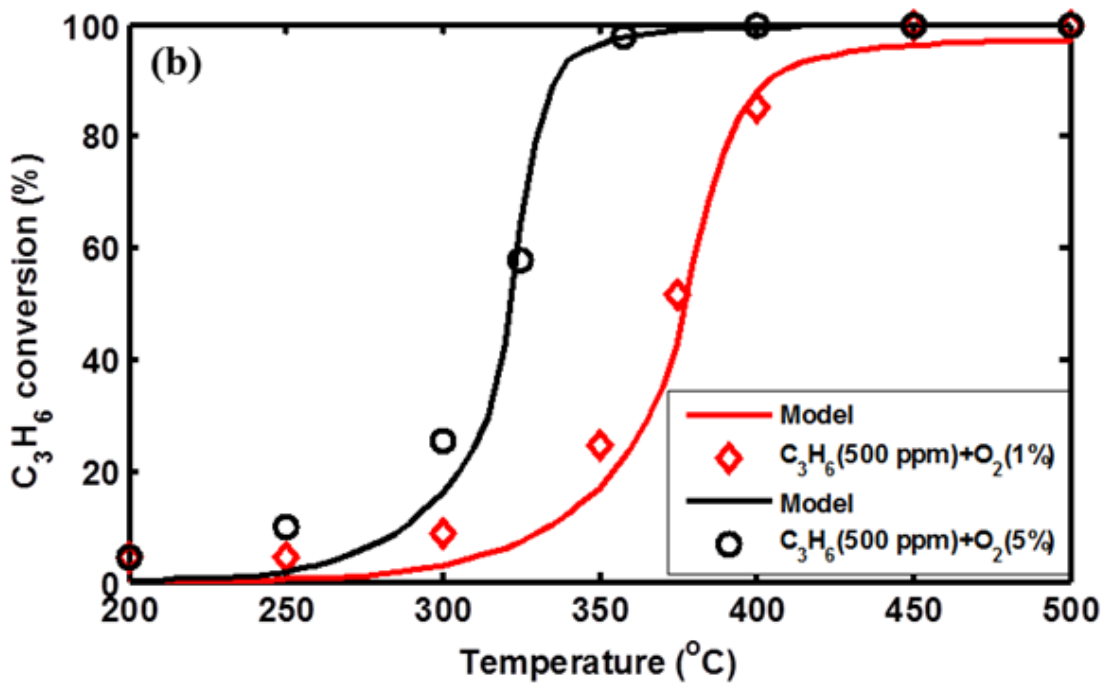
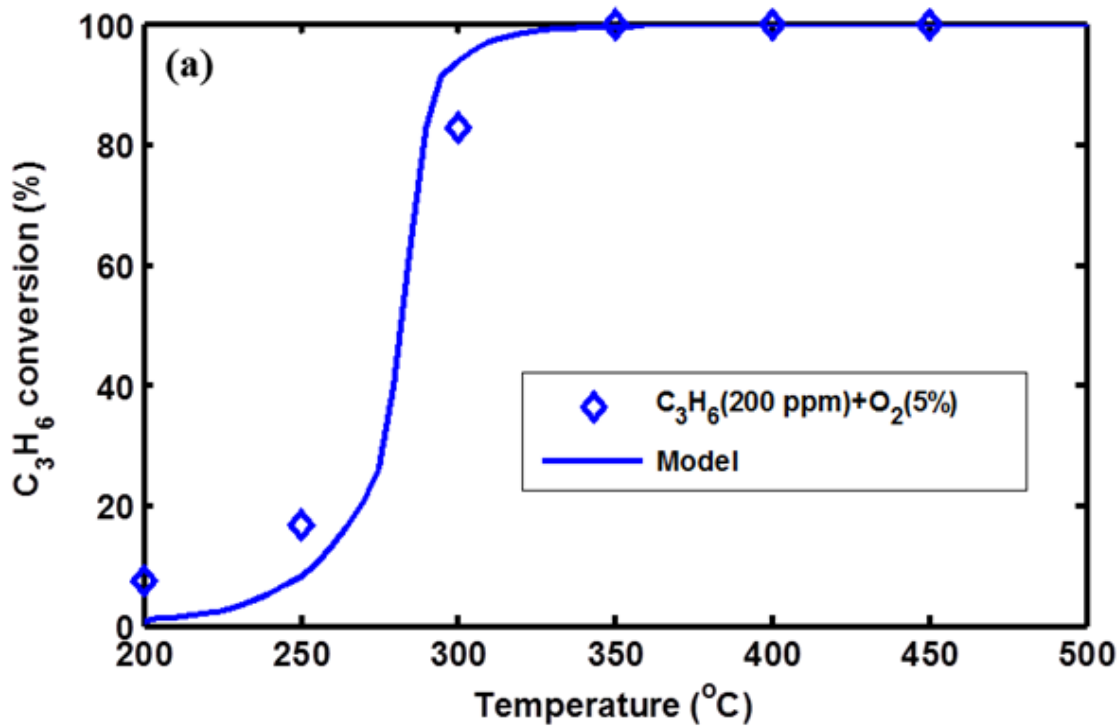
	Reaction	Rate expression
R5	$C_3H_6 + S_2 \leftrightarrow C_3H_6-S_2$	$k_{5,f} \cdot x_{wc,C_3H_6} \cdot \theta_{S_2} \cdot C_{S_2} - k_{5,b} \cdot \theta_{C_3H_6-S_2} \cdot C_{S_2}$
R6	$C_3H_6 + Cu(II) \leftrightarrow C_3H_6(Cu(I))$	$k_{6,f} \cdot x_{wc,C_3H_6} \cdot \theta_{Cu(II)} \cdot C_{S_1} - k_{6,b} \cdot \theta_{C_3H_6} \cdot C_{S_1}$
R2	$O_2 + Cu(II) \leftrightarrow O_2 (Cu(II))$	$k_{2,f} \cdot x_{wc,O_2} \cdot \theta_{Cu(II)} \cdot C_{S_1} - k_{2,b} \cdot \theta_{O_2} \cdot C_{S_1}$
R7	$C_3H_6(Cu(I)) + O_2 (Cu(II)) \rightarrow$ $C_3H_5(Cu(I)) + (Cu(II))O(OH)$	$k_{7,f} \cdot \theta_{C_3H_6} \cdot \theta_{O_2} \cdot C_{S_1} \cdot C_{S_1}$
R8	$C_3H_5(Cu(I)) + O_2 (Cu(II)) \rightarrow$ $C_3H_4O(Cu(I)) + (Cu(II))OH$	$k_{8,f} \cdot \theta_{C_3H_5} \cdot \theta_{O_2} \cdot C_{S_1} \cdot C_{S_1}$
R9	$C_3H_4O(Cu(I)) + 2O_2 (Cu(II)) \rightarrow$ $3CO(Cu(I)) + 2H_2O$	$k_{9,f} \cdot \theta_{C_3H_4O} \cdot \theta_{O_2} \cdot C_{S_1} \cdot C_{S_1}$
R3	$2CO(Cu(I)) + O_2 (Cu(II)) \rightarrow 2CO_2$ $+ 2Cu(I) + Cu(II)$	$k_{3,f} \cdot \theta_{CO} \cdot \theta_{O_2} \cdot C_{S_1} \cdot C_{S_1}$
R1	$CO(Cu(I)) \leftrightarrow CO + Cu(II)$	$k_{1,b} \cdot \theta_{CO} \cdot C_{S_1} - k_{1,f} \cdot x_{wc,CO} \cdot \theta_{Cu(II)} \cdot C_{S_1}$
R10	$2C_3H_4O(Cu(I)) + 7O_2$ $(Cu(II)) \rightarrow 6CO_2 + 2Cu(I) + 3Cu(II) +$ $4H_2O(Cu(II))$	$k_{10,f} \cdot \theta_{C_3H_6-S_1} \cdot \theta_{O_2} \cdot C_{S_1} \cdot C_{S_1}$
R11	$2C_3H_6-S_2 + 9O_2 (Cu(II)) \rightarrow 6CO_2$ $+ 3Cu(II) + 6H_2O(Cu(II)) + 2S_2$	$k_{11,f} \cdot \theta_{C_3H_6-S_2} \cdot \theta_{O_2} \cdot C_{S_1} \cdot C_{S_2}$
R4	$Cu(I) + O_2 \rightarrow O_2 (Cu(II))$	$k_{4,f} \cdot \theta_{Cu(I)} \cdot x_{wc,O_2} \cdot C_{S_1}$
R12	$(Cu(II))O(OH) + (Cu(II))OH \leftrightarrow O_2$ $(Cu(II)) + H_2O(Cu(II))$	$k_{12,f} \cdot \theta_{OOH} \cdot \theta_{OH} \cdot C_{S_1} \cdot C_{S_1} - k_{12,b} \cdot \theta_{O_2} \cdot \theta_{H_2O}$ $\cdot C_{S_1} \cdot C_{S_1}$
R13	$H_2O(Cu(II)) \leftrightarrow Cu(II) + H_2O$	$k_{13,f} \cdot \theta_{H_2O} \cdot C_{S_1} - k_{13,b} \cdot x_{wc,H_2O} \cdot \theta_{Cu(II)} \cdot C_{S_1}$

Table 6-7. Experiments with $C_3H_6 + O_2$

	C_3H_6 concentration (ppm)	O_2 conc. (%)	Temperature ($^{\circ}C$)	Figures
1	200	5	200 – 500	Figure 6-4a
2	300	5	200 – 500	Figure 6-4c
3	500	1	200 – 500	Figure 6-4b
4	500	5	200 – 500	Figure 6-4b
5	200	1	200 – 500	Figure 6-5a
6	500	5	200 – 500	Figure 6-5a
7	750	5	200 – 500	Figure 6-5b

Having estimated the kinetic parameters for steps R1-R4 from CO oxidation, we fixed those values and estimated the remaining kinetic parameters for reaction steps R5-R11. This was done by fitting the steady state C_3H_6 and CO effluent concentrations obtained during the C_3H_6 oxidation bench flow reactor experiments (Tables 6-6 and 6-7, Experiments 1-4). The kinetic parameters for reaction steps R12 and R13 were manually adjusted. In order to validate the kinetic model, we compared model predictions for C_3H_6 conversion obtained from a separate set of experiments. Figures 6-5a and 6-5b show that the model predicts reasonably well the C_3H_6 conversion for wide range of C_3H_6 (200-750 ppm) and O_2 concentrations (0.5-5%) over wide range of temperature. The model is not able to predict the C_3H_6 conversion as well below $300^{\circ}C$. We have confirmed that oxygenates are not formed as by-products of C_3H_6 oxidation because on analyzing effluent gas from C_3H_6 oxidation by a mass spectrometer (QMS; MKS Spectra Products; Cirrus LM99) only CO, CO_2 and H_2O were observed. Thus, the likely reason is that we

have not accounted for formation of coke like species via C_3H_6 oligomerization on Bronsted acid sites.



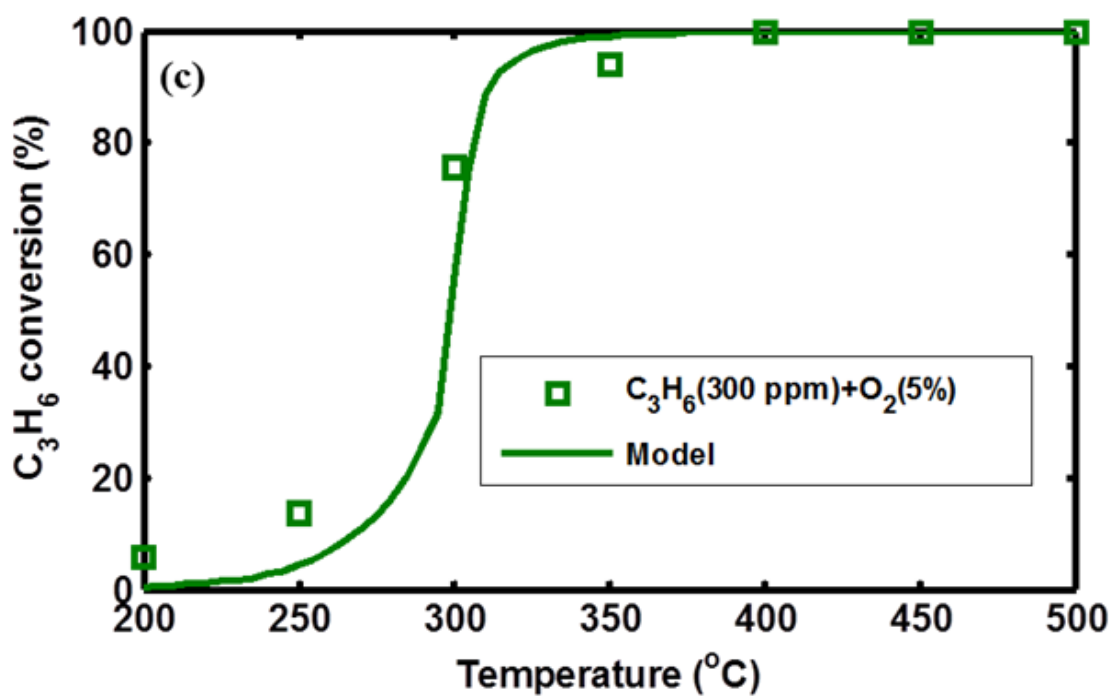
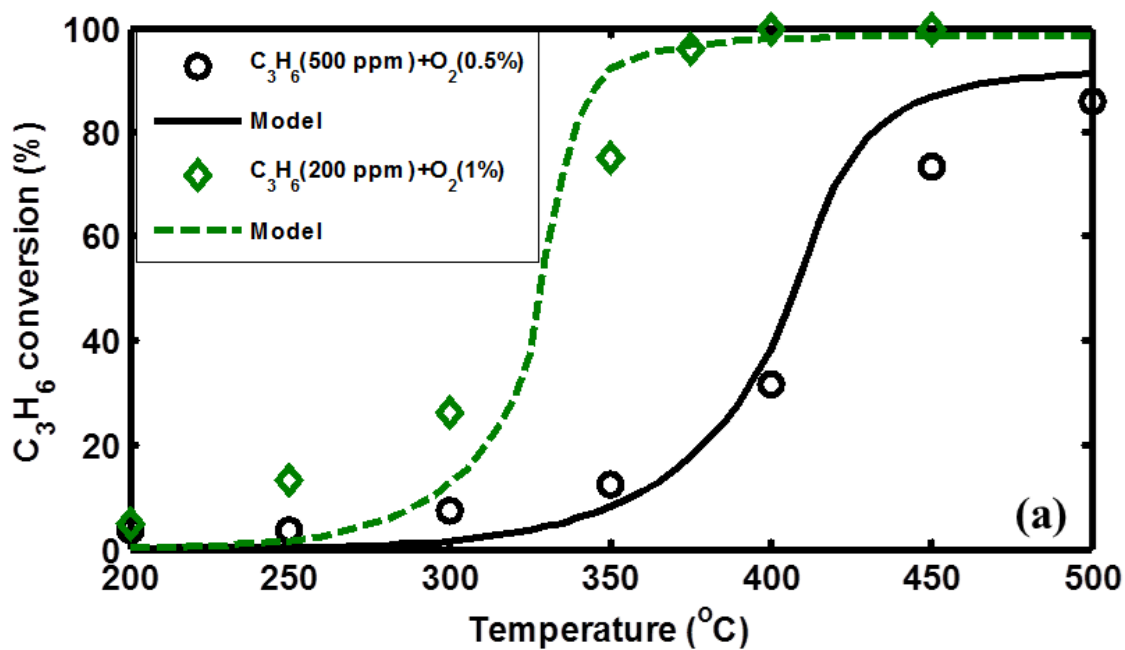


Figure 6-4. Fitted light-off curves of C₃H₆ (a) C₃H₆ = 200 ppm, O₂ = 5 %, Balance gas: Ar, (b) C₃H₆ = 500 ppm, O₂ = 1 and 5 %, (c) C₃H₆ = 300 ppm, O₂ = 5 %, Balance gas: Ar.



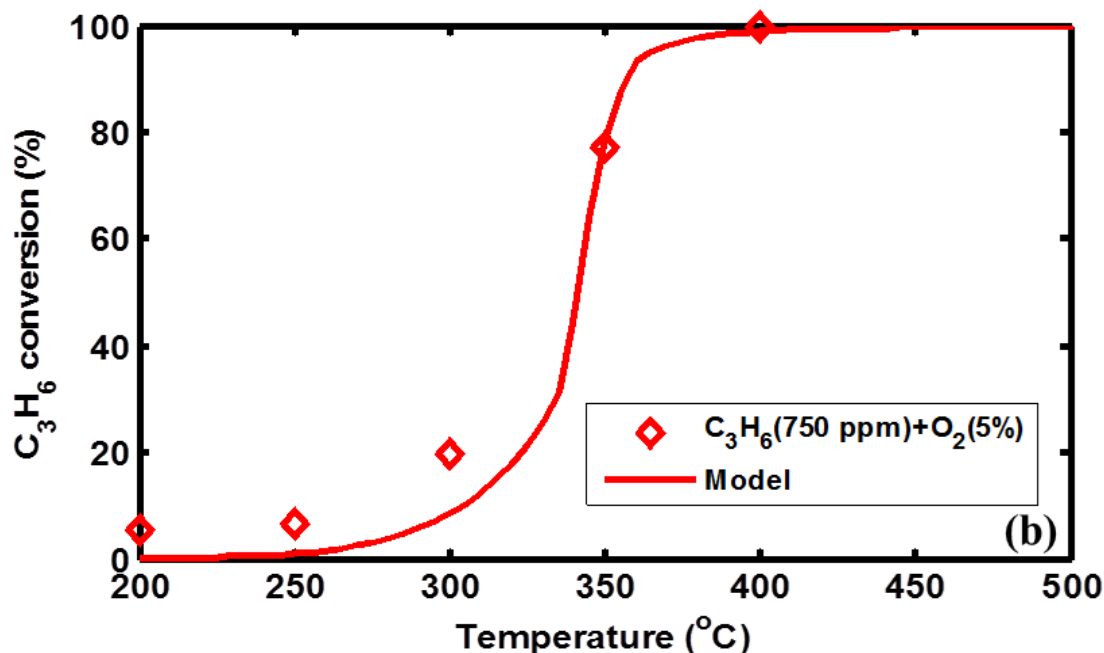


Figure 6-5. Comparison between measured and predicted C_3H_6 conversion versus temperature (a) $C_3H_6 = 200$ and 500 ppm, $O_2 = 1$ and 0.5% , Balance gas: Ar, (b) $C_3H_6 = 750$ ppm, $O_2 = 5\%$, Balance gas: Ar.

6.2.5 Kinetic model for $C_3H_6 + NO + O_2$

The kinetic model for $C_3H_6 + NO + O_2$ consists of reaction steps R1-R15. For the selective catalytic reduction of NO by C_3H_6 the key step involved is the proposed formation of an isocyanate species from the reaction of NO with the surface oxygenate [133]. Two reaction steps R14 and R15 are added to account for the participation of NO. R14 represents the NO selectively reacting with $C_3H_4O(Cu(I))$ to form $C_2H_2-NCO(Cu(I))$ which is further oxidized to N_2 in R15. It was shown in our recent study [133] that NO uptake on Cu-SSZ13 is small and has a desorption temperature around $225^\circ C$. It has also been shown that NO uptake is negligible in the presence of C_3H_6 in the feed [133]. Thus, we have not considered the NO adsorption-desorption step in our model. We also showed in a series of steady state and transient experiments with C_3H_6+NO/NO_2+O_2 that NO_2 is

not formed as an intermediate during the NO selective reduction with C₃H₆ [133]. Hence, we have not considered the NO oxidation in the overall mechanism. The spatially resolved concentration profiles of reacting species for the (NO + C₃H₆ + O₂) reaction system clearly suggest that NO is only reduced to N₂ [133].

Table 6-8. Reaction steps involving NO

R14.	$C_3H_4O(Cu(I)) + NO \rightarrow C_2H_2-NCO(Cu(I)) + H_2O$	$k_{14,f} \cdot \theta_{C_3H_4O} \cdot X_{wc,NO} \cdot C_{S1}$
R15.	$2C_2H_2-NCO(Cu(I)) + 5O_2 (Cu(II)) \rightarrow 2CO(Cu(I)) + N_2 + 2H_2O(Cu(II)) + 4CO_2 + 3Cu(II)$	$k_{15,f} \cdot \theta_{NCO} \cdot \theta_{O_2} \cdot C_{S1} \cdot C_{S1}$

Having estimated the kinetic parameters for R1-R13, the remaining parameters for R14 and R15 (Table 6-8) were estimated by keeping the values of other parameters fixed and then fitting the steady state effluent concentrations of C₃H₆ and NO using the Levenberg-Marquardt method. The data that were used for both fitting and for validation of the model are shown in Table 6-9. The values of kinetic parameters for R1-R15 are provided in Table 10. Figures 6-7a and 6-7b show that model predicts both C₃H₆ and NO light off temperature and conversion quantitatively.

Table 6-9 Experiments with C₃H₆+NO+O₂

	C ₃ H ₆ conc. (ppm)	O ₂ conc. (%)	NO conc. (ppm)	Temperature (°C)	Figures
1	500	5	500	200 – 550	Figure 6
2	500	5	500	200 – 550	Figure 7a
3	750	5	250	200 – 550	Figure 7b

Table 6-10 Kinetic parameters used in the simulation

Parameters	Value (s^{-1})/($\text{moles}^{-1}\text{m}^3\text{s}^{-1}$)	Parameters	Values (kJ/mol)
Af1	6.765×10^6	Ef1	0.0
Ab1	7.480×10^8	Eb1	57.3
Af2	1.631×10^7	Ef2	0.0
Ab2	1.191×10^{10}	Eb2	43.3
Af3	1.232×10^8	Ef3	135.4
Af4	1.025×10^7	Ef4	82.2
Af5	1.144×10^2	Ef5	0.0
Ab5	1.992×10^5	Eb5	67.2
Af6	2.916×10^6	Ef6	0.0
Ab6	2.687×10^8	Eb6	77.3
Af7	7.366×10^3	Ef7	75.5
Af8	9.197×10^4	Ef8	89.6
Af9	9.441×10^4	Ef9	79.0
Af10	2.691×10^5	Ef10	90.0
Af11	2.672×10^5	Ef11	90.0
Af12	1.908×10^5	Ef12	60.0
Ab12	1.908×10^5	Eb12	120.0
Af13	1.0×10^{12}	Ef13	70.0
Ab13	1.0×10^2	Eb13	0.0
Af14	1.284×10^{11}	Ef14	91.19
Af15	1.095×10^2	Ef15	63.2

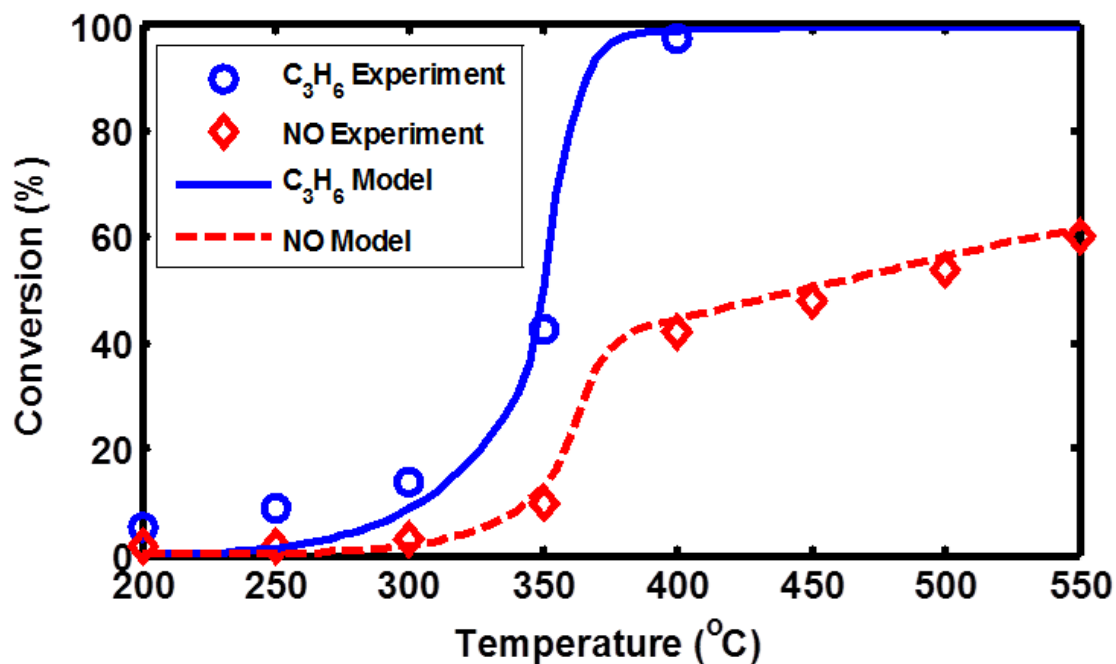
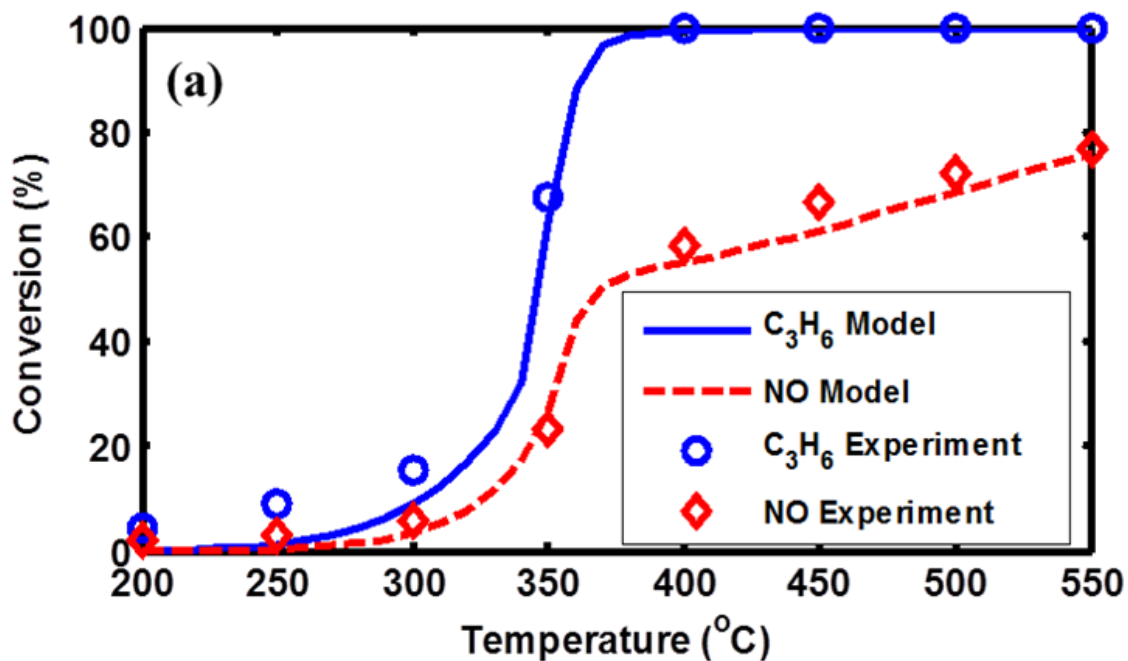


Figure 6-6. Fitted C₃H₆ and NO conversion versus temperature (C₃H₆ = 500 ppm, NO = 500 ppm, O₂ = 5%, Balance gas: Ar)



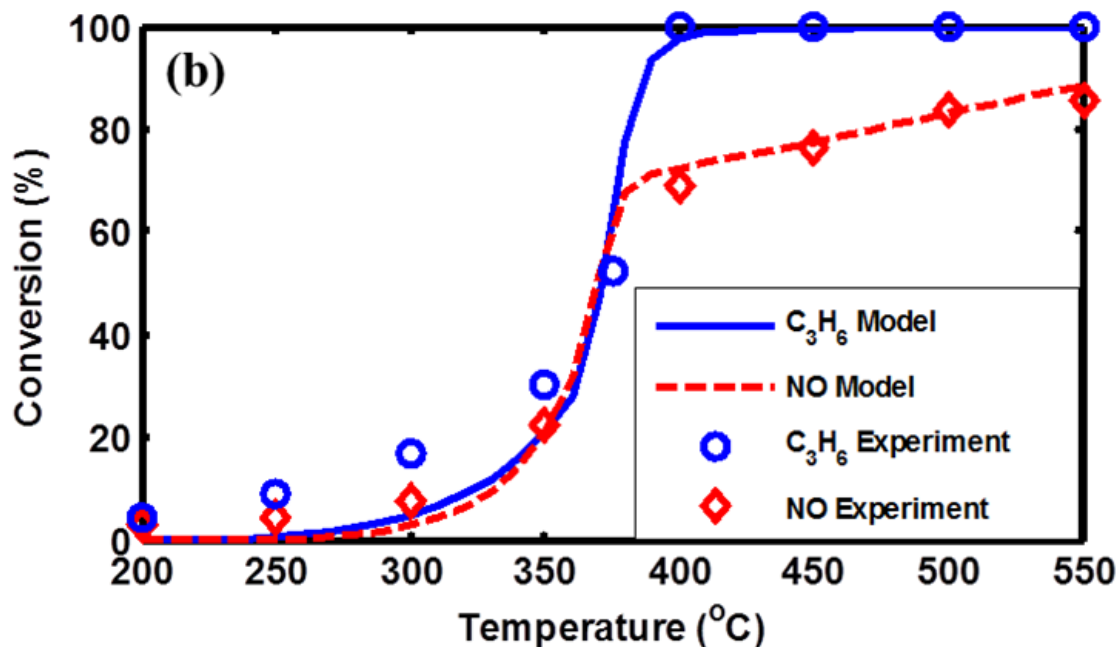


Figure 6-7. Comparison between measured and predicted C_3H_6 and NO conversion versus temperature (a) $C_3H_6 = 500$ ppm, NO = 250 ppm, $O_2 = 5\%$, Balance gas: Ar, (b) $C_3H_6 = 750$ ppm, NO = 250 ppm, $O_2 = 5\%$, Balance gas: Ar.

6.3 Results and Discussion

The developed monolith model captures the experimental trends both qualitatively and quantitatively for CO oxidation ($CO + O_2$), C_3H_6 oxidation ($C_3H_6 + O_2$) and lean NO reduction with C_3H_6 ($NO + C_3H_6 + O_2$). Differential kinetic experiments (conversion <15%) were carried out in the temperature range of 250-300°C to determine the CO and O_2 orders reaction orders during CO oxidation. It was found that CO oxidation is of positive order with respect to both CO (~0.4) and O_2 (~0.7) (Rate is in $\text{moles.m}^{-3}.\text{s}^{-1}$, concentration is in moles.m^{-3}). A mechanistically-based kinetic model should be able to predict the reaction orders. To check if this was the case we simulated CO oxidation under differential conditions in the same 250-300°C temperature range. Figures 6-8a and 6-8b show the logarithmic plot of rate of CO consumption vs. CO inlet

concentration and O₂ inlet concentration, respectively. The predicted reaction order with respect to CO and O₂ was found to be 0.3 and 0.65, respectively, in good agreement with the data.

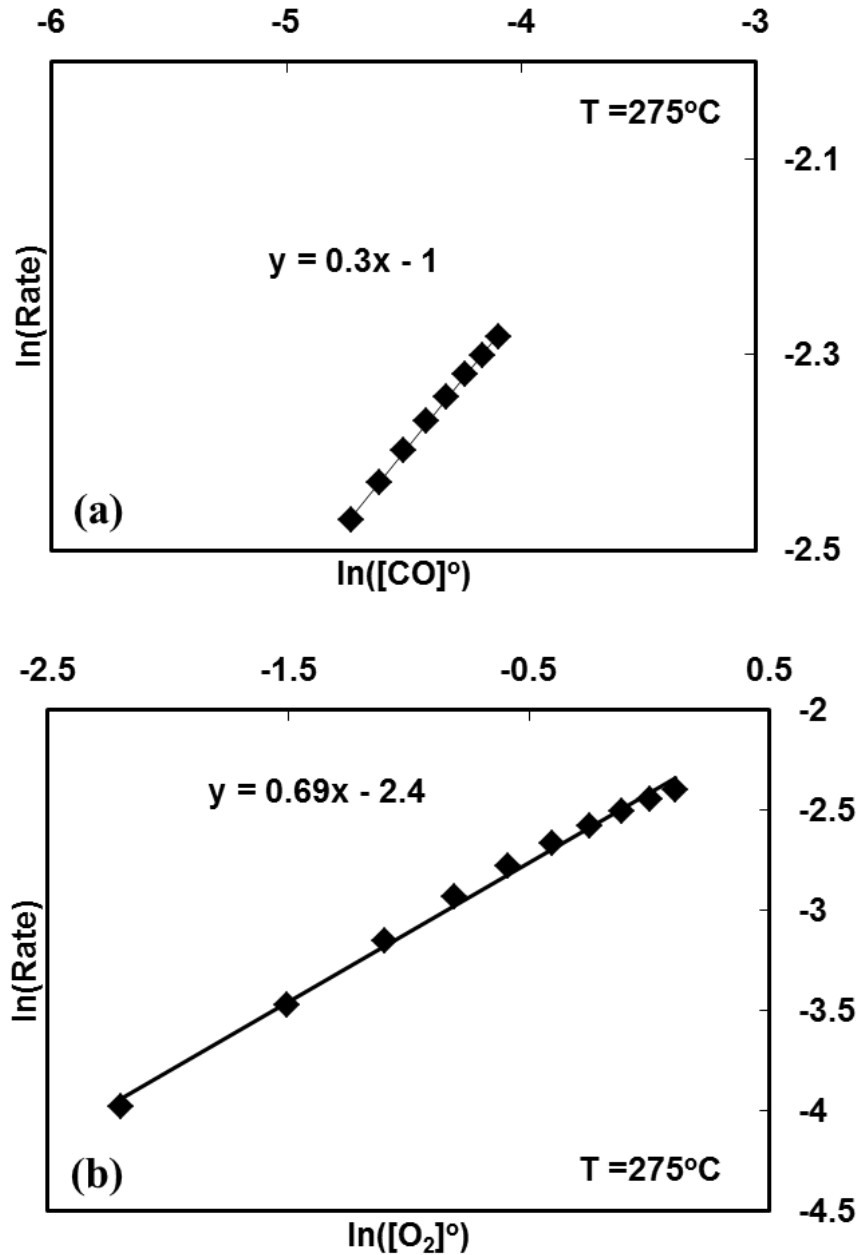


Figure 6-8. (a) Predicted dependence of CO oxidation rates on CO (5% O₂, 400–800 ppm CO), (b) Predicted dependence of CO oxidation rates on O₂. Feed for CO order: 0.5-5% O₂, 500 ppm CO, Balance gas: Ar) GHSV = 57,000 h⁻¹

It has been shown through *in-situ* DRIFTS that surface oxygenates are intermediates during C₃H₆ oxidation on Cu-SSZ13 [87, 133, 134, 140, 141]. As described above, the mechanistic model includes the formation of oxygenates which may be further oxidized to CO and CO₂. The validated C₃H₆ oxidation model predicts the light-off curves for C₃H₆ for different feed composition quite well. Figure 6-9 shows the light-off curves obtained from the model for a range of C₃H₆ inlet concentration (100-800 ppm) and 1% O₂. Differential kinetic studies carried out for C₃H₆ oxidation show a positive order with respect to O₂ and negative order with respect to C₃H₆ [133]. The model clearly predicts the negative order with respect to C₃H₆ as there is shift in light off temperature from 275°C to 425°C as the C₃H₆ concentration is increased from 100 ppm to 800 ppm. Similarly, Figure 6-10a shows that even at higher O₂ concentration (5%) in the feed C₃H₆ has an inhibiting effect on the C₃H₆ oxidation. On other hand, Figure 6-10b shows that C₃H₆ light-off curve shifts towards the left on increasing the O₂ concentration in the feed. There is a decrease in the light off temperature from 425°C to 325°C on increasing the O₂ concentration from 0.5% to 5%. We also performed simulations for C₃H₆ oxidation under differential conditions in the temperature range of 250-300°C in order to determine the reaction orders with respect to C₃H₆ and O₂. The reaction order with respect to C₃H₆ was found to be in range of -0.5 to -0.7 whereas the order with respect to O₂ was found to be +1 (see Figure 6-11).

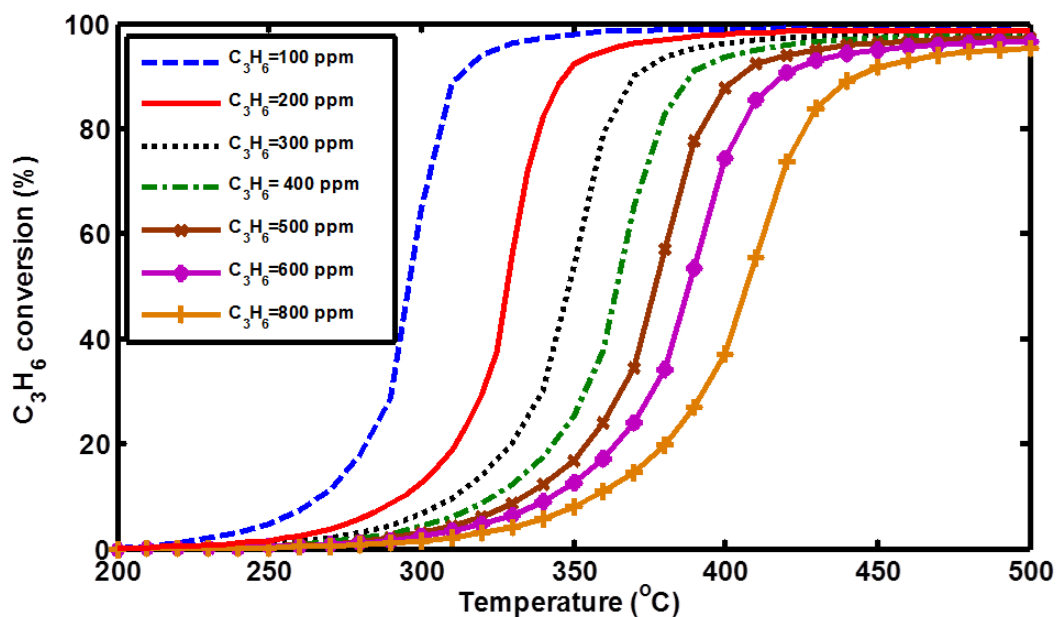
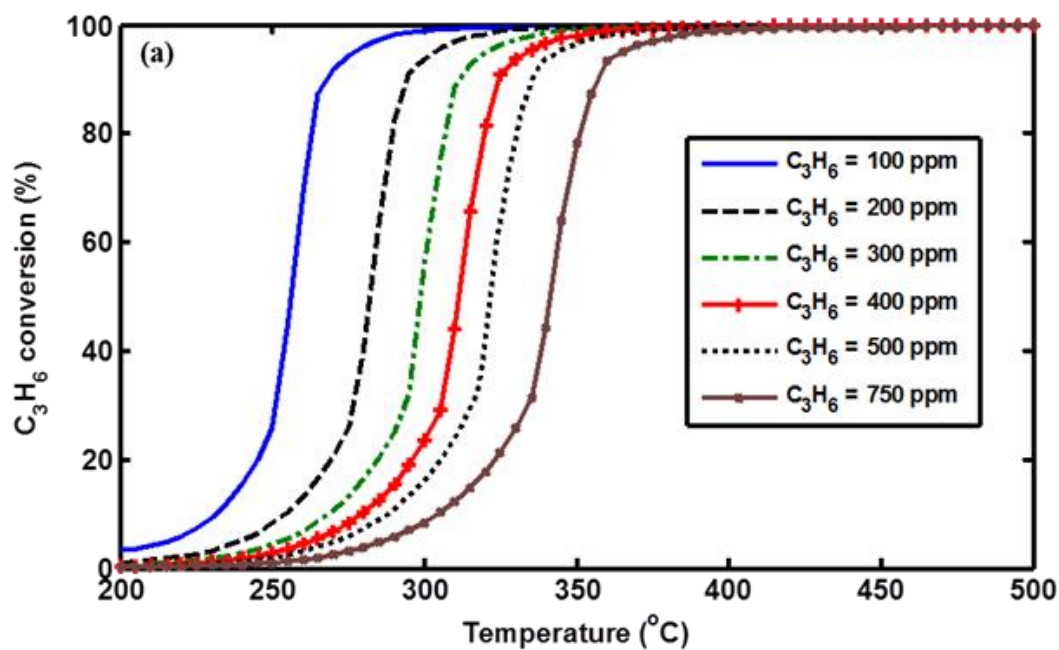


Figure 6-9. Predicted light- off curves of C_3H_6 ($C_3H_6 = 100\text{-}800$ ppm, $O_2 = 1\%$, Balance gas: Ar)



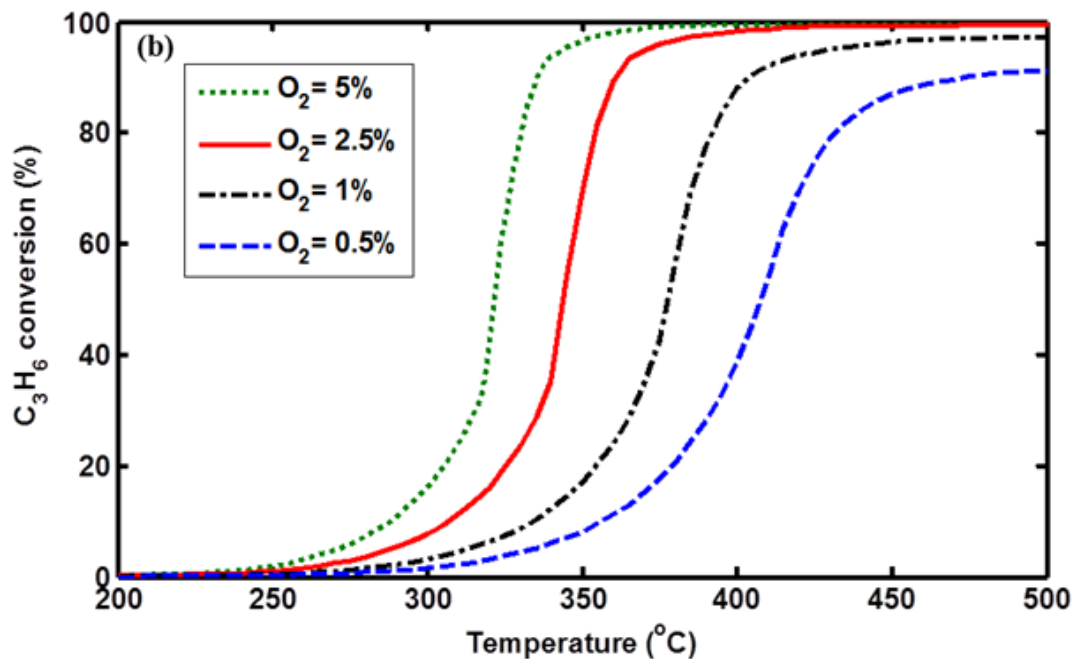
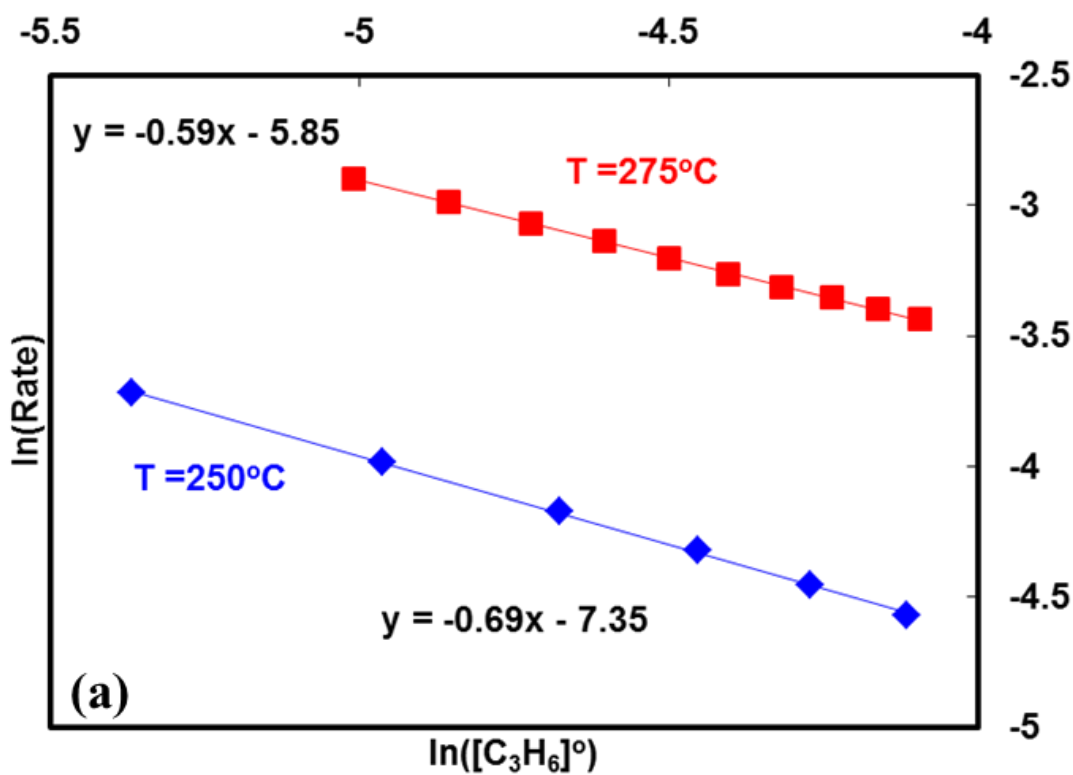


Figure 6-10. Predicted light-off curves of C_3H_6 (a) $C_3H_6 = 100$ -750 ppm, $O_2 = 5\%$, Balance gas: Ar, (b) $C_3H_6 = 500$ ppm, $O_2 = 0.5$ -5%, Balance gas: Ar.



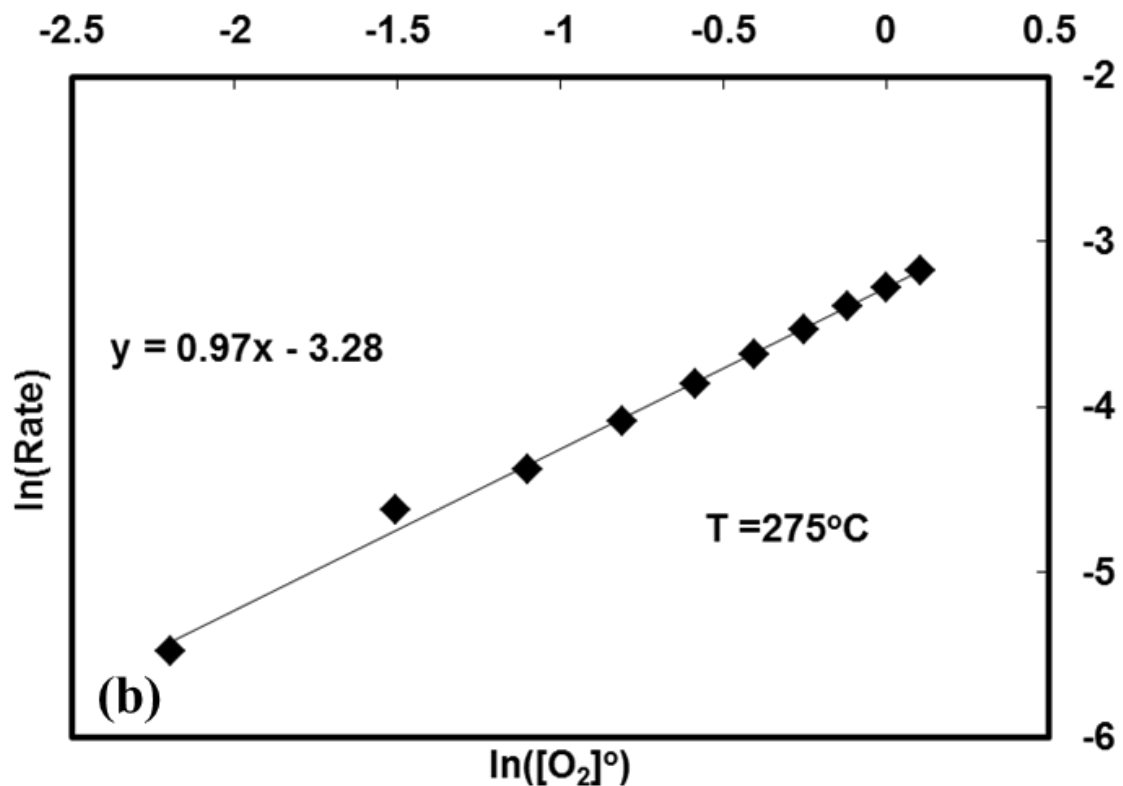


Figure 6-11. (a) Predicted dependence of C₃H₆ oxidation rates on C₃H₆ (5% O₂, 200–800 ppm C₃H₆) (b) Predicted dependence of C₃H₆ oxidation rates on O₂. Feed for C₃H₆ order: 0.5-5% O₂, 500 ppm C₃H₆, Balance gas: Ar)

It is instructive to examine the model predictions of the surface oxygenate coverages with temperature. Figure 6-12 shows the predicted coverage of C₃H₄O(Cu(I)) within the monolith washcoat with temperature for C₃H₆ = 500 ppm and O₂ = 1%. There is an increase in $\theta_{\text{C}_3\text{H}_4\text{O}}$ up to the light-off temperature (375°C), while above light-off the coverage starts decreasing. This clearly confirms the role of the oxygenate as an intermediate in C₃H₆ oxidation reaction. Figure 11 shows the predicted Cu(I) coverage during C₃H₆ oxidation for a feed composition of 500 ppm C₃H₆ and 1% O₂. The Cu(I) coverage is at a maximum around the light-off temperature (400°C) when surface C₃H₆ derived species are oxidized leaving behind the reduced Cu(I) species, as represented by

steps R9 and R10. The Cu(I) species formed are then re-oxidized to Cu(II) by O₂ as shown in step R4. As a result, there is a decrease in Cu(I) coverage above the light-off temperature. Similarly, Figure 6-13 shows the predicted Cu(I) coverage during C₃H₆ oxidation for a feed composition of 500 ppm C₃H₆ and 5% O₂. Again, the maximum Cu(I) coverage is around the light-off temperature (350°C). Hence, the oxidation state of Cu during the reaction depends on the feed composition

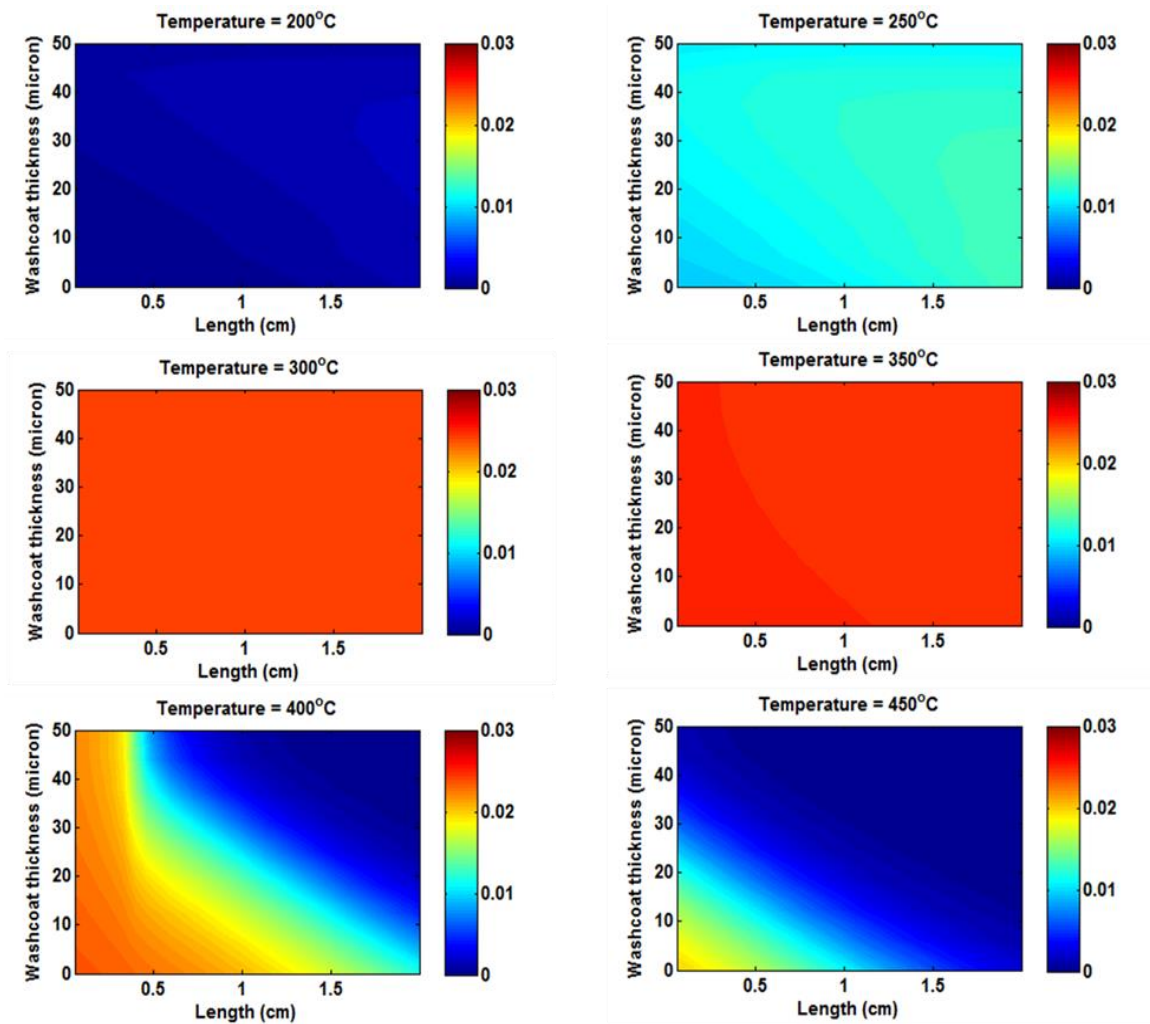


Figure 6-12. Predicted coverage of C₃H₄O(Cu(I)) within the washcoat (C₃H₆ = 500 ppm, O₂ = 1 %, Balance gas: Ar)

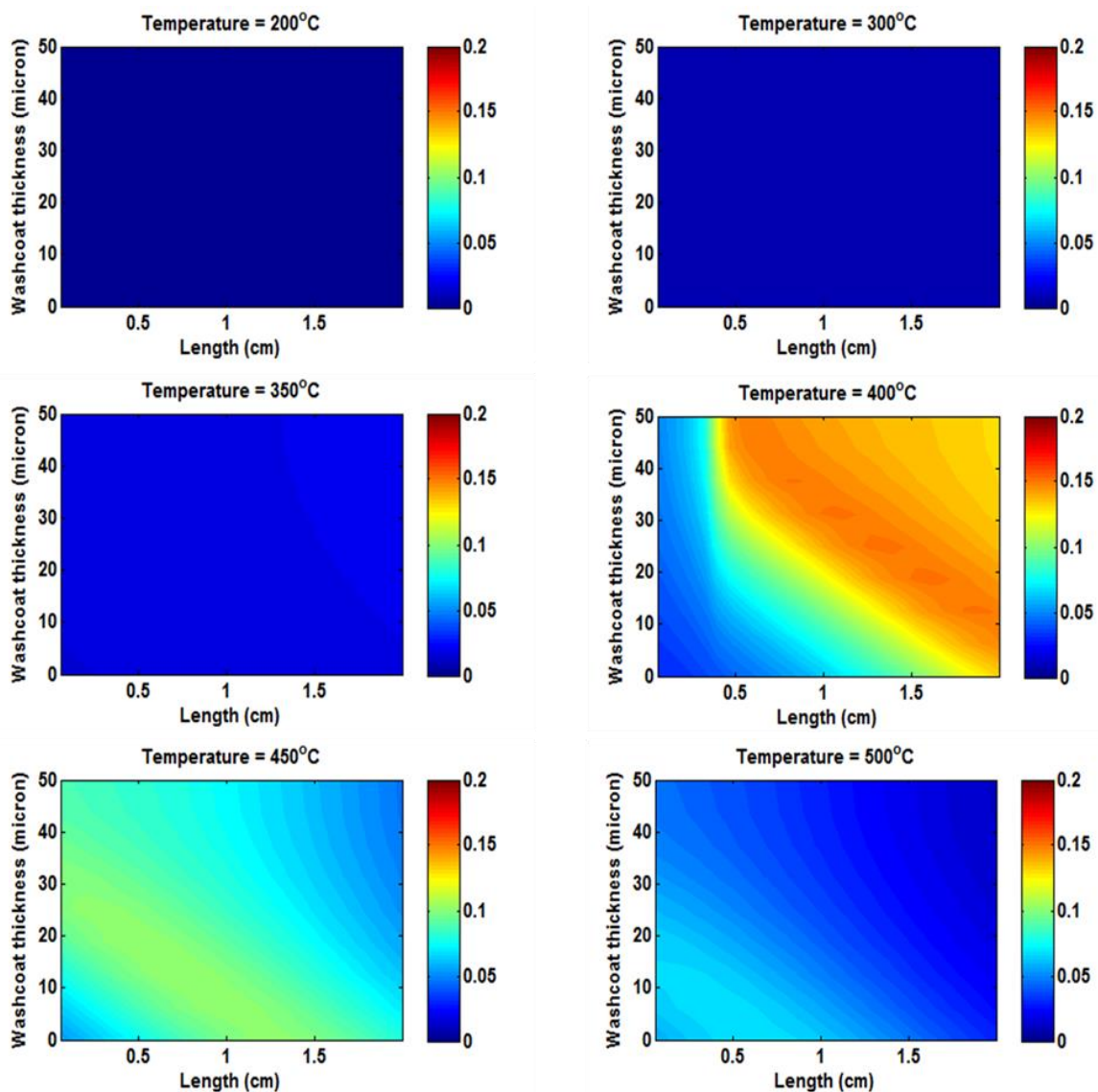


Figure 6-13. Predicted coverage of Cu(I) within the washcoat ($C_3H_6 = 500$ ppm, $O_2 = 1$ %, Balance gas: Ar)

The critical step in the $C_3H_6 + NO + O_2$ reaction system is the selective reaction of NO with the C_3H_6 derived oxygenates to form surface C_xH_yNCO isocyanate, which may be further reduced to N_2 . In addition to serving as a reductant of NO, C_3H_6 can also be oxidized to CO and CO_2 , which results in NO conversion less than 100% at higher temperature. These competing reactions lead to interesting dependencies on the inlet feed composition. Figure 6-14a shows the dependence of NO conversion with temperature for

different NO to C₃H₆ ratios. The NO inlet concentration is kept constant (250 ppm) and C₃H₆ inlet concentration is increased from 500 ppm to 1000 ppm. Due to an increase in the inlet C₃H₆ concentration there is an increase in C₃H₆ light-off temperature (refer to Figure 6-10) due to the established negative-order effect discussed earlier. Per the proposed mechanism, propylene oxidation leads to the formation of surface oxygenates which are the key intermediates for NO reduction. The surface oxygenates formed at higher temperature react with NO to form surface isocyanate species which are further reduced to N₂. In this regime the rate of NO formation is positive order with respect to C₃H₆. With the increase in the C₃H₆ inlet concentration there is increase in NO conversion at 400°C from about 50% to 80% while at 550°C the NO conversion increases from 60% to 90%. Figure 6-14b shows the dependence of NO conversion on the inlet O₂ concentration in feed. On increasing the inlet O₂ concentration from 5% to 10% there is a 30% increase in the NO conversion in the 300°C to 350°C temperature range. This shows that by increasing the O₂ concentration there is formation of oxygenates at lower temperature which is followed by formation of surface R-NCO species that are further reduced to N₂. Above 350°C there is a decrease in the NO conversion as higher O₂ concentration in the feed results in higher rate of competing C₃H₆ oxidation reaction.

The model can also be used to evaluate the effect of Cu loading. Figure 6-15 shows the NO conversion for different ion-exchange levels. As we increase the concentration of Cu sites by increasing the ion-exchange level from 30% to 90% there is increase in NO conversion in 300°C to 375°C temperature range. Figure 6-16a shows the plot of calculated ratios of cup-mixing C₃H₆ mole fraction in the fluid phase to averaged intrawashcoat C₃H₆ mole fraction ($X_{fm,C3H6}/\langle X_{wc,C3H6} \rangle$) in the 250°C to 450°C

temperature range. This plot shows that below 325°C there is negligible effect of washcoat diffusion since the ratio of $X_{fm,C_3H_6}/\langle X_{wc,C_3H_6} \rangle \sim 1$. However at higher temperatures, 325°C to 450°C washcoat diffusion limitations become significant for C_3H_6 as indicated by $X_{fm,C_3H_6} \gg \langle X_{wc,C_3H_6} \rangle$. Figure 6-16b shows that there is no washcoat diffusional limitations for NO over the 250°C to 450°C temperature range since the ratio of $X_{fm,NO}/\langle X_{wc,NO} \rangle \sim 1$.

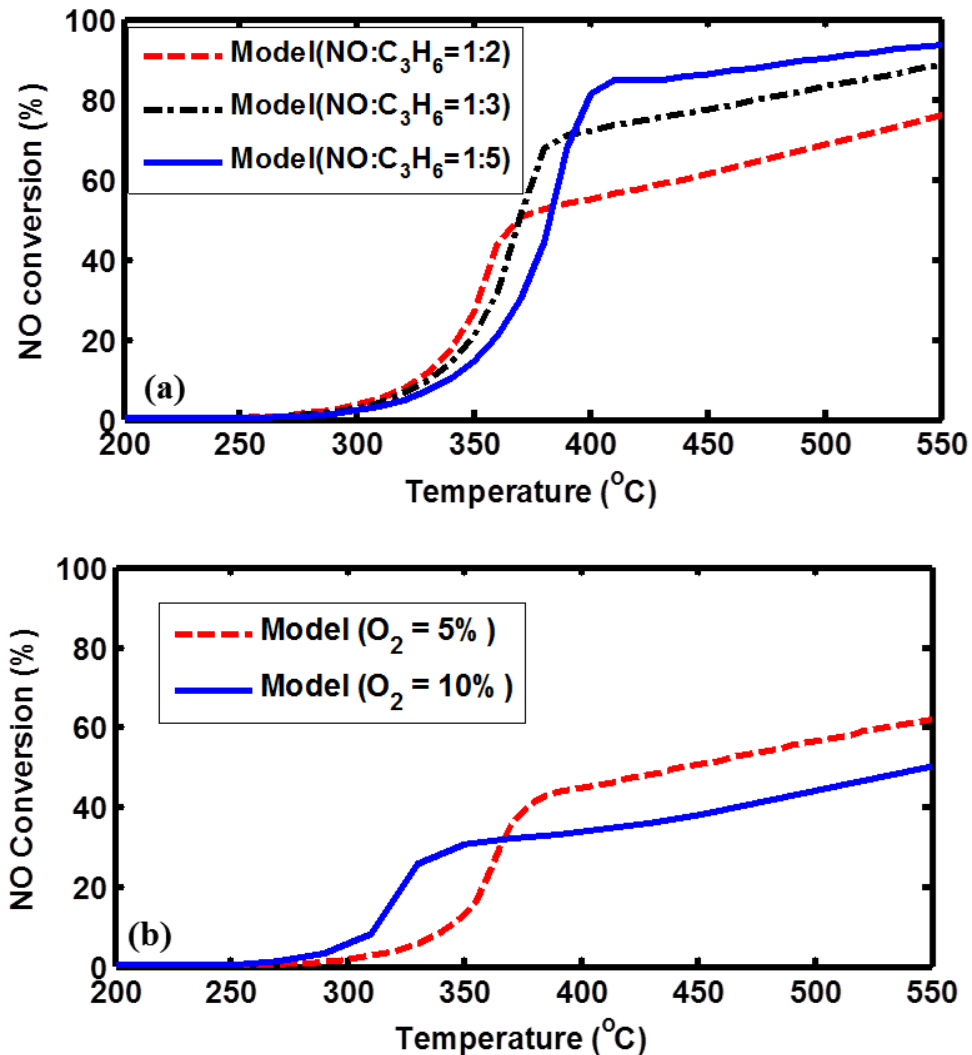


Figure 6-14 (a) NO conversion versus temperature (C₃H₆ = 500, 750, 1000 ppm, NO = 250 ppm, O₂ = 5 %,) (b) NO conversion versus temperature for different inlet O₂ concentration (C₃H₆ = 500 ppm, NO = 500 ppm, O₂ = 5% & 10%)

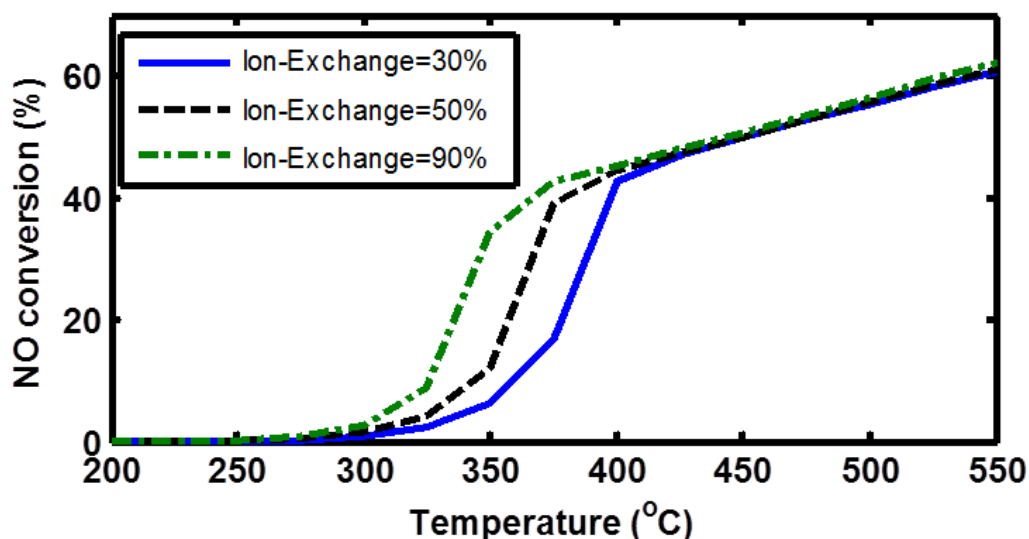


Figure 6-15. Predicted NO conversion for different ion exchange ratios (NO = 500 ppm, C₃H₆ = 500 ppm, O₂ = 5 %, Balance gas: Ar)

It has been shown experimentally that there is increase in the light-off temperature of C₃H₆ when NO is added to feed. Figure 6-17a shows both data and model predictions for the steady state C₃H₆ conversion dependence with temperature for C₃H₆ oxidation and NO selective reduction with C₃H₆. The model captures the inhibition of NO on C₃H₆ conversion as the C₃H₆ light-off temperature increases from 320°C to 370°C for a feed composition with 500 ppm C₃H₆, 5% O₂ and 0 or 500 ppm NO, respectively. Similarly, Figure 6-17b also shows the inhibition of NO for different feed composition (750 ppm C₃H₆, 5% O₂ and 0 or 250 ppm NO), confirming that the model is consistent with the experimental observations.

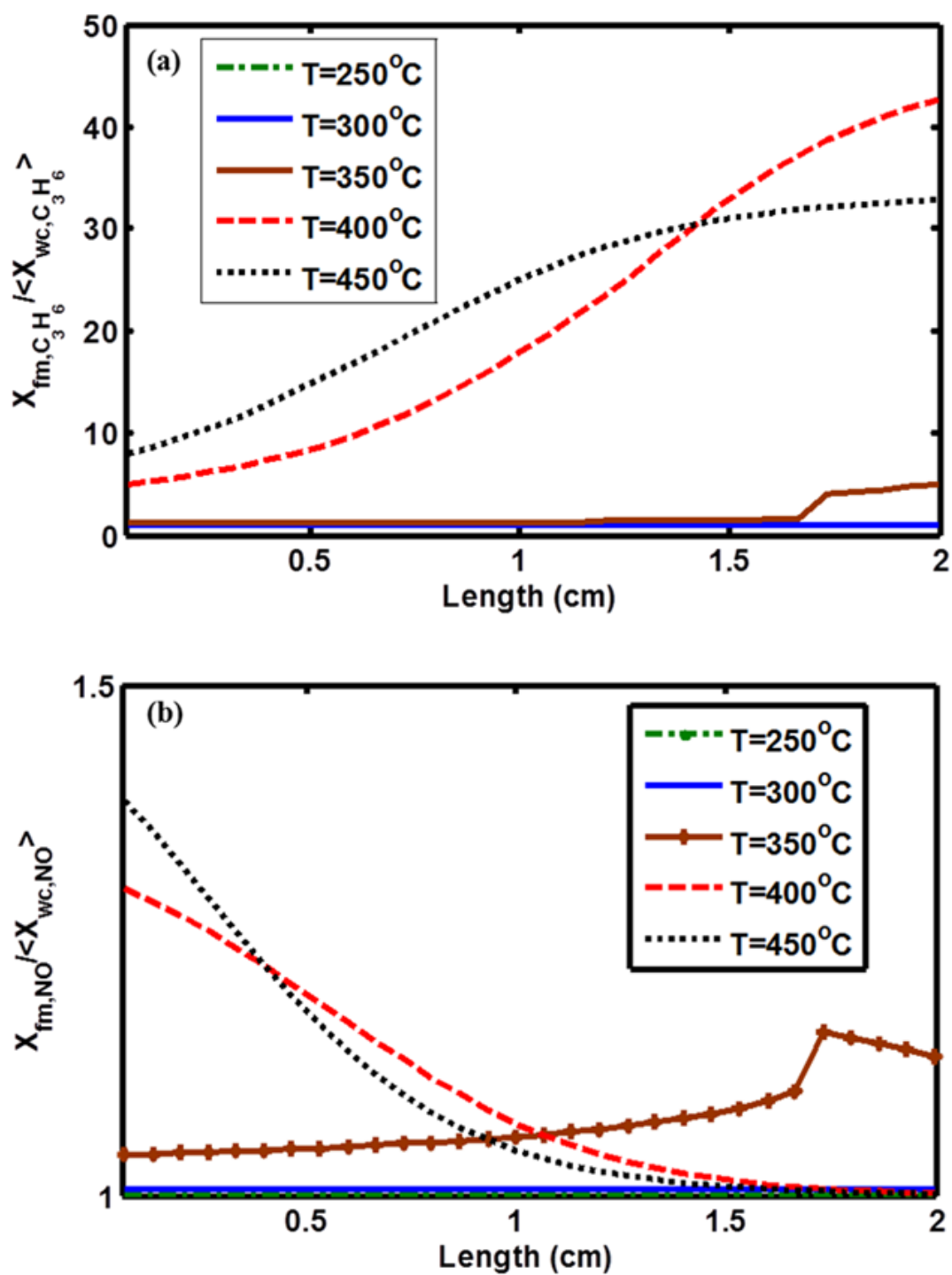


Figure 6-16. (a) Ratio of cup-mixing C_3H_6 mole fraction in fluid phase to intrawashcoat C_3H_6 mole fraction with axial position, (b) Ratio of cup-mixing NO mole fraction in fluid phase to intrawashcoat NO mole fraction with length

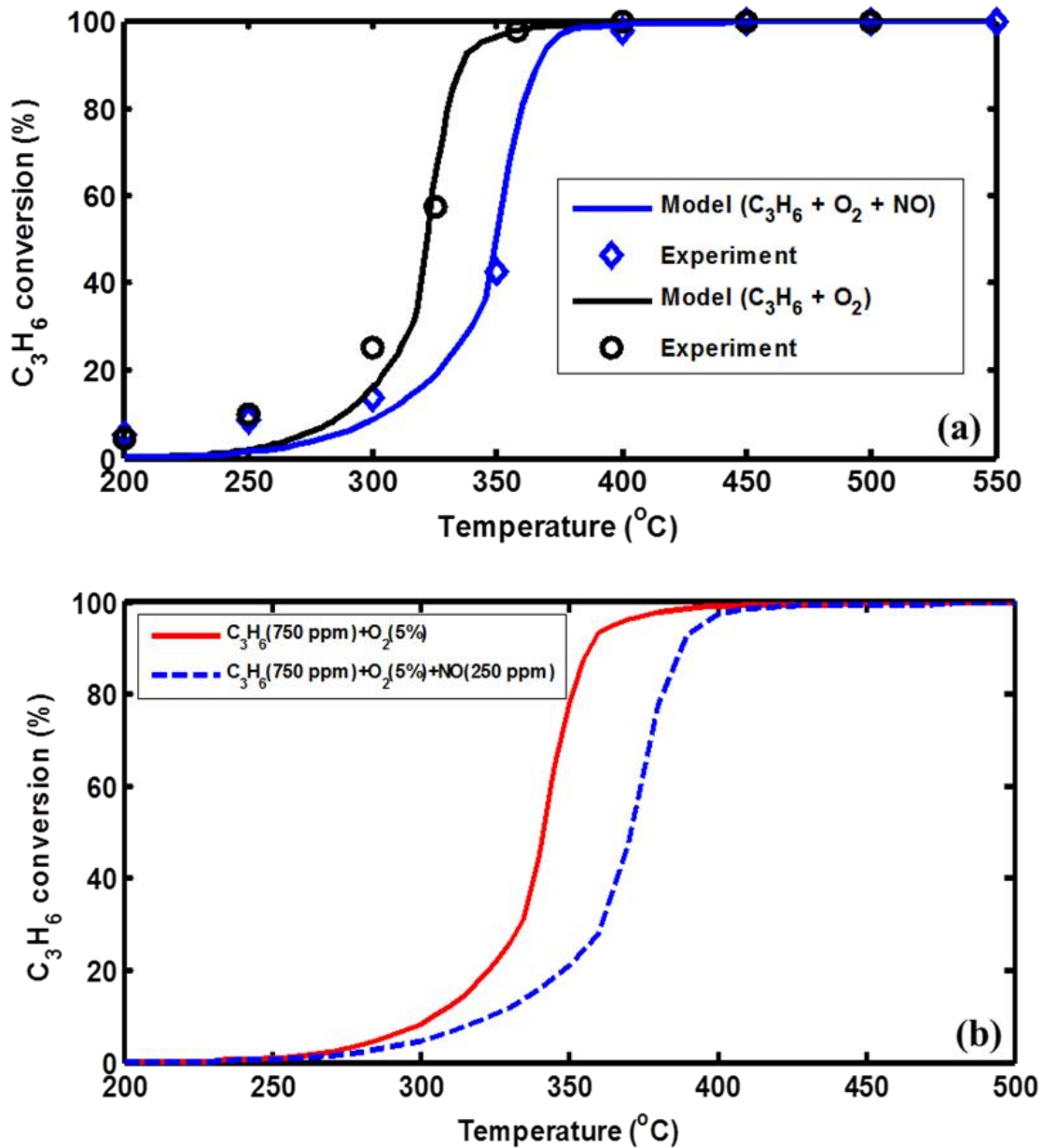


Figure 6-17. (a) C_3H_6 light off curves with and without NO in feed ($C_3H_6 = 500$ ppm, NO = 0 or 500 ppm, $O_2 = 5\%$), (b) C_3H_6 light off curves with and without NO in feed ($C_3H_6 = 750$ ppm, NO = 0 or 250 ppm, $O_2 = 5\%$)

The present model for NO selective reduction with C_3H_6 is based on the experimental evidence that oxygenates are the common intermediate for both C_3H_6 oxidation and selective catalytic reduction of NO. The formation of the R-NCO species

during NO selective reduction with C_3H_6 was confirmed earlier by *in-situ* DRIFTS studies [133, 140]. Oxygenates formed during the reaction can react further with oxygen to form CO and CO_2 or react selectively with NO to form an isocyanate species. Further evidence for such a surface species was shown in our previous study [133] in a transient experiment in which the catalyst, first exposed to 500 ppm C_3H_6 and 5% O_2 and allowed to reach steady state (ca. 45 minutes), was then exposed to 500 ppm NO for 10 minutes at 300°C, 325°C and 350°C. A slight increase in the C_3H_6 outlet concentration was observed at 300°C. In contrast, at 325°C and 350°C, in the vicinity of the light-off temperature for C_3H_6 oxidation for this feed composition, there was an instantaneous increase in C_3H_6 effluent concentration upon introduction of NO in the feed. Even after NO was shut off the C_3H_6 effluent concentration did not return to the initial value in ca. 30 minutes. This indicated that surface oxygenates formed during the C_3H_6 oxidation, reacted with NO selectively to form stable intermediates (-NCO surface species) that poison the active sites for C_3H_6 oxidation. The isocyanate species that are formed block the active catalytic sites and thus inhibit other reactions. In order to verify the model capability to explain this experimentally observed transient behavior, simulations were performed at 300°C, 325°C and 350°C similar to the transient experiments with C_3H_6 , O_2 and NO. Figure 6-18 shows that the model predicts the transient behavior qualitatively quite well. We also plotted the predicted averaged oxygenate and isocyanate coverages with time at 325°C (Figure 6-19). It shows that upon introduction of NO in the feed there is a decrease in the oxygenate coverage and increase in the R-NCO coverage. This clearly shows that NO reacts with the surface oxygenate to form R-NCO surface species leading to decrease in

the oxygenate coverage. The R-NCO surface species poison the active sites and thus inhibit C_3H_6 oxidation resulting in the increase in C_3H_6 effluent concentration.

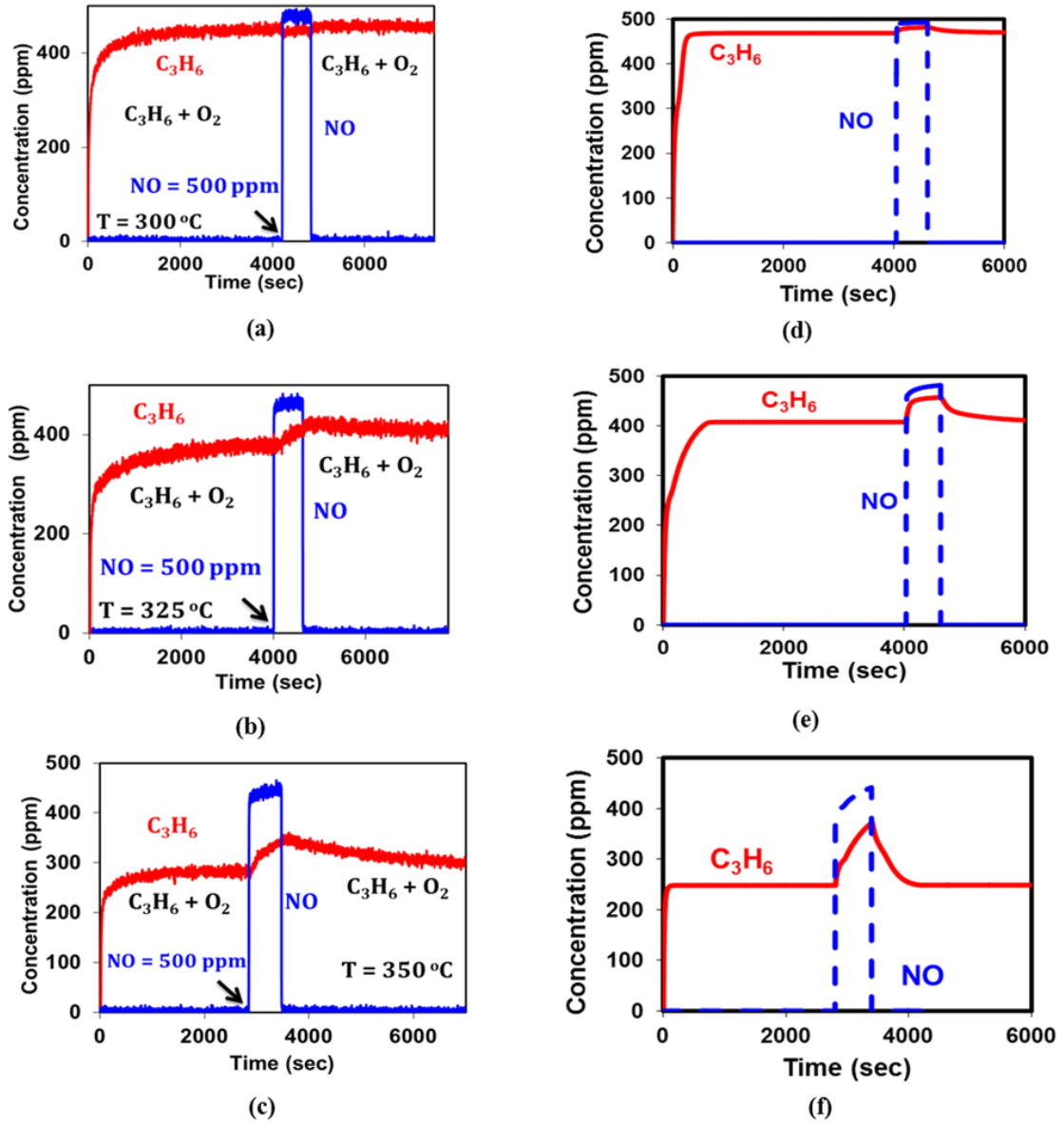


Figure 6-18. (a) C_3H_6 and NO outlet concentration with time at (b) 300 °C, (b) 325 °C, (c) 350 °C (Experiment) (d) 300 °C, (e) 325 °C, (f) 350 °C ($C_3H_6 = 500$ ppm, NO = 0 or 500 ppm, $O_2 = 5\%$, Balance gas: Ar, Model predictions)

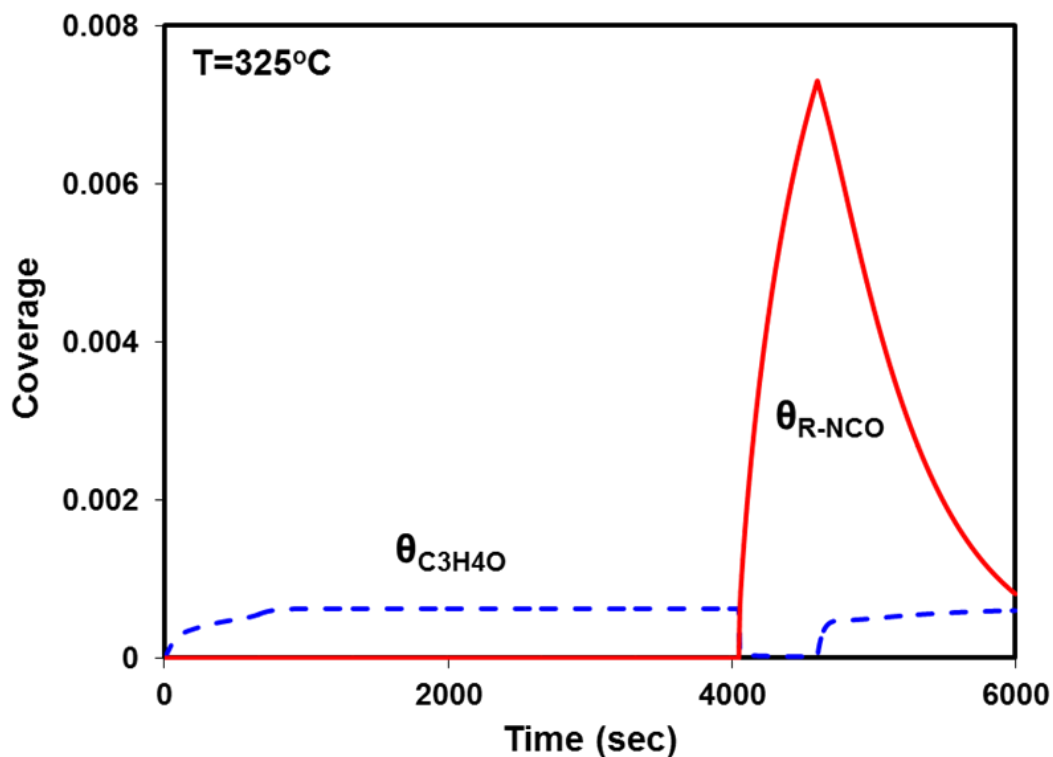


Figure 6-19. Predicted averaged oxygenate and isocyanate species coverage on Cu sites with time ($C_3H_6 = 500$ ppm, $NO = 0$ or 500 ppm $O_2 = 5\%$, Balance gas: Ar)

The poisoning of the active catalytic sites by R-NCO surface species can be better explained by analyzing steady state intrawashcoat R-NCO coverage with temperature for $C_3H_6+NO+O_2$ reaction system. Figure 6-20 shows the steady state coverage of R-NCO species within the washcoat for feed composition with 500 ppm C_3H_6 , 500 ppm NO and 5% O_2 . These predictions show that in the 325°C to 350°C temperature range most of the sites are covered with the R-NCO species. The isocyanate species act as poison and inhibit other reactions. Due to this both C_3H_6 and NO conversion is low below 350°C. The corresponding NO conversion plot (refer to Figure 6-6) has a sigmoidal shape in which the NO conversion increases sharply in the 350°C to 375°C temperature range

which is also consistent to the sharp decrease in R-NCO coverage in the same temperature range. Beyond that range the NO conversion increases more gradually because of the competing oxidation of C_3H_6 at higher temperatures (above $375^\circ C$). Hence, once the R-NCO species start reacting with O_2 to form N_2 , CO, CO_2 and H_2O , the sites become available for other side reactions also (CO oxidation and C_3H_6 oxidation). Finally, a parametric sensitivity analysis of CO oxidation, C_3H_6 oxidation and $C_3H_6+NO+O_2$ reaction system was performed. These calculations indicated that the rate determining step of the CO oxidation is the surface oxidation step R3. The CO oxidation rate is also sensitive to step R4 that involves re-oxidation of Cu(I) to Cu(II) as on changing the rate constant by factor of 0.1 there is a notable decrease in the CO conversion in wide temperature range. For the C_3H_6 oxidation a parametric sensitivity study suggested that R7 to R9 are the most important steps. Similar to the CO oxidation, the C_3H_6 oxidation rate is also sensitive to step R4, as on changing the rate constant by factor of 0.01 there is a significant decrease in the C_3H_6 conversion. For the $C_3H_6+NO+O_2$ reaction system steps R7 to R9, R14 and R15 are the most important steps. The rate of the NO selective reduction is also sensitive to step R4 as decreasing the rate constant by factor of 0.01 resulted in a decrease in the C_3H_6 conversion above $350^\circ C$ but an increase in the NO conversion occurred in the same temperature range. Thus, we can conclude that the fraction of Cu(I) to Cu(II) species plays a potentially important role in the kinetics of NO selective reduction with C_3H_6 .

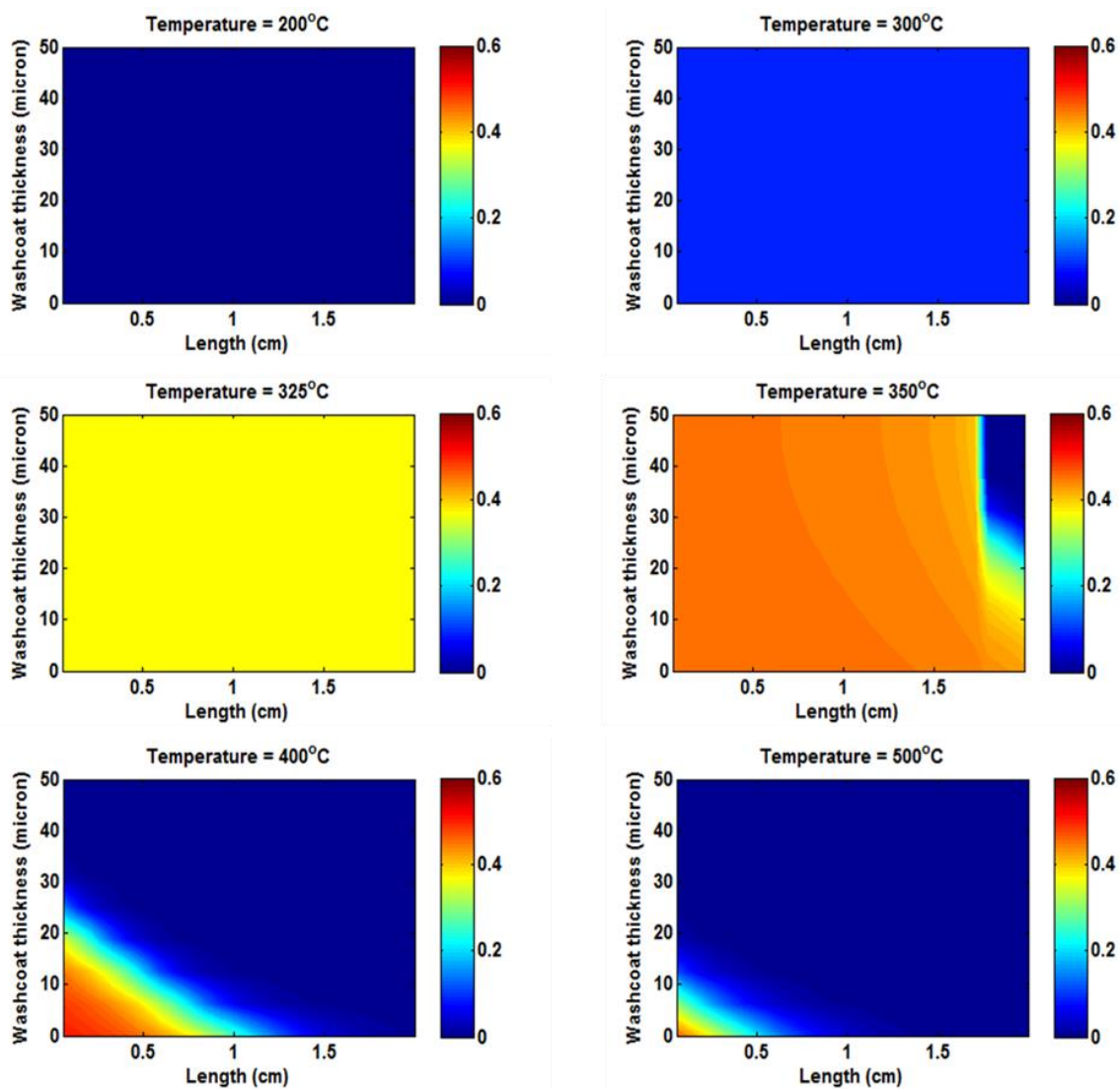


Figure 6-20. Predicted coverage of $-NCO$ species within the wash-coat ($C_3H_6 = 500$ ppm, $NO = 500$ ppm $O_2 = 5\%$, Balance gas: Ar)

6.4 Conclusions

We developed a predictive kinetic model for lean NO selective catalytic reduction with C_3H_6 on Cu-SSZ13 monolithic catalyst based on bench scale flow reactor studies and *in-situ* DRIFTS measurements [133]. The reaction mechanism involves reaction between oxygenates (partially oxidized hydrocarbon species) and NO to form isocyanates species ($-NCO$), detected by DRIFTS which are further reduced to N_2 . The reaction

scheme is incorporated into a (1+1) D monolith reactor model and kinetic parameters are estimated using steady state data obtained from bench scale flow reactor studies [133].

The developed monolith model captures the experimental trends for CO oxidation ($\text{CO} + \text{O}_2$), C_3H_6 oxidation ($\text{C}_3\text{H}_6 + \text{O}_2$) and NO reduction with C_3H_6 ($\text{NO} + \text{C}_3\text{H}_6 + \text{O}_2$) quite well. The predicted reactions orders for both CO and C_3H_6 oxidation are in good agreement with experimental data. The C_3H_6 oxidation model predicts the light off curves for C_3H_6 for different feed composition quite well. For the $\text{C}_3\text{H}_6 + \text{NO} + \text{O}_2$ reaction system, the model predicts the C_3H_6 and NO conversions over wide temperature range and for different feed composition quite well. The model captures the experimentally observed increase in C_3H_6 light-off temperature in presence of NO in the feed as surface oxygenates formed during the C_3H_6 oxidation, reacted with NO selectively to form stable intermediates (-NCO surface species) that poison the active sites for C_3H_6 oxidation. The model also predicts the transient behavior for $\text{C}_3\text{H}_6 + \text{O}_2$ and $\text{C}_3\text{H}_6 + \text{NO} + \text{O}_2$ qualitatively quite well.

In view of the combined LNT-SCR approach for NO_x conversion our model provides insight about non- NH_3 pathways (hydrocarbons, oxygenates, isocyanates etc.) for NO_x reduction across the SCR [68, 69]. It was shown by Xu et al. [69] that NO_x conversion is enhanced at the highest temperatures (above 375°C) by the SCR catalyst despite little breakthrough of NH_3 from the LNT. This can be explained by our simulation results that lean NO reduction with C_3H_6 is significant above 350°C . Similarly, Crocker et al. [145] showed experimentally that C_3H_6 and other C_3H_6 -derived hydrocarbon species inhibited reactions between NO and NH_3 present as a surface intermediate generated *in-situ* from C_3H_6 -NO reactions. Our model is also consistent

with this finding that surface intermediates formed during NO reduction with C₃H₆ (R-NCO) poison the catalyst surface and inhibit other reactions. Hence, the model provides useful insight in the role of hydrocarbon species for NO_x reduction over wide temperature range and for different feed compositions.

CHAPTER 7 Steady-state and Dynamic Hysteresis Effects During Co-oxidation of CO and C₃H₆ over Pt/Al₂O₃ Diesel Oxidation Monolithic Catalyst

7.1 Introduction

Carbon dioxide (CO) and Hydrocarbons (HCs) are the major pollutants from lean burn vehicle engines. For diesel engines, diesel oxidation catalysts (DOCs) are used to convert CO and HCs to CO₂ and H₂O. Recent advances in low temperature combustion (LTC) diesel engines lead to higher net efficiencies and lower NO_x and particulate matter (PM) emissions as compared to current diesel engine technologies. However, the LTC engine has lower exhaust temperature that results in higher levels of CO and hydrocarbons (HCs) than that of today's engine. Hence it is important to study the light-off behavior of exhaust gases at lower temperature and high level of CO and HCs.

The oxidation of CO on Pt has been studied extensively [16, 146-154]. CO oxidation is known to occur through a Langmuir-Hinshelwood mechanism, in which the reaction between the adsorbed CO and O₂ is the rate limiting step. A similar approach is used for C₃H₆ oxidation on Pt [152, 153]. Voltz et al., [152, 153, 155-156] found that both CO and C₃H₆ are self-inhibiting. Furthermore, in a CO+C₃H₆ mixture, CO inhibits C₃H₆ oxidation and vice-versa due to competitive adsorption over active catalytic sites [152, 153, 155-156]. It is well known in the literature that multiple steady states leading to ignition, extinction and hysteresis exist for exothermic reactions, such as CO and C₃H₆ oxidation on Pt/Al₂O₃. The possible reasons for steady state multiplicity are: (1) high adiabatic temperature rise due to heat generated from exothermic reaction (2) non-

monotonic (or negative order) kinetics (3) low heat Peclet number leading to thermal feedback [147-151, 157, 158].

In this study, we first developed a global kinetic model for co-oxidation of CO and C₃H₆ on Pt/Al₂O₃ monolithic catalyst by using data published by Abedi et al., [155]. The global kinetic model is developed in steps, starting with CO oxidation, followed by C₃H₆ oxidation and then the CO+C₃H₆ reaction system. The global kinetic model developed is used to study the hysteresis behavior that occurs during temperature ramp-up and ramp-down experiments at a constant rate with a CO and C₃H₆ mixture [154-156, 159, 160]. This work also focused on steady state hysteresis and in particular the effect of inlet feed composition and heat Peclet number on the region of multiplicity.

7.2 Model Development

7.2.1. Reactor model

A low-dimensional model of a catalytic monolith channel with washcoat diffusion is used in this study [114]. The model is developed by averaging the convection-diffusion-reaction (CDR) equations in the transverse (radial) direction (in fluid and washcoat phase), and using the concept of external and internal mass transfer coefficients [114, 117]. It has been shown that the low dimensional model gives comparable results when compared to the detailed solution [114]. The details of the model development and applications are provided in a series of papers by Joshi et al., [111, 112, 117, 124]. The model consists of species and energy balances in the fluid and washcoat phase. The heat and mass transfers in the transverse direction between the bulk of fluid and washcoat are accounted for by the use of overall heat and mass transfer coefficients. The key assumptions in the model are: (i) laminar flow in the monolith channel, (channel

Reynolds number ($4\langle u \rangle R_{\Omega_1} / \nu$) ~ 12 to 36) (ii) axial diffusion in the fluid phase is neglected as compared to convection (high axial Peclet number, $\langle u \rangle L / D_m = 175$ to 1766) (iii) the reaction mixture is dilute so average values for physical properties may be used.

The species balances in the gas phase consist of accumulation, convection and external mass transfer from bulk fluid to washcoat:

$$\frac{\partial C_{fm,j}}{\partial t} + \langle u \rangle \frac{\partial C_{fm,j}}{\partial z} = -\frac{1}{R_{\Omega_1}} k_{mo,j} (C_{fm,j} - \langle C_{wc} \rangle_j), \quad (2-1)$$

where, $C_{fm,j}$ and $\langle C_{wc} \rangle_j$ represent the cup-mixing mole concentration of species j in the fluid phase and volume averaged concentration of species j in the washcoat, respectively.

$\langle u \rangle$ is the average fluid velocity, R_{Ω_1} is the hydraulic radius defined as the ratio of channel area (open to flow) to channel perimeter, and $k_{mo,j}$ is the overall mass transfer coefficient of species j given by

$$\frac{1}{k_{mo,j}} = \frac{1}{k_{mi,j}} + \frac{1}{k_{me,j}}, \quad (2-2)$$

where, $k_{mi,j}$ and $k_{me,j}$ are the internal and external mass transfer coefficients, respectively.

The mass transfer coefficients are computed using the following relations:

$$k_{me,j}(z) = \frac{Sh_e D_{f,j}}{4R_{\Omega_1}} \text{ and} \quad (2-3)$$

$$k_{mi,j} = \frac{Sh_{i,\infty} D_{e,j}}{R_{\Omega_2}}, \quad (2-4)$$

where, $D_{f,j}$ and $D_{e,j}$ are the fluid phase diffusivity and effective washcoat diffusivity of species j , respectively. R_{Ω_2} is the effective transverse diffusion length in the washcoat

defined as the ratio of washcoat cross-sectional area to the interfacial perimeter. Sh_e is the external Sherwood number obtained by using the correlation given by Ramanathan et al., [115]. Likewise, Sh_i is the internal Sherwood number, the details of which are provided in the work by Joshi et al., [111, 112, 114].

Similarly, the species balances for component j in the washcoat are given as

$$\varepsilon_{wc} R_{\Omega_2} \frac{\partial \langle C_{wc} \rangle_j}{\partial t} = k_{mo,j} (C_{fm,j} - \langle C_{wc} \rangle_j) + R_{\Omega_2} \sum_{i=1}^N \varrho_{ij} R_i (\langle C_{wc} \rangle_1, \langle C_{wc} \rangle_2, \dots, \langle C_{wc} \rangle_s, T_s), \quad (2-5)$$

where, ε_{wc} , ϱ_{ij} and R_i represent the washcoat porosity, stoichiometric coefficients of species j in reaction i and volumetric reaction rate (per unit washcoat volume) of reaction i , respectively. T_s is the solid temperature.

Likewise, the enthalpy balances in fluid and solid phase are given below:

$$\rho_f c_{pf} \frac{\partial T_f}{\partial t} + \langle u \rangle \rho_f c_{pf} \frac{\partial T_f}{\partial z} = -\frac{1}{R_{\Omega_2}} h (T_f - T_s) \quad \text{and} \quad (2-6)$$

$$R_{\Omega_w} \rho_w c_{pw} \frac{\partial T_s}{\partial t} = R_{\Omega_w} k_w \frac{\partial^2 T_s}{\partial z^2} + h (T_f - T_s) + R_{\Omega_2} \sum_{j=1}^N R_j (\langle C_{wc} \rangle_1, \langle C_{wc} \rangle_2, \dots, \langle C_{wc} \rangle_s, T_s) (-\Delta H_j), \quad (2-7)$$

where, ρ_f , $c_{p,f}$, h_f , T_f and T_s are the density of gas, specific heat capacity of gas, heat transfer coefficient, gas phase temperature and solid (washcoat + support) temperature respectively. The effective solid phase (wall) heat capacity and thermal conductivity are computed as $R_{\Omega_w} \rho_w c_{p,w} = R_{\Omega_2} \rho_c c_{p,c} + R_{\Omega_s} \rho_s c_{p,s}$ and $R_{\Omega_w} k_w = R_{\Omega_2} k_c + R_{\Omega_s} k_s$ respectively.

The subscripts c and s refer to catalyst (washcoat) and support respectively

The initial, inlet and boundary conditions are given below:

$$\begin{aligned}
C_{fm,j}(z,t=0) &= C_{fm,j0}(z) \\
\langle C_{wc} \rangle_j(z,t=0) &= \langle C_{wc} \rangle_{j0}(z), \\
C_{fm,j}(z=0,t) &= C_{j,in}(t)
\end{aligned}
\tag{2-8}$$

$$\begin{aligned}
T_f(z=0,t) &= T_{fin}(t) \\
T_f(z,t=0) &= T_{f0}(z) \\
T_s(z,t=0) &= T_{s0}(z), \\
\frac{\partial T_s}{\partial z}(z=0,L,t) &= 0.
\end{aligned}
\tag{2-9}$$

$C_{fm,j0}(z)$, $\langle C_{wc} \rangle_{j0}(z)$, $T_{f0}(z)$, and $T_{s0}(z)$ are initial fluid phase concentration of species j , initial washcoat concentration of species j , and initial fluid and solid temperatures, respectively. $T_{fin}(t)$ is the inlet fluid temperature. The values of parameters used in the simulation are provided in Tables 7.1 and 7.2.

Table 7.1 Constant parameters used in the simulation

Parameter	Value
$R_{\Omega 1}$	262.5 μm
$R_{\Omega 2}$	25 μm
L	2cm or 6.35cm
Sh_e	4.34
$Sh_{i,\infty}$	3.0
Nu	4.34
ϵ_{wc}	0.4
λ	25
$R_{\Omega w}$	107.55 μm

Table 7.1 (Continued)

ρ_f	0.7 kg/m ³
C_{pf}	1068 J/kg/K
$\langle C_p \rangle$	30 J/mol/K
k_f	0.0386 W/m/K
ρ_w	2000 kg/m ³
C_{pw}	1000 J/kg/K
k_w	2 W/m/K
R_g	8.314 J/mol/K
Pe_h	51 or 5
P	0.03
ΔH°_{CO}	-283.0 kJ/mol
$\Delta H^\circ_{C_3H_6}$	-1925.9 kJ/mol

Table 7.2 Temperature dependent parameters used in the simulation

Parameter	Value / Expression
$\langle u \rangle$	$0.587 \times (T_f/273.15)$ m/s
D_{f,CO_2}	$0.825 \times 10^{-9} \times T_f^{1.7148}$ m ² /s
D_{f,O_2}	$1.13 \times 10^{-9} \times T_f^{1.7019}$ m ² /s
D_{f,C_3H_6}	$4.237 \times 10^{-10} \times T_f^{1.7844}$ m ² /s
D_{f,H_2O}	$1.62 \times 10^{-9} \times T_f^{1.7033}$ m ² /s
$D_{f,CO}$	$1.13 \times 10^{-9} \times T_f^{1.7148}$ m ² /s

7.2.2 Kinetic model and parameter estimation

In this section, we develop global kinetic model for the simultaneous oxidation of CO and C₃H₆ over Pt/Al₂O₃ monolithic catalyst. The global reactions occurring are:



The model kinetic parameters are estimated from transient bench-flow reactor studies carried out in study done by Abedi et al., [155]. The catalyst properties used in the model are summarized in Table 7.3. In order to estimate the kinetic parameters for the co-oxidation of CO and C₃H₆, we follow a step-wise approach. Kinetic parameters estimated from independent reaction systems (CO and C₃H₆ oxidations) are incorporated into the model for the CO + C₃H₆ + O₂ reaction system. Specifically, first a global kinetic model for CO oxidation (CO + O₂) is developed by fitting the model with data of CO TPO (Temperature programmed oxidation) [155]. Then a global kinetic model C₃H₆ oxidation reaction (C₃H₆ + O₂) by fitting C₃H₆ conversion data obtained from C₃H₆ TPO experiment [155]. Finally, we fixed the values of kinetic parameters obtained from independent CO and C₃H₆ oxidation global kinetic models and estimated the rest kinetic parameters by fitting the model with CO and C₃H₆ conversion data obtained from simultaneous CO and C₃H₆ transient light-off experiment [155]. In most cases, the Levenberg-Marquardt method was used to converge on the parameter estimates.

Table 7.3 Catalyst properties

Catalyst	Components	Pt loading (g/ft ³)
DOC	Pt/Al ₂ O ₃	95

7.2.2.1 Global kinetic model for CO oxidation

The rate of CO oxidation is based on a Langmuir-Hinshelwood type mechanism with the surface reaction between two adsorbed species being the rate determining step. The rate is expressed in mol/m³-washcoat/s. The rate expression for CO oxidation is defined

$$R_{CO} = \frac{k_1 Y_{CO} Y_{O_2}}{(1 + K_{CO} Y_{CO})^2}.$$

The rate expression is consistent with the experimentally observed reaction orders with respect to CO. For $K_{CO} \ll 1$ the rate is positive order (+1) with respect to CO whereas, for $K_{CO} \gg 1$ the rate is negative order (-1) with respect to CO. The rate constant and adsorption equilibrium constant are defined

$$k_1 = A_1 \exp\left(\frac{-E_1}{R_g T_s}\right) \text{ and}$$

$$K_{CO} = A_{CO} \exp\left(\frac{-\Delta H_{CO}}{R_g T_s}\right).$$

The kinetic parameters are estimated by fitting model with CO conversion data obtained from transient bench flow reactor experiment in which temperature was ramped at a rate of 3°C/min [155]. Figure 7.1 shows the fitted result. The model is able to capture the experimental light-off trend quite well. The fitted values of kinetic parameters $\frac{E_1}{R_g}$ and $\frac{-\Delta H_{CO}}{R_g}$ are 14421 K and 1166 K, respectively. The estimated values of $\frac{E_1}{R_g}$ and $\frac{-\Delta H_{CO}}{R_g}$ for CO oxidation by Voltz et al., [152] are 10825 K and 961 K, respectively. This difference may be attributed to the fact that Voltz et al., [152] performed the kinetic studies on a pelleted platinum–alumina catalyst, whereas our model is fitted with experiments performed on Pt/Al₂O₃ monolithic catalyst.

7.2.2.2 Global kinetic model for C₃H₆ oxidation

Similarly, the rate of C₃H₆ oxidation is also based on a Langmuir-Hinshelwood type mechanism with the surface reaction between two adsorbed species being the rate determining step. The rate is expressed in mol/m³-washcoat/s. The rate expression for C₃H₆ oxidation is defined as

$$R_{C_3H_6} = \frac{k_2 Y_{C_3H_6} Y_{O_2}}{(1 + K_{C_3H_6} Y_{C_3H_6})^2}.$$

It has been observed experimentally that C₃H₆ is also self-inhibiting [155]. Hence, the rate expression is consistent with the experimentally observed reaction orders with respect to C₃H₆. For $K_{C_3H_6} \ll 1$ the rate is positive order (+1) with respect to C₃H₆ whereas, for $K_{C_3H_6} \gg 1$ the rate is negative order (-1) with respect to C₃H₆. The rate constant and adsorption equilibrium constant are defined as

$$k_2 = A_2 \exp\left(\frac{-E_2}{R_g T_s}\right) \text{ and}$$

$$K_{C_3H_6} = A_{C_3H_6} \exp\left(\frac{-\Delta H_{C_3H_6}}{R_g T_s}\right).$$

The kinetic parameters are estimated by fitting model with data obtained from C₃H₆ TPO experiment in which temperature was ramped at a rate of 3°C/min in presence of 10% O₂ [155]. Figure 7. 2 shows the fitted result. The model fits well with the experimental data. The fitted values of kinetic parameters $\frac{E_2}{R_g}$ and $\frac{-\Delta H_{C_3H_6}}{R_g}$ are 11306 K and 117 K, respectively. The estimated values of $\frac{E_1}{R_g}$ and $\frac{-\Delta H_{C_3H_6}}{R_g}$ for C₃H₆ oxidation by Voltz et al. [152] are 11427 K and 361 K, respectively.

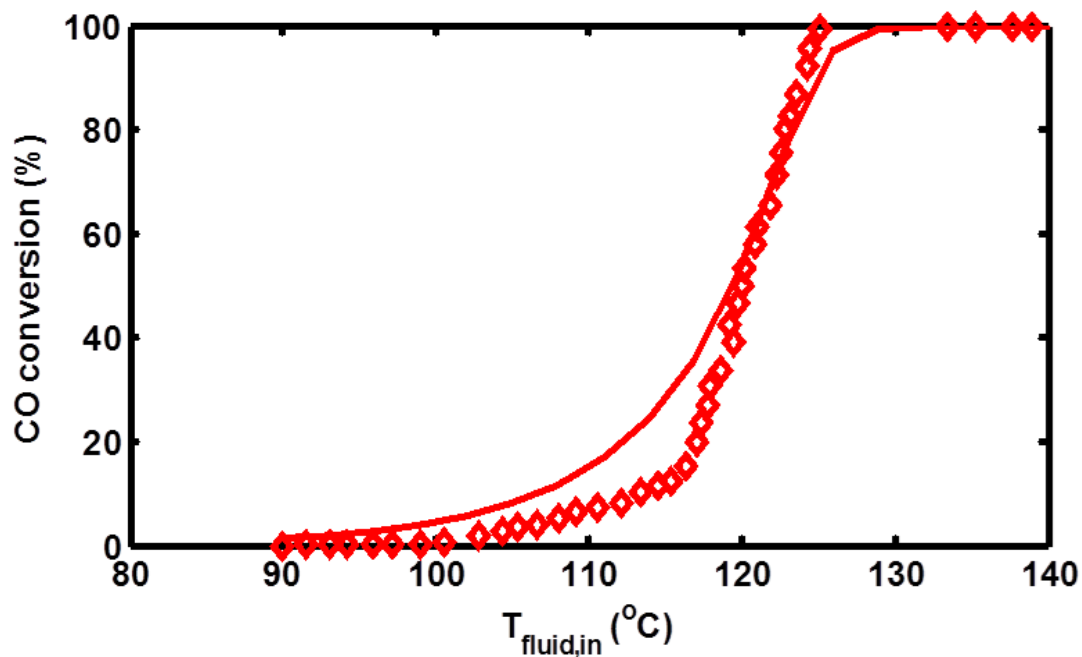


Figure 7-1. Fitted light-off curve of CO (Abedi et al. [155], CO = 1000 ppm, 10% O₂, 10% H₂O, 10% CO₂; Space velocity of 25,000 h⁻¹ at STP; Temperature ramp = 3°C/min)

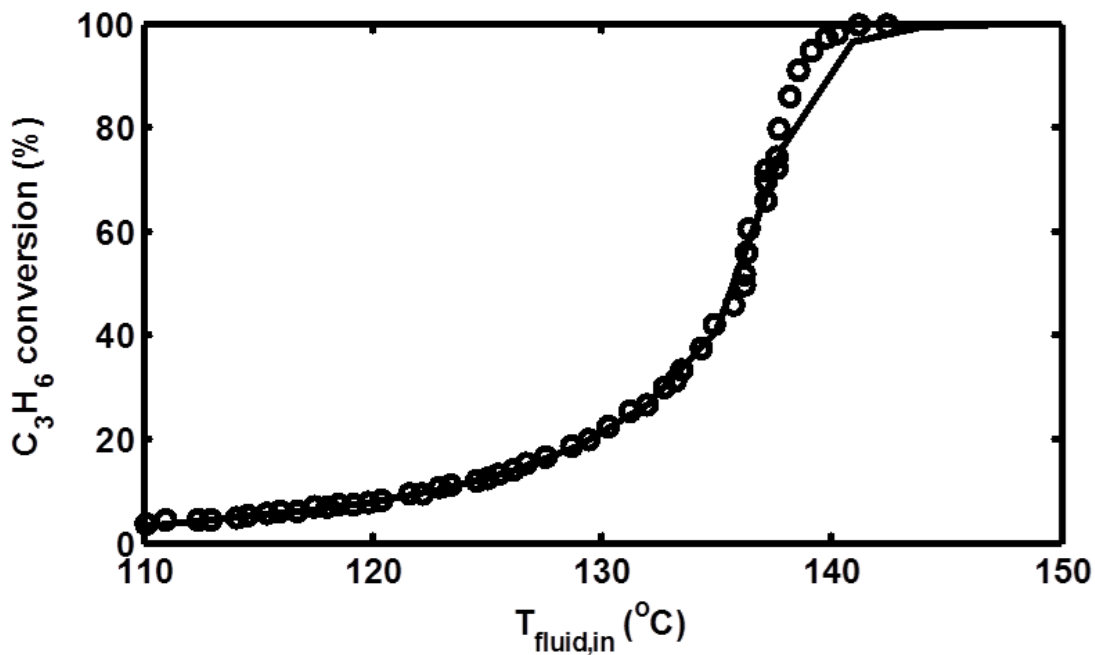


Figure 7-2. Fitted light-off curve of C₃H₆ (Abedi et al. [155], C₃H₆ = 800 ppm, 10% O₂, 10% H₂O, 10% CO₂; Space velocity of 25,000 h⁻¹ at STP; Temperature ramp = 3°C/min)

7.2.2.3 Global kinetic model for CO + C₃H₆ oxidation

It has been shown experimentally [155] that C₃H₆ inhibits CO oxidation and CO inhibits C₃H₆ oxidation. In order to account this inhibition effect the rate expressions for both CO and C₃H₆ oxidation are modified by adding extra inhibition term in the denominator. The modified rate expressions are as follow:

$$R'_{CO} = \frac{k_1 Y_{CO} Y_{O_2}}{(1 + K_{CO} Y_{CO} + K_{IC_3H_6} Y_{C_3H_6})^2} \text{ and}$$

$$R'_{C_3H_6} = \frac{k_2 Y_{C_3H_6} Y_{O_2}}{(1 + K_{C_3H_6} Y_{C_3H_6} + K_{ICO} Y_{CO})^2}.$$

To account for the inhibition on the rate of CO oxidation by C₃H₆ the term $K_{IC_3H_6} Y_{C_3H_6}$ is added to the denominator $(1 + K_{CO} Y_{CO})$ of CO oxidation rate. Similarly, to account for the inhibition of CO on C₃H₆ oxidation the term $K_{ICO} Y_{CO}$ is added to the denominator $(1 + K_{C_3H_6} Y_{C_3H_6})$ of C₃H₆ oxidation rate. The kinetic parameters are given by

$$K_{ICO} = A_{ICO} \exp\left(\frac{-\Delta H_{ICO}}{R_g T_s}\right) \text{ and}$$

$$K_{IC_3H_6} = A_{IC_3H_6} \exp\left(\frac{-\Delta H_{IC_3H_6}}{R_g T_s}\right).$$

The kinetic parameters $K_{IC_3H_6}$ and K_{ICO} are estimated by fitting the TPO data obtained with CO and C₃H₆ mixture [155]. Figure 7-3a and 7-3b show the fitted results. The calibrated model predicts the data very well.

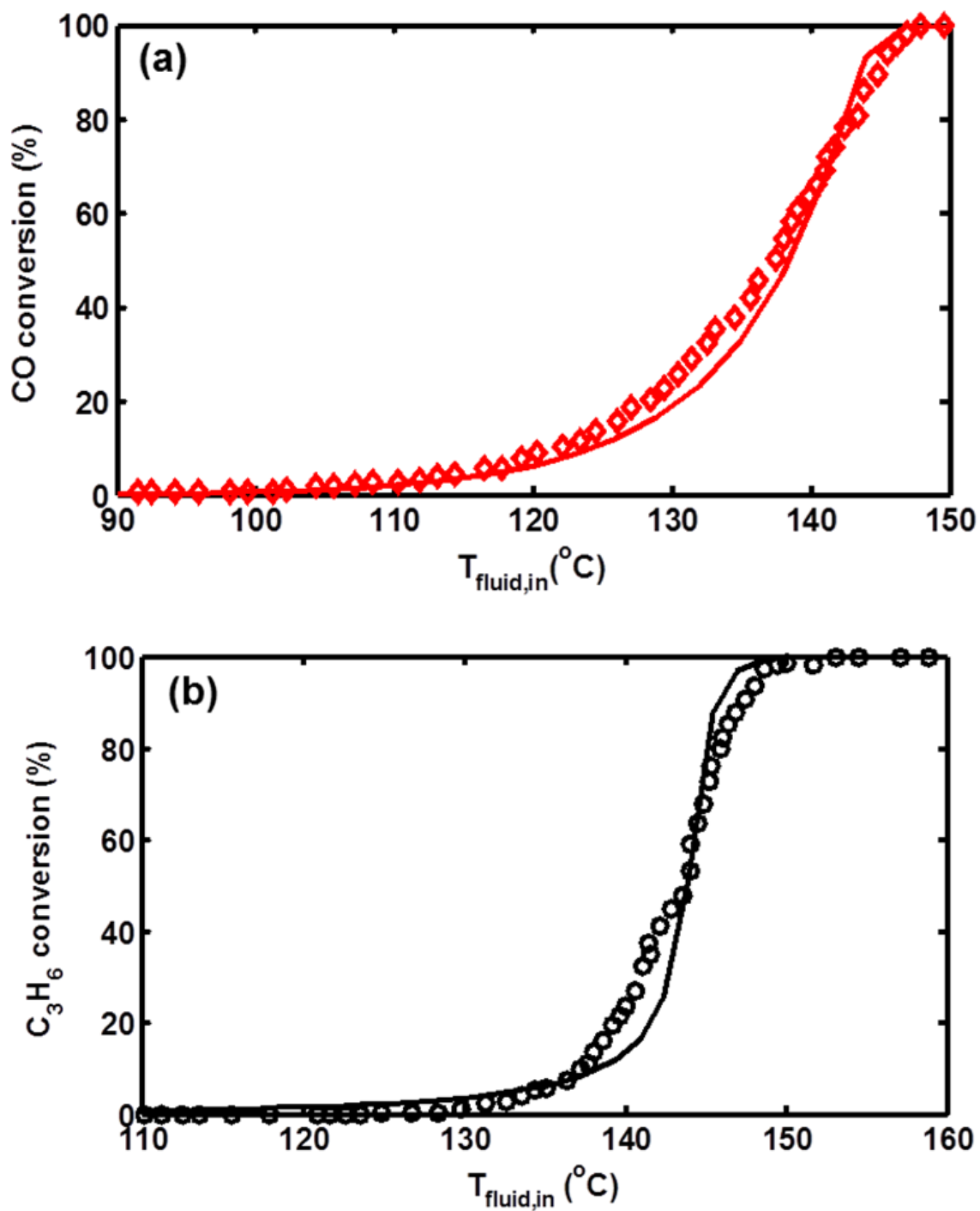


Figure 7-3. (a) Fitted light-off curve of CO (b) Fitted light-off curve of C_3H_6 (CO = 1000 ppm, C_3H_6 = 800 ppm, 10% O_2 , 10% H_2O , 10% CO_2 ; Space velocity of $25,000 \text{ h}^{-1}$ at STP; Temperature ramp = $3^{\circ}\text{C}/\text{min}$) [155]

In order to validate the kinetic model, we compared the CO conversion and C₃H₆ conversion obtained from additional TPO data set and model predictions without any further adjustment in the parameters. Figures 7-4a and 7-4b show that the model predicts well the CO and C₃H₆ light-off. Figure 7-5a shows the comparison between R_{CO} (CO = 1000 ppm, O₂ = 10%) and R'_{CO} (CO = 1000 ppm, C₃H₆ = 500 ppm, O₂ = 10%). R'_{CO} is almost 1/4th of R_{CO} showing strong C₃H₆ inhibition on CO oxidation. Similarly, Figure 7-5b shows the comparison between R_{C₃H₆} (C₃H₆ = 1000 ppm, O₂ = 10%) and R'_{C₃H₆} (C₃H₆ = 1000 ppm, CO = 500 ppm, O₂ = 10%). R'_{C₃H₆} is almost half of R_{C₃H₆}. The kinetic parameters are listed in Table 7-4.

Table 7-4. Kinetic parameters used in the simulation

Parameters	Value (moles/ m ³ /s)/(-)	Parameters	Values (K)
A ₁	1.28×10 ²¹	$\frac{E_1}{R_g}$	14421.46
A _{CO}	88.59	$\frac{-\Delta H_{CO}}{R_g}$	1161.88
A ₂	1.36×10 ¹⁷	$\frac{E_2}{R_g}$	11306.24
A _{C₃H₆}	2508.28	$\frac{-\Delta H_{C_3H_6}}{R_g}$	117.0
A _{ICO}	2090.13	$\frac{-\Delta H_{ICO}}{R_g}$	300.0
A _{IC₃H₆}	323.06	$\frac{-\Delta H_{IC_3H_6}}{R_g}$	1100.0

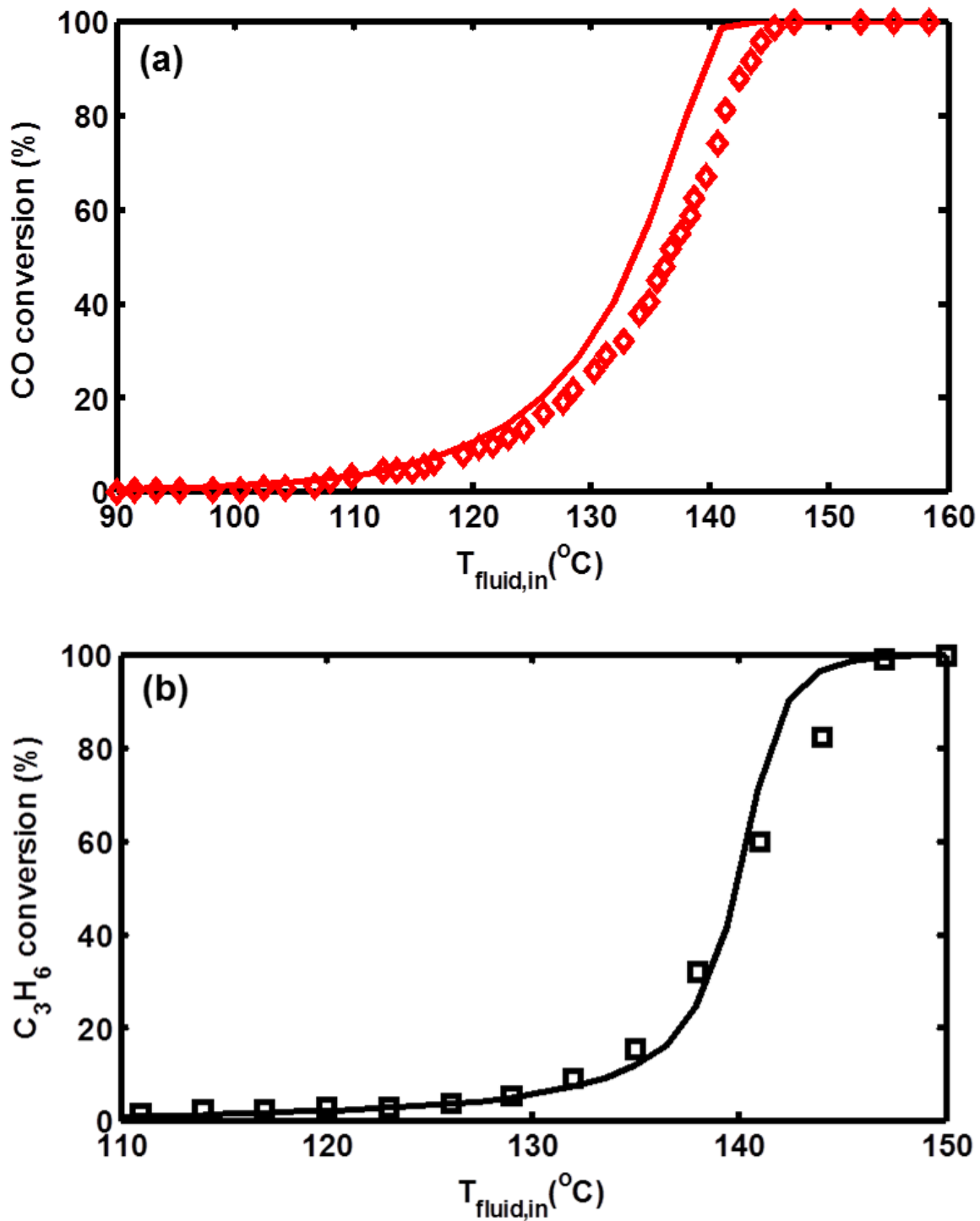


Figure 7-4. (a) Comparison between measured and predicted CO conversion (b) Comparison between measured and predicted C_3H_6 conversion (CO = 1000 ppm, C_3H_6 = 500 ppm, 10% O_2 ; Temperature ramp = $3^{\circ}\text{C}/\text{min}$ [155])

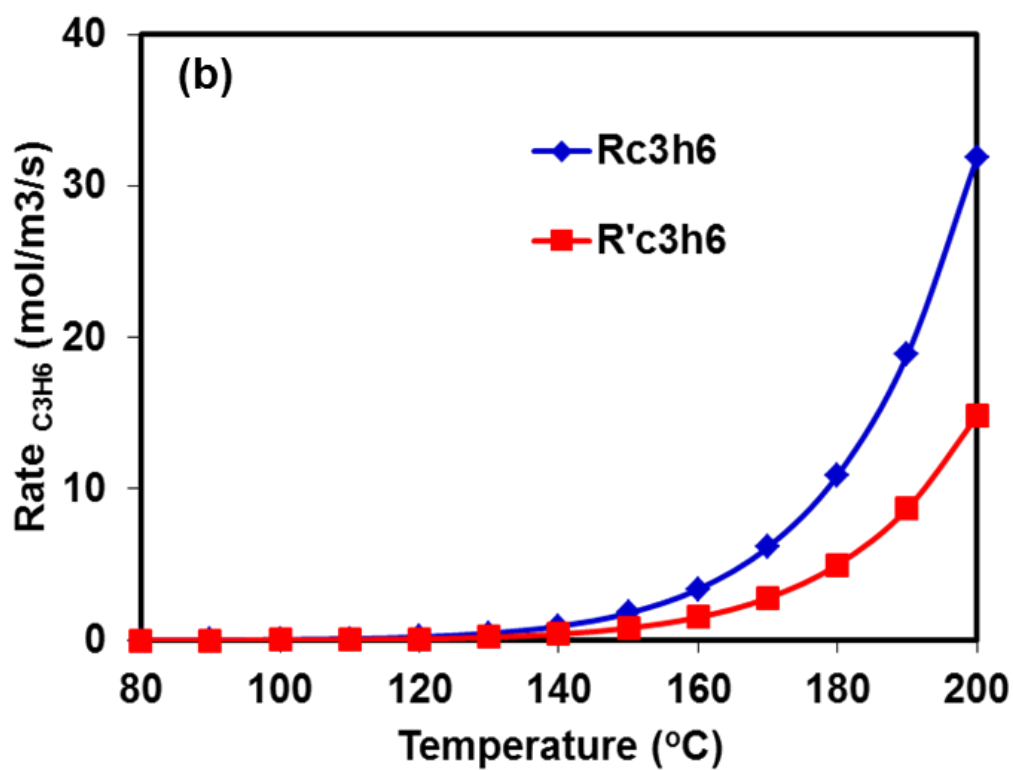
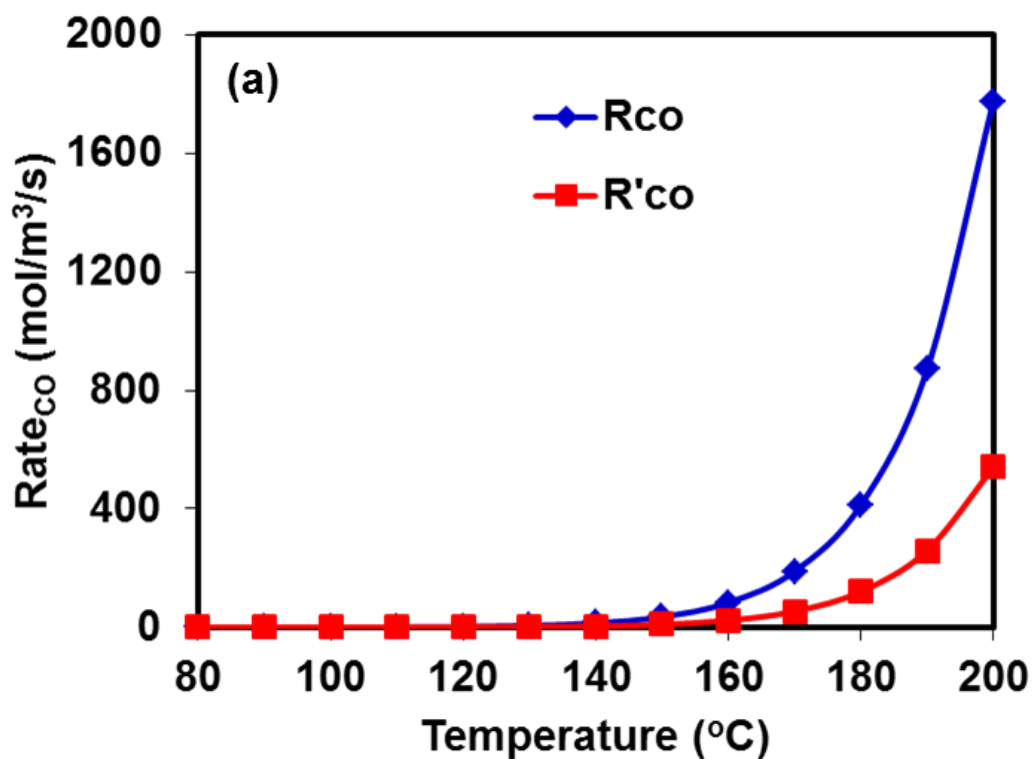


Figure 7-5. (a) Comparison between predicted CO oxidation rates in absence and in presence of C₃H₆ in the feed, (b) Comparison between predicted C₃H₆ oxidation rates in absence and in presence of CO in the feed

7.3. Results and Discussion

7.3.1. Dynamic hysteresis

CO and C₃H₆ co-oxidation studies show hysteresis behavior when the temperature is ramped up and down at a constant rate. In order to understand this dynamic hysteresis behavior we simulated oxidation of CO and C₃H₆ mixture at different ramp rates. For the simulation low CO and C₃H₆ inlet mole fractions are taken such that adiabatic temperature rise is very low (<25°C). The adiabatic temperature rise for co-oxidation of 500 ppm CO and 300 ppm C₃H₆ is 24°C. In order to confirm that for 500 ppm CO, 300 ppm C₃H₆ and 10% O₂ there is no steady state multiplicity, simulation was carried out in which the inlet fluid temperature is first increased from 80°C to 190°C in steps of 5°C and after that temperature was decreased from 190°C to 80 °C in steps of 5°C. Figures 7-6a and 7-6b show the steady state CO and C₃H₆ conversions as a function of the inlet fluid temperature. The exit CO and C₃H₆ conversions follow the same path during temperature ramp-up and ramp-down. Hence, this CO+C₃H₆ mixture does not exhibit steady state hysteresis.

Simulations were performed for same CO (500 ppm) and C₃H₆ (300 ppm) inlet concentrations in which the inlet fluid temperature was increased and decreased at different constant ramp rates. Figures 7-7a and 7-7b shows the CO and C₃H₆ exit conversions with the inlet fluid temperature when the temperature is increased from 80°C to 190°C at a rate of 3°C/min and then decreased from 190 °C to 80 °C at same rate. These plots show small hysteresis loop. Similarly, Figures 8a and 8b shows the CO and C₃H₆ exit conversions with the inlet fluid temperature when the temperature is increased from 80 °C to 190 °C at a rate of 10 °C/min and then decreased from 190 °C to 80 °C at

same rate. These plots show that the width of the hysteresis loop is larger with the higher ramp rate. The inlet gas temperatures corresponding to 50% CO and C₃H₆ conversion, T₅₀, during ramp-up and ramp-down at different ramp-rates are listed in Tables 7-5 and 7-6, respectively. These data show that the temperature difference (ΔT) at 50% conversion between ramp-up and ramp-down increased with higher ramp-rate. Hence, during ramp-down higher CO and C₃H₆ conversions are obtained at lower inlet fluid temperature as compared to ramp-up. A possible reason is that the catalyst temperature change lags behind the inlet temperature change during the ramp-down. Hence, a critical ramp rate exists beyond which the hysteresis appears or disappears. For this case, the critical ramp rate is 0.5 °C/min as hysteresis practically disappears at this ramp rate (Tables 7-5 and 7-6). Figures 7-9a and 7-9b show the fluid and solid temperature spatial profiles during ramp down at a rate of 10°C/min. The back of the monolith is ignited even at lower inlet fluid temperature. At inlet fluid temperature of 120°C, 1/4th of the monolith back is still at 140°C. Thus, the part of the monolith length with higher temperature will lead to higher CO and C₃H₆ conversion. In order to confirm further that this hysteresis is only due to transport delays and not due to heat generation, we performed temperature ramp-up and ramp-down simulation at a constant rate of 10°C/min but with the heat of reaction term set to zero. Figures 7-10a and 7-10b show the CO and C₃H₆ conversion with inlet fluid temperatures. The hysteresis observed further confirms that hysteresis obtained during temperature ramp-up and ramp-down experiment is only due to transport delay between inlet to the back of the monolith.

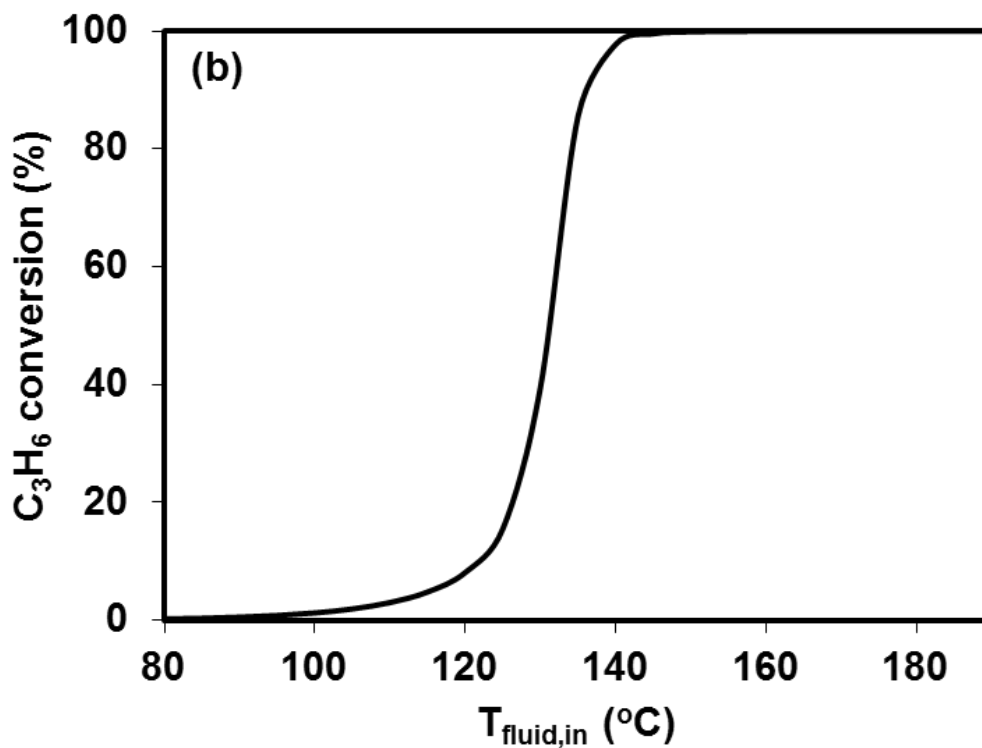
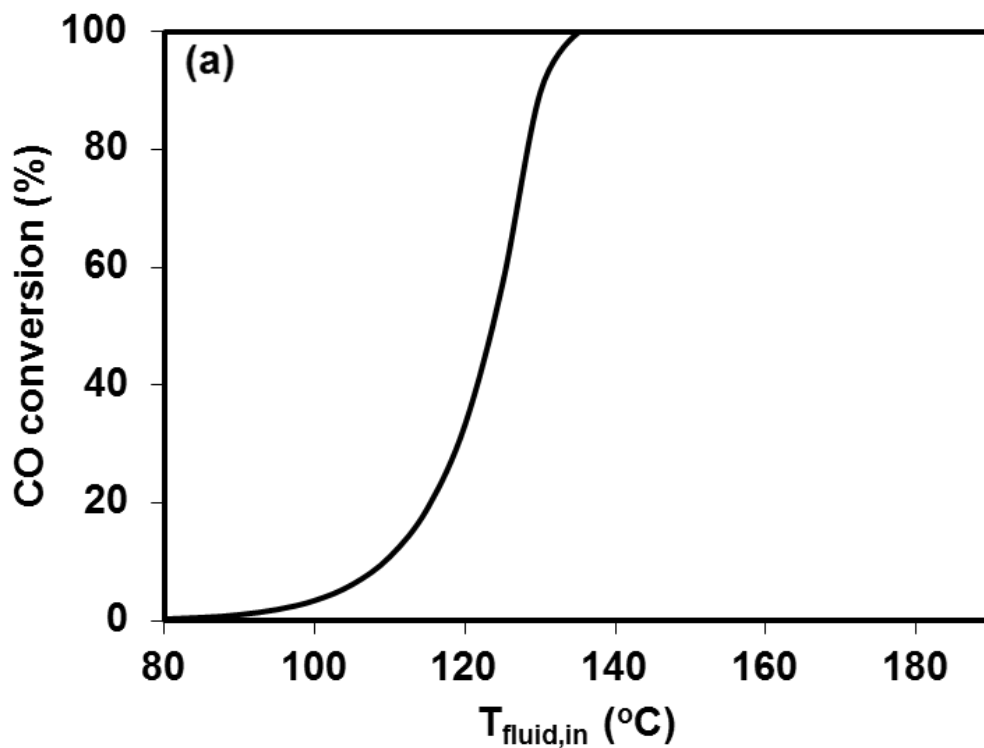


Figure 7-6. (a) Predicted steady state CO conversion versus inlet fluid temperature (b) Predicted steady state C_3H_6 conversion versus inlet fluid temperature (CO = 500 ppm, C_3H_6 = 300 ppm, 10% O_2 ; Space velocity of $25,000 \text{ h}^{-1}$ at STP)

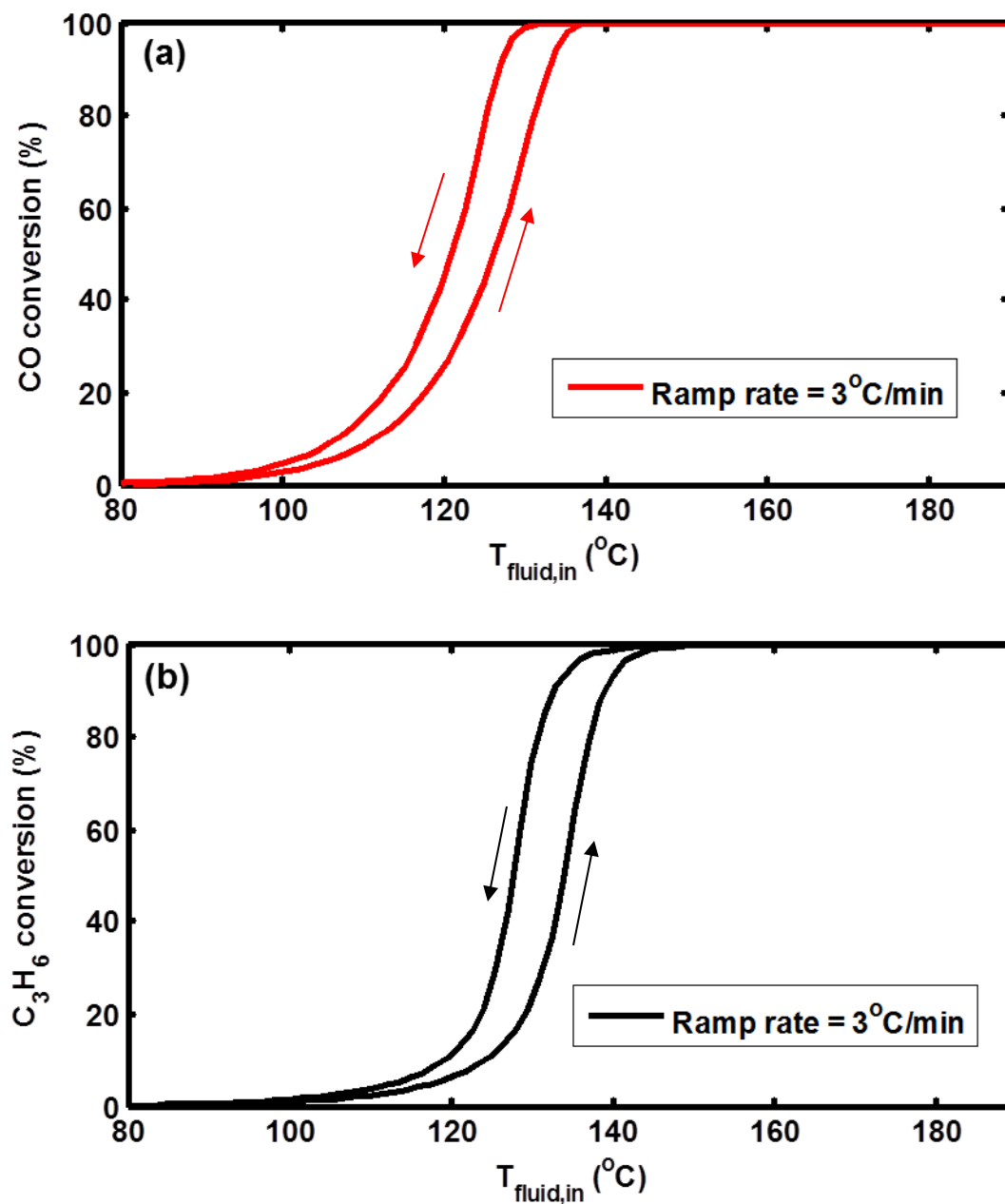


Figure 7-7. (a) Predicted CO conversion versus inlet fluid temperature (b) Predicted C_3H_6 conversion versus inlet fluid temperature (CO = 500 ppm, C_3H_6 = 300 ppm, 10% O_2 ; GHSV of $25,000 \text{ h}^{-1}$ at STP; Temperature ramp = $3^{\circ}\text{C}/\text{min}$)

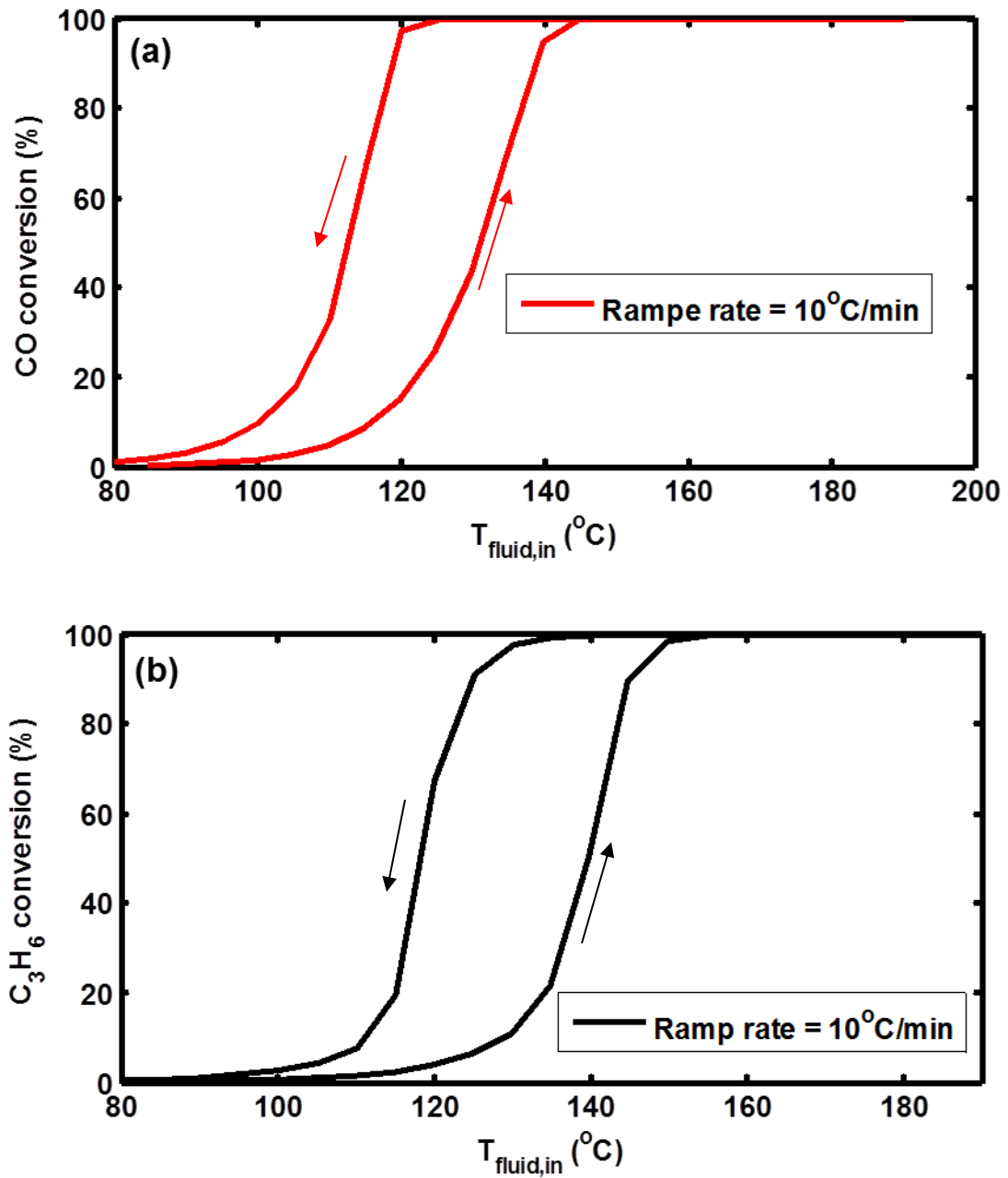


Figure 7-8. (a) Predicted CO conversion versus inlet fluid temperature (b) Predicted C_3H_6 conversion versus inlet fluid temperature (CO = 500 ppm, C_3H_6 = 300 ppm, 10% O_2 ; GHSV of $25,000 \text{ h}^{-1}$ at STP; Temperature ramp = $10^{\circ}\text{C}/\text{min}$)

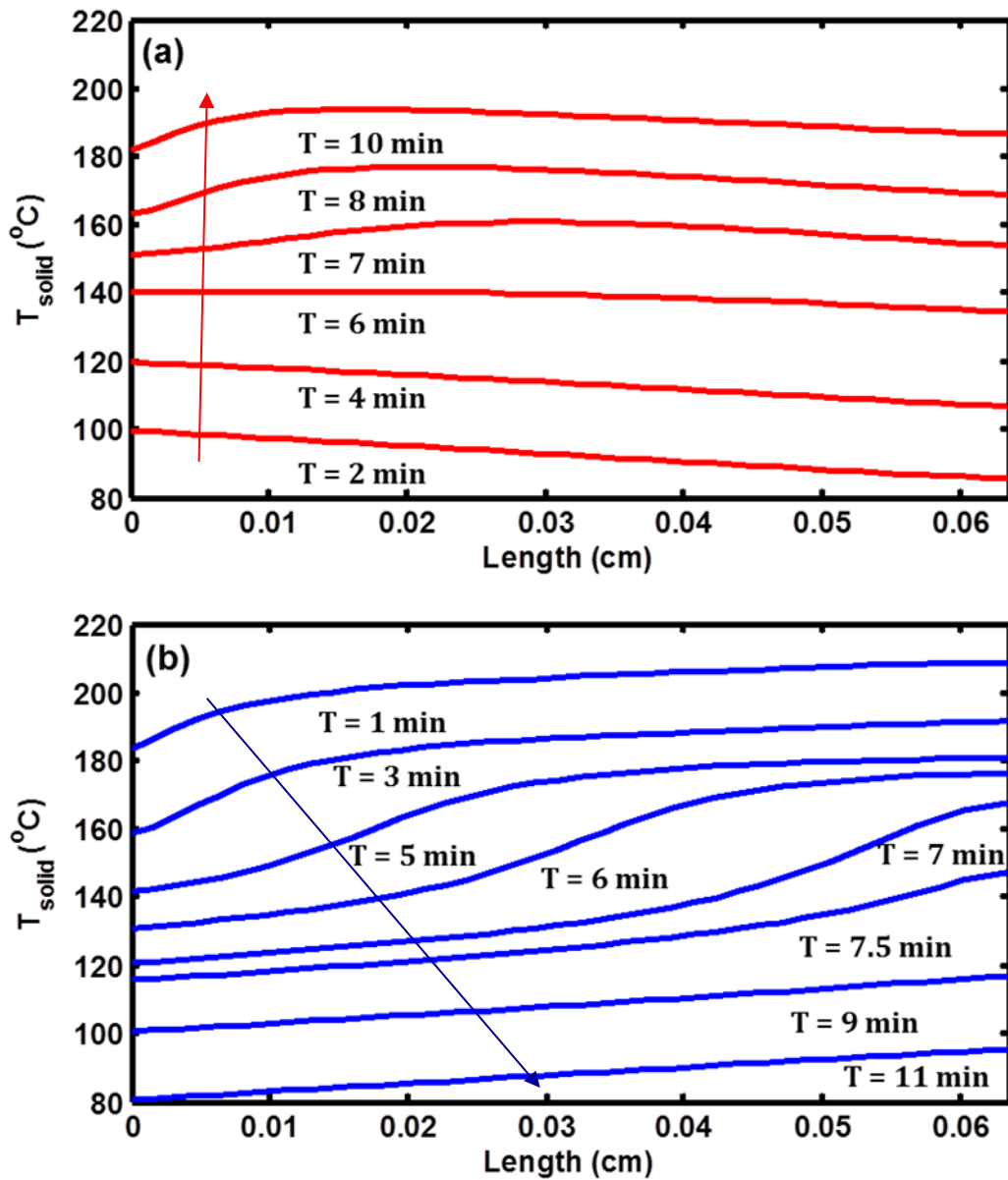


Figure 7-9. (a) Predicted spatial profile of solid temperature (a) during ramp up from 80°C to 190°C (b) during ramp down from 190°C to 80°C ($\text{CO} = 500$ ppm, $\text{C}_3\text{H}_6 = 300$ ppm, 10% O_2 ; Temperature ramp = $10^{\circ}\text{C}/\text{min}$)

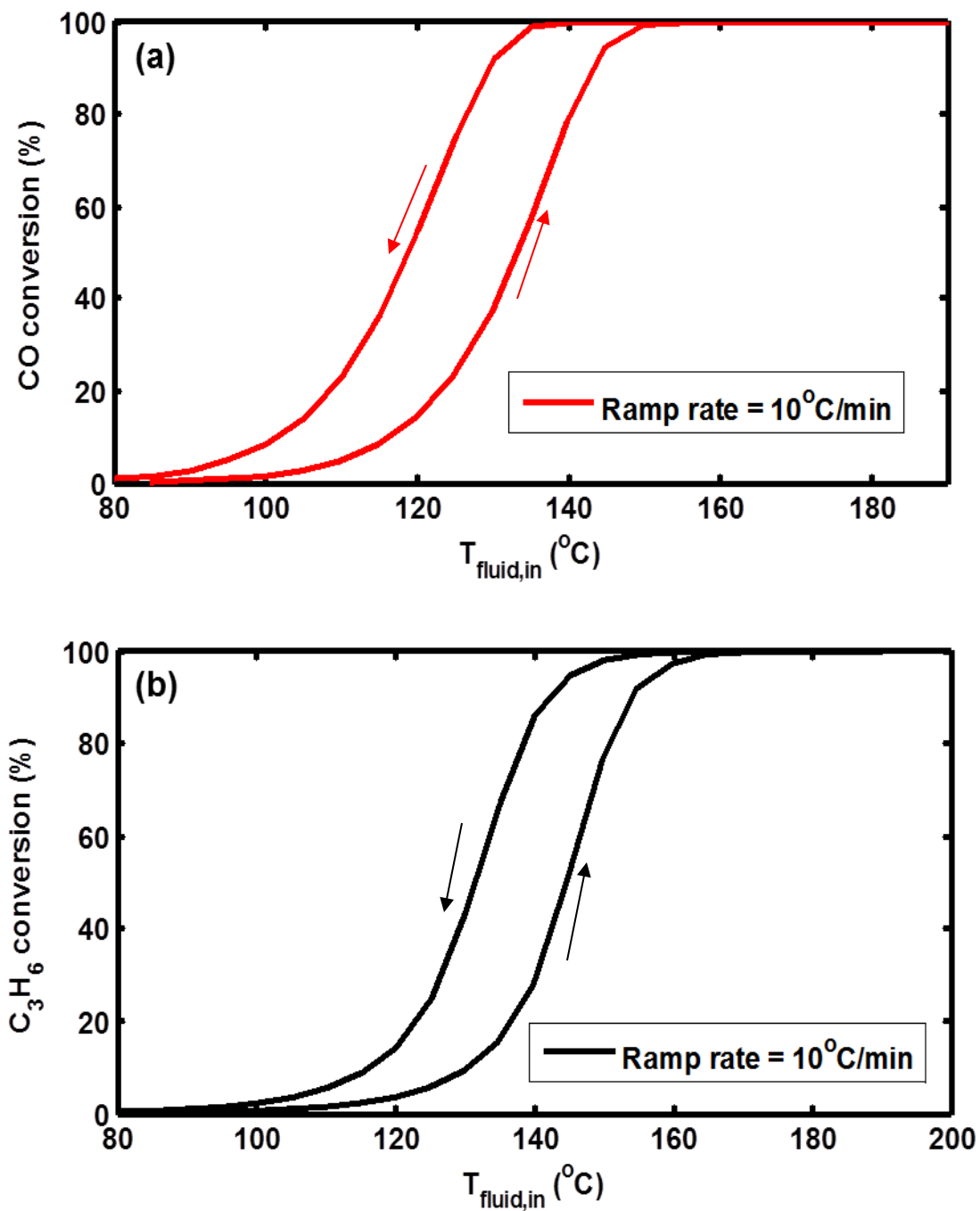


Figure 7-10. (a) Predicted CO conversion versus inlet fluid temperature (b) Predicted C_3H_6 conversion versus inlet fluid temperature (CO = 500 ppm, C_3H_6 = 300 ppm, 10% O_2 ; Temp. ramp = $10^{\circ}\text{C}/\text{min}$; Heat of reaction = 0 kJ/mol)

7.3.2. Steady state hysteresis

The steady state hysteresis depends on the adiabatic temperature rise (ΔT_{ad}) due to the heat generated by the exothermic reaction as well as heat Peclet number (Pe_h). One of the reasons for steady state multiplicity is high adiabatic temperature rise that leads to increase in the rate of reaction during extinction as the catalyst is at higher temperature compared to measured inlet gas temperature. Gundlapally and Balakotaiah [158] have shown in the recent study that the region of multiple steady states expands with decrease in Peclet heat number. The adiabatic temperature rise and heat Peclet number are defined

$$\Delta T_{ad} = \frac{(\Delta H_{R,CO})Y_{CO}}{\langle C_P \rangle} + \frac{(\Delta H_{R,C_3H_6})Y_{C_3H_6}}{\langle C_P \rangle} \sim 9433Y_{CO} + 64200Y_{C_3H_6} \text{ and}$$

$$Pe_h = \frac{\langle u \rangle L \rho_f C_{pf} R_{\Omega 1}}{k_w R_{\Omega w}}.$$

To illustrate this, simulation was performed for 2000 ppm CO, 1200 ppm C₃H₆ and 10% O₂ ($\Delta T_{ad} = 96^\circ\text{C}$ and $Pe_h = 5$). In order to get ignition and extinction curves temperature is increased from 90°C to 200°C in steps of 5°C and then decreased from 200°C to 90°C in steps of 5°C. Figures 7-11a and 7-11b shows ignition and extinction curves of CO and C₃H₆. CO conversion is 42% at 140°C whereas C₃H₆ conversion is 5%. Both CO and C₃H₆ ignited between 140°C to 145°C as both CO and C₃H₆ conversions are 100% at 145°C. This suggest that initially, the catalyst surface is covered with both CO and C₃H₆ and with increase in temperature CO starts desorbing and O₂ starts adsorbing on the surface. Once O₂ adsorb on the surface, it reacts with CO to form CO₂ leaving more vacant sites for O₂ adsorption. Once there is enough oxygen on the surface it reacts with C₃H₆. Figures 7-12a and 7-12b shows the CO and C₃H₆ ignition and extinction curves for 2000 ppm CO, 2000 ppm C₃H₆ and 10% O₂. The heat of reaction of C₃H₆ oxidation is much higher than the heat of reaction of CO oxidation hence, increase in the

C_3H_6 inlet mole fraction significantly moves the extinction point to lower temperature. Figure 7-13 shows the solid temperature spatial profile when the temperature is decreased from $200^\circ C$ to $70^\circ C$ in steps of $5^\circ C$. The extinction is between $90^\circ C$ and $85^\circ C$ as there is no conversion at $85^\circ C$. Above $90^\circ C$ both CO and C_3H_6 conversions are 100% as back of the catalyst length has temperature greater than ignition temperature ($145^\circ C$). Table 7-7 shows the extinction and ignition temperatures for CO and C_3H_6 for different feed compositions. Hence, region of steady state multiplicity depend on the feed composition.

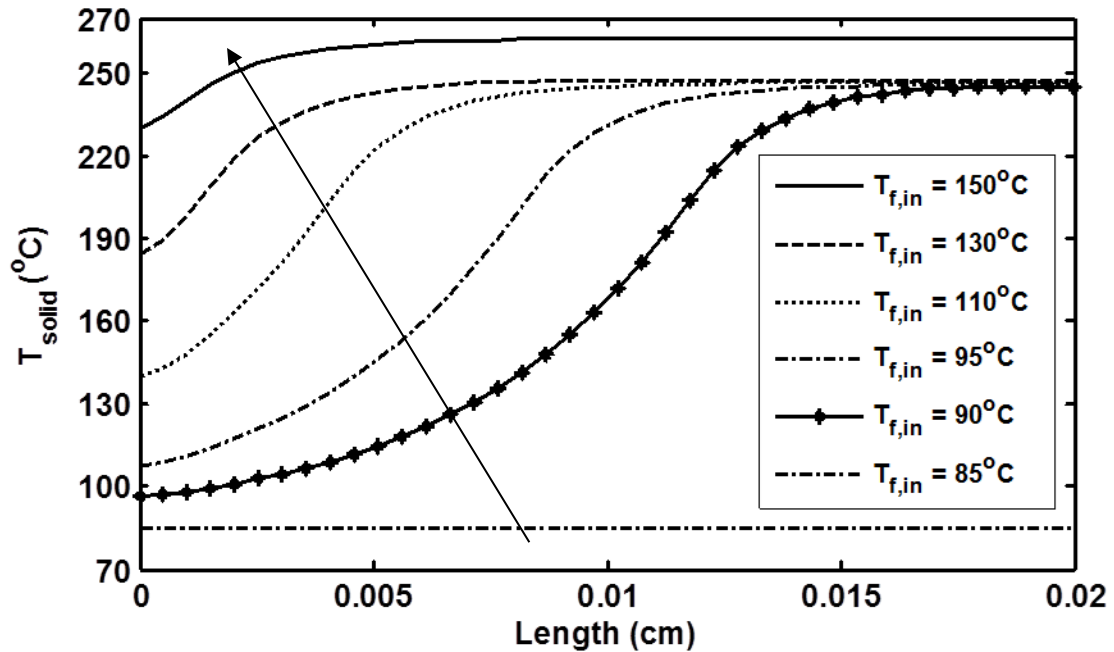


Figure 7-11. Predicted steady state spatial profile of solid temperature when inlet fluid temperature is decreased in steps of $5^\circ C$ from $200^\circ C$ to $70^\circ C$ (CO = 2000 ppm, C_3H_6 = 2000 ppm, 10% O_2 ; GHSV of $25,000\ h^{-1}$ at STP, $Pe_h = 5$)

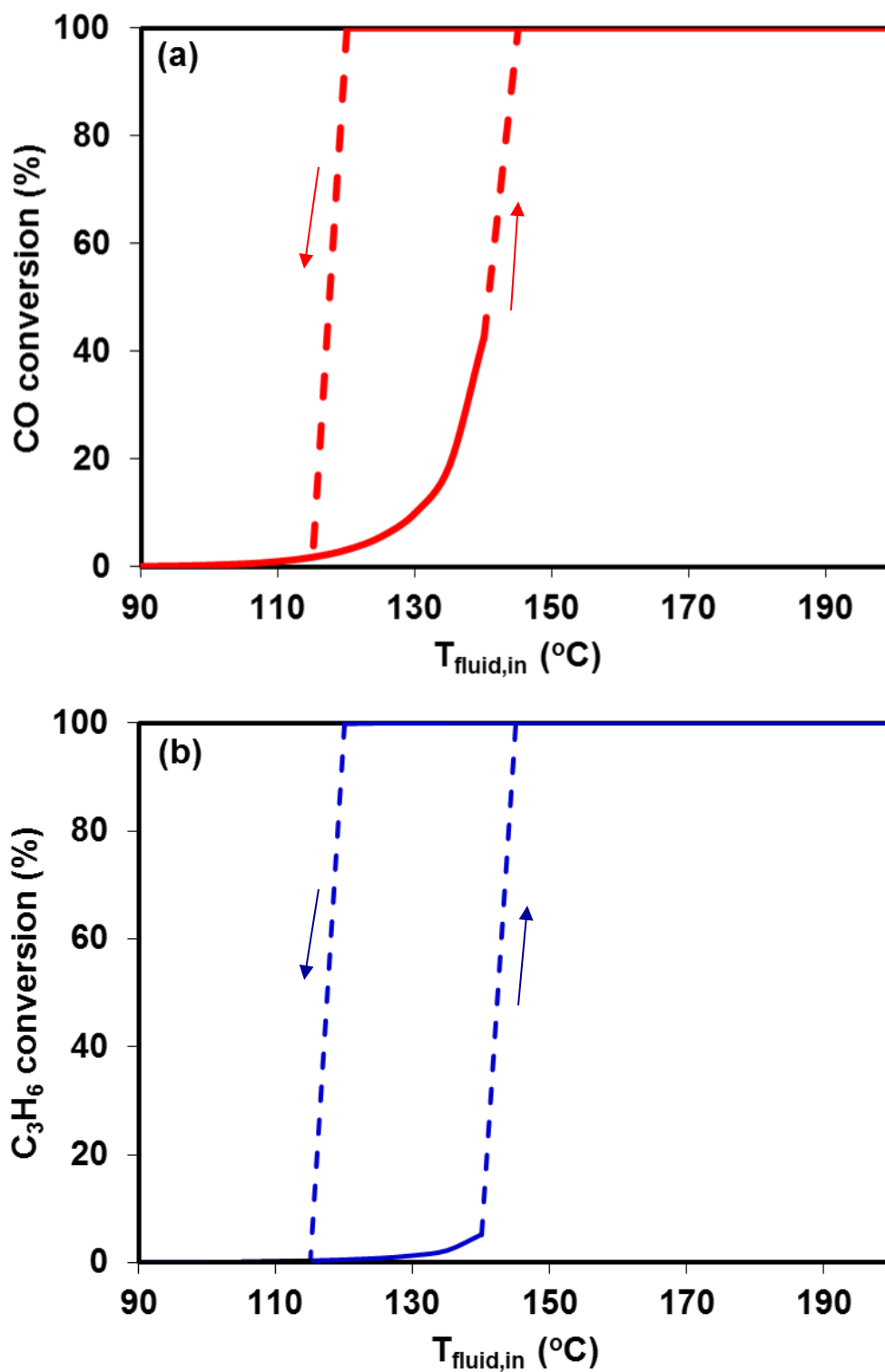


Figure 7-12. (a) Predicted steady state CO conversion vs inlet fluid temperature (b) Predicted steady state C_3H_6 conversion vs inlet fluid temperature (CO = 2000ppm, C_3H_6 = 1200ppm, 10% O_2 ; GHSV of $25,000 \text{ h}^{-1}$ at STP, $\text{Pe}_h = 5$)

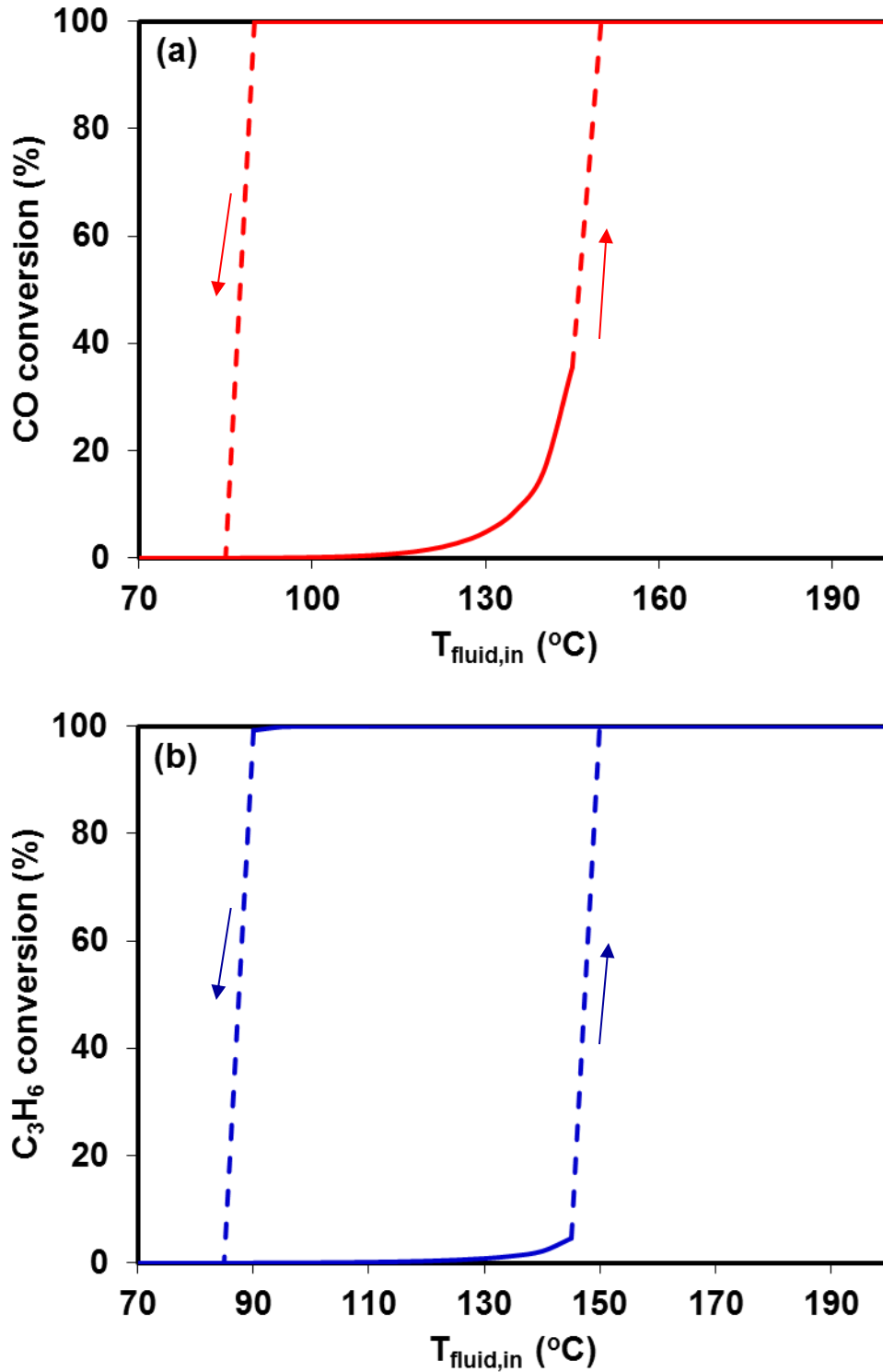
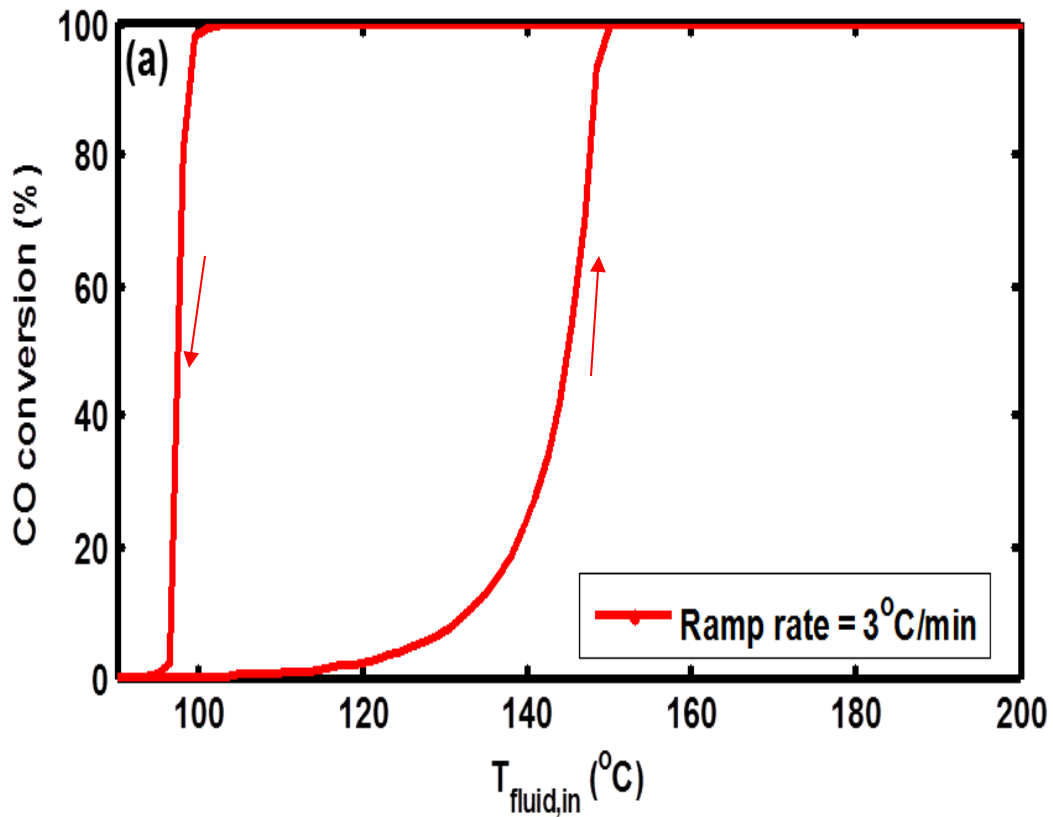


Figure 7-13. (a) Predicted steady state CO conversion versus inlet fluid temperature (b) Predicted steady state C_3H_6 conversion versus inlet fluid temperature (CO = 2000ppm, $\text{C}_3\text{H}_6=2000\text{ppm}$, 10% O_2 ; GHSV of $25,000\text{ h}^{-1}$ at STP, $\text{Pe}_h = 5$)

For 2000 ppm CO, 1200 ppm C₃H₆ and 10% O₂, simulation was performed in which temperature was first increased from 90°C to 200°C at a rate of 3°C/min and then decreased from 200°C to 90°C at a same rate. Figures 7-14a and 7-14b show there is increase in the width of hysteresis loop as compared to steady state hysteresis. This suggests that for this case hysteresis is due to the combined effect of both adiabatic temperature rise and transport delay due to ramping.



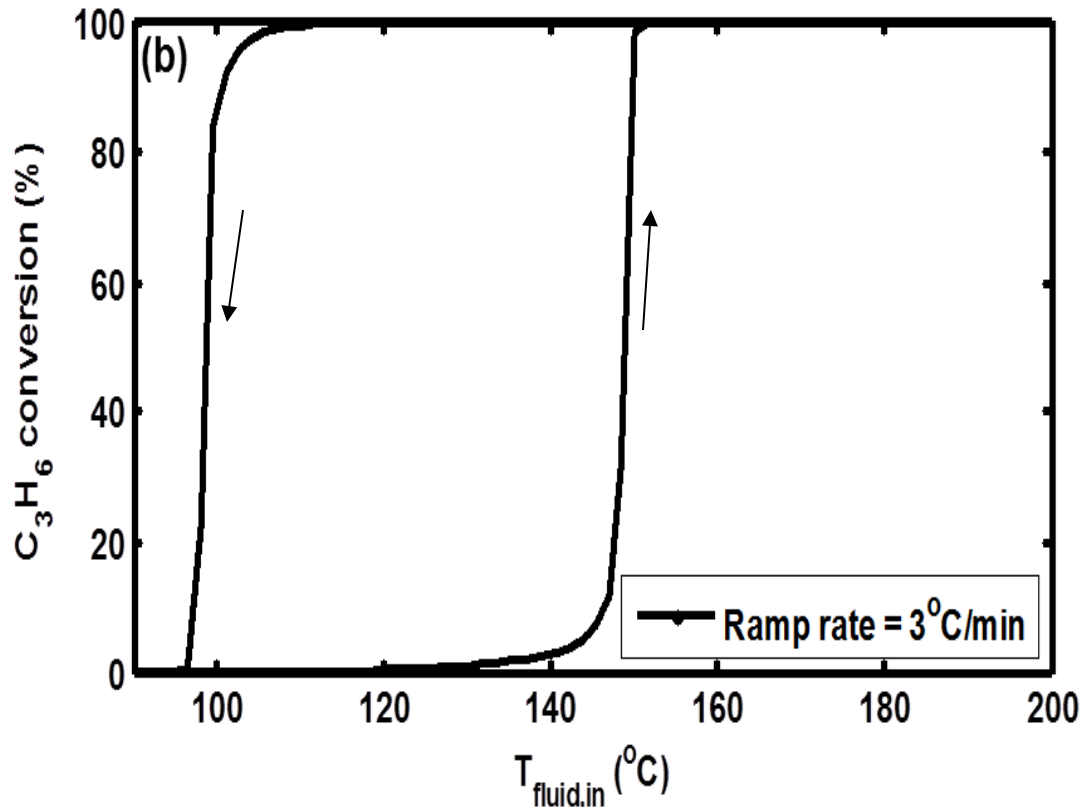


Figure 7-14 (a) Predicted CO conversion vs inlet fluid temperature (b) Predicted C₃H₆ conversion vs inlet fluid temperature (CO = 2000 ppm, C₃H₆ = 1200 ppm, 10% O₂; GHSV of 25,000 h⁻¹ at STP; Pe_h = 5; Temp ramp = 3°C/min)

All the above simulations were performed for 2cm monolith length with Peclet heat number of 5. In order to show that steady state multiplicity also depend on Peclet heat number, simulation was performed for 2000 ppm CO, 1200 ppm C₃H₆ and 10% O₂ but for larger Peclet heat number of 51. The Peclet heat number is increased from 5 to 51 by increasing the monolith length from 2cm to 6.35 cm and keeping transverse Peclet number ($P = \frac{\langle u \rangle R_{01}^2}{LD_f}$) constant. Figures 7-15a and 7-15b show that for monolith of 6.35cm steady state multiplicity disappears. This clearly shows that steady state multiplicity depends on heat Peclet number.

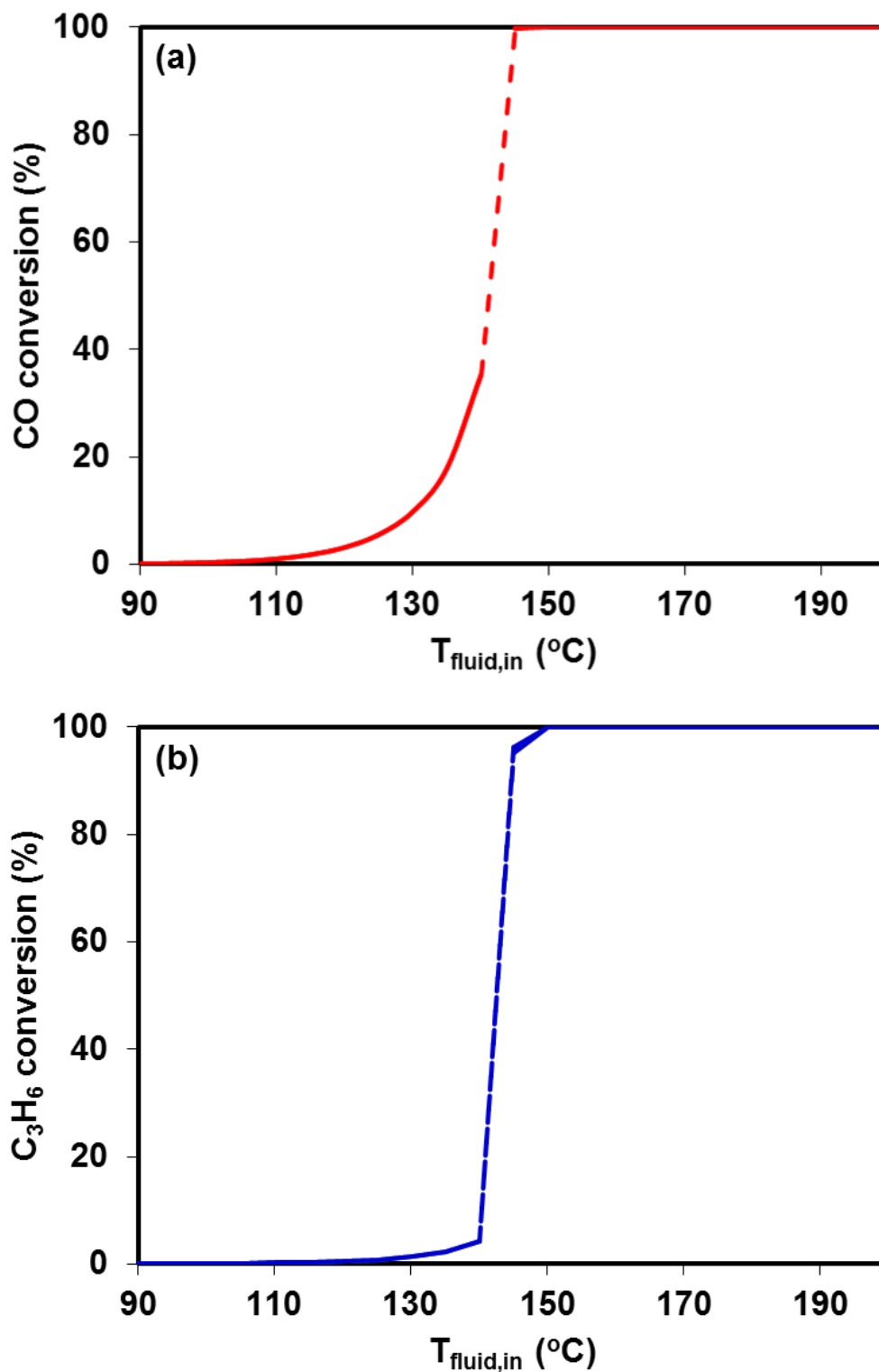
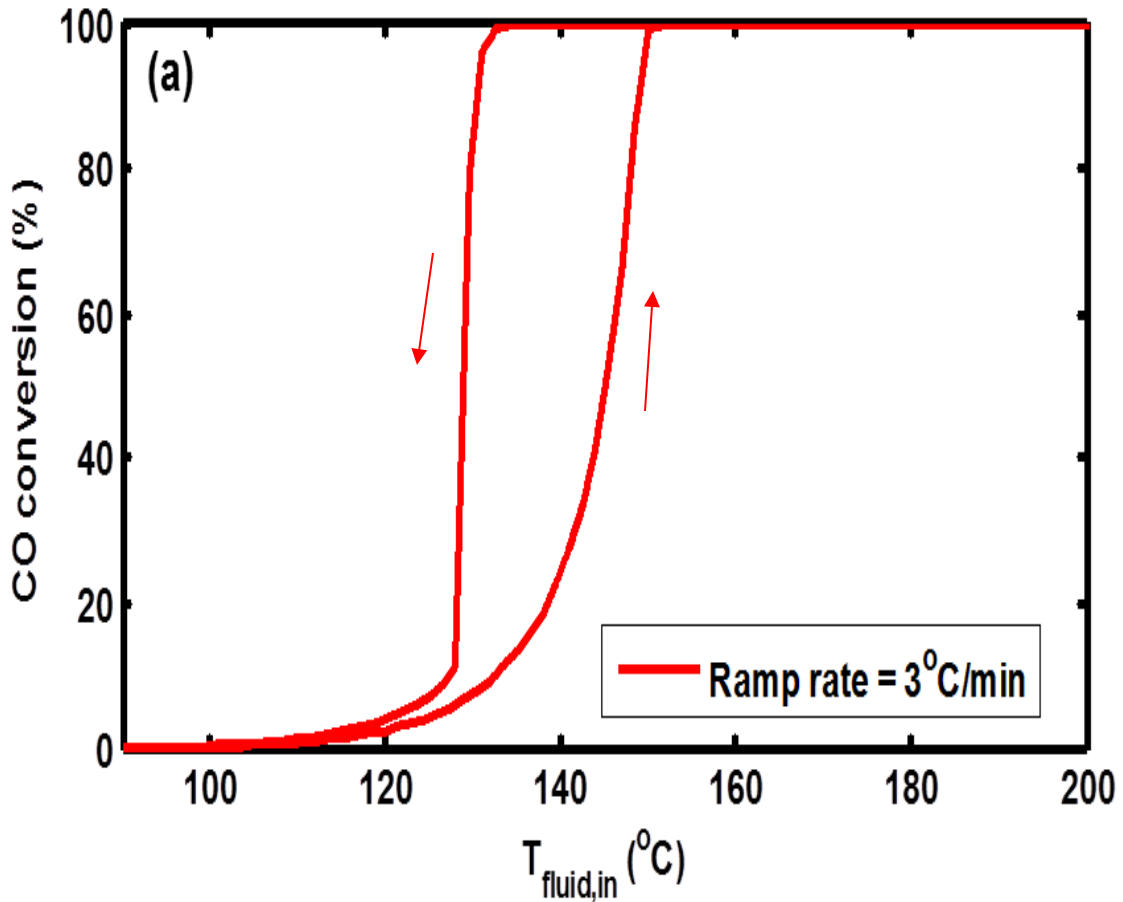


Figure 7-15. (a) Predicted steady state CO conversion versus inlet fluid temperature (b) Predicted steady state C_3H_6 conversion versus inlet fluid temperature (CO =2000ppm, C_3H_6 =1200ppm, 10% O_2 ; GHSV of $25,000\text{h}^{-1}$ at STP; $\text{Pe}_h = 51$)

For 6.35cm monolith length (Peclet heat number = 51) and for 2000 ppm CO, 1200 ppm C₃H₆ and 10% O₂, simulation was performed in which temperature was first increased from 90°C to 200°C at a rate of 3°C/min and then decreased from 200°C to 90°C at a same rate. Figures 16a and 16b show there is transient hysteresis due to ramping even there is no steady state hysteresis. This further confirms that dynamic hysteresis can exist even there is no steady state multiplicity.



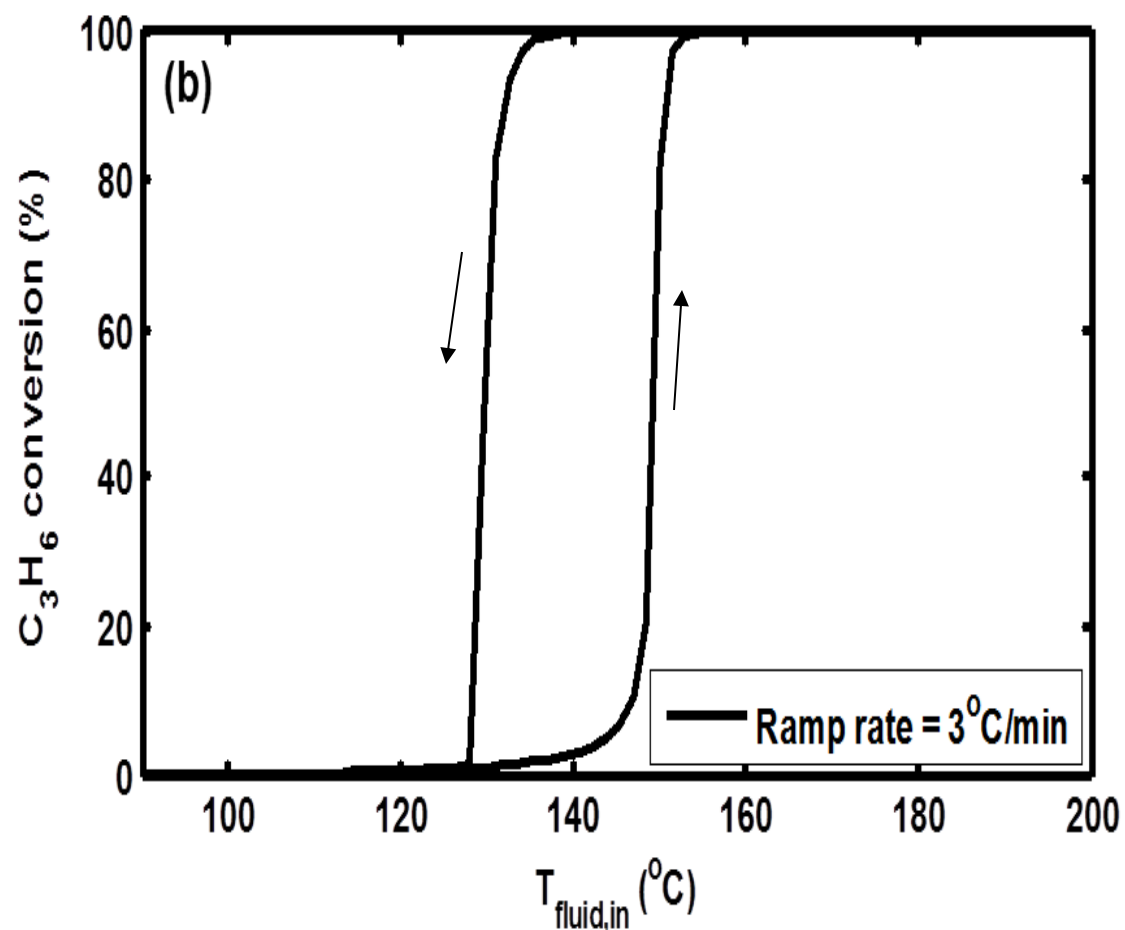


Figure 7-16 (a) Predicted CO conversion vs inlet fluid temperature (b) Predicted C₃H₆ conversion vs inlet fluid temperature (CO = 2000 ppm, C₃H₆ = 1200 ppm, 10% O₂; GHSV of 25,000 h⁻¹ at STP; Pe_h = 51; Temp ramp = 3°C/min)

7.4. Conclusions

We developed a global kinetic model for co-oxidation of CO and C₃H₆ over Pt/Al₂O₃ monolithic catalyst based on bench scale flow reactor experiments [155]. In order to investigate the light-off characteristics of diesel oxidation catalyst TPO experiments are carried out [154, 155, 159]. During TPO of CO+C₃H₆ mixture hysteresis is observed when temperature is first increased and then decreased with a constant ramp-rate. In order to explain this we performed simulations for feed composition with low CO

and C₃H₆ inlet fractions ($\Delta T_{ad} < 25^{\circ}\text{C}$) in which temperature is ramped up and down with a constant rate. As heat generated is negligible so dynamic hysteresis observed is only due to the lag between catalyst temperature change and inlet fluid temperature change. We also performed simulations to show the effect of inlet feed composition and heat Peclet number on steady state multiplicity. For the longer monoliths the region of steady state multiplicity shrinks due to higher heat Peclet number. Similarly, on increasing the CO and C₃H₆ inlet mole fractions the width of steady state hysteresis loop also increases. This study will help experimentalist to analyze their experimental data.

CHAPTER 8 Conclusions and Recommendations for Future Work

8.1 Conclusions

In this chapter, we summarize the main contributions and conclusions of the current work. Some recommendations for the future directions of the research are also provided based on the findings of this dissertation. The main contributions of this work are: (i) Elucidate the mechanistic steps and key intermediates involved in selective catalytic reduction of NO_x with C_3H_6 over Cu-SSZ13 catalyst based on steady state and transient bench flow reactor studies and in-situ DRIFTS measurements, (ii) development of new mechanistically based predictive kinetic model for lean NO reduction with C_3H_6 that provides useful insight in the role of hydrocarbon species for NO_x reduction over wide temperature range and for different feed compositions, and (iii) development of a new global kinetic model for co oxidation of CO and C_3H_6 over Pt/ Al_2O_3 diesel oxidation monolithic catalyst in order to study dynamic and steady state hysteresis. The main findings of the dissertation are summarized below.

We carried out a comprehensive experimental study on lean NO_x reduction with C_3H_6 on Cu-SSZ13 using both bench flow reactor and *in-situ* DRIFTS. To our knowledge, this is the first study on the detailed understanding of underlying mechanism of NO_x reduction with C_3H_6 on small pore Cu zeolite. This study focused on elucidating the underlying mechanism of lean NO_x reduction with C_3H_6 . Both steady state and transient data showed the potential role of oxidation state of Cu in determining the reaction chemistry and pathways. The steady state data showed the rate of decomposition of NO_2 to NO is higher in the presence of C_3H_6 and may be attributed to the reduction of

Cu^{+2} to Cu^{+1} by C_3H_6 . NO_2 being strong oxidizing agent re oxidize the reduced Cu sites. The steady state and transient data clearly show that NO inhibits the C_3H_6 oxidation reaction. Transient experiments with $\text{C}_3\text{H}_6+\text{O}_2+\text{NO}$ reveal that NO inhibition is observed only around and above the light-off temperature of C_3H_6 oxidation. The transient data at light-off temperature also shows the poisoning of active catalytic sites by surface intermediates formed during NO exposure in presence of $\text{C}_3\text{H}_6+\text{O}_2$. This suggests that inhibition is due to the formation of N-containing hydrocarbon species ($\text{C}_x\text{H}_y\text{O}_z\text{N}_t$) that poison the active sites. This also suggests the role of intermediates of C_3H_6 oxidation in NO reduction. We proposed that oxygenates which are the intermediates of C_3H_6 oxidation react with NO to form N-containing hydrocarbon species which are further reduced to N_2 .

In-situ DRIFTS studies were also performed to complement our bench flow-reactor studies. *In-situ* DRIFTS studies were carried out to study the key surface intermediates formed during lean NO reduction with C_3H_6 and their evolution with time. It is shown that below the light-off temperature of C_3H_6 oxidation the catalytic surface is covered saturated and unsaturated hydrocarbon species. Whereas, at light-off temperature oxygenates (formates, acetates, acrolein like species) are also present on the catalytic surface. This confirms that oxygenates are intermediates in C_3H_6 oxidation. It is shown that below the C_3H_6 oxidation light-off temperature, no peak corresponding to nitrogen containing compound is observed upon exposure to $\text{NO}+\text{C}_3\text{H}_6+\text{O}_2$ to the catalyst while above the light-off temperature, peak corresponding to -NCO species is observed. *In-situ* DRIFTS studies confirmed the formation of N-containing intermediates. . Hence, through both bench flow reactor studies and *in-situ* DRIFTS studies it is concluded that the SCR

mechanism involves reaction between oxygenates (partially oxidized hydrocarbon species) and NO to form isocyanates species (-NCO), which are further reduced to N₂.

A mechanistic-based kinetic model is developed for selective catalytic reduction of NO with C₃H₆ on Cu chabazite (Cu-SSZ13) monolithic catalyst based on bench scale flow reactor studies and *in-situ* DRIFTS measurements. The SCR mechanism involves reaction between oxygenates (partially oxidized hydrocarbon species) and NO to form isocyanates species (-NCO), detected by DRIFTS which are further reduced to N₂. We have shown in an earlier study that reaction intermediates, most likely surface isocyanates, poison the active sites on the catalytic surface resulting in the inhibition of other reactions [133]. The kinetic model was developed in steps, starting with steady-state CO oxidation, followed by C₃H₆ oxidation, and then the C₃H₆ + NO + O₂ reaction system. This approach ensured consistency in the parameter estimation and resulted in a more robust model. The models for CO+O₂, C₃H₆+O₂ and C₃H₆+NO+O₂ were also validated using a new set of steady state experiments. The developed monolith model captures the experimental trends for CO oxidation (CO + O₂), C₃H₆ oxidation (C₃H₆ + O₂) and NO reduction with C₃H₆ (NO + C₃H₆ + O₂) quite well. The C₃H₆ and CO oxidation model predicts the light off curves for C₃H₆ and CO for different feed composition and over wide temperature range quite well. For the C₃H₆+NO+O₂ reaction system, the model predicts the C₃H₆ and NO conversions quantitatively over wide temperature range and for different feed composition. The model captures the inhibition of NO on C₃H₆ oxidation. The model predicts the increase in steady state C₃H₆ light-off temperature in presence of NO in the feed. The model also captures the experimentally observed transient trends for C₃H₆+O₂ and C₃H₆+NO+O₂ reaction systems. The model

captures experimentally observed poisoning of active catalytic sites during NO exposure in presence of $C_3H_6+O_2$ due to the formation of stable $-NCO$ species. NO reacts selectively with surface oxygenates to form $-NCO$ species that block the sites and inhibit other reactions. In view of the combined LNT-SCR approach for NO_x conversion our model provides insight about non- NH_3 pathways (hydrocarbons, oxygenates, isocyanates etc.) for NO_x reduction across the SCR [68, 69, 145].

Finally, we developed a global kinetic model for co-oxidation of CO and C_3H_6 over Pt/ Al_2O_3 monolithic catalyst based on bench scale flow reactor experiments [155]. In order to investigate the light-off characteristics of diesel oxidation catalyst TPO experiments are carried out [154, 155, 159]. Dynamic hysteresis is observed during temperature programmed oxidation of $CO+C_3H_6$ mixture in which temperature is increased and decreased at a constant ramp rate. The predicted solid temperature spatial profile during temperature ramp-up and ramp-down explains that the catalyst temperature change lags behind the inlet temperature change during the ramp-down. We performed simulations to show that the width of the dynamic hysteresis loop increases with increase in the ramp rate. We have also shown that a critical ramp-rate exists beyond which the dynamic hysteresis appears or disappears. We studied the effect of adiabatic temperature rise (ΔT_{ad}) and heat Peclet number (Pe_h) on steady state hysteresis. We have shown that the region of steady state multiplicity depends on inlet feed composition as ΔT_{ad} depends on inlet mole fractions of CO and C_3H_6 . The width of the steady state hysteresis loop increases with increase in mole fractions of CO and C_3H_6 . We have also shown that steady state multiplicity disappears for $Pe_h \rightarrow \infty$ as there will be no thermal feedback.

8.2 Recommendations for future work

Based on the findings of the current study, a few recommendations are provided for the future experimental and modeling studies in the area of aftertreatment system, and are discussed below.

We studied the selective catalytic reduction of NO_x with C_3H_6 over Cu-SSZ13 catalyst in view of combined NSR-SCR system. The current study provided useful insights regarding the role of hydrocarbon species over wide temperature range and feed composition. The experimental study can be extended by including H_2O and CO_2 in the feed. In order to elucidate non- NH_3 pathways for NO_x reduction both bench-flow and *in-situ* DRIFTS experiments can be carried out by using oxygenates and amines as possible reductants. The kinetic model developed in this study only for NO reduction with propylene. The model can be extended by including NO_2 and H_2O in the feed. The current kinetic model for lean NO reduction with C_3H_6 can be coupled with NH_3 -SCR kinetic model in order to predict the NO conversion when both NH_3 and C_3H_6 is present in the feed. In the second part of work, we developed a global kinetic model for co oxidation of CO and C_3H_6 over Pt/ Al_2O_3 monolithic catalyst. The model can be extended by including NO in the feed in order to have real exhaust conditions.

References

- [1] A. Güthenke, D. Chatterjee, M. Weibel, B. Krutzsch, P. Kočí, M. Marek, I. Nova, E. Tronconi, "Current Status of Modeling Lean Exhaust Gas Aftertreatment Catalysts," in: B.M. Guy (Ed.) *Advances in Chemical Engineering*, Academic Press, 2007, pp. 103-283.
- [2] M.P. Harold, "Nox Storage and Reduction in Lean Burn Vehicle Emission Control: A Catalytic Engineer's Playground," *Current Opinion in Chemical Engineering*, 1 (2012) 303-311.
- [3] S. Roy, A. Baiker, "NO_x Storage–Reduction Catalysis: From Mechanism and Materials Properties to Storage–Reduction Performance," *Chemical Reviews*, 109 (2009) 4054-4091.
- [4] M. Takeuchi, S. Matsumoto, "NO_x Storage-Reduction Catalysts for Gasoline Engines," *Topic of Catalysis*, 28 (2004) 151-156.
- [5] US EPA, "Cars and Light-Duty Trucks-Tier 3", <http://www.dieselnet.com/>, (2013).
- [6] R.M. Heck, R.J. Farrauto, S.T. Gulati, "Catalytic Air Pollution Control Commercial Technology", Third ed., *John Wiley & Sons*, New Jersey, 2009.
- [7] R. Burch, "Knowledge and Know-How in Emission Control for Mobile Applications", *Catalysis Reviews: Science and Engineering*, 2004 (46)271-334.
- [8] R. Burch, P. J. Millington, "Selective Reduction of Nitrogen Oxides by Hydrocarbons under Lean-burn Conditions using Supported Platinum Group Metal Catalysts", *Catalysis Today*, 1995 (26) 185-206.

- [9] R. Burch, T.C. Watling, "Kinetics of the Reduction of NO by C₃H₆ and C₃H₈ over Pt based Catalysts under Lean-burn Conditions", *Studies in Surface Science and Catalysis*, 1998 (116) 199-211.
- [10] W. S. Epling, L. E. Campbell, A. K. Yezerets, N. W. Currier, J. E. Parks II, "Overview of the Fundamental Reactions and Degradation Mechanisms of NO_x Storage/Reduction Catalysts", *Catalysis Reviews: Science and Engineering*, 2004(46)163-245.
- [11] B. J. Cooper, J. E. Thoss, "Role of NO in Diesel Particulate Emission Control", *SAE Technical Paper*, 890404, 1989, doi:10.4271/890404.
- [12] R. Allansson, P. Blakeman, B. Cooper, H. Hess, "Optimising the Low Temperature Performance and Regeneration Efficiency of the Continuously Regenerating Diesel Particulate Filter (CR-DPF) System", *SAE Technical Paper*, 2002-01-0428, 2002, doi:10.4271/2002-01-0428.
- [13] J. Gieshoff, A. Schäfer-Sindlinger, P. Spurk, J. van den Tillaart, "Improved SCR Systems for Heavy Duty Applications", *SAE Technical Paper*, 2000-01-0189, 2000, doi:10.4271/2000-01-0189.
- [14] R. J. Farrauto, K. E. Voss, "Monolithic diesel oxidation catalysts", *Applied Catalysis B: Environmental*, 1996(10) 29-51.
- [15] K. Irani, W. S. Epling, R. Blint, "Effect of hydrocarbon species on no oxidation over diesel oxidation catalysts", *Applied Catalysis B: Environmental*, 2009(92) 422-428.
- [16] A. Russell, W. S. Epling, "Diesel Oxidation Catalysts", *Catalysis Reviews: Science and Engineering*, 53 (2011) 337-423.

- [17] M. Kaneeda, H. Iizuka, T. Hiratsuka, N. Shinotsuka, M. Arai, "Improvement of Thermal Stability of NO Oxidation Pt/Al₂O₃ Catalyst by Addition of Pd", *Applied Catalysis B: Environmental*, 90 (2009) 564–569.
- [18] A. Morlang, U. Neuhausen, K. Klementiev, F. Schutze, G. Miehe, H. Fuess, E. Lox, "Bimetallic Pt/Pd Diesel Oxidation Catalysts Structural Characterisation and Catalytic Behaviour", *Applied Catalysis B: Environmental*, 60 (2005) 191–199.
- [19] M. Twigg, "Roles of Catalytic Oxidation in Control of Vehicle Exhaust Emissions", *Catalysis Today*, 117(2006) 407–418.
- [20] T. Watanabe, K. Kawashima, Y. Tagawa, K. Tashiro, H. Anoda, K. Ichioka, S. Sumiya, G. Zhang, "New DOC for Light Duty Diesel DPF System", *SAE Technical Paper Series*, 2007-01-1920, 2007.
- [21] A. Setiabudi, M. Makkee, J. A. Moulijn, "The Role of NO₂ and O₂ in the Accelerated Combustion of Soot in Diesel Exhaust Gases", *Applied Catalysis B: Environmental*, 50 (2004) 185–194.
- [22] M. D. Amiridis, T. Zhang, R. J. Farrauto, "Selective Catalytic Reduction of Nitric Oxide by Hydrocarbons", *Applied Catalysis B: Environmental*, 10 (1996) 203–227.
- [23] R. Burch, J.P. Breen, F.C. Meunier, "A Review of the Selective Reduction of NOx with Hydrocarbons under Lean-burn Conditions with Non-zeolitic Oxide and Platinum Group Metal Catalysts", *Applied Catalysis B: Environmental*, 39 (2002) 283–303.
- [24] M. Shelef, "Selective Catalytic Reduction of NOx with N-free Reductants", *Chemical Reviews*, 1995(95)209–225.

- [25] Y. Traa, B. Burgers, J. Weitkamp, "Zeolite-Based Materials for the Selective Catalytic Reduction of NO_x with Hydrocarbons", *Microporous and Mesoporous materials*, 1999 (30) 3-41.
- [26] D. Chatterjee, P. Kočí, V. Schmeißer, M. Marek, M. Weibel, B. Krutzsch, "Modelling of a Combined Storage and SCR Catalytic System for Diesel Exhaust Gas Aftertreatment," *Catalysis Today*, 151 (2010) 395-409.
- [27] N. Takahashi, H. Shinjoh, T. Iijima, T. Suzuki, K. Yamazaki, K. Yokota, H. Suzuki, N. Miyoshi, S. Matsumoto, T. Tanizawa, T. Tanaka, S. Tateishi, K. Kasahara, "The New Concept 3-way Catalyst for Automotive Lean-burn Engine: NO_x Storage and Reduction Catalyst," *Catalysis Today*, 27 (1996) 63-69.
- [28] Y. Ren, M.P. Harold, "NO_x Storage and Reduction with H₂ on Pt/Rh/BaO/CeO₂: Effects of Rh and CeO₂ in the Absence and Presence of CO₂ and H₂O," *ACS Catalysis*, 1 (2011) 969-988.
- [29] W.S. Epling, L.E. Campbell, A. Yezerets, N.W. Currier, J.E. Parks, "Overview of the Fundamental Reactions and Degradation Mechanisms of NO_x Storage/Reduction Catalysts," *Catalysis Reviews*, 46 (2004) 163-245.
- [30] W.S. Epling, J.E. Parks, G.C. Campbell, A. Yezerets, N.W. Currier, L.E. Campbell, "Further Evidence of Multiple NO_x Sorption Sites on NO_x Storage/Reduction Catalysts," *Catalysis Today*, 96 (2004) 21-30.
- [31] P. Forzatti, L. Castoldi, I. Nova, L. Lietti, E. Tronconi, "NO_x Removal Catalysis under Lean Conditions," *Catalysis Today*, 117 (2006) 316-320.

- [32] K.S. Kabin, P. Khanna, R.L. Muncrief, V. Medhekar, M.P. Harold, "Monolith and TAP Reactor Studies of NO_x Storage on Pt/BaO/Al₂O₃: Elucidating the Mechanistic Pathways and Roles of Pt," *Catalysis Today*, 114 (2006) 72-85.
- [33] A. Kumar, M.P. Harold, V. Balakotaiah, "Isotopic Studies of NO_x Storage and Reduction on Pt/BaO/Al₂O₃ Catalyst using Temporal Analysis of Products," *Journal of Catalysis*, 270 (2010) 214-223.
- [34] J. Kwak, D. Kim, T. Szailer, C.F. Peden, J. Szanyi, "NO_x Uptake Mechanism on Pt/BaO/Al₂O₃ Catalysts," *Catalysis Letters*, 111 (2006) 119-126.
- [35] L. Lietti, L. Righini, L. Castoldi, N. Artioli, P. Forzatti, "Labeled ¹⁵N₂O Study on N₂ and N₂O Formation Over Pt–Ba/Al₂O₃ NSR Catalysts," *Topic of Catalysis*, 56 (2013) 7-13.
- [36] G. Liu, P.-X. Gao, "A Review of NO_x Storage/Reduction Catalysts: Mechanism, Materials and Degradation Studies," *Catalysis Science & Technology*, 1 (2011) 552-568.
- [37] J.-Y. Luo, W.S. Epling, "New Insights into the Promoting Effect of H₂O on a Model Pt/Ba/Al₂O₃ NSR catalyst," *Applied Catalysis B: Environmental*, 97 (2010) 236-247.
- [38] H. Mahzoul, J.F. Brilhac, P. Gilot, "Experimental and Mechanistic Study of NO_x Adsorption over NO_x Trap Catalysts," *Applied Catalysis B: Environmental*, 20 (1999) 47-55.
- [39] R.L. Muncrief, P. Khanna, K.S. Kabin, M.P. Harold, "Mechanistic and Kinetic Studies of NO_x Storage and Reduction on Pt/BaO/Al₂O₃," *Catalysis Today*, 98 (2004) 393-402.

- [40] I. Nova, L. Lietti, L. Castoldi, E. Tronconi, P. Forzatti, "New Insights in the NO_x Reduction Mechanism with H₂ over Pt–Ba/γ-Al₂O₃ Lean NO_x Trap Catalysts under Near-isothermal Conditions," *Journal of Catalysis*, 239 (2006) 244-254.
- [41] I. Nova, L. Lietti, P. Forzatti, "Mechanistic Aspects of the Reduction of Stored NO_x over Pt–Ba/Al₂O₃ Lean NO_x Trap Systems," *Catalysis Today*, 136 (2008) 128-135.
- [42] L. Olsson, H. Persson, E. Fridell, M. Skoglundh, B. Andersson, "A Kinetic Study of NO Oxidation and NO_x Storage on Pt/Al₂O₃ and Pt/BaO/Al₂O₃," *The Journal of Physical Chemistry B*, 105 (2001) 6895-6906.
- [43] B. Pereda-Ayo, J.R. González-Velasco, R. Burch, C. Hardacre, S. Chansai, "Regeneration Mechanism of a Lean NO_x Trap (LNT) Catalyst in the Presence of NO Investigated using Isotope Labelling Techniques," *Journal of Catalysis*, 285 (2012) 177-186.
- [44] G. Zhou, T. Luo, R.J. Gorte, "An Investigation of NO_x Storage on Pt–BaO–Al₂O₃," *Applied Catalysis B: Environmental*, 64 (2006) 88-95.
- [45] P. Broqvist, I. Panas, H. Grönbeck, "The Nature of NO_x Species on BaO(100): An Ab Initio Molecular Dynamics Study," *The Journal of Physical Chemistry B*, 109 (2005) 15410-15416.
- [46] N.W. Cant, I.O.Y. Liu, M.J. Patterson, "The Effect of Proximity between Pt and BaO on Uptake, Release, and Reduction of NO_x on Storage Catalysts," *Journal of Catalysis*, 243 (2006) 309-317.

- [47] B.M. Shakya, M.P. Harold, V. Balakotaiah, "Crystallite-Scale Model for NO_x Storage and Reduction on Pt/BaO/Al₂O₃: Pt Dispersion Effects on NO_x Conversion and Ammonia Selectivity," *Catalysis Today*, 184 (2012) 27-42.
- [48] R.D. Clayton, M.P. Harold, V. Balakotaiah, C.Z. Wan, "Pt Dispersion Effects During NO_x Storage and Reduction on Pt/BaO/Al₂O₃ Catalysts," *Applied Catalysis B: Environmental*, 90 (2009) 662-676.
- [49] Y. Sakamoto, K. Okumura, Y. Kizaki, S. Matsunaga, N. Takahashi, H. Shinjoh, "Adsorption and Desorption Analysis of NO_x and SO_x on a Pt/Ba Thin Film Model Catalyst," *Journal of Catalysis*, 238 (2006) 361-368.
- [50] L. Cumarantunge, S.S. Mulla, A. Yezerets, N.W. Currier, W.N. Delgass, F.H. Ribeiro, "Ammonia is a Hydrogen Carrier in the Regeneration of Pt/BaO/Al₂O₃ NO_x Traps with H₂," *Journal of Catalysis*, 246 (2007) 29-34.
- [51] W.S. Epling, A. Yezerets, N.W. Currier, "The Effects of Regeneration Conditions on NO_x and NH₃ Release from NO_x Storage/Reduction Catalysts," *Applied Catalysis B: Environmental*, 74 (2007) 117-129.
- [52] L. Lietti, I. Nova, P. Forzatti, "Role of Ammonia in the Reduction by Hydrogen of NO_x Stored over Pt–Ba/Al₂O₃ Lean NO_x Trap Catalysts," *Journal of Catalysis*, 257 (2008) 270-282.
- [53] S.S. Mulla, S.S. Chaugule, A. Yezerets, N.W. Currier, W.N. Delgass, F.H. Ribeiro, "Regeneration Mechanism of Pt/BaO/Al₂O₃ Lean NO_x Trap Catalyst with H₂," *Catalysis Today*, 136 (2008) 136-145.

- [54] T. Szailer, J.H. Kwak, D.H. Kim, J.C. Hanson, C.H.F. Peden, J. Szanyi, "Reduction of Stored NO_x on Pt/Al₂O₃ and Pt/BaO/Al₂O₃ catalysts with H₂ and CO," *Journal of Catalysis*, 239 (2006) 51-64.
- [55] Z. Liu, J.A. Anderson, "Influence of Reductant on the Thermal Stability of Stored NO_x in Pt/Ba/Al₂O₃ NO_x Storage and Reduction Traps," *Journal of Catalysis*, 224 (2004) 18-27.
- [56] K. Kamasamudram, N.W. Currier, X. Chen, A. Yezerets, "Overview of the Practically Important Behaviors of Zeolite-based Urea-SCR Catalysts, using Compact Experimental Protocol," *Catalysis Today*, 151 (2010) 212-222.
- [57] P.S. Metkar, M.P. Harold, V. Balakotaiah, "Experimental and Kinetic Modeling Study of NH₃-SCR of NO_x on Fe-ZSM-5, Cu-chabazite and Combined Fe- and Cu-zeolite Monolithic Catalysts," *Chemical Engineering Science*, 87 (2013) 51-66.
- [58] P.S. Metkar, N. Salazar, R. Muncrief, V. Balakotaiah, M.P. Harold, "Selective Catalytic Reduction of NO with NH₃ on Iron Zeolite Monolithic Catalysts: Steady-state and Transient Kinetics," *Applied Catalysis B: Environmental*, 104 (2011) 110-126.
- [59] M. Colombo, I. Nova, E. Tronconi, "Detailed Kinetic Modeling of the NH₃-NO/NO₂ SCR Reactions over a Commercial Cu-zeolite Catalyst for Diesel Exhausts After treatment," *Catalysis Today*, 197 (2012) 243-255.
- [60] M.P. Ruggeri, A. Grossale, I. Nova, E. Tronconi, H. Jirglova, Z. Sobalik, "FTIR *in situ* Mechanistic Study of the NH₃-NO/NO₂ "Fast SCR" Reaction over a Commercial Fe-ZSM-5 Catalyst," *Catalysis Today*, 184 (2012) 107-114.

- [61] M. Colombo, I. Nova, E. Tronconi, "A Comparative Study of the NH₃-SCR Reactions over a Cu-zeolite and a Fe-zeolite Catalyst," *Catalysis Today*, 151 (2010) 223-230.
- [62] M. Colombo, I. Nova, E. Tronconi, V. Schmeißer, B. Bandl-Konrad, L. Zimmermann, "NO/NO₂/N₂O–NH₃ SCR Reactions over a Commercial Fe-zeolite Catalyst for Diesel Exhaust Aftertreatment: Intrinsic Kinetics and Monolith Converter Modelling," *Applied Catalysis B: Environmental*, 111–112 (2012) 106-118.
- [63] M. Devadas, O. Kröcher, M. Elsener, A. Wokaun, N. Söger, M. Pfeifer, Y. Demel, L. Mussmann, "Influence of NO₂ on the Selective Catalytic Reduction of NO with Ammonia over Fe-ZSM5," *Applied Catalysis B: Environmental*, 67 (2006) 187-196.
- [64] L. Olsson, H. Sjövall, R.J. Blint, "A Kinetic Model for Ammonia Selective Catalytic Reduction over Cu-ZSM-5," *Applied Catalysis B: Environmental*, 81 (2008) 203-217.
- [65] H. Sjövall, R.J. Blint, L. Olsson, "Detailed Kinetic Modeling of NH₃ SCR over Cu-ZSM-5," *Applied Catalysis B: Environmental*, 92 (2009) 138-153.
- [66] H. Sjövall, R.J. Blint, A. Gopinath, L. Olsson, "A Kinetic Model for the Selective Catalytic Reduction of NO_x with NH₃ over an Fe-zeolite Catalyst," *Industrial and Engineering Chemistry Research*, 49 (2010) 39-52.
- [67] A. Grossale, I. Nova, E. Tronconi, D. Chatterjee, M. Weibel, "NH₃–NO/NO₂ SCR for Diesel Exhausts Aftertreatment: Reactivity, Mechanism and Kinetic

- Modelling of Commercial Fe- and Cu-Promoted Zeolite Catalysts," *Topic of Catalysis*, 52 (2009) 1837-1841.
- [68] J. Wang, Y. Ji, Z. He, M. Crocker, M. Dearth, R.W. McCabe, "A Non-NH₃ Pathway for NO_x Conversion in Coupled LNT-SCR Systems," *Applied Catalysis B: Environmental*, 111–112 (2012) 562-570.
- [69] L. Xu, R.W. McCabe, "LNT+*in situ* SCR Catalyst System for Diesel Emissions Control," *Catalysis Today*, 184 (2012) 83-94.
- [70] R. Burch, J. P. Millington, A. P. Walker, "Mechanism of the Selective Reduction of Nitrogen Monoxide on Platinum-Based Catalysts in the Presence of Excess Oxygen", *Applied Catalysis B: Environmental*, 4 (1994) 65-94.
- [71] R. Burch, J. P. Millington, "Role of Propene in the Selective Reduction of Nitrogen Monoxide in Copper-Exchanged Zeolites", *Applied Catalysis B: Environmental*, 2 (1993) 101-116.
- [72] M. Shelef, "On the Mechanism of Nitric Oxide Decomposition Over Cu-ZSM-5", *Catalysis Letters*, 15 (1992) 305-310.
- [73] F. Dorado, P. B. García, A. de Lucas, J. M. Ramos, A. Romero, "Hydrocarbon Selective Catalytic Reduction of NO Over Cu/Fe-pillared Clays: Diffuse reflectance infrared spectroscopy studies", *Journal of Molecular Catalysis A: Chemical*, 332 (2002) 45-52.
- [74] L. Li, N. Guan, "HC-SCR reaction pathways on ion exchanged ZSM-5 catalysts", *Microporous and Mesoporous Materials*, 117 (2009) 450-457.

- [75] G. P. Ansell, A. F. Diwell, S. E. Golunski, J. W. Hayes, R. R. Rajaram, T. J. Truex, A. P. Walker, "Mechanism of the Lean NO_x reaction over Cu/ZSM-5", *Applied Catalysis B: Environmental*, 2 (1993) 81-100.
- [76] O. Gorce, F. Baudin, C. Thomas, P. Da Costa, G. Djéga-Mariadassou, "On the Role of Organic Nitrogen-containing Species as Intermediates in the Hydrocarbon-assisted SCR of NO_x", *Applied Catalysis B: Environmental*, 54 (2004) 69-84.
- [77] G. Centi, A. Galli, S. Perathoner, "Reaction Pathways of Propane and Propene conversion in the presence of NO and O₂ on Cu/MFI", *Journal of the Chemical Society, Faraday Transactions*, 92 (1996) 5129-5140.
- [78] V. A. Bell, J. S. Feeley, M. Deeba, R. J. Farrauto, "In Situ High Temperature FTIR Studies of NO_x Reduction with Propylene Over Cu/ZSM-5 Catalysts", *Catalysis Letters* 29 (1994) 15-26.
- [79] A. P. Walker, "Mechanistic Studies of the Selective Reduction of NO_x Over Cu/ZSM-5 and Related systems", *Catalysis Today*, 26 (1995) 107-128.
- [80] N. W. Hayes, R. W. Joyner, E. S. Shpiro, "Infrared Spectroscopy Studies of the Mechanism of the Selective Reduction of NO_x over Cu-ZSM-5 catalysts", *Applied Catalysis B: Environmental*, 8 (1996) 343-363.
- [81] R. H. H. Smits, Y. Iwasawa, "Reaction Mechanisms for the Reduction of Nitric Oxide by Hydrocarbons on Cu-ZSM-5 and related Catalysts", *Applied Catalysis B: Environmental*, 6 (1995) 201-207.
- [82] M. Iwamoto, H. Takeda, "Pulse Study on Reactivity of Ethene Adsorbed on Cu-MFI with Nitrogen Oxides and Oxygen", *Catalysis Today*, 27 (1996) 71-78.

- [83] K. A. Bethke, C. Li, M. C. Kung, B. Yang, H. Kung, "The Role of NO₂ in the Reduction of NO by Hydrocarbon over Cu-ZrO₂ and Cu-ZSM-5 Catalysts", *Catalysis Letters*, 31 (1995) 287-299.
- [84] M. Shelef, C. N. Montreuil, H. W. Jen, "NO₂ formation over Cu-ZSM-5 and the Selective Catalytic Reduction of NO", *Catalysis Letters*, 26 (1994) 277-284.
- [85] J. O. Petunchi, K. W. Hall, "On the Role of Nitrogen Dioxide in the Mechanism of the Selective Reduction of NO_x over Cu-ZSM-5 Zeolite", *Applied Catalysis B: Environmental*, 2 (1993) 17-26.
- [86] J. Y. Luo, H. Oh, C. Henry, W. Epling, "Effect of C₃H₆ on Selective Catalytic Reduction of NO_x by NH₃ over a Cu/zeolite catalyst: A Mechanistic Study", *Applied Catalysis B: Environmental*, 123-124 (2012) 296-305.
- [87] Q. Ye, L. Wang, R. T. Yang, "Activity, Propene Poisoning Resistance and Hydrothermal Stability of Copper Exchanged Chabazite-like Zeolite Catalysts for SCR of NO with Ammonia in Comparison to Cu/ZSM-5", *Applied Catalysis A: General* 427-428 (2012) 24-34.
- [88] G. P. Ansell, P. S. Bennett, J. P. Cox, J. C. Frost, P. G. Garar, A.-M. Jones, R. R. Rajaram, A. P. Walker, M. Litorell, G. Smedler, "The Development of a Model Capable of Predicting Diesel Lean NO_x Catalyst Performance under Transient Conditions", *Applied Catalysis B: Environmental* 10 (1996) 183-201.
- [89] R. A. Wilber, A. L. Boehman, "Numerical Modeling of the Reduction of Nitric Oxide by Ethylene over Cu-ZSM-5 under Lean Conditions", *Catalysis Today* 50 (1999) 125-132.

- [90] D. K. Captain, C. Mihut, J. A. Dumesic, M. D. Amiridis, "On the Mechanism of the NO Reduction by Propylene over Supported Pt Catalysts", *Catalysis Letter*, 83 (2002) 3-4.
- [91] F. Can, X. Courtois, S. Royer, G. Blanchard, S. Rousseau, D. Duprez, "An Overview of the Production and use of Ammonia in NSR+SCR Coupled System for NOx Reduction from Lean Exhaust Gas," *Catalysis Today*, 197 (2012) 144-154.
- [92] L. Castoldi, R. Bonzi, L. Lietti, P. Forzatti, S. Morandi, G. Ghiotti, S. Dzwigaj, "Catalytic Behaviour of Hybrid LNT/SCR Systems: Reactivity and *in situ* FTIR Study," *Journal of Catalysis*, 282 (2011) 128-144.
- [93] Y. Liu, M.P. Harold, D. Luss, "Coupled NOx Storage and Reduction and Selective Catalytic Reduction using Dual-layer Monolithic Catalysts," *Applied Catalysis B: Environmental*, 121–122 (2012) 239-251.
- [94] Y. Liu, Y. Zheng, M. Harold, D. Luss, "Lean NOx Reduction with H₂ and CO in Dual-Layer LNT–SCR Monolithic Catalysts: Impact of Ceria Loading," *Topic of Catalysis*, 56 (2013) 104-108.
- [95] Y. Liu, Y. Zheng, M.P. Harold, D. Luss, "Lean NOx Reduction on LNT-SCR Dual-layer Catalysts by H₂ and CO," *Applied Catalysis B: Environmental*, 132–133 (2013) 293-303.
- [96] J. Theis, M. Dearth, R. McCabe, "LNT+SCR Catalyst Systems Optimized for NOx Conversion on Diesel Applications," *SAE Technical Paper 2011-01-0305*, (2011).
- [97] A. Lindholm, H. Sjövall, L. Olsson, "Reduction of NOx over a Combined NSR and SCR System," *Applied Catalysis B: Environmental*, 98 (2010) 112-121.

- [98] A.S. Kota, D. Luss, V. Balakotaiah, "Modeling Studies on Lean NO_x Reduction by a Sequence of LNT–SCR Bricks," *Industrial & Engineering Chemistry Research*, 51 (2012) 6686-6696.
- [99] B.M. Shakya, M.P. Harold, V. Balakotaiah, "Modeling and Analysis of Dual-layer NO_x Storage and Reduction and Selective Catalytic Reduction Monolithic Catalyst," *Chemical Engineering Journal* 237 (2014) 109-122.
- [100] J.H. Kwak, R.G. Tonkyn, D.H. Kim, J. Szanyi, C.H.F. Peden, "Excellent Activity and Selectivity of Cu-SSZ-13 in the Selective Catalytic Reduction of NO_x with NH₃", *Journal of Catalysis*, 275 (2010) 187-190.
- [101] D.W. Fickel, E. D'Addio, J.A. Lauterbach, R.F. Lobo, The ammonia selective catalytic reduction activity of copper-exchanged small-pore zeolites, *Applied Catalysis B: Environmental*, 102 (2011) 441-448.
- [102] I. Bull, W.-M. Xu, P. Burk, S. Boorse, W.M. Jaglowski, G.S. Koermer, A. Moini, J.A. Patchett, J.C. Dettling, M.T. Caudle, Copper CHA zeolite catalysts, in, 2009.
- [103] N. Salazar, "Selective Catalytic Reduction of NO_x by NH₃ over a Fe Zeolite Monolith Catalyst", in: Chemical Engineering, University of Houston, 2009.
- [104] R.D. Clayton, "Steady State and Cyclic Studies of Pt/BaO/Al₂O₃ Lean NO_x Traps", in: Chemical Engineering, University of Houston, 2008.
- [105] Y. Ren, "Effects of Rh, CeO₂ and Regeneration Conditions on NSR Monolith Catalysts using H₂ as the Reductant", in: Chemical Engineering, University of Houston, 2011.
- [106] A. Cybulski, J.A. Moulijn, "Monoliths in Heterogeneous Catalysis", *Catalysis Reviews*, 36 (1994) 179-270.

- [107] W.S. Epling, A. Yezerets, N.W. Currier, “The Effects of Regeneration Conditions on NO_x and NH₃ Release from NO_x Storage/Reduction Catalysts”, *Applied Catalysis B: Environmental*, 74 (2007) 117-129.
- [108] R.M. Heck, R.J. Farrauto, S.T. Gulati, Catalytic Air Pollution Control Commercial Technology, Third ed., John Wiley & Sons, New Jersey, 2009.
- [109] R.M. Heck, S. Gulati, R.J. Farrauto, “The Application of Monoliths for Gas Phase Catalytic Reactions”, *Chemical Engineering Journal* 82 (2001) 149-156.
- [110] A. Güthenke, D. Chatterjee, M. Weibel, B. Krutzsch, P. Kočí, M. Marek, I. Nova, E. Tronconi, “Current Status of Modeling Lean Exhaust Gas Aftertreatment Catalysts”, in: B.M. Guy (Ed.) Advances in Chemical Engineering, Academic Press, 2007, pp. 103-283.
- [111] S.Y. Joshi, M.P. Harold, V. Balakotaiah, “On the Use of Internal Mass Transfer Coefficients in Modeling of Diffusion and Reaction in Catalytic Monoliths”, *Chemical Engineering Science*, 64 (2009) 4976-4991.
- [112] S.Y. Joshi, M.P. Harold, V. Balakotaiah, “Overall Mass Transfer Coefficients and Controlling Regimes in Catalytic Monoliths”, *Chemical Engineering Science*, 65 (2010) 1729-1747.
- [113] A.C. Hindmarsh, “ODEPACK, A Systematized Collection of ODE Solvers”, *IMACS Transactions on Scientific Computation* 1 (1983) 55-64.
- [114] S.Y. Joshi, M.P. Harold, V. Balakotaiah, “Low-Dimensional Models for Real Time Simulations of Catalytic Monoliths”, *AIChE Journal*, 55 (2009) 1771-1783.

- [115] K. Ramanathan, V. Balakotaiah, D.H. West, “Light-off Criterion and Transient Analysis of Catalytic Monoliths”, *Chemical Engineering Science*, 58 (2003) 1381-1405.
- [116] D. Bhatia, R.D. Clayton, M.P. Harold, V. Balakotaiah, “A Global Kinetic Model for NO_x Storage and Reduction on Pt/BaO/Al₂O₃ Monolithic catalysts”, *Catalysis Today*, 147, Supplement (2009) S250-S256.
- [117] V. Balakotaiah, “On the Relationship between Aris and Sherwood numbers and Friction and Effectiveness factors”, *Chemical Engineering Science*, 63 (2008) 5802-5812.
- [118] P.T. Boggs, R.H. Byrd, J.E. Rogers, R.B. Schnabel, “User’s Reference Guide for ODRPACK—software for Weighted Orthogonal Distance Regression”, *National Institute of Standards and Technology Internal Report*, (1991) 89-4103.
- [119] J. Xu, R. Clayton, V. Balakotaiah, M. P. Harold, “Experimental and Microkinetic Modeling of Steady-State NO Reduction by H₂ on Pt/BaO/Al₂O₃ Monolith catalysts”, *Applied Catalysis B: Environmental*, 77 (2008) 395-408.
- [120] L.Olsson, H. Sjövall, R. J. Blint, “Detailed Kinetic Modeling of NO_x Adsorption and NO Oxidation over Cu-ZSM-5”, *Applied Catalysis B: Environmental*, 87 (2009) 200-210.
- [121] P. S. Metkar, V. Balakotaiah, M. P. Harold, “Experimental and Kinetic Modeling Study of NO Oxidation: Comparison of Fe and Cu-zeolite Catalysts”, *Catalysis Today*, 184 (2012) 115-128.

- [122] A. Grossale, I. Nova, E. Tronconi, "Study of a Fe-zeolite-based System as NH₃-SCR catalyst for Diesel Exhaust Aftertreatment", *Catalysis Today*, 136 (2008) 18-27.
- [123] C. Torre-Abreu, C. Henriques, F. R. Ribeiro, G. Delahay, M. F. Ribeiro, "Selective Catalytic Reduction of NO on Copper-Exchanged Zeolites: the Role of the Structure of the Zeolite in the Nature of Copper-Active Sites", *Catalysis Today*, 54 (1999) 407-418.
- [124] S. Y. Joshi, Y. Ren, M. P. Harold, V. Balakotaiah, "Experimental and Theoretical Investigation of Controlling Regimes during Lean Oxidation of Methane and Propylene on Pt/Al₂O₃ Monolithic Reactors", *Industrial & Engineering Chemistry Research*, 51 (2011) 7482-7492.
- [125] M. P. Harold, M. Sheintuch, D. Luss, "Analysis and Modeling of Multiplicity Features. 2. Isothermal Experiments", *Industrial & Engineering Chemistry Research*, 26 (1987) 794-804.
- [126] D. J. Liu, H. J. Robota, "On the Mechanism of NO Selective Catalytic Reduction by Hydrocarbons over Cu-ZSM-5 via X-ray Absorption Spectroscopic Study", *The Journal of Physical Chemistry B*, 103 (1999) 2755-2765.
- [127] K. Krishna, M. Makkee, "Coke Formation over Zeolites and its Influence on Selective Catalytic Reduction of NO_x", *Applied Catalysis B: Environmental*, 59 (2005) 35-44.

- [128] G. Li, X. Wang, C. Jia, Z. Liu, “An In Situ Fourier Transform Infrared Study on the Mechanism of NO Reduction by Acetylene over Mordenite-based Catalysts”, *Journal of Catalysis*, 257 (2008) 291–296.
- [129] F. Garin, P. Girard, S. Ringler, G. Maire, N. Davias, “Mechanistic Studies of NO_x Reduction Reactions under Oxidative Atmosphere on Alumina Supported 1 wt% Pt and 1 wt% Pt–0.5 wt% Zn catalysts (Part I)”, *Applied Catalysis B: Environmental*, 20 (1999) 205–218.
- [130] B. I. Mosqueda-Jiménez, A. Jentys, K. Seshan, J. A. Lercher, “On the Surface Reactions during NO Reduction with Propene and Propane on Ni-exchanged Mordenite”, *Applied Catalysis B: Environmental*, 46 (2003) 189–202.
- [131] K. Eränen, F. Klingstedt, K. Arve, L. E. Lindfors, D. Y. Murzin, “On the Mechanism of the Selective Catalytic Reduction of NO with Higher Hydrocarbons over a Silver/Alumina Catalyst”, *Journal of Catalysis*, 227 (2004) 328–343.
- [132] P. Sazama, L. Capek, H. Drobna, Z. Sobalik, J. Dedecek, K. Arve, B. Wichterlova, “Enhancement of Decane-SCR-NO_x over Ag/alumina by Hydrogen. Reaction Kinetics and In Situ FTIR and UV–vis Study”, *Journal of Catalysis* 232 (2005) 302–317.
- [133] R. Raj, M. P. Harold, V. Balakotaiah, “NO Inhibition Effects During Oxidation of Propylene on Cu-chabazite Catalyst: a Kinetic and Mechanistic Study”. *Industrial Engineering Chemistry Research*, 52 (2013) 15455–15465.

- [134] R. Q Long, R. T. Yang, “In Situ FT-IR Study of Rh–Al–MCM-41 Catalyst for the Selective Catalytic Reduction of Nitric Oxide with Propylene in the Presence of Excess Oxygen”, *Journal of Physical Chemistry B*, 103 (1999) 2232-2238.
- [135] L. Čapek, K. Novoveská, Z. Sobalík, B. Wichterlová, L. Cider, E. Jobson, “Cu-ZSM-5 Zeolite Highly Active in Reduction of NO with Decane Under Water Vapor Presence: Comparison of Decane, Propane and Propene by In Situ FTIR”, *Applied Catalysis B: Environmental*, 60 (2005) 201-210.
- [136] N. Sivasankar, H. Frei, “Direct Observation of Kinetically Competent Surface Intermediates upon Ethylene Hydroformylation over Rh/Al₂O₃ Under Reaction Conditions by Time-Resolved Fourier Transform Infrared Spectroscopy”, *Journal of Physical Chemistry C*, 115 (2011) 7545-7553.
- [137] P. S. Metkar, M. P. Harold, V. Balakotaiah, “Experimental and Kinetic Modeling Study of NH₃-SCR of NO_x on Fe-ZSM-5, Cu-chabazite and Combined Fe- and Cu-zeolite Monolithic Catalysts”, *Chemical Engineering Science*, 87 (2013) 51-66.
- [138] J. S. McEwen, T. Anggara, W. F. Schneider, V. F. Kispersky, J. T. Miller, W. N. Delgass, F. H. Ribeiro, “Integrated Operando X-ray Absorption and DFT Characterization of Cu–SSZ-13 Exchange Sites during the Selective Catalytic Reduction of NO_x with NH₃”, *Catalysis Today*, 184 (2012) 129–144.
- [139] U. Deka, I. Lezcano-Gonzalez, B. M. Weckhuysen, A. M. Beale, “Local Environment and Nature of Cu Active Sites in Zeolite-Based Catalysts for the Selective Catalytic Reduction of NO_x”, *ACS Catalysis*, 3 (2013) 413–427.

- [140] J. Liu, X. Li, Q. Zhao, C. Hao, D. Zhang, "Insight into the Mechanism of Selective Catalytic Reduction of NO_x by Propene over the Cu/Ti_{0.7}Zr_{0.3}O₂ Catalyst by Fourier Transform Infrared Spectroscopy and Density Functional Theory Calculations", *Environmental Science Technology*, 47 (2013) 4528–4535.
- [141] N. W. Hayes, R. W. Joyner, E. S. Shpiro, "Infrared Spectroscopy Studies of the Mechanism of the Selective Reduction of NO_x over Cu-ZSM-5 Catalysts", *Applied Catalysis B: Environmental*, 8 (1996) 343-363.
- [142] J. Szanyi, J. H. Kwak, H. Zhu, C. H. F. Peden, "Characterization of Cu-SSZ13 NH₃ SCR catalysts: an In Situ FTIR Study", *Phys. Chem. Chem. Phys.* 15 (2013) 2368–2380.
- [143] D.-J. Liu, H. J. Robota, "On the Mechanism of NO Selective Catalytic Reduction by Hydrocarbons over Cu-ZSM-5 via X-ray Absorption Spectroscopic Study", *Journal of Physical Chemistry B*, 103 (1999) 2755-2765.
- [144] L. Kevan, J. S. Yu, "Copper ion Catalysis of Complete and Partial Oxidation of Propylene on X and Y zeolites: Correlation of Electron Spin Resonance and Product Analysis", *Res. Chem. Int.* 15 (1991) 67-80.
- [145] M. -Y. Kim, J. -S. Choi, M. Crocker, "Roles of C₃H₆ in NH₃ Generation and NO_x Reduction over a Cu-chabazite SCR Catalyst under Lean/rich Cycling Conditions", *Catalysis Today*, 231 (2014) 90-98.

- [146] I. Langmuir, "The Mechanism of the Catalytic Action of Platinum in the Reactions $2\text{CO} + \text{O}_2 = 2\text{CO}_2$ and $2\text{H}_2 + \text{O}_2 = 2\text{H}_2\text{O}$ ", *Transactions of the Faraday Society*, 17 (1922) 621.
- [147] Roberts, G. W., and C. N. Satterfield, "Effectiveness Factor for Porous Catalysts. Langmuir-Hinshelwood Kinetic Expressions for Bimolecular Surface Reactions," *Industrial & Engineering Chemistry Fundamentals*, 5 (1966) 317.
- [148] J. Wei, R. Becker, "The Optimum Distribution of Catalytic Material on Support Layers in Automotive Catalysis", *Advances in Chemistry Series*, 143 (1975) 116.
- [149] L. L. Hegedus, S. H. Oh, K. Baron, "Multiple Steady States in an Isothermal, Integral Reactor: The Catalytic Oxidation of Carbon Monoxide over Platinum-Alumina", *AIChE Journal*, 23 (1977) 632-642.
- [150] M. P. Harold, D. Luss, "An Experimental Study of Steady-State Multiplicity Features of two Parallel Catalytic Reactions", *Chemical Engineering Science*, 40 (1985) 39 -52.
- [151] M. P. Harold, M. E. Garske, "Kinetics and Multiple Rate States of CO Oxidation on Pt I. Model Development and Multiplicity Analysis", *Journal of Catalysis*, 127 (1991) 524-552.
- [152] S. E. Voltz, C. R. Morgan, D. Leiderman, S. M. Jacob, "Kinetic Study of Carbon Monoxide and Propylene Oxidation on Platinum Catalysts", *Industrial & Engineering Chemistry Product Research & Development*, 12 (1973), 294-301.

- [153] S. H. Oh, J. C. Cavendish, L. L. Hegedus, “Mathematical Modeling of catalytic Converter light off: Single-Pellet Studies”, *AIChE Journal*, 26 (1980) 935-943.
- [154] S. Salomons, R.E. Hayes, M. Votsmeier, A. Drochner, H. Vogel, S. Malmberg, J. Gieshoff, “On the Use of Mechanistic CO oxidation Models with a Platinum Monolith Catalyst”, *Applied Catalysis B: Environmental*, 70 (2007) 305–313.
- [155] A. Abedi, R. E. Hayes, M. Votsmeier, W. S. Epling, “Inverse Hysteresis Phenomena during CO and C₃H₆ Oxidation over a Pt/Al₂O₃ Catalyst”, *Catalysis Letter*, 142 (2012) 930–935.
- [156] C. Sola, A. Abedi, R. E. Hayes, W. S. Epling, M. Votsmeier, “Investigating Carbon Monoxide and Propene Oxidation on a Platinum Diesel Oxidation Catalyst”, *Canadian Journal of Chemical Engineering*, 9999 (2014) 1–10.
- [157] D. Bhatia, M. P. Harold, V. Balakotaiah, “Kinetic and Bifurcation Analysis of the Co Oxidation of CO and H₂ in Catalytic Monolith Reactors”, *Chemical Engineering Science*, 64 (2009) 1544-1558.
- [158] S. R. Gundlapally, V. Balakotaiah, “Analysis of the Effect of Substrate Material on the Steady-State and Transient Performance of Monolith Reactors”, *Chemical Engineering Science*, 92 (2013) 198-210.
- [159] S. Salomons, M. Votsmeier, R. E. Hayes, A. Drochner, H. Vogel, J. Gieshof, “CO and H₂ oxidation on a Platinum Monolith Diesel Oxidation Catalyst”, *Catalysis Today*, 117 (2006) 491–497.

- [160] M. Khosravi, C. Sola, A. Abedi, R. E. Hayes, W. S. Epling, M. Votsmeier, “Oxidation and Selective Catalytic Reduction of NO by Propene Over Pt and Pt:Pd Diesel Oxidation Catalysts”, *Applied Catalysis B: Environmental*, 147 (2014) 264-274.